DNA–SCHOTTKY DIODES FOR DETECTION OF ALPHA PARTICLES

HASSAN MAKTUFF JABER AL-**TA'II**

FACULTY OF SCIENCE

UNIVERSITY OF MALAYA

KUALA LUMPUR

2016

DNA-SCHOTTKY DIODES FOR DETECTION OF ALPHA PARTICLES

HASSAN MAKTUFF JABER AL-TA'II

THESIS SUBMITTED IN FULFILMENT OF
THE REQUIREMENTS FOR THE DEGREE OF
DOCTOR OF PHILOSOPHY

FACULTY OF SCIENCE
UNIVERSITY OF MALAYA
KUALA LUMPUR

2016

UNIVERSITY OF MALAYA
ORIGINAL LITERARY WORK DECLARATION

Name of Candidate: **HASSAN MAKTUFF JABER**

Registration/Matric No: **SHC130012**

Name of Degree: **Doctor of Philosophy**.

Title of Thesis ("this Work"):

DNA-SCHOTTKY DIODES FOR DETECTION OF ALPHA PARTICLES

Field of Study: **Radiation Physics**

 I do solemnly and sincerely declare that:

(1) I am the sole author/writer of this Work;

(2) This Work is original;

(3) Any use of any work in which copyright exists was done by way of fair dealing and for permitted purposes and any excerpt or extract from, or reference to or reproduction of any copyright work has been disclosed expressly and sufficiently and the title of the Work and its authorship have been acknowledged in this Work;

(4) I do not have any actual knowledge nor do I ought reasonably to know that the making of this work constitutes an infringement of any copyright work;

(5) I hereby assign all and every rights in the copyright to this Work to the University of Malaya ("UM"), who henceforth shall be owner of the copyright in this Work and that any reproduction or use in any form or by any means whatsoever is prohibited without the written consent of UM having been first had and obtained;

(6) I am fully aware that if in the course of making this Work I have infringed any copyright whether intentionally or otherwise, I may be subject to legal action or any other action as may be determined by UM.

Candidate's Signature   Date:

Subscribed and solemnly declared before,

Witness's Signature   Date:

 Name:

 Designation:

ABSTRACT

Physical properties of materials are significantly influenced by radiation, especially alpha radiation. When an energetic electron beam penetrates through a biomaterial such as deoxyribonucleic acid (DNA), various modifications occur according to the characteristics of the type of radiation involved. DNA, the blueprint of life, has in recent times been shown to feature exciting semiconducting behavior. It has opened-up great prospects in utilizing these DNA diodes in nanotechnology and nanoelectronics. Therefore, DNA electronics could allow for more sensitive, accurate and effective sensors to be developed and fabricated. The aims of this study were to develop a metal-semiconductor or Schottky diode and measure its electrical characteristics or diode parameters such as ideality factor, series resistance and barrier height under both the presence and absence of alpha radiation. These parameters were measured using conventional current-voltage (I–V) method, Cheung and Cheung's functions and modified Norde's function. The present work was conducted in three stages. The first involves utilizing DNA as a semiconducting material in three different metal-DNA-metal (MDM) structures. Aluminium (Al) thin film evaporated using thermal evaporation technique was used for fabricating the MDM structures; Al/DNA/Silicon (Si)/Al, Al/DNA/Indium tin oxide (ITO) and DNA/Al. Its electrical behaviors before and after exposure to alpha irradiation (up to 40 min or 0.24 Gy) were studied through its (I–V) response curves. Acquisition of the I–V curves demonstrated that the DNA based MDM diodes exhibited clear rectifying behavior. This was followed by the second stage, which involved real-time detection of alpha particle by means of the I–V–time profile using the Al/DNA/Al structure with 30 μm gap between the electrodes. We obtained the Φ barrier height value calculated by using the conventional method for non-radiated structure at about 0.715 eV, increasing to 0.737 eV after 4 min of radiation. Barrier height values were observed to increase after 20, 30 and 40 min of radiation, except for 6, 8 and 10 min, which registered a decrease of about 0.67 eV. This was in comparison with the Cheung and Cheung's method, which registered 0.6983 eV for non-radiated increasing to 0.7528 after 2 min of irradiation. The barrier height values meanwhile were observed to decrease after 4 min (0.61 eV) to 40 min (0.6945 eV). The study shows that conventional thermionic emission model could be practically utilized for estimating the diode parameters including the effect of series resistance. These changes in the electronic properties of the Al/DNA/Al junctions could therefore be utilized in the manufacture of sensitive alpha particle sensors. Finally, the last stage of this work involves utilizing the Al/DNA/Al structure as a humidity sensor based on the environmental conditions exposed to low and high doses of radiation under varying percentage relative humidity (%RH). We also examined the effect of different humidity conditions on the capacitive and resistive response of the Al/DNA/Al Schottky barrier structures when bombarded by time-dependent dosages of alpha particles. Results for the low doses observed generally pointed towards a decrease in the resistance value from the pristine to the radiated structures. A high of 1678 to a low of 6.523 KΩ and 1512 to 1.801 KΩ were observed for the non-radiated and 2 min of alpha irradiation, respectively. It was also demonstrated that under the effect of humidity, the capacitance of the DNA thin film increased from 0.05894 to 92.736 nF, with rising RH levels. These observations may suggest the exciting possibility of utilizing Al/DNA/Al Schottky barrier diodes as potentially sensitive humidity sensors.

ABSTRAK

Sifat-sifat fizikal bahan dipengaruhi dengan ketara oleh radiasi terutama radiasi alfa. Apabila pancaran elektron bertenaga tinggi menembusi bahan-bio seperti asid deoksiribonukleik (DNA), pelbagai pengubahsuaian berlaku mengikut jenis radiasi yang terlibat. DNA, iaitu pelan terperinci untuk benda hidup, sejak kebelakangan ini telah menunjukkan tingkah laku semikonduktor yang menarik. Ia telah membuka prospek yang besar dalam menggunakan diod DNA ini dalam teknologi nano dan nano-elektronik. Oleh itu, elektronik DNA mampu membuatkan sensor menjadi lebih sensitif, tepat dan berkesan untuk dibangunkan dan direka. Tujuan kajian ini adalah untuk membangunkan satu logam semikonduktor (atau Schottky diod), dan mengukur parameter elektrik diod berkenaan seperti faktor idealistis, rintangan siri dan ketinggian halangan dengan kehadiran dan ketiadaan sinaran alfa. Parameter ini diukur dengan menggunakan kaedah konvensional I–V, fungsi Cheung dan fungsi Norde yang diubahsuai. Kajian ini dijalankan dalam tiga peringkat. Peringkat yang pertama melibatkan penggunaan DNA sebagai bahan semikonduktor dalam tiga struktur logam-DNA-logam (MDM) yang berbeza. Filem nipis Aluminium (Al) disejat dengan menggunakan teknik penyejatan haba dalam mereka struktur MDM; Al/DNA/Silikon (Si)/Al, Al/DNA/Indium tin oksida (ITO) dan DNA/Al. Tingkah laku elektrik sebelum dan selepas pendedahan kepada sinaran alfa (sehingga 40 minit atau 0.24 Gy) dikaji melalui lengkuk tindak balas IV. Perolehan lengkuk IV menunjukkan bahawa DNA berasaskan diod MDM mempamerkan kelakuan rektifikasi yang jelas. Ini diikuti oleh peringkat kedua, yang melibatkan pengesanan masa nyata zarah alfa melalui profil IV-masa dengan menggunakan struktur Al/DNA/Al dengan jarak 30 µm di antara elektrodnya. Kami memperoleh nilai Φ ketinggian yang dikira dengan menggunakan kaedah konvensional bagi struktur yang tidak dipancarkan pada kira-kira 0.715 eV, dan meningkat kepada 0.737 eV selepas 4 min pancaran radiasi. Nilai-nilai ketinggian halangan diperhatikan meningkat selepas 20, 30 dan 40 min radiasi, akan tetapi pada 6, 8 dan 10 minit, ia mencatatkan penurunan sebanyak kira-kira 0.67 eV. Dapatan ini dapat dibandingkan dengan kaedah Cheung yang mencatatkan nilai 0.6983 eV bagi yang tidak dipancarkan, dan meningkat kepada 0.7528 selepas 2 min penyinaran. Nilai-nilai ketinggian halangan sementara itu diperhatikan berkurangan selepas 4 min (0.61 eV) - 40 min (0.6945 eV). Kajian ini menunjukkan bahawa model konvensional pelepasan ion haba boleh digunakan untuk menganggar parameter diod termasuk kesan rintangan siri. Perubahan dalam sifat-sifat elektronik daripada simpang Al/DNA/Al ini boleh digunakan dalam pembuatan sensor sensitif kepada alpha zarah. Akhir sekali, peringkat terakhir kerja-kerja ini melibatkan penggunaan struktur Al/DNA/Al sebagai sensor kelembapan berdasarkan keadaan persekitaran yang terdedah kepada radiasi dos rendah dan tinggi dengan peratusan kelembapan (%RH) yang berbeza-beza. Kami mengkaji kesan keadaan kelembapan yang berbeza pada kapasitif dan rintangan tindak balas daripada halangan Schottky struktur Al/DNA/Al apabila dibedil dengan dos zarah alfa. Keputusan yang diperhatikan untuk dos rendah umumnya menunjukkan penurunan nilai rintangan dari struktur murni kepada struktur yang dipancarkan. Nilai rintangan yang tinggi 1678 ke paras 6.523 KΩ dan 1.512-1.801 KΩ telah diperhatikan untuk masing-masing yang tidak dipancar dan 2 min dengan pancaran sinar alfa. Ia juga menunjukkan, bahawa di bawah %RH yang meningkat, kapasitan filem DNA nipis juga meningkat dari 0.05894 ke-92.736 nF. Pemerhatian ini mencadangkan potensi yang menarik bagi diod Schottky Al/DNA/Al sebagai sensor yang sensitif kepada kelembapan.

ACKNOWLEDGEMENTS

TABLE OF CONTENTS

LIST OF FIGURES

LIST OF TABLES

LIST OF SYMBOLS AND ABBREVIATIONS

AFM   :   Atomic Force Microscopy

SFM   :   Scanning Force Microscopy

SEM   :   Scanning Electron Microscopy

STM   :   Scanning Tunneling Microscopy

DNA   :   Deoxyribonucleic Acid

UV-Vis   :   Ultraviolet-visible

FESEM   :   Field Emission Scanning Electron Microscopy

NGs   :   Nano Gaps

A   :   Adenine

G   :   Guanine

C   :   Cytosine

T   :   Thymine

dsDNA   :   Double Stranded DNA

ssDNA   :   Single Stranded DNA

LUMO   :   Lowest Unoccupied Molecular Orbital

HOMO   :   Highest Occupied Molecular Orbital

EF   :   Fermi Level

PE   :   Photoelectric Effects

CMOS   :   Complementary Metal–Oxide–Semiconductor

DC   :   Direct Current

RF   :   Radio Frequency

I–V   :   Current-Voltage

PECVD   :   Plasma Enhanced Chemical Vapor Deposition

CPD   :   Critical Point Dryer

DOF	:	Depth of Focus
PGMEA	:	Propylene Glycol Monomethyl Ether Acetate
MEMS	:	Micro Electro Mechanical Systems
EGA	:	Ethylene Glycol Acetate
E_g	:	Band Gap Energy
eV	:	Electron Volt
PVD	:	Physical Vapor Deposition
MDM	:	Metal-DNA-Metal
ITO	:	Indium Tin Oxide
CVD	:	Chemical Vapor Deposition
PL	:	Photoluminescence
SWCNT	:	Single-Walled Carbon Nanotube
LEEPS	:	Low-Energy Electron Point Source
α	:	Alpha Particles
PCR	:	Polymerase Chain Reaction
CNTs	:	Carbon Nanotubes
Pt	:	Platinum
min	:	Minute
hr	:	Hour
PEDOT:PSS	:	Poly(3,4-ethylenedioxythiophene):poly(4-styrenesulfonic)

LIST OF SYMBOLS AND ABBREVIATIONS

Activation Energy (eV)	:	E_a
Average Cross-section (cm) ^{2}	:	A
Boltzmann's Constant (j/K)	:	K
Concentration of DNA (ng/nL)	:	C
Current (A)	:	I
Diode Ideal Factors	:	n
Distance Between the Electrodes (nm)	:	d
Effective Mass (gr)	:	m*
Electron Affinity (eV)	:	$q\chi$
Electron Charge (C)	:	q
Fermi Level (eV)	:	E_F
Hopping Distance (nm)	:	a
Intrinsic Resistance (Ω)	:	R
Length of the DNA (nm)	:	L
Length of the Primer (nm)	:	N
Number of Junctions along a Percolated Path	:	M
Planck's Constants (j.s)	:	H
Potential Barrier Height (eV)	:	Φ_b
Richardson Constant (Acm^{-2}K^{-2})	:	A*
Relative Humidity (%)	:	RH
Schottky Barrier height (eV)	:	Φ_B
Sequence Length (nm)	:	L_{DNA}
Series Resistance	:	R_S

Source Measurement Unit : SMU

Thermal Voltage (eV) : V_{Th}

Tunneling Decay Length (nm) : B

Work Function (eV) : ϕ_m

LIST OF APPENDICES

Appendix A: Results of different experiments

Appendix B: Values of Richardson constant.

Appendix C: Supplementary

CHAPTER 1: GENERAL INTRODUCTION

1.1 Introduction

In recent years, deoxyribonucleic acid (DNA) has been used in interesting applications in various fields (Dugasani et al., 2015). Such applications have been reported since Watson and Crick first discovered the structure of DNA in 1953 (J. Watson & Crick, 2003). However, the fact that their model of the DNA molecule directly resulted from the observations of the X-ray diffraction patterns acquired by Franklin Rosalind (Klug, 1968) cannot be ignored.

DNA is central to every living organism and is a subject of interest for its physical properties, particularly for many potential applications in photonics and molecular electronics (Al-Ghamdi et al., 2012). DNA can be synthesized artificially and extracted from living organisms in a pure form. It is a stable molecule even under high temperature conditions (90°C) (Al-Ghamdi et al., 2012; Gupta & Saraf, 2009). The DNA molecule is also considered an interesting engineering material due to its self-assembling capability (Rothemund et al., 2004). Over the past few decades, DNA research has developed into an important area of research due to their potential applications in molecular electronics, biosensors, computer architectures and massive memories (Kulkarni et al., 2013). DNA molecules are known to have electrical properties and recently, their technological applications have become one of the hottest topics (Deng et al., 2006; Förch et al., 2009). In addition, it was reported that short fragments of DNA form self-assembled structures on substrate surfaces via connections between the edges (Doi et al., 2012).

DNA forms the blueprint of life and it is one of the most promising materials because of several unique advantages, including the capability to form a nanometer-scale molecular film, its adjustable length and it's self-assembly property. Understanding the mechanism of electrical conduction through a DNA molecule is

essential for electronic device applications. Furthermore, charge transport in DNA molecules is also related to the radiation damage and repair mechanism of DNA in biological contexts (Sönmezoğlu et al., 2010).

Adleman was the first person to suggest utilizing the DNA molecule and its self-assembling abilities as computational elements (Adleman, 1994). The self-assembly can also be utilized to create artificial DNA structures. DNA has had a significant effect on molecular electronics because of its two famous characteristics, namely the self-assembly and recognition of the molecule (Wagenknecht, 2005). Two important developments in science and technology have facilitated the collaboration between the fields of biology and molecular electronics.

These developments have paved the way for molecular biology to extend to interdisciplinary applications outside biology (Seeman, 2003; Seeman & Belcher, 2002). Molecular electronics has become a significant emerging research field. Research pathways can be divided into two main parts. First depends on the analysis of electron transport within single molecules to determine the probability of observing any physical effects on molecular scales. Second is the search for new materials and methods to assemble molecular electronic devices, as described by (Braun & Keren, 2004). Another part of this work involves investigating the radiation sensitivity of an Al/DNA/Al structure (DNA-built devices) to determine its suitability as a suitable candidate for radiation impact detectors/sensors.

In this work, we employed semiconducting DNA-based Schottky structures as sensors for alpha radiation using the principles of a metal-semiconductor diode. Radiation as a particle can interact with DNA causing double strand breaks (DSBs), which causes etched particle tracks due to the imprints of the strands on the surface. First, an aluminum (Al) thin film was deposited on the strand surface before the

radiation. Second, we use an LCR meter to measure the capacitance and resistance of

DNA during irradiation under humidity conditions.

1.2   Background and Scope

The DNA molecule, which is important in Biology because it contains the genetic

code of all living species, has recently caught the attention of chemists and physicists. A

major reason for this interest is the potential use of DNA in nanoelectronic devices, both

as a template for assembling nanocircuits and as an element of such circuits. Listed

below are some important research papers (**Table 1.1**).

Table 1.1: Some scientific papers published on DNA sensors.

Year	Title and Summary	References
2007	Photoelectrical effect and current-voltage characteristics in DNA metal Schottky barriers. The first observation of unusual photoelectrical effects under visible and near infrared illumination and the diode-type rectifying (I–V) characteristics of the DNA-metal devices. These phenomena can be attributed to the contacts in a DNA-metal semiconductor, namely, the Schottky barriers. The observed photoelectrical effect was measured ~1.52 eV Schottky barrier height for DNA-gold contacts.	(Grote & De Yu 2007)
2008	DNA-based organic-on-inorganic semiconductor Schottky structures. The DNA-based structure showed rectifying behavior, demonstrating that DNA was a semiconductor-like material with a wide optical band energy gap of 4.12 eV and resistivity of 1.6×10^{10} Ω.cm, which is indicative of p-type conductivity.	(Ö. Güllü et al., 2008)
2009	Electrical and interface properties of Au/DNA/n-Si organic-on-inorganic structures. The results show that the interface state density decreases with decreases in both the film thickness and coverage rate of the DNA in an acetate buffer, thus modifying the electronic parameters of the Au/DNA/n-Si diodes.	(Okur et al., 2009)
2010	Electrical characteristics of DNA-based metal-insulator-semiconductor structures. This structure showed excellent rectifying behavior with a	(Sönmezoğlu et al., 2010)

3

Year	Title and Summary	References
	typical ideality factor of 1.22 and the DNA film increased the effective barrier height by influencing the space charge region of Si.	
2011	p-Si/DNA photoconductive diode for optical sensor applications. The photo response of the Al/p-Si/DNA/Ag diode is better than that of the Al/p-Si/Ag diode. The ideality factor and barrier height values of the Al/p-Si/DNA/Ag diode were 1.2±0.1 and 0.56±0.02 eV, respectively.	(R. K. Gupta et al., 2011)
2011	DNA strand patterns on Aluminium thin films. A new patterning method using DNA strands capable of producing nanogaps of less than 100 nm was proposed and investigated. The chemical etching method was used in this work for obtain the nanogap without the need for lithography method. When the DNA strands transfer directly onto thin film of Al on silicon (Si) substrate and the chemical interactions between the DNA strands and Al lead to produces nanometer scale after 20 min in random shape. This method is considered to be simple and cost effective that can be employed in microelectronics and nano-bioelectronics.	(Khatir et al., 2011)
2012	Series resistance controlling photo sensor of Ag/DNA/p-Si/Al diode. The series resistance of the diode decreased with increasing light intensity and increased with decreasing frequency under constant light intensity. Ideality factor and barrier height of the diode were found to be 2.26 and 0.72 eV, respectively.	(R. Gupta et al., 2012)
2012	Current density-voltage analysis and interface characterization in Ag /DNA /p-InP structures. The structure showed excellent rectifying behaviour. The values of the main electrical parameters of these structures, such as ideality factor (n), barrier height and average series resistance, were found to be 1.087, 0.726 eV and 66.92 Ω, respectively.	(Güllü et al., 2012)
2013	Charge-controlled fixation of DNA molecules on silicon surface and electro-physical properties of Au–DNA–Si interface. In this report, the structures Au–DNA–(n-Si) were investigated using I–V and frequency-dependent admittance measurements. The result indicated that the charge density was controlled by the electronic states determined by the Fermi level of the metal and by the enhanced diode quality, which was also increased by the presence of a molecular mesh at the interface. However, the charge density was controlled by the electronic states through the semiconductor and was increased by the presence of molecular ropes. Finally, the DNA phosphate groups contacted or were close to the substrate surface.	(Bazlov et al., 2013)
2013	A novel nanometric DNA thin film as a sensor for alpha radiation.	(Kulkarni et

Year	Title and Summary	References
	The morphological changes and optical responses of artificially designed DNA thin films in response to exposure to alpha radiation were observed. The significant changes in the reflected intensity of the exposed DNA thin film suggest that a thin film made of biomolecules can be a promising candidate for the development of online radiation sensors.	al., 2013)
2014	Dual detection of ultraviolet and visible lights using a DNA-CTMA/GaN photodiode with electrically different polarity. This work showed that DNA-CTMA/n-GaN could be utilized as a photodiode in the visible and ultraviolet regions of light. The light source could be determined using the I–V curve, particularly by examining the polarity and the photocurrents. These two factors could determine the type of charge transport in the DNA-CTMA (dependent on the light wavelengths) and the charge contacts between DNA-CTMA and n-GaN.	(M. S. P. Reddy et al., 2014)
2014	Real time measurement of DNA degradation under radiation by silicon Nano-tweezers (SNT) coupled with microfluidic cavity. The authors utilized one of the methods for enhancing radiation therapy and understanding the biophysical mechanism of radiation damage on DNA. SNT sensing of the resonant properties could be utilized to measure the DNA degradation and to damage DNA molecules. The authors calculated the DNA rope rigidity, the DNA degradation and the number of equivalent DNA molecules through the SNT measurement of the resonant frequency with a trapped DNA bundle.	(Chiang, 2014)
2015	Rectification of DNA films self-assembled in the presence of electric field. This work determined the electrical characteristics of an ITO/DNA/Al device with and without alignment to an electric field. The rectifying behaviour increased after alignment, suggesting that the orientation of DNA strands affects the conductivity because the alignment of the electric field with the DNA films affects the barrier height, ideality factor and series resistance. Thus, this device could be used to fingerprint different types of DNA strands and could be useful for biomedical technology applications.	(Chan et al., 2015)

1.3   Motivations

A biosensor is a device that transforms a biological response into an electrical indicator. It can therefore be used to examine biological samples (e.g., virus, tissue and bacteria), changes in environmental systems (water, acid rain and humidity) and industrial products.

Advancements in technology have led to increasing demand for DNA-driven electronic devices. The application of a combination of biotechnology and electronics to obtain nanomaterials resulted in the development of high-precision and extra-sensitive nanobio-electronic devices, which found useful applications in medical science, defense and safety (Saxena & Satheesh, 2013). Previous studies used DNA molecules as sensor in micro- and nanoelectronics, but nothing has been reported about the use of DNA as a radiation sensor or detector.

This study investigated the use of DNA molecules as radiation sensors by detecting electrical current through the molecules. The main purpose of this study was to examine the possibility of DNA molecules for industrial and medical applications. These applications include radiation sensors, radiation monitoring devices and hypersensitivity phenomena detection.

1.4 Objectives

The main aim of this research is to investigate the electrical properties of metal-DNA-metal device under the influence of an external alpha (α) radiation. In order to achieve this main aim, several specific objectives have been identified as follows;

i) Investigate the DNA-Schottky behavior using different materials (Al, ITO and Si wafer)

ii) Investigate the potential barrier and assess the saturation current and the I_s behavior under different doses of alpha irradiation.

iii) Evaluate the series resistance behavior under different dosages.

iv) Investigate the humidity response of the Al/DNA/Al device for different doses of radiation.

v) Investigate the real time response of the Al/DNA/Al device for different doses of radiation.

1.5   Thesis Outline

The thesis is organized into 5 chapters. Chapter 1 provides an introduction to the subject and objectives of the research and provides an outline of the thesis.

Chapter 2 meanwhile highlights and reviews the major literature regarding different aspects of the research. Some basic theories and previous studies related to this research are discussed in detail.

Chapter 3 discusses the experimental details of this research work and it also focuses on the thin film deposition and device fabrication methods. This chapter highlights measurement and various characterization techniques and the theoretical features of some characterization tools are also discussed here.

Chapter 4 describes the electrical characterization of the DNA. In particular, the investigation is based on the electrical features determined from the I–V curves of Al/DNA/ITO, Al/DNA/Si and Al/DNA/Al. A Keithley 236 Source Measurement Unit (SMU) is utilized to supply the voltage and to measure the resulting current of the devices. Three different methods: conventional, Cheung and Cheung's and Norde's methods, that are used to determine the electronic parameters of the diode (e.g., the ideality factor, n, effective barrier height, Φ_b and series resistance R_s) are explained in detail here. All experimental data are analyzed and discussed in depth.

Finally, chapter 5 outlines a number of important conclusions that can be drawn from this research and future works. A summary of the research methodology that has been carried-out in this work is as shown in **Figure 1.1**.
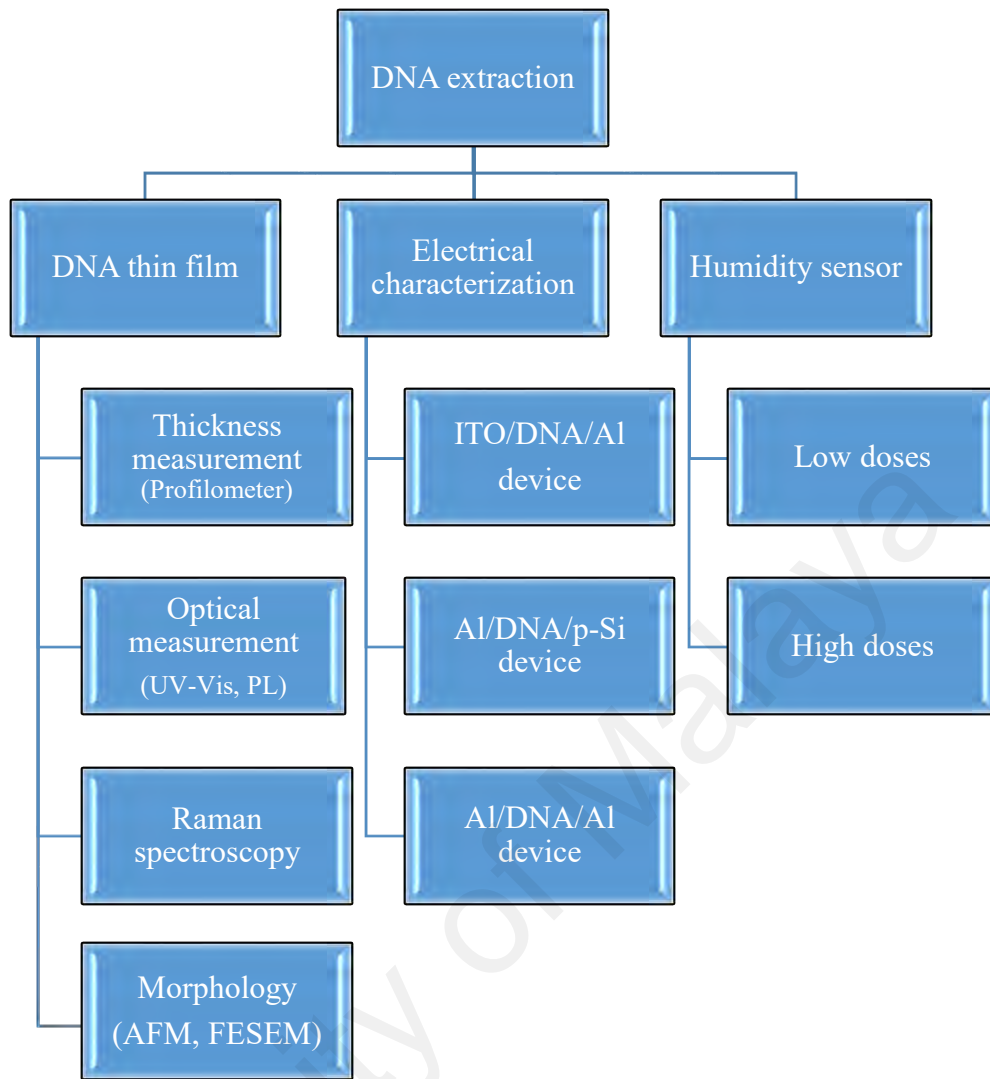
Figure 1.1: Summary of the research methodology.

CHAPTER 2: LITERATURE REVIEW

2.1 Introduction

The biggest challenge for researchers to manufacture very tiny electronic devices has been resolved in the past few years. The solution actually required a significant change in the process of fabricating electronic circuits (Vu et al., 2010). This dilemma seemed to be a limiting step in the development of some of these devices. The solution came from the arrangement of DNA, which was attractive to all the researchers because DNA has electrical conduction properties. DNA has been used in all fields, including engineering, chemistry, physics, biology, computer science and biomedical research, because of its extremely small size, rapid development and high energy efficiency. Additionally, DNA has two significant characteristics. Self-assembly properties and electronic features. Thus, DNA can be used practically in nanostructures fabrication (Gates et al., 2014; Sun & Kiang, 2005). DNA can also be used as a template for materials such as palladium and silver nanowires (Al-Hinai et al., 2016; Bhalla et al., 2003).

2.2 Biological Effect of Ionizing Radiation

2.2.1 Introduction to DNA

DNA is a nucleic acid that has the genetic instructions required for an organism to develop, survive and reproduce. DNA is also found in the mitochondria, which is considered to be the energy houses. The amount of this DNA here is however smaller compared to DNA found in the cell nucleus. Chemical building blocks that form DNA are called nucleotides. DNA consists of three components; a sugar (deoxyribose) group, one of four types of nitrogen bases and a phosphate group. **Figure 2.1** shows the structures of the nitrogen bases, which are adenine (A), thymine (T), guanine (G) and cytosine (C) (Massey, 2005).
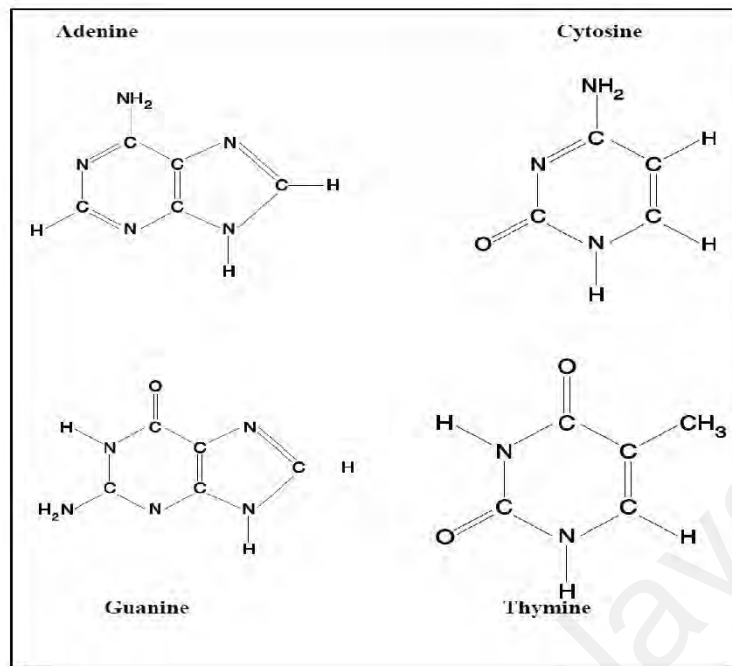
Figure 2.1: Types of bases; thymine (T), cytosine (C), adenine (A) and guanine (G) (Massey, 2005).

The three-dimensional structure of DNA is presented in **Figure 2.1**. DNA bases connect in a particular fashion in which C pairs with G and A with T, known as the base-pairing rules. All bases have a sugar-phosphate as a backbone. The backbone is assembled from alternating phosphate molecules and ribose sugars that are extremely polar. Since the backbone is polar, it is hydrophilic and can be immersed in water. The resulting two long strands form a twist termed a double helix determined by the arrangement of the nucleotides. The width of DNA is approximately 2.37 nm and the width shows little variation with base structure. Distance between one base pair and the next is 0.33 nm. The helix pitch is the distance to complete one turn of the helix and is approximately 3.4 nm. This pitch does not depend on the base conformation.

2.3 Structure of DNA

DNA is an essential part of cells in living organisms and is in charge of the genetic information. It is packed into structures in cells called chromosomes and

consists of monomer units called nucleotides. Each nucleotide in turn contains a 5-carbon sugar ring (deoxyribose), a nitrogenous base (one of four types) linked to the sugar and a phosphate backbone, as shown in **Figure 2.2**. DNA polymer is known as a polynucleotide (Ohayon, 2011). The negatively charged sugar-phosphate chain system forms a spine and each sugar is attached to one base. DNA can be classified into two types. For double-strand break (dsDNA), collections of two nucleotides can be connected to form two sugar-phosphate spines via their bases, which hydrogen bond together to form a base pair. In contrast, for the single-strand break (ssDNA), individual nucleotides connect to form one sugar-phosphate backbone.

DNA has four different types of nucleotides that are parts of two groups, pyrimidines and purines. The following have been found in DNA; adenine (A) and guanine (G) are purines, whereas cytosine (C) and thymine (T) are pyrimidines. **Figure 2.2**(a) presents the chemical structure and general design of DNA (Hughes, 2008; Ohayon, 2011).

DNA has self-assembly and excellent recognition capable features due to the complementary nature of its base pairs. Additionally, there are particular geometric requirements for the formation of hydrogen bonds between heterocyclic amines. A probable application of this (hydrogen bonding principle) is the heterocyclic amine base pairing. **Figure 2.2**(a) shows T-A pair connections via two hydrogen bonds denoted as (T=A) and also shows that the C-G pair connects through three hydrogen bonds abbreviated as (C-G); these characteristics are shown in **Figure 2.2**(b).
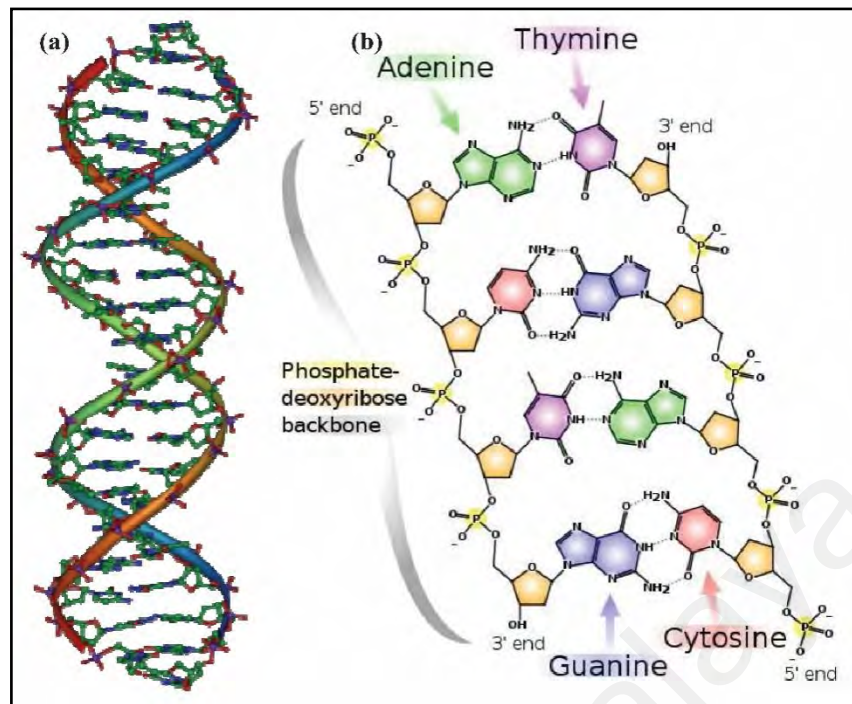
Figure 2.2: (a) View of DNA double helix construction and (b) chemical construction of DNA (Saenger, 1984).

2.3.1 Watson - Crick Model for DNA Structure
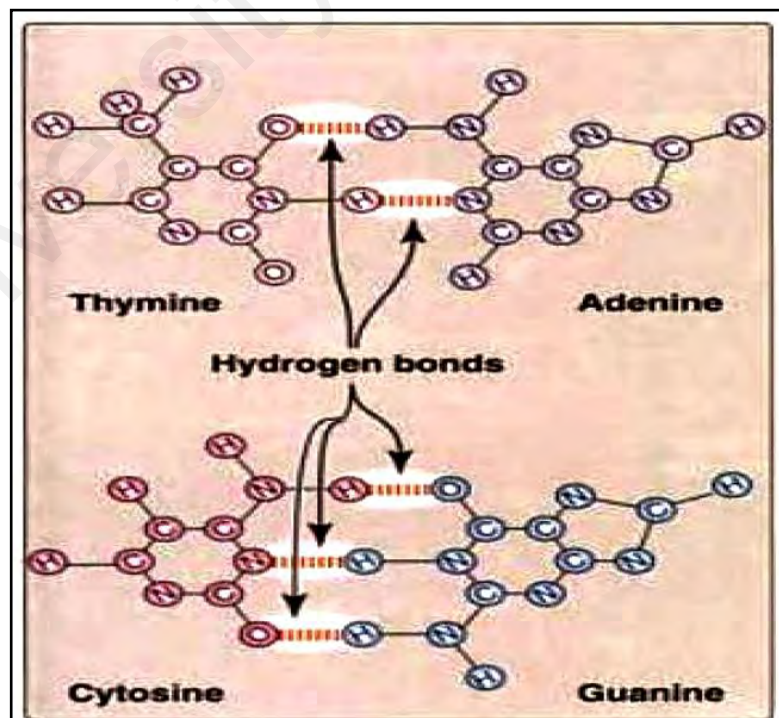
Figure 2.3: A-T and C-G structures (Champe et al., 2005).

In 1953, Watson and Crick suggested a configuration for double-stranded DNA (dsDNA) with hydrogen bonding either between cytosine and guanine or between adenine and thymine. Thus, two DNA single strands form a double-stranded helical. **Figure 2.2**(a) shows a double-stranded helix structure of DNA and **Figure 2.3** shows the hydrogen bonding between two coupled base pairs in DNA. The important point is that only certain pairs of bases will fit into the structure (J. D. Watson & Crick, 1953), as illustrated in **Figure 2.3**.

2.3.2 Conductivity in DNA

DNA molecules play an important role in all living species and in recent time have been utilized in nanoelectronic instruments (Esfandyarpour et al., 2016). This possibility encourages researchers in physics and chemistry to frequently utilize DNA in molecular electronics (Lund et al., 2016; Singh et al., 2005). It is easy to synthesize DNA in any type of sequence that might be needed due to its self–assembly characteristics and the highly specific binding between single strands of DNA because of charged backbone, low thermal and chemical stability (J. Lu et al., 2009; Maeda et al., 2001; Tans et al., 1998).

The intrinsic conductivity of DNA has been an unsolved problem. Previously, experimental results demonstrated all types of conductivities, such as Ohmic, insulating (De Pablo et al., 2000; Porath et al., 2000; Storm et al., 2001; Y Zhang et al., 2002) ,superconductivity (Murakami, 1992) and semiconducting properties (Y. Okahata et al., 1998; Slinker et al., 2011; Yoo et al., 2001).

The conductivity effect occurs through several factors that play a significant role. Examples of these factors include the DNA sequence, the length of the DNA molecule, the type of DNA molecule (strands versus single molecules), environment of DNA (water, magnetic field and counter ions), microstructure of DNA (dependent on

humidity, stretching, or combing preparation conditions), interface characteristics (free-standing molecules or surface-bound DNA) and preparation protocols (Boutry, 2010; Požar, 2004).

2.4 Basic Theory

2.4.1 Schottky Barrier Height Based on DNA

The Schottky barrier, which exhibits rectification at a metal-semiconductor interface, is named after Walter Schottky, who developed the first model of barrier formation. Braun (Bethe, 1942) who is accredited with the discovery of the metal-semiconductor contact in 1874, is regarded as the founder of one of the oldest semiconductor devices. Since there, many experimental and theoretical studies have been performed. In 1938, Walter Schottky (Schottky, 1938) and Mott (Mott, 1938) independently observed and established the oldest model of potential barrier formation and rectification across the metal-semiconductor interface by calculating the height and the shape of the barrier. In the most important development, Bathe proposed thermionic emission during the Second World War (Bethe, 1942).

In the 1950s, thin film deposition was promoted by the development of high vacuum systems that provided more stable and reproducible contacts (Rhoderick & Williams, 1988). Thus, devices became smaller and faster and this change paved the way to a full understanding of the current transport at metal-semiconductor interfaces (Vick, 2011).

For most of the recently used Schottky diodes, the (diameter range of 10 μm-1 mm) was used, the connections were fabricated utilizing a variety of techniques, such as thermal evaporation, sputtering, electron beam evaporation and pulsed laser deposition, generally in high vacuum conditions to avoid oxidation of the metal (Allen, 2008).
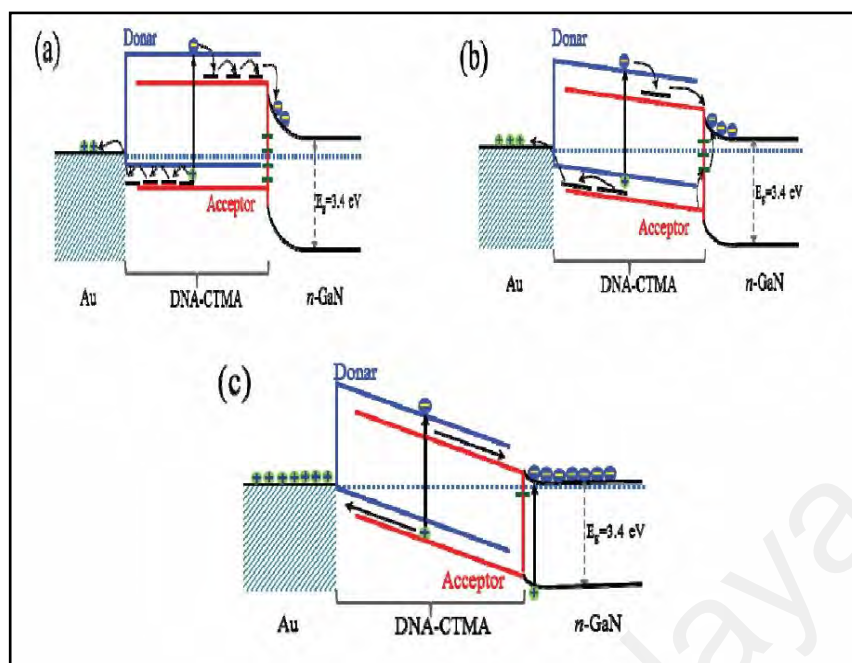
Figure 2.4: Energy band diagrams of DNA-based GaN photodiodes (DG-PDs) for (a) dark, (b) halogen and (c) UV illumination cases. (M. S. P. Reddy et al., 2014).

The materials that can be used for sensor fabrication exhibit semiconducting or conducting behaviour. These materials include silicon, ferrous and non-ferrous metals and alloys, ceramics, glasses, organic and nanomaterials (Dyakonov & Sariciftci, 2003). DNA displays semiconductor conduction upon connection with a metal (Dulić et al., 2009; Ö. Güllü et al., 2008; Khatir et al., 2014b; Roy et al., 2008). Based on the work of Reddy et al (M. S. P. Reddy et al., 2014) , schematic diagrams of the energy bands in a metal (gold) and an n-type semiconductor (n-GaN) in ideal conditions before and after contact under dark were obtained as shown in **Figure 2.4**.

2.5 Electrical Conduction of DNA

The electronic characteristics of DNA are affected by several factors, such as the DNA environment, DNA length, temperature, base pair sequence and contact with electrodes (Roy et al., 2008). All of these factors can determine whether DNA has the electrical characteristics of an insulator, semiconductor or conductor. DNA length affects the electrical characteristics because an increase in the DNA length leads to

15

more defects along the DNA molecule, thereby changing the π-orbital position and charge trap behaviour and causing the DNA to become an insulator. Environmental conditions play an important role in DNA conductivity. The conditions include vacuum and ambient environments. In vacuum, DNA exhibits high electrical resistance because fewer water molecules can pass through the DNA structure and alter the conductivity to match the environment. Temperature is one of the main factors that changes the resistance of the DNA placed between two electrodes. Temperature increases lead to an increase in charge mobility, thus increasing the DNA conductivity.

2.5.1 DNA as Insulator
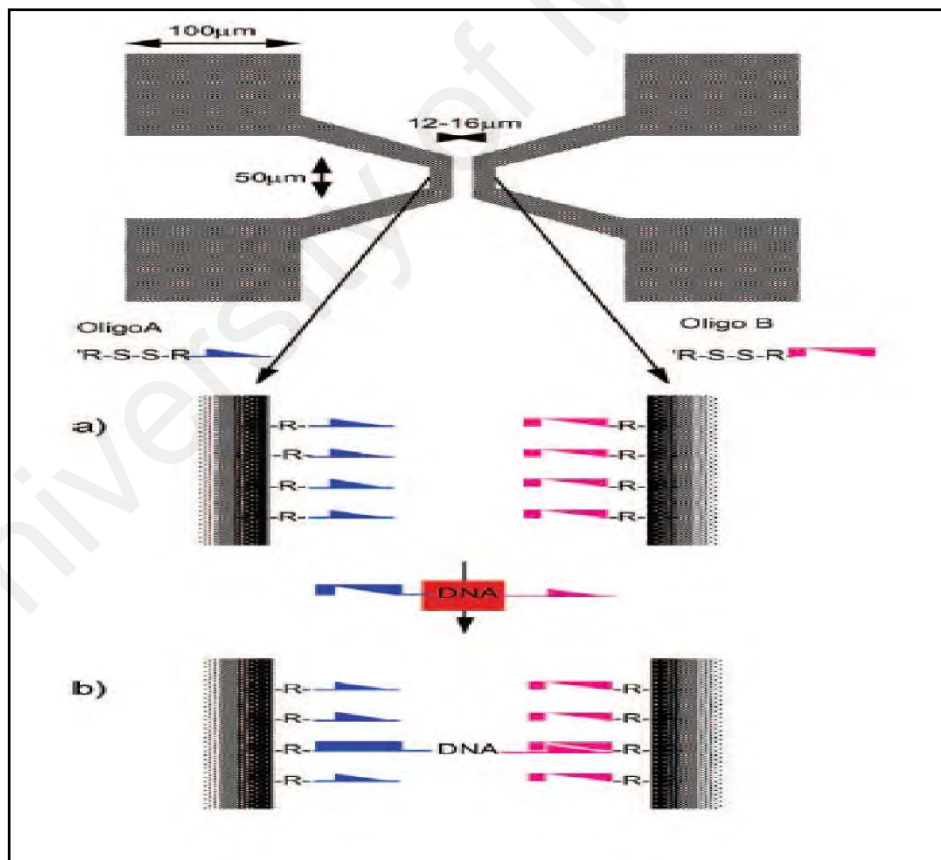
Figure 2.5: Structure of a silver wire linking two gold conductors. The top left picture displays the electrode pattern (0.53×0.5 mm) utilized in the tests. The two 50 μm long, parallel electrodes are linked to four (100×100 mm) bonding pads. (a) Oligonucleotides with two different sequences attached to the electrodes. (b) M-DNA bridge connecting the two electrodes. (Braun et al., 1998).

In 1998, Braun and his colleagues achieved the first electrical measurement by studying the electrical conduction of λ-DNA (Braun et al., 1998). The investigation was performed by placing λ-DNA between gold electrodes that were separated by 12 – 16 μm on a fabricated structure on glass substrate, as shown in **Figure 2.5**. The λ-DNA was connected to the electrodes by hybridizing two distant surface-bound 12-base oligonucleotides to a fluorescently labeled λ-DNA. That had two 12-base sticky ends, where each of the ends was complementary to one of the two different sequences attached to the Au electrodes. The authors obtained the I–V plot by using a device having an internal resistance of >100 GΩ and electrical measurements were made on the silver wire. The current was not detectable for voltages less than 10 V. From these results, it was concluded that DNA acted as an insulator.
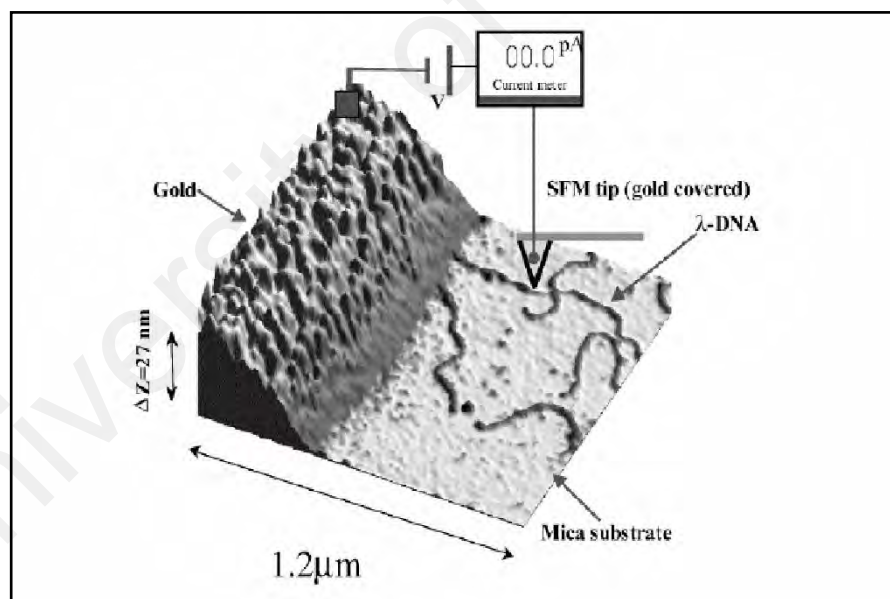
Figure 2.6: Schematic of an electrical circuit using gold-DNA-gold on a mica substrate and an SFM image (De Pablo et al., 2000).

De Pablo and his coworkers investigated the electrical conductivity of λ-DNA (De Pablo et al., 2000). The examination was performed by placing DNA molecules between two gold electrodes, deposited through thermal evaporation on a mica substrate that was 4 μm wide using a thin-wire shadow masking method. Another method

involves using a gold-coated tip for scanning force microscopy (SFM), as shown in **Figure 2.6.** A non-contact SFM image was taken of the left boundary of the mica canal. Silicon nitride cantilevers that were successively coated with 20 nm titanium and 60 nm Au layers were used as conductive cantilevers. I–V properties were measured for different distances to evaluate the indicated insulator behavior in the range of $0 – 10$ V without recording any current and the resistance was 1 GΩ.

The measured minimum DNA resistivity was approximately 10^4 Ω.cm. Furthermore, to improve the sensitivity of electrical measurements, the length of DNA molecules was increased approximately 15 μm and the DNA was placed between Au electrodes that were separated by approximately 3 μm. The number of DNA molecules was expected to be more than 1000. While bias voltage of up to 12 V was applied between electrodes, the current measured was below the noise level of 1 pA. The minimum resistivity (ρ) was calculated to be about 10^6 Ω.cm and the resistance was 10^{16} Ω/molecule.

Porath and his team investigated the electrical transportation properties through DNA (Porath et al., 2000). The measurement was performed using a fabricated surface device with a 10.4 nm length and a 30 base pair poly(G)-poly(C) DNA-based film by solution processing. DNA was located between platinum (Pt) separated by 12 nm gaps, as shown in **Figure 2.7**. From the I–V relationship that the authors obtained under two conditions, atmospheric and vacuum (10^{-6} Torr), the electrical conduction of DNA was observed, thus confirming that current was passing through the DNA. The results found using a voltage gap of approximately 2.0 V showed insulating features of DNA in two environments and the resistance was 2.0 GΩ. Electrical properties were also studied under different temperatures, ranging from 4.0-300 K. The curve of the differential conductance dI/dV against V displayed a peak structure, with a peak spacing of 0.1-0.5

eV. I–V curves for three different samples displayed a voltage gap at low temperature and the width of the gap increased with increasing temperature.
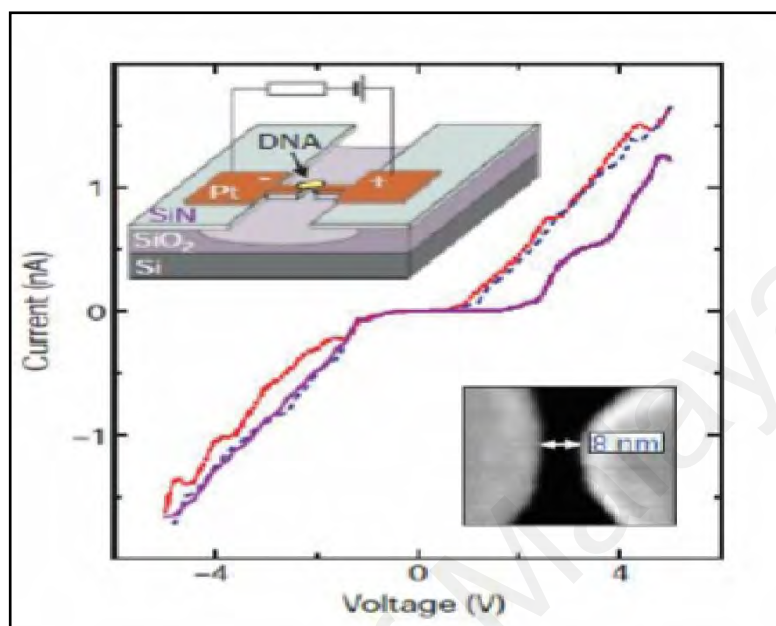
Figure 2.7: I–V plots for ssDNA. The top of the graph is a schematic diagram for the experimental device. The bottom shows a gap of 8 nm between two electrodes (Porath et al., 2000).

Storm with his group investigated and measured the electrical transport through poly(dG)-poly(dC) DNA (Storm et al., 2001). The examination was achieved by fabricating a poly(dG)-poly(dC) DNA-based film by solution processing and placing the film on the surface of Au/Ti electrodes separated by a 40–500 nm gap on SiO_2/mica, which acted as the substrate. This procedure involved using electron-beam lithography and a subsequent lift-off process, as shown in **Figure 2.8**. The electrical conduction of DNA was measured at room temperature under ambient conditions.

This study measured the electrical conduction of three groups. In the first group, the electrical conduction was measured through dsDNA placed between two gold electrodes with a gap of 300 nm on SiO_2, with a length and width of 0.5 and 10 nm, respectively. This device did not show any conduction through the DNA strand for voltages of up to 10 V, the recorded current record was less than 1 pA and the results

indicated a resistance of 1.0 TΩ. In the second group, the design was changed to use Pt electrodes and the gap was 40 nm. DNA conductivity was also not found in this group. In the third group, dsDNA was mixed with poly(dG)-poly(dC) and placed between Pt electrodes with spacing of 200 nm and 100 nm on a SiO$_2$ substrate. This case also showed a lack of electrical conduction through the DNA and the resistance was 1.0 TΩ. Collectively, these results indicate that DNA acted as an insulator for lengths greater than 40 nm.
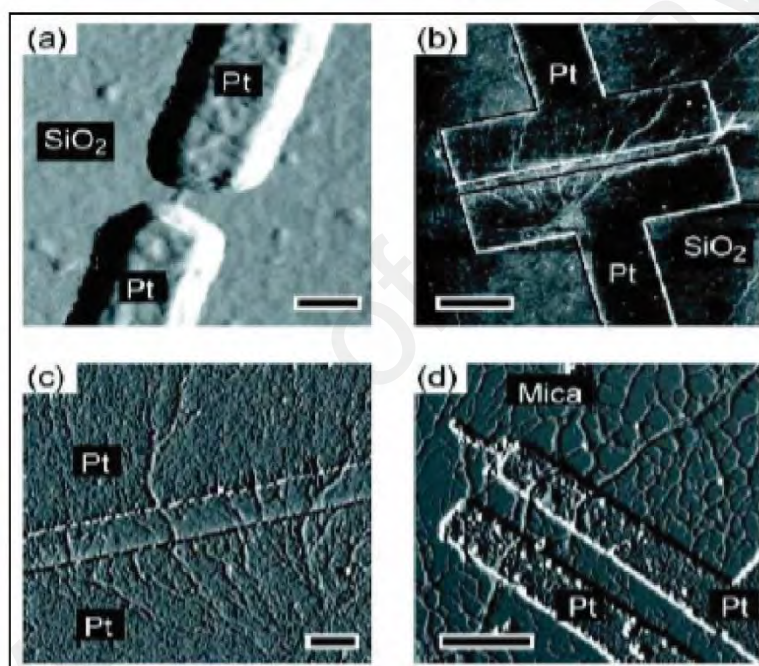
Figure 2.8: AFM images of several DNA assembly-based devices. The images show the absence of conduction. (a) Mixed sequence DNA between the two platinum electrodes on SiO$_2$ with a gap of 40 nm. Scale bar: 50 nm. (b) An image of poly (dG).poly(dC) DNA bundles on Pt electrodes. The platinum electrodes are separated by 200 nm and the scale bar is 1 mm. (c) High-magnification image of the device presented in (b). Some DNA bundles appear spread over the two electrodes. Scale bar: 200 nm. (d) Fabrication of two Pt electrodes on mica with poly(dG).poly(dC) DNA bundles placed on the electrodes. Scale bar: 500 nm (Storm et al., 2001).

Zhang and co-workers examined the electrical conductivity of DNA by utilizing DNA covalently connected to gold electrodes on the microscale (Y Zhang et al., 2002). The investigation was performed at the interface between the Au electrodes and DNA.

Then, a thiol group was used to link the Au-DNA-Au structures; the electrodes were separated by 4 μm and the thickness was 4 μm. All the measurements were performed in vacuum ($< 10^{-7}$ Torr) at 295 K and in the absence of buffer solution. The voltage was changed between -20 to 20 V, but the I–V curve does not show any current through the λ-DNA and Au electrodes; the resistivity was 10^6 Ω.cm at 20 V.

H.-Y. Lee and his team of co-researchers investigated the effect of oxygen and humidity on DNA conductance (H.-Y. Lee et al., 2002). The examination was performed under vacuum at 10^{-3} Torr. A structure was fabricated that contained Au/Ti electrodes separated by a gap of 100–200 nm on Si substrates by using electron-beam lithography and the double-angle evaporation technique. The drop casting method was used in these experiments for both poly(dC)-poly(dG) and poly(dA)-poly(dT) DNA films. The authors obtained an I–V plot and found that the resistance of the poly(dA)-poly(dT) DNA film was 2.0 GΩ, 10 times smaller than that of poly(dC)-poly(dG) in the air. Furthermore, the poly(dA)-poly(dT) DNA film was subjected to an oxygen ambient and the conductance was 10 times lower due to the lower oxidation potential of dG compared with that of dA.

Taniguchi and his colleagues investigated the electrical characteristics of poly(dA) poly(dT) and poly(dG) poly(dC) DNA thin films doped with iodine (I_2) molecules (Taniguchi et al., 2003). The experiment involved the fabrication of a structure containing gold electrodes separated by a gap of 30-50 nm on SiO_2 substrates using electron-beam lithography. The thickness of the electrodes was 50 nm. Then, an iodine layer was deposited on the gold/DNA/gold (GDG) structure under a vacuum of less than 10^{-5} Torr. The poly(dG)-poly(dC) and poly(dA)-poly(dT) DNA lengths were 1.7-2.9 μm and 0.5-1.5 μm, respectively. The authors measured the I–V relationship as a function of the iodine doping time and found that the current increased at longer doping times. Doped poly(A)-poly(T) had a lower current than that of the doped poly(dG)-poly(dC)

DNA. The I$_2$-doped poly(dA)-poly(dT) and poly(dG)-poly(dC) DNA formed conducting DNAs that showed a high conductivity of 0.1 and 30 nA, respectively, at 1 V for 20 hr. Finally, the authors demonstrated that charge transfer occurs between DNA and iodine molecules and the hole and ion current form the total current. In the same year, another work compared carbon nanotubes and the classical fabrication by determining the characteristics of the I–V curve (Zhou et al., 2003). From this information, it was concluded that the electrical resistivity was in the range of TΩ.
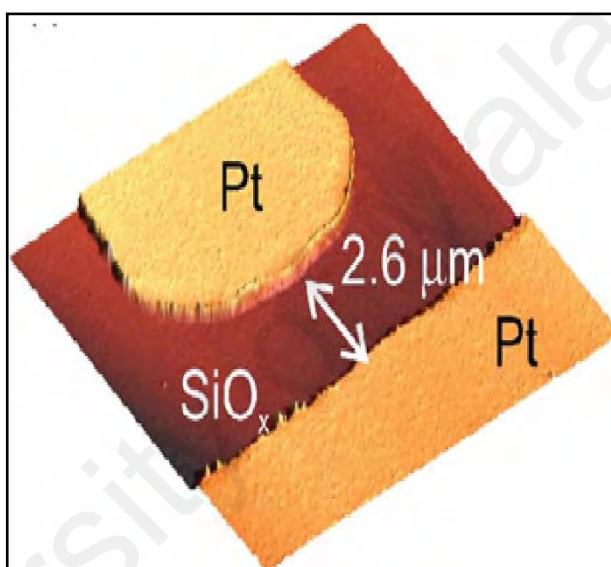
Figure 2.9: AFM image of two electrodes forming a 2.6 µm gap (Kleine et al., 2004).

The electrical features of a λ-DNA thin film was studied by Kleine and his co-workers in 2004 (Kleine et al., 2004). The investigation was performed using microscale fabrication technique to obtain a surface structure with platinum (Pt) electrodes separated by a 20-3000 nm gap on glass substrates. All the low I–V spectroscopy measurements were achieved under ambient conditions with a controlled low humidity. The authors measured the I–V curve as a function of the humidity, which ranged from 30-60% RH. DNA conductivity can be described by the ionic transport through capillary condensation in the vicinity of the deposited DNA molecules.

Furthermore, the I–V curve showed that the electrical conductivity decreased to 4×10^{-15} AV^{-1} μm^{-1} and the resistance (10^{15} Ω) was measured under a controlled argon atmosphere, as shown in **Figure 2.9**.

Almost all researchers used the technique described by Legrand (Legrand et al., 2006), who examined the dc electrical conductivity of dsDNA (Roy et al., 2008; Welch et al., 2011). The investigation was performed by fabricating gold nanoscale electrodes in the shape of a finger and separated by a gap of 70 nm, with a length of 1.0 μm and width of 160 nm on Si covered by 100 nm of SiO$_2$ substrate using electron-beam lithography. The measurement was performed in an aqueous environment and the authors concluded that the resistance of a DNA molecule was more than 100 GΩ in this condition, indicating insulating behavior.
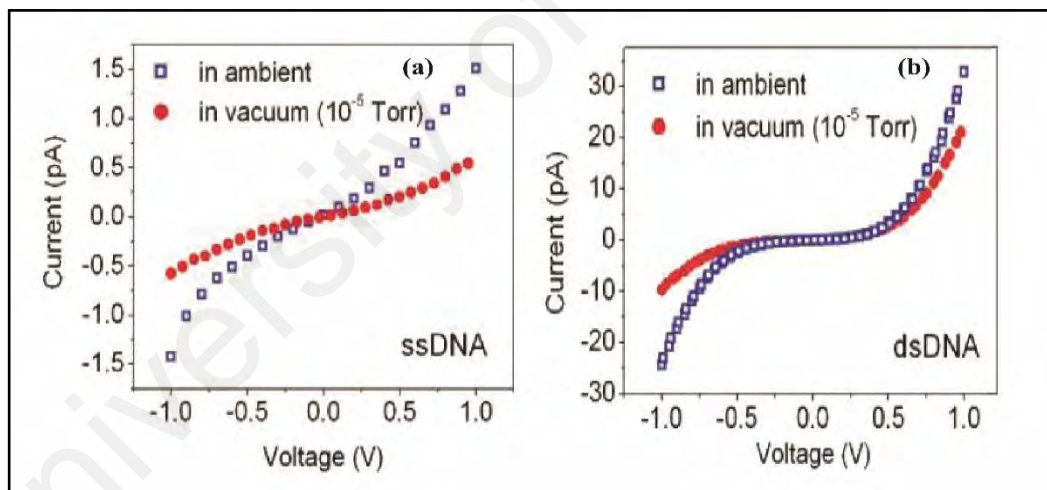
Figure 2.10: Current flow at room temperature through a single ssDNA molecule (Roy et al., 2008).

Additionally, Roy and his group investigated the electrical conductivity of ssDNA and dry dsDNA using SWNTs (Roy et al., 2008). The analysis was performed using nanoscale surface fabrication of a structure containing single-wall carbon nanotube (SWNT) electrodes separated by a 27 nm gap. Then, 80 base pairs of genomic DNA were added. The measurement was performed at a RH of 43%. Measuring the I–V curve

of the ssDNA, demonstrated that the dry dsDNA showed non-linear properties, a current between 24-40 pA at 1.0 V and a resistance from 25-40 $\times 10^{12}$ Ω. Results indicated semiconducting behaviour for the trapped DNA fragment encoding a specific gene but devoid of any periodic arrangement of the base pairs, as shown in **Figure 2.10**(a). High vacuum (10^{-5} Torr) measurements showed an increase in the resistance (50-65 GΩ) of the dsDNA molecule compared with that in ambient conditions, as shown in the figure. The gate voltage-dependent I–V properties indicated that the dsDNA between SWNTs and a drain electrode show p-type behaviour. ssDNA behaved as an insulator in this case due to the lack of a current, as shown in **Figure 2.10**(b).

2.5.2 DNA as Semiconductor

Y. Okahata and co-workers investigated the electrical conductivity of a DNA-aligned cast film (Y. Okahata et al., 1998). The study was performed by mixing salmon DNA with cationic amphiphiles. Polyion complex precipitates were then gathered and freeze dried. The resulting white powder was found to be only soluble in organic solvents. As such, the powder was dissolved in chloroform and reprecipitated two times using diethyl ether in a $CHCl_3$/ etOH solution and the product was deposited on a Teflon plate. After the solvent was evaporated, a transparent film was obtained. In the DNA-lipid complex film, DNA strands could be aligned in the same direction as the direction in which the film was stretched. Then, the film was placed on a comb-shaped Au electrode, as shown in **Figure 2.11** and DC conductivity was measured. The author analysed the I–V curve properties of the DNA film. In case 1, the DNA was aligned perpendicular to the gold electrodes and showed a high Ohmic current of approximately 0-4.1 μA and the current increased linearly under vacuum and atmospheric (10^{-1} mmHg (Torr)) conditions. In contrast for the DNA film in case 2, the DNA strands were aligned parallel to the electrodes and negligible current was observed. It was established

that electric current might pass through the stacked base pairs of the aligned DNA strands film. From these results, the electrical conductivity was determined to be 5.6 $\times 10^{-5}$ and 10^{-9} S.cm^{-1} for DNA that was immobilized in the parallel and perpendicular directions, respectively (Y. Okahata et al., 1998; Yoshio Okahata et al., 1998). Finally, when the experiment was performed in vacuum, the electrical resistance only changed to 10^7-10^8 Ω.cm (Yoshio Okahata et al., 1998).

In 1999, Fink & Schönenberger investigated the electrical conduction of λ-DNA (Fink & Schönenberger, 1999). Analysis was performed by placing a solution of λ-DNA chains into a hole made on gold and the sample was then coated with a carbon foil. The DNA solution contained 0.3 μg/ml DNA, 10 μM Tris-HCl and 1.0 μM EDTA (pH 8.0). After the buffer solution evaporated, the DNA molecules became connected and formed a shape along the holes. All the measurements of the DNA molecule were performed using a low energy electron point source (LEEPS) microscope. I–V measurement was performed at room temperature and in a vacuum of 10^{-7} Torr. The end of a metal-coated tip (tungsten) was used as another electrode to contact the DNA rope. From the I–V curve, two states can be deduced, as shown in **Figure 2.12**. For the 600 nm-long DNA molecule in **Figure 2.12**(a), the I–V curve was linear, with fluctuations in the range of ±20 mV. According to the I–V curve, the resistance was 2.5×10^6 Ω. **Figure 2.12**(b) shows parallel resistors that each had a resistance of 1.4×10^6 Ω. In other state 900 nm-long DNA molecule, the resistance was 3.3×10^6 Ω. The structures containing DNA molecules with these two lengths demonstrated good semiconductor characteristics and the semiconductor behaviour decreased as the DNA length increased. These results indicate that the ropes of DNA act as a semiconductor in the absence of radiation damage.
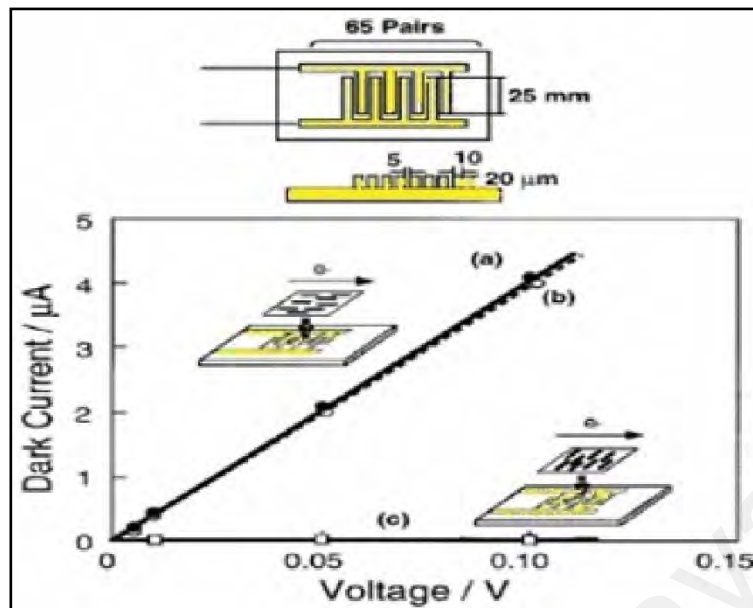
Figure 2.11: Dark current versus voltage for DNA stands that were parallel and perpendicular to the direction of a comb-like electrode (Y. Okahata et al., 1998).
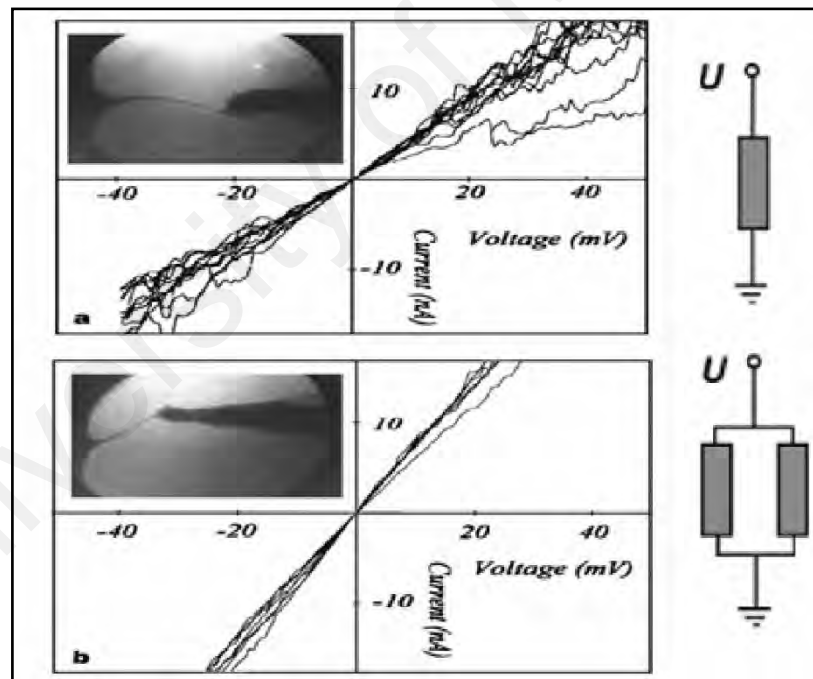
Figure 2.12: (a) I–V characteristics of a 600 nm long DNA rope and the (b) I–V plot of two DNA ropes attached to the AFM manipulation (Fink & Schönenberger, 1999).

Tran and his group also investigated the electrical conduction of λ-DNA (Tran et al., 2000). The analysis was performed using λ- DNA purchased from Sigma-Aldrich and BioLabs and the measurements were obtained without electrodes. This method is

similar to the well-known cavity perturbation method using microwave absorption (Tran et al., 2000). DNA conductivity was measured as a function of temperature based on the cavity loss when DNA was added to sensitive resonance of cavities at 12.0 and 100 GHz. DNA conductivity was observed to change with temperature in different environments (dry and buffer) as shown in **Figure 2.13**. Electrical conductivity decreased exponentially as the temperature was decreased to 200 K and then remained almost constant for T<200 K. The DNA conductivity was calculated from the formula $\sigma = \sigma_o \exp\left(-\Delta/2KT\right)$ where σ_o represents the DNA conductivity at room temperatures, T is the temperature, K is the Boltzmann constant and Δ represents the band gap. Values of the DNA band gap, Δ, that were calculated from the slopes were 0.3 and 0.33 eV in dry and buffer environments, respectively. The electrical conductivity values were meanwhile measured at 1.2×10^3 and 1.9×10^2 S.cm^{-1} for DNA in the dry and buffer environments, respectively. As such the value of the DNA conductivity in buffer was higher than the value for the dry DNA.
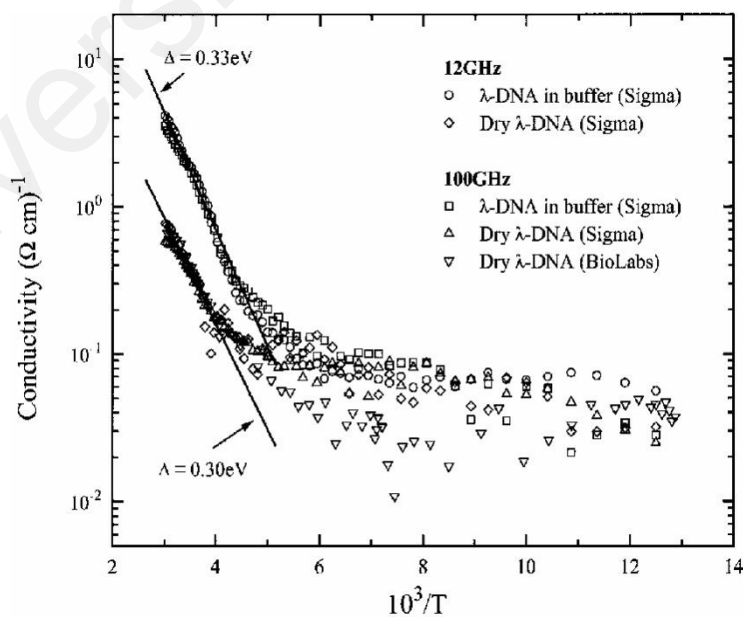
Figure 2.13: Conductivity-temperature variation of lambda DNA for two different conditions (dry and in buffer) at frequencies of 12 and 100 GHz (Tran et al., 2000).

In 2000, Cai and co-workers measured the electrical conductivity of poly(dG)-poly(dC) and poly(dT)-poly(dA) DNA networks (Cai et al., 2000). In this study a (250 ng/ml) DNA solution was prepared on a mica substrate in the presence of Tris–HCl buffer. First, the evaporation method was used to form a gold layer, which acted as an electrode, on one end of the DNA molecule. I–V properties were measured by applying a bias voltage of ±5 V between two types of electrodes, fabricating a structure with polynucleotides on a gold layer and using an AFM tip at room temperature (**Figure 2.14**(a)). Loading force of the AFM tip was controlled and ranged from 20-40 nN. The I–V curve was used to conclude that the resistance changed with the length of poly(dG)-poly(dC) and poly(dT)-poly(dA) DNA for the voltage range of ±0.2 V, as shown in **Figure 2.14**(b) This figure indicates that the resistance changes exponentially with DNA length and can be attributed to defects in the contact between two homogenous strands of poly(dG)-poly(dC) and poly(dT)-poly(dA) that ranged in length from 50-200 nm. The I–V curve also showed two different behaviours of poly(dG)-poly(dC) DNA.

Figure 2.14(c) displays the linear Ohmic behaviour and **Figure 2.14**(d) shows the rectifying characteristics for the 100 nm length. Otherwise, the I–V plot for the poly(dT)-poly(dA) DNA shows an S-shape. Finally, the results show a higher resistance for poly(dT)-poly(A) than for poly(dG)-poly(dC). The base sequence, poly(dG)-poly(dC) shows better conductance than does poly(dT)-poly(A) and therefore can act as a semiconductor nanowire.
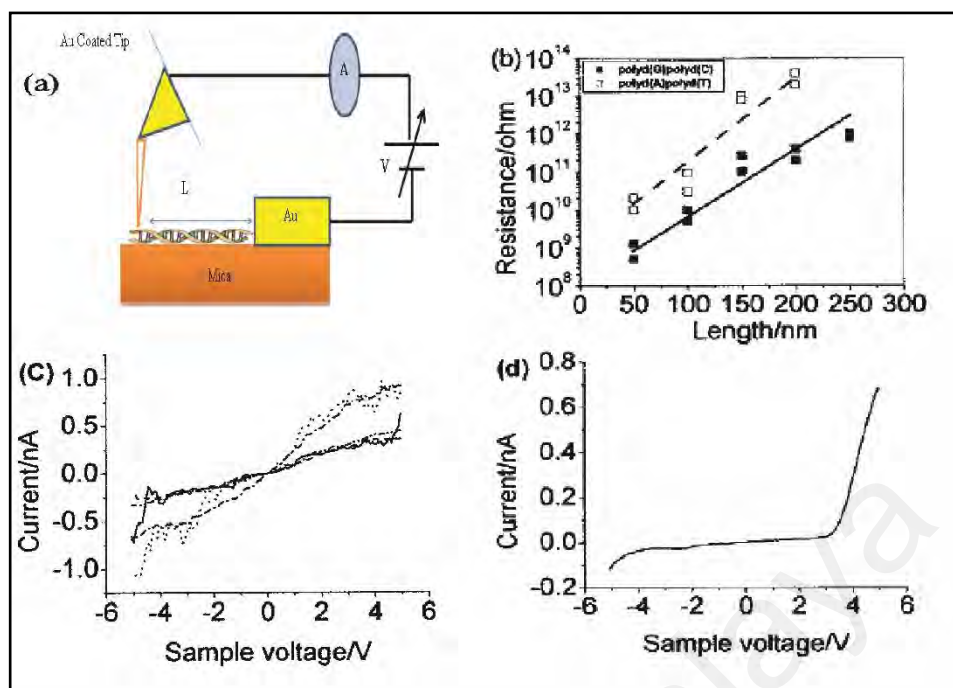
Figure 2.14: Diagram of the experiment for measuring the electric conduction with two gold electrodes. One electrode was connected to one end of a DNA molecule, the other was a gold-coated AFM tip. (b) Variation in the resistance with DNA length for two sequences, poly(dG)-poly(dC) and poly(dA)-poly(dT). (c) I–V characteristics of poly(dG)-poly(dC) with linear and Ohmic behaviour for L=100 nm (Cai et al., 2000).

In another work, the electrical conduction through poly(dA)-poly(dT) and poly(dG)-poly(dC) DNA molecules was investigated by fabricating a structure containing Au/Ti electrodes separated by a 20 nm gap on Si/SiO$_2$ substrates using electron-beam lithography (Yoo et al., 2001). DNA molecules were deposited between the electrodes using the trapping technique. The tested polynucleotides, poly(dA)-poly(dT) and poly(dG)-poly(dC) DNA molecules, were 1.7-2.9 µm and 0.5-1.5 µm long respectively. More than 20 samples were fabricated and the electrical features were measured under vacuum at various temperatures, ranging from 4.2 K to room temperature and ambient conditions. I–V plots as function of temperature are shown in **Figure 2.15**(a,b), which showed the linear behaviour at room temperature and the nonlinear behaviour at low temperature for poly(dA)-poly(dT). Electrical resistance was calculated from the I–V curve at room temperature, where the calculated resistance of 1.3 MΩ for poly(dG)-poly(dC) was less than the value for poly(dA)-poly(dT), which

was 100 MΩ. I–V properties were also studied at different gate voltages. For poly(dA)-poly(dT) at room temperature, the I–V curve demonstrated a more nonlinear shape for negative values of the gate voltage and the gap near zero voltage value increased. However, for positive gate voltages, the current showed a nonlinear shape and the gap was at 20 V. Poly(dG)-poly(dC) showed the opposite properties and the gap near zero voltage increased as the gate voltage changed from negative to positive (**Figure 2.15**(a-b)). The study indicated that poly(dA)-poly(dT) acts as an n-type semiconductor and poly(dG)-poly(dC) showed p-type behaviour.
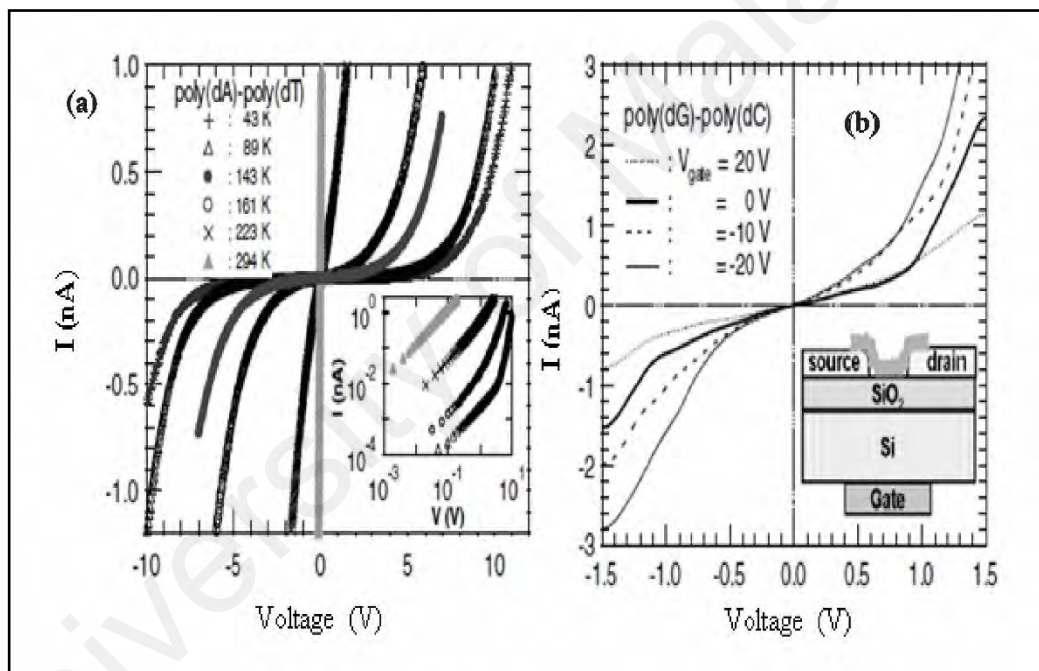
Figure 2.15: (a) I–V characteristics of poly(dA)-poly(dT) and poly(dG)-poly(dT) at different temperatures, (b) I–V relationship of poly(dG)-poly(dT) at different gate voltages and room temperature (Yoo et al., 2001).

Rakitin and his colleagues examined the electrical characteristics of two types of ropes, (B-DNA) and (M-DNA) (Rakitin et al., 2001). The investigation was performed by fabricating a structure containing Au electrodes separated by a gap of 1-30 μm on insulating substrates using electron-beam lithography. Four types of DNA were prepared in 20 mM NaBo3 buffer at pH 9.0 (or 20 mM tris, pH 7.5) with 10.0 mM NaCl

and 0.1 mM Zn^{2+} or 2 mM EDTA. The tested M-DNA contained a Zn metal ion that replaced the imino proton of every base pair. In total, 100 molecules of DNA were immobilized between the Au electrodes. Authors showed a semiconductor-like plateau at approximately 200 mV to B-DNA type (**Figure 2.16**), but M-DNA did not exhibit this type of plateau which were measured from I–V curve of B-DNA and M-DNA under vacuum (10^{-3} Torr). These results suggest that the qualitative difference in the I–V features of M-DNA and B-DNA samples at low values of bias could only be attributed to a difference in their conduction mechanisms.
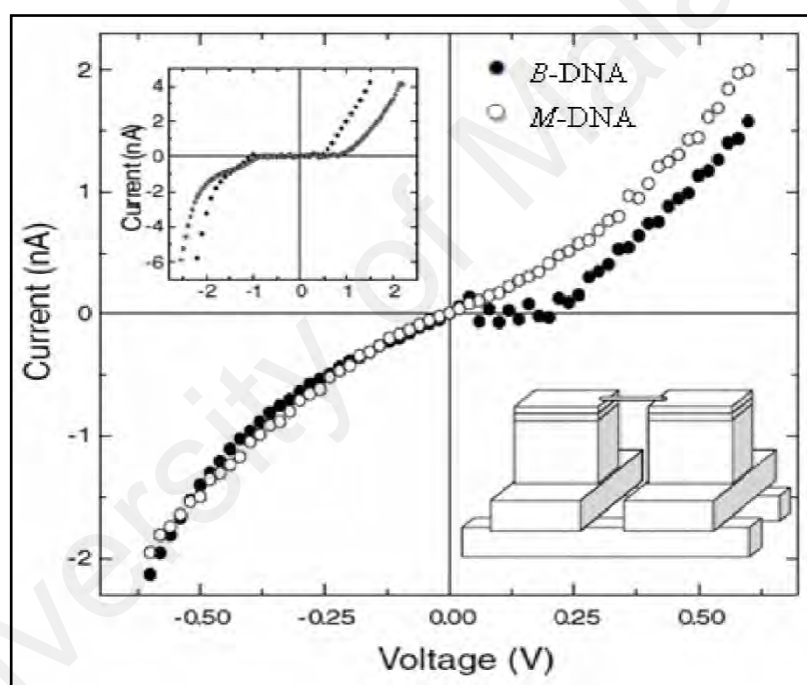
Figure 2.16: I-V plots for two types of DNA, M-DNA and B-DNA, under a vacuum condition at room temperature. The graph indicates a lack of a plateau in the I-V curve of M-DNA. In contrast, B-DNA displays a plateau. Length of the DNA fiber is 15 mm and the fibers are separated by 10 mm. At the bottom right is a schematic of the experimental set up. The upper left has two I-V plots of the sample structures measured in vacuum at room temperature (Au-oligomer-B-DNA-oligomer-Au in series) (Rakitin et al., 2001).

Researchers have also measured I–V features of nicked and repaired λ-DNA (Hartzell et al., 2003). The analysis was performed by fabricating a structure that contained Au /Cr electrodes (30 nm/8 nm thickness) separated by a gap of 8 μm on SiO$_2$

(450 nm thickness) substrates using electron-beam lithography. Samples were dried under a flow of N_2 gas. The measured linear λ-DNA had two short overhang regions that were 12 bases long on both sides that were complementary to single strands that were 12 bases long. Single strands were labeled with C3 using S–S disulphide groups at the 3′ ends. These single-stranded sequences were complementary to the 12 unpaired bases of each overhang region and were hybridized to these regions, effectively providing a complete and double-stranded molecule with a gap in each strand. The DNA could be repaired by removing the phosphate group at the 5′ ends and utilizing an alkaline phosphate group to avoid circularization of the λ-DNA. I–V curve was measured by applying an AC voltage under ambient conditions at room temperature. The resulting I–V curve shows a nonlinear shape, with a conductivity gap of up to ±3 V. However, for the repaired λ-DNA, the I–V relationship was linear, indicating Ohmic behaviour. The electrical conductivity of the repaired λ-DNA was 3×10^{-3} $(\Omega.cm)^{-1}$. Changes in the conductivity rely on the different conditions such as changes in the geometry of the connection, the number of strands and the electrical contact nature could be in the range of 6×10^{-4}-3×10^{-3} $\Omega.cm^{-1}$.

Xu and co-workers measured the electrical conductance of single thiolated poly(GC)-poly(GC) DNA molecules (Xu et al., 2005). The investigation was performed using 12 bp, thiolated poly(GC)-poly(GC) DNA that was placed on gold (111) and the measurements were obtained at ultrahigh vacuum, 10^{-10} Torr. I–V plot was obtained from different DNA locations by using scanning tunneling spectroscopy (STS) and concluded that the DNA did not exhibit any electrical conductivity features. The separation between the tip, the sample and the applied voltage of STS can affect the test. To avoid this problem, the normalized conductance (dI/dV)/(I/V) was calculated from digital I–V data using a simple offset method. Conductance sharply increased at two

different positions; the lower (LUMO) and higher (HOMO) edges at -1.33 V and +1.55 V respectively. The DNA band gap was 2.88 eV, indicating semiconductor behaviour.

Venkatramani and colleagues measured the I–V relationship and the photoconductivity of a DNA thin film (Venkatramani et al., 2009). The inspection was achieved by using salmon DNA (13-19 µm thickness) that was placed between two layers: the top and bottom electrodes of gold/copper and ITO, respectively (with 1000 Å and 700 Å thickness). A photocurrent was generated with a 0.75 mW laser at 605 nm. I–V relationship was measured and the current was found to be nonlinear at the voltage of ±1.1 V, with slight rectification at ≤ ±0.3 V. The measured resistance was 17.6 MΩ. Various hypotheses were proposed for the observed photoresponse, such as ionic and electron/hole transport mechanisms driven by a combination of different intrinsic potentials and photoinduced potentials. The accumulated charge that was injected from the metal at the DNA-metal interface was proposed as a cause for the photoinduced response.

Güllü and others meanwhile evaluated the electrical properties of an Al/DNA/p-Si structure (Ö. Güllü et al., 2008). It was achieved by placing a genomic DNA solution between the top and bottom electrodes, which were Al (inorganic) and a p-type silicon wafer (semiconductor). First, 10 µl of DNA solution was added to the front of the Si substrate. The solution evaporated after 24 hr and the thickness of DNA thin film obtained was 59.1 nm. All the electrical characteristics were measured at room temperature and in the dark. From the I–V curve obtained the Al/DNA/p-Si junction displayed rectifying behaviour. The barrier height (Φ) and ideality factor were 0.76 eV and 2.86, respectively, as determined using the thermionic or conventional method. Cheung and Cheung's method meanwhile was used to determine the ideality factor and the series resistance, which was measured at 3.93 and 2.86 KΩ, respectively, from the dV/d(ln I) plot. Barrier height and series resistance were also calculated to be 0.76 eV

and 2.83 KΩ, respectively, from the H(I)-I plot. The Barrier height value was calculated to be 1.52 eV from the capacitance-voltage plot. Optical absorbance spectrum demonstrated that the DNA film behaved as a semiconductor the optical energy band gap was 4.12 eV and the resistivity of DNA was $1.6 \times 10^{10} \Omega.cm$.

In other works Guo et al., and Feldman et al., measured the electrical conductivity of a single DNA duplex bridging a carbon nanotube gap (Feldman et al., 2008; Guo et al., 2008) . The strategy was established using a surface device that was fabricated from a DNA film by solution processing. The film was placed between SWNTs on n-type silicon semiconductor substrates using chemical vapour deposition (CVD). DNA sequences were modified with amines on either the 5′ terminus or both the 3′ and 5′ terminus and these samples were coupled to SWNTs electrodes through amide linkages. Electrical characteristics of the device were analysed by measuring the I–V relationship. The device showed a resistance of 0.1-5.0 MΩ for a 6 nm length of dsDNA. These resistance indicated semiconductor characteristics for the DNA. A single mismatch of GT or CA in a 15-mer DNA increased the resistance of the duplex 300-fold relative to the resistance of the corresponding sample without the mismatch. Resistance was measured between $0.5\text{-}155 \times 10^{6}$ Ω, indicating insulating features. Authors believed that the DNA was able to exhibit conduction over significant distances, enabling the direct measurement of the resistance of a single well-matched DNA molecule.

The evaluation of the electrical conductivity of a single DNA bridging a gold layer was carried-out by Dulić and co-workers (Dulić et al., 2009). The verification was produced using a surface device that was fabricated from a DNA film by solution processing, where the film was located between the junction of gold electrodes and conventional electron beam lithography was used. A mechanically controllable break junction (MCBJ) device was fabricated on a Kapton substrate. Planar dimensions were 20 mm × 6 mm and the substrate thickness was 0.5 mm. The surface was then coated

with a layer of polyimide using the spin coating method. Sequences of the DNA1 and DNA2 samples contained 42% and 75% CG content, respectively. Sample was placed between the gold electrodes in the MCBJ device, as shown in **Figure 2.17**(c).
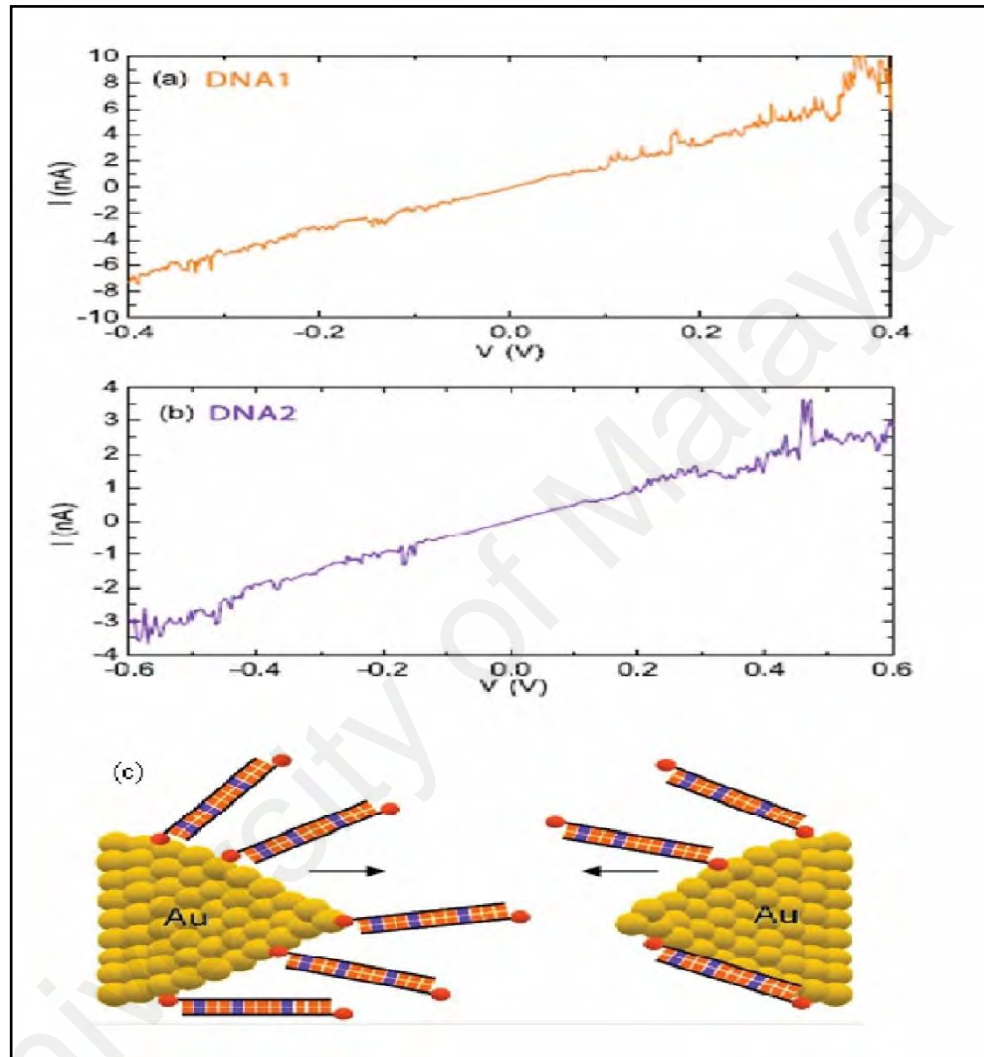
Figure 2.17: (a) I–V relationship of DNA1 and (b) DNA2, which were placed between two gold electrodes of the MCBJ. (c) The diagram shows the gap between the two gold electrode structures (Dulić et al., 2009).

This study used two different 12 bp DNA molecules; DNA1, which contained three separate A:T pairs and DNA2, which contained three islands with two adjacent A:T pairs and one separate A:T pair. Measurement was performed in a dry environment. Researchers obtained the I–V curve for DNA1 and DNA2 (**Figure 2.17**(a) and (b)), which shows the Ohmic behaviour of these DNA samples and the equivalent linear fits

yielded conductance values of 17 ns for DNA1 and 4.7 ns for DNA2. These results indicate that conductance of DNA1 appears to be higher than that of DNA2 due to the greater GC content, which improves the DNA structure. Additionally, these results indicate the semiconductor characteristics of these DNA.
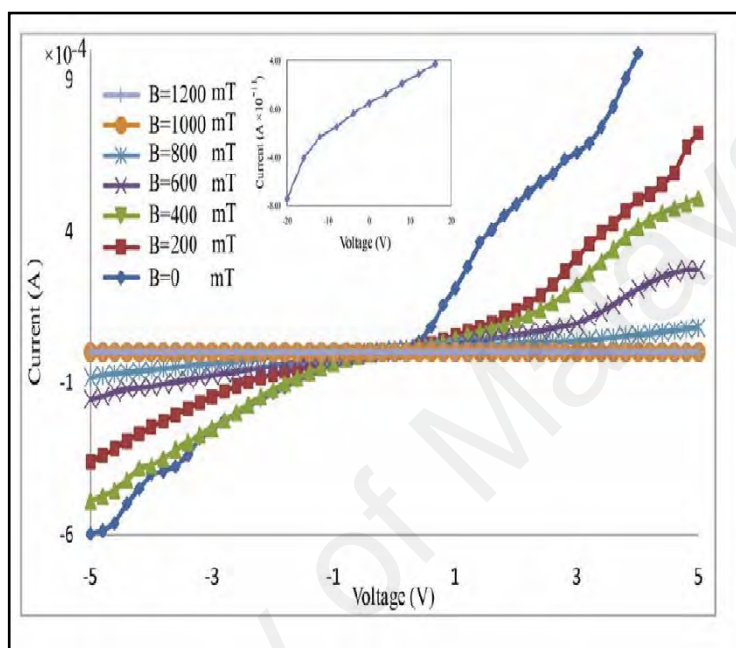
Figure 2.18: The relation between the current and voltage versus magnetic field (Khatir et al., 2012).

In a work in our laboratory (LDMRC) in 2012, the I–V properties of an Au-DNA-Au junction under a magnetic field was investigated (Khatir et al., 2012). The study was performed using a surface device that was fabricated by dropping 70–100 µl to create a DNA film by solution processing. The resulting film was located between gold electrodes on Si/SiO$_2$ substrates created using the UV-lithography method. GDG junction was placed vertically in a magnetic field. DNA that was extracted from *Boesenbergia rotunda* had the following content; A (22%), T (20%), G (35%) and C (23%). Magnetic field ranged from 0-1200 mT with increases in steps of 200 mT. I–V graphs for the GDG junction were obtained under the different magnetic fields which demonstrated rectifying behaviours. The current grew exponentially with voltage, as

shown in **Figure 2.18**. As such, the DNA strands exhibited semiconductor behaviour. The barrier height increased with increases in the magnetic field with the value of the barrier height being 0.878 eV in the absence of magnetic field.
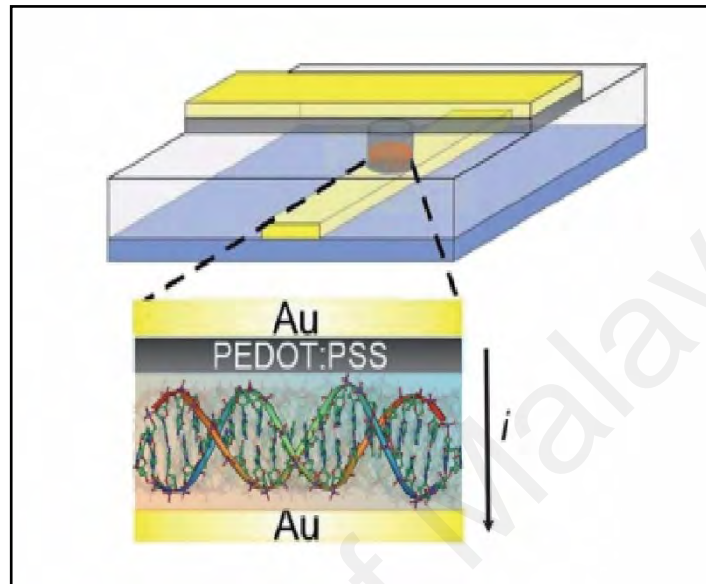
Figure 2.19: Diagram showing the construction of the Au/DNA/PEDOT:PSS/Au device. The cross charge transport was measured through the DNA molecule and the diameter ranged from 5 μm to 100 μm (Katsouras et al., 2013).

The nature of charge transport in DNA was studied by Katsouras et al., who investigated the charge transfer through a single DNA in a molecular junction that had a large area (Katsouras et al., 2013). This was achieved using a sandwich device that was fabricated from a DNA film by solution processing, with the film located between gold electrodes and the PEDOT:PSS polymer (**Figure 2.19**). Gold layer was deposited through the conventional electron beam deposition technique. Conducting polymer of the PEDOT:PSS layer was prepared using the spin coating method and deposition on the DNA. DNA molecules had various lengths (14, 22 and 30) and were incubated for different times. Using the I–V profile, resistance of the diode that only contained PEDOT:PSS diode was lower than the fabricated diode containing Au/PEDOT:PSS/double-stranded DNA/Au when the DNA was incubated for a short

time. Plot of the log of the current density versus the voltage indicated a linear relationship between the current and the area of the device measuring between 5 and 100 µm in diameters. Resistance of the DNA layer, as calculated from the I–V plot, was 4.0 MΩ.µm^2.
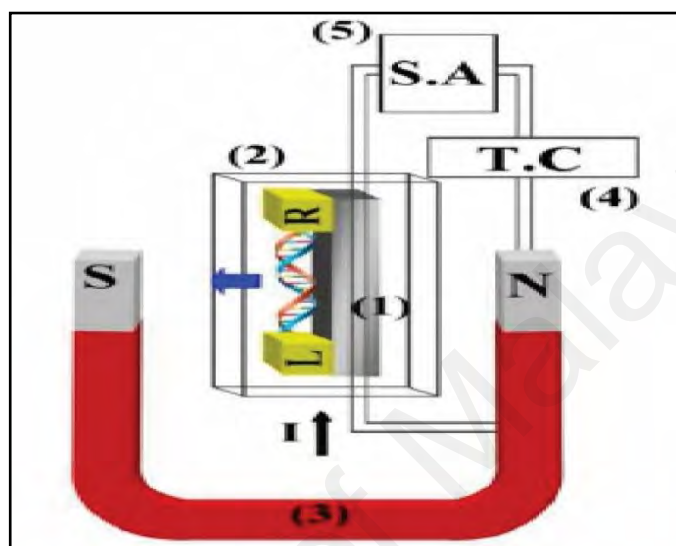
Figure 2.20: Schematic diagram with the following labels,(1) chip holder and connection to a dewar, (2) cryostat system, (3) magnetic field generator and detector, (4) temperature controlling (T.C.) device and (5) semiconductor analyzer for I–V measurement (Khatir et al., 2014a).

In another work by Khatir and co-workers, the I–V properties of a Au/DNA/Au junction in the presence of external electromagnetic and thermal fields was studied (Khatir et al., 2014b). The consideration was done using a fabricated surface device. Solution processing was used to place a DNA film between gold electrodes (100 nm thickness) separated by a gap of 10 µm on Si/SiO$_2$ substrates created using the UV-lithography method. using the same DNA source and content from her previous work (Khatir et al., 2012) was placed vertically in a magnetic field (**Figure 2.20**). Magnetic field was varied from 0-1200 mT with increases of 200 mT and the temperature was also varied (25–55°C). I–V graphs for the GDG junction under magnetic fields at various temperatures were generated. In the absence of a magnetic field, the current

grew exponentially with a low threshold voltage as the temperature was increased to 45°C and then declined, as shown in **Figure 2.21**.

In contrast, in the presence of a constant magnetic field and temperature, the I–V curves exhibited rectifying behaviour for a forward bias, as shown in **Figure 2.22**. Barrier height as function of the temperature increased significantly after 45°C due to the change from DNA double bonds to single bonds, which resulted in an increase in the junction resistance and saturation current. Richardson constant increased gradually with the magnetic field due to the increase in the carrier effective mass and the decrease in the mobility. These results from the I–V curves suggested semiconducting diode-like properties of the DNA in the GDG structures.

The current increased exponentially for low threshold voltage and exhibited rectification in the forward bias region, as shown in **Figure 2.23**. Logarithm of the resistance grew gradually with increases in the electromagnetic field because of the cyclotron effects in charge carriers in electric and magnetic fields. Metal-DNA-metal junction provides a good option for the fabrication of magnetic diodes and sensors (Khatir et al., 2014a).
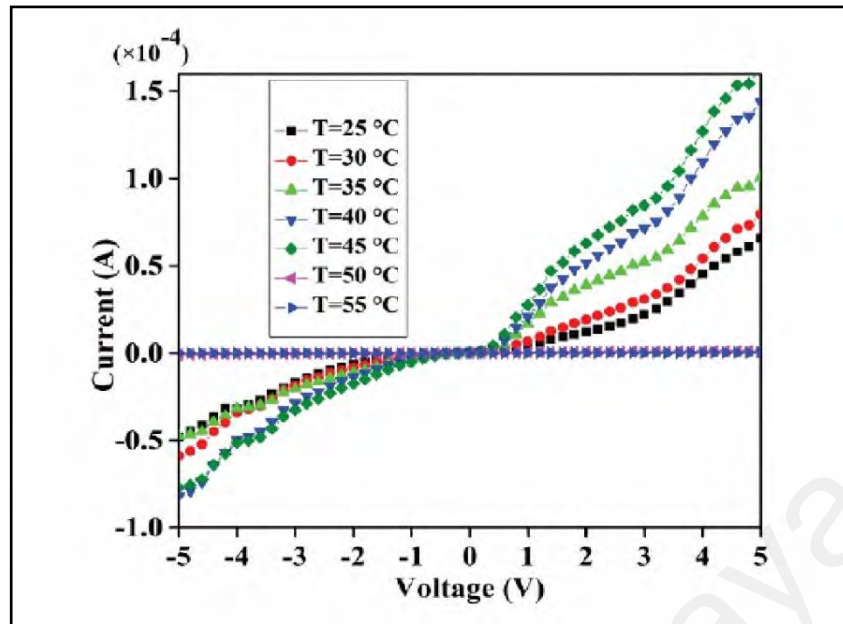
Figure 2.21: Relationships of current and voltage at various temperatures (25-55°C) (Khatir et al., 2014b).
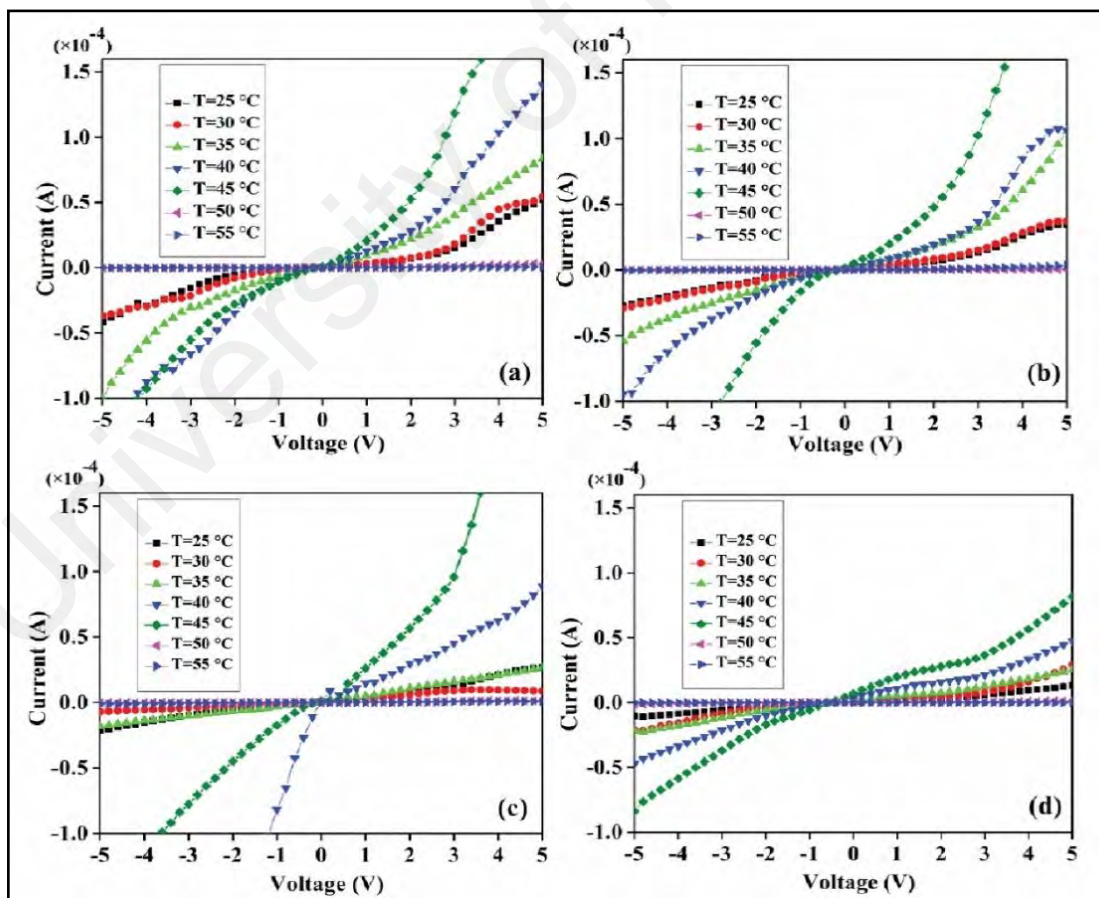
Figure 2.22: I–V curves at different temperatures (a) 200 mT, (b) 400 mT, (c) 600 mT, (d) 800 mT (Khatir et al., 2014b).
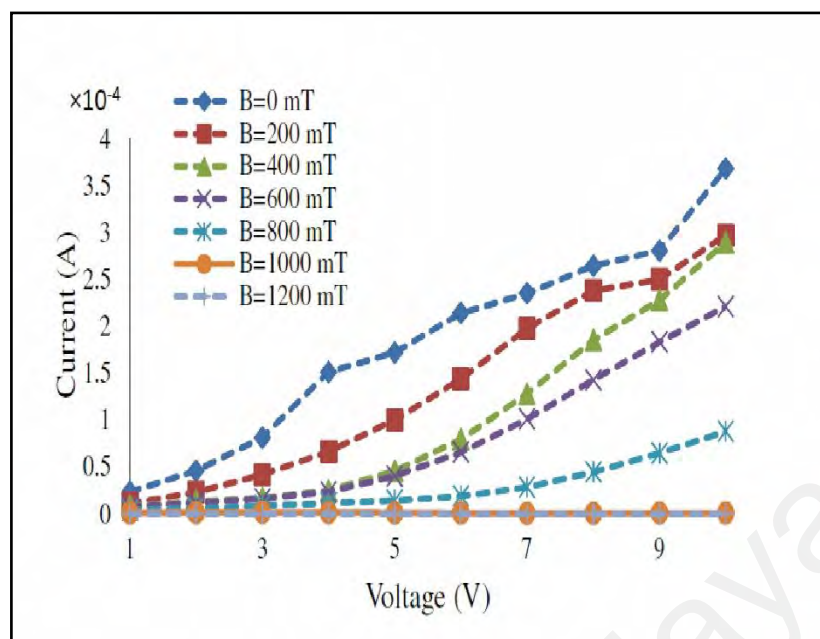
Figure 2.23: I–V curve showing the Au/DNA/Au junction behavior (Khatir et al., 2014a).

In another work by the same author and her co-workers (Khatir et al., 2015) the I–V properties of the Au/DNA/Au junction in the presence of an external magnetic field was measured. A DNA film generated by solution processing was placed between gold electrodes separated by different gaps (20, 30, 40 and 50 μm) on Si/SiO_2 substrates using the UV-lithography method. Using the same settings as in their previous works, the I–V curves was obtained and interpreted as follows. First, the current was observed to decrease in the forward region with increases in the electrical field caused by the interaction between the electromagnetic field and unpaired electrons with different gaps and the charge transfer. Second, the increase in the resistance on a logarithm scale with increases in the electromagnetic field could be attributed to the cyclotron effects of charge carriers. Third, the Schottky barrier height of the diode increased as the gap size increased and due to the effects of the electromagnetic field. Finally, the ideality factor for the GDG diode decreased with increases in the magnetic field. I–V relationship indicated semiconducting behaviour and was found to increase as the gap size increased.

Yudiarsah and co-workers in 2014 studied the effect of backbone disruption on the electrical conductivity of poly(dG)-poly(dC) DNA molecules and the differential conductance at W=0–10 eV and frequencies of 0.51 and 5.12 meV at room temperature (Yudiarsah et al., 2014). Tight binding Hamiltonian theoretical model was used for calculations. Landauer-Büttiker equation was employed in this study. Authors assumed that the voltage through the electrodes decreased gradually. I–V properties generated provided some factors to help determine the transmission probabilities. W was used to describe the backbone disruption strength. The value of I decreased with W and V increased for values of W from 2–3 eV. In contrast, the current increased with W at low voltage. W caused this improvement in the transport, possibly indicating that the DNA conductance was increasing with increasing humidity. Prior to this, in 2003 Jo and his co-workers (Jo et al., 2003) showed that the conductance of DNA in ambient air was higher than that of DNA in vacuum (H.-Y. Lee et al., 2002). The authors determined that the conductance increased with increases in the frequency at 0.5 and 5.12 meV due to the high level of backbone disruption (Yudiarsah et al., 2014).

2.5.3   DNA as Conductor

Kasumov and colleagues measured the conductivity of double-stranded DNA using a combing process (Kasumov et al., 2001). The investigation was made by using a λ-DNA film created by solution processing and a fabricated surface device; where the film was placed between superconducting carbon (C) (2 nm thickness) and rhenium (Re)/Cr electrodes (30 nm/8 nm thickness) that were separated by a gap of 0.52 μm on mica substrates prepared using sputtering method, **Figure 2.24**. The bilayer electrodes were cut into three parts using a laser beam. After the deposition of the DNA structure on the Re/C-covered mica substrate by a low-power laser beam, three different DNA windows were formed for the electronic transport measurement (DNA1 and DNA2 had

un-etched windows that were 30 and 120 μm wide; DNA3 had two or three molecules).

Temperatures ranged from room temperature to temperatures below the super-conductivity transition of Re/C electrodes. I–V curves generated, showed that the resistance increased as the temperature decreased down to 1 K for DNA1, DNA2 and DNA3, as shown in **Figure 2.24**(b). The resistance of these DNA samples at room temperature was 17, 11 and 40 KΩ for DNA1, DNA2 and DNA3, respectively. In contrast, at temperatures below the superconducting transition of the Re/C electrodes at approximately 1 K, the resistances of DNA1 and DNA2 were 75% lower at 0.05 K for DNA1 and 15% lower for DNA2. The resistance of DNA2 increased slightly below 0.1 K as the applied magnetic field strength was changed. Transitions to a lower resistance state could be ascribed to the effect of the superconducting-normal-superconducting (SNS) structures formed by DNA1 and DNA2 between the two superconducting electrodes. These outcomes indicate that DNA could be conducting at sub-mK temperatures and that phase coherence was retained over several hundred nm.
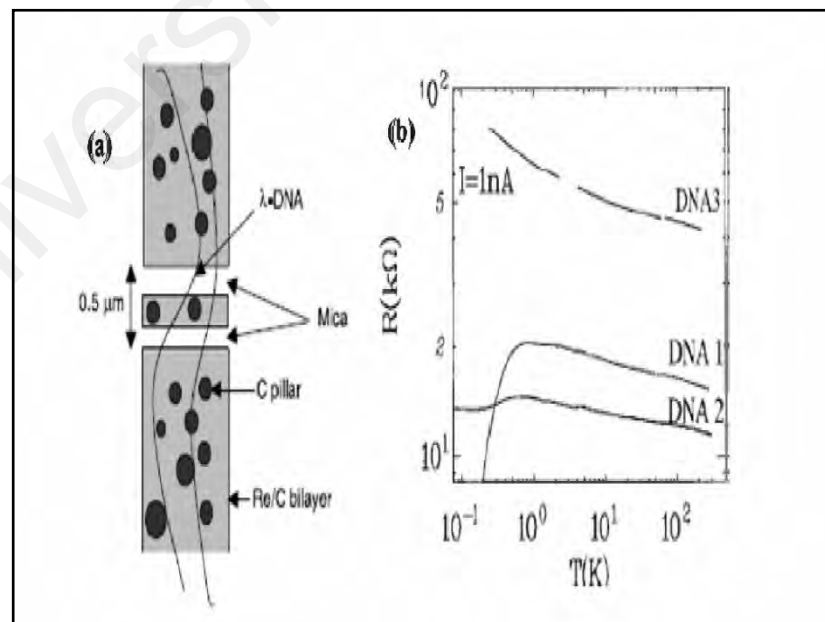
Figure 2.24: (a) Schematic drawing of the measured sample, with DNA molecules placed between Re/C electrodes on a mica substrate. (b) Resistance as a function of temperature for the three DNA molecules (Kasumov et al., 2001).

Researchers have also studied the thickness and low-temperature conductivity of DNA molecules (Kasumov et al., 2004). A DNA film produced by solution processing was placed between Pt electrodes (3 nm thickness) separated by a gap of 200–500 nm on mica substrates using a focused ion beam. Transport measurements were performed on the DNA molecules at low temperature of 4 K. The resistance was 55 KΩ at room temperature and increased moderately to 95 KΩ as the temperature decreased to 4 K. However at 1 K, the behaviour becomes non–Ohmic with the characteristics of a 1D conductor with repulsive electron–electron interactions. Charge transport was measured at temperatures less than 1 K and exhibited the expected parasitic ionic conduction. All these outcomes verified that it's possible to establish a conductive DNA rope through careful use of surface chemistry that did not disrupt the double-stranded structure.

Recently, DNA has been used as a conductive cladding layer in polymer electro-optic (EO) waveguide modulators (Heckman et al., 2011). This was due to their low optical loss and high electrical conductivity relative to those of their inorganic polymer counterparts. Additionally, the DNA biopolymer cladding layer provided relative poling efficiencies of 96%, in contrast to the UV15 (UV curable epoxy) poling efficiencies of only 51%.

2.6   DNA Applications in Nanotechnology

2.6.1   DNA as Sensor

Devices that produce a commensurable change in output in response to a known input stimulus are called sensors. Sensors can be classified into three main categories: First; physical sensors that measure features such as temperature, pressure and flow. Second; chemical sensors that measure the concentration or identity of a chemical substance, such as gasoline, ethanol, carbon monoxide, or other molecules. And the third; biosensors are those that measure biologically active substances, which can be

cellular, such as toxic plague bacteria or anthrax spores, supramolecule-like flu viruses, or molecule-like protein toxins, such as *Staphylococcus enterotoxin* B (SEB) (Setter et al., 2006).

The term biosensor consists of the word "bio" and "sensor". These components can be connected through the following four methods; physical adsorption, covalent bonding, matrix entrapment and member entrapment. The "bio" element can be from tissue, enzyme, living cell and antibody while the sensor element may be an electrical potential or electrical current. Biosensors can be utilized in many fields, such as industry, biomedicine and military applications. Biosensors that have been used to detect DNA are well known and can help in detecting and characterizing single molecules of DNA (Mohanty & Kougianos, 2006).

DNA specificity provides an application mechanism for its use as a sensor. The basic technique underlying chemical sensors is a response between the sensor and the target. If the chemical to be revealed is ssDNA, then nature already provided the material that the sensor must utilize to complete the reaction; the complementary strand. Although the principle is very simple, the application of this response in a sensor that provides an output requires some skill. Single strands have been attached to AFM cantilevers (**Figure 2.25**) and were dipped in the tested solution. If the complementary strand is present, this strand will bind to the attached one, thus producing some stress and a deflection of the cantilever. A different type of DNA sensor is one where the complementary binding leads to or cancels a fluorescent signal. Some companies have already begun to sell these so-called DNA chips (Dewarrat, 2002).
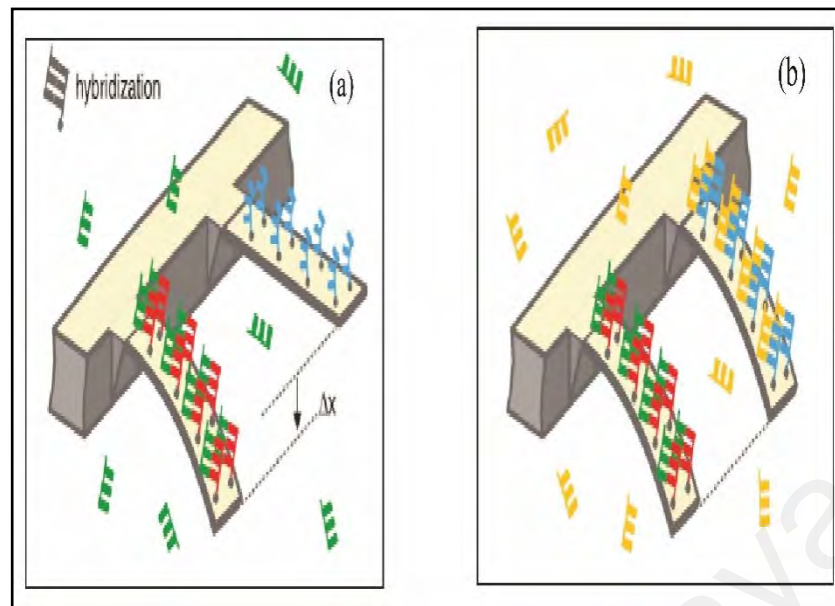
Figure 2.25: Detection system using an AFM cantilever. (a) Hybridization occurs on the cantilever, which provides a sequence (red) that matches the nucleotide in the solution (green), increasing the differential signal Δx. (b) Injection of the second oligonucleotide (yellow) causes the cantilever to become functionalized with the second oligonucleotide (blue); thus, the cantilever bends (Fritz et al., 2000).

2.6.2 DNA as Nanowire

The new class of sensors has a nanoscale size, enabling measurements in the smallest of environments, such as individual cells. DNA is a natural template for nanofabrication because the linear polynucleotide chain has a width of 2 nm and a length of 0.34 nm per nucleoside sub-unit (Jianrong et al., 2004). Nanowires are widely known as significant elements in the development of certain futuristic nanoscale devices because nanowires are one-dimensional (Q. Gu et al., 2006). Semiconductor nanowires can be utilized as diode logic gates (Huang et al., 2001). Nanowire-based sensors have detected trace quantities of biomolecules and chemicals in nanoelectro-mechanical systems (Cui et al., 2001; Hahm & Lieber, 2004; Maiti et al., 2003). Many manufacturing methods have been examined for the generation of nanowires, including template-based methods, laser-assisted catalytic growth and vapour–liquid–solid growth (Q. Gu et al., 2006). DNA is uniquely suitable to molecular recognition: A pairs specifically with T and G pairs specifically with C.

DNA has been used as a template to grow conducting silver nanowires as reported by Braun et al (Braun et al., 1998). The basic assembly scheme for constructing Ag nanowire attached to two gold electrodes is outlined in **Figure 2.5**. The photolithography method was utilized to separate the two gold electrodes by a defined distance (12-16 μm) and the electrodes were deposited onto a glass slide. Furthermore, the gold electrodes were modified with non-complementary hexane disulphide modified oligonucleotides through well-established thiol adsorption chemistry on Au.

Other groups such as Martin et al. in 1999 also reported the fabrication of Au and Pt wires utilizing DNA as a template or key (B. R. Martin et al., 1999). The basic idea in this work was to fabricate and functionalize (gold or platinum metal) wires with the exchange and formation of complexes between the metal and the DNA bases. I–V features were measured to reveal the conductivity profile of these nanowires. In addition, the researchers reported that luminescent, self-assembled poly(p-phenylene vinylene) wires could be formed that were acceptable for use in optical applications (Sun & Kiang, 2005). The work has great potential for additional research to control the width of the wire and the contact resistance between the gold electrode and the silver wires and for uses with other metals and materials.

The simplest method of stretching DNA templates during nanowire fabrication is molecular combing (Bensimon et al., 1994; Q. Gu et al., 2006). This technique is widely used because it does not require chemical modification of DNA molecules. It can be utilized on various hydrophobic or hydrophilic surfaces and can produce molecules that are well dispersed and strongly bound to the substrate, a condition favourable for the subsequent nanowire metallization and characterization. Alternatively and less favourable techniques are electrophoretic and hydrodynamic stretching (Q. Gu et al., 2006).

In 2003, Yan proposed and reported a DNA nanostructure that had a square aspect ratio (Yan et al., 2003). This DNA readily self-assembled into two different lattice forms; nanoribbons and two-dimensional nanogrids. The 4×4 tile had four-arm DNA junctions pointing in four directions. Similar nanogrids that have a large cavity size might serve as binding or tethering sites for other molecular components.

Magnetic cobalt nanowires were reported to be fabricated using palladium (Pd) nanonuclei for selectively catalysed deposition of cobalt on DNA (Q. Gu et al., 2005). DNA templates were also utilized to assemble non-metals, including conductive polymers, semiconducting polymers (Eichen et al., 1998; Ma et al., 2004; Nickels et al., 2004) and semiconductors (Coffer et al., 1996; Dittmer & Simmel, 2004; Torimoto et al., 1999).

Bacteriophage λ-DNA was used as a template to fabricate conductive nanowires of Pd (Richter et al., 2001; Richter et al., 2000). The wires had an estimated conductivity of 2×10^4 S.cm^{-1}, only ten times smaller than that of bulk Pd and the average diameter was 50 nm. DNA was also used to template the assembly of gold nanowires between conventionally patterned gold contacts on a silicon wafer substrate (Manning et al., 2005). It is likely that biological molecules, specifically DNA, can be used to template the assembly of nanowires and functionalized nanogap electrodes from nanoparticles. The diameter of the resulting nanowire has been reported to depend on the exposure time (Manning et al., 2005).

A metallic DNA network was proposed and fabricated by J. Lu and co-workers (J. Lu et al., 2009). The process was controlled through one-step, photo-induced synthesis of silver nanoparticles on the DNA network. DNA concentration and reduction time of silver cations were the main factors governing the mesh size of the Ag–DNA network and the diameter of the Ag–DNA nanowires. The Ag–DNA network fabricated in this work shows an excellent current response for assessing RH levels.

2.7 Environment Effect

2.7.1 Humidity Properties

DNA is considered one of the most important genetic materials and can easily be purified from either animal or plant and DNA does not increase the amount of industrial waste generated at the global level (Yamada & Sugiyama, 2008). DNA has self-assembly and surface modification abilities, enabling a multitude of possible nanostructures. For nanowire materials in particular (Artacho et al., 2003), the electrical conductivity of the DNA molecule depends on various factors, such as the length, ambient conditions, base sequence, characteristics of the substrate surface, humidity and the ion density inside the DNA molecule (Kodama et al., 2009).
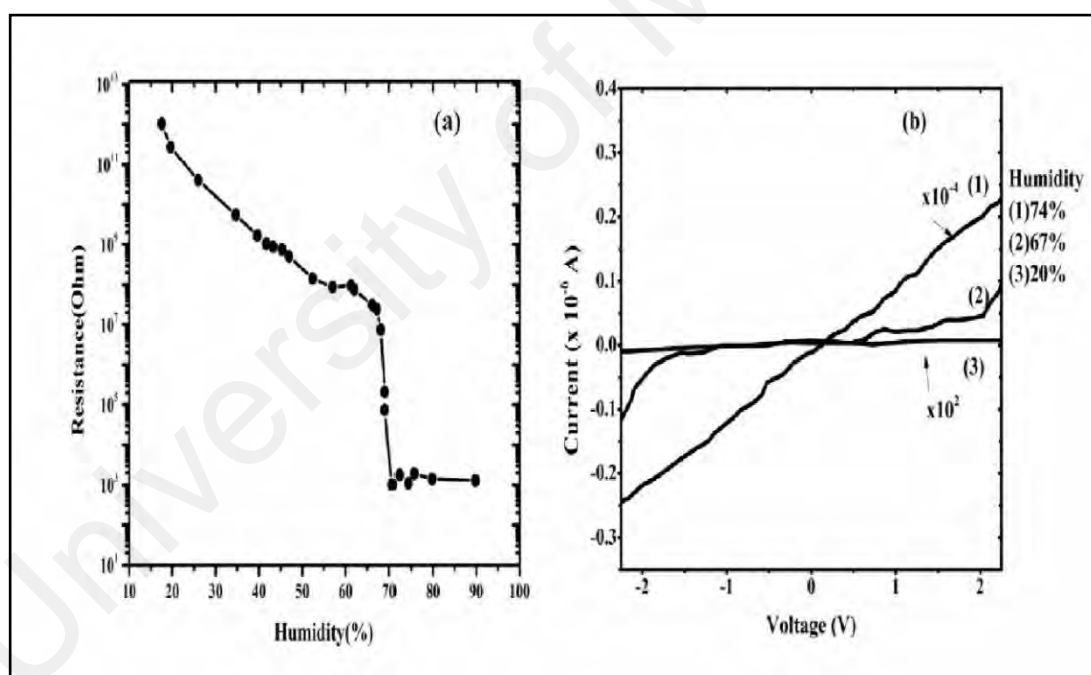
Figure 2.26: (a) Relation between the AO-DNA complex resistance values and the humidity. (b) Characteristic I–V curves of the AO-DNA complex at 74%, 67% and 20% humidity (J. Gu et al., 2002).

Humidity sensors can be classified into mechanical, capacitive, thermoelemental, resistive and oscillating, depending on which detection method is used (Chatzandroulis et al., 2002; Huang et al., 2007; Rittersma, 2002). Large humidity sensors, which are

constructed to determine humidity through variations in electrical characteristics (e.g., electrical resistance), use electrolytes (Carr-Brion, 1986) metal oxides, organic polymers (Ingram et al., 2003) and porous semiconductors (Hoa et al., 2000) as sensitive materials.

J. Gu studied the electrical conduction through dry DNA exposed to light in different humidities (J. Gu et al., 2002). The experiment was carried-out using 2 µl of a poly(dG-dC)-poly(dG-dC) DNA film (5 µm thickness) generated by solution processing. The film was later placed on a structure with comb-shaped gold electrodes (78 nm thickness) separated by a 10 µm gap on SiO_2 substrate. In this test, 10 µl of DNA solution was mixed with the same volume of diluted acridine orange (AO) solution. I–V plots shown in **Figure 2.26**(a) were obtained from the experiment. These showed that the resistance decreased gradually as RH increased to 70% and higher. These variations in resistance could be attributed to a substantially increased concentration of transported charges. Current values increased from picoamperes to milliamperes after the humidity reached 70%. The I–V relationships at three different humidities were used to obtain three curve profiles (arches, S-shapes and linear) as shown in **Figure 2.26**(b).

I–V plots were obtained for various values of RH (20-40%). For the humidity range from 47-69 %, there was an S-shaped semi-conductive I–V plot because the current grew gradually. Once the applied voltage was increased to the threshold value and was greater than 70%, linear behavior was observed. When the humidity increased, the ion (H^+, OH^-) concentration increased, thereby charges passed through the film. I–V relationship was studied under constant humidity (70%) with and without the light exposure. The conductivity barely increased with light exposure under conditions of relatively high humidity. Thus, ionic conductivity was the main mechanism instead of

band or hopping conductivity. Resistance value in the dark state was five times greater than that in the photo-induced condition at 18% RH.

Otsuka and his group meanwhile measured the electrical conductivity of a DNA film between nanogap electrodes to determine the effects of humidity (Otsuka et al., 2002). The investigation was performed by fabricating 10 comb-shaped gold nano-electrodes separated by gaps of 100 nm on a SiO_2/Si substrate through a combination of photolithography and a double-angle evaporation technique, as shown in **Figure 2.27**(a). I–V curve was measured at various humidities (30-95%) and in vacuum. The resistance of poly(dG)-poly(dC) was 1.7×10^{10} Ω and 3.9 GΩ under the atmospheric and vacuum conditions respectively. Generally, the resistance decreased gradually from 10^9 Ω at 30% RH to 1 MΩ at 90% RH, as shown in **Figure 2.27**(b).

Resistance decreased by three orders of magnitude; the change was exponential and occurred because of the increases in the number of water molecules adsorbed by the DNA. In contrast, the conductivity increased with RH%. The change was attributed to the three components of DNA; phosphoric acids, sugars and bases. Water molecules are easily adsorbed and form hydrogen bonds with the phosphoric acid, leading to a hydrophilic phosphoric acid around the base pairs of DNA. The authors adopted an equivalent circuit to fit the experimental data. Consisting of three parts R_1, C_1 and R_S represent the contributions to the resistance and capacitance, respectively in **Figure 2.27**(c). The values of these components were 1.5 KΩ, 16 nF and 0.32 KΩ.

Kleine and co-workers evaluated the ionic transport generation by assessing the impact of humidity on DNA (Kleine et al., 2004). Conductivity was measured for DNA that was placed between Pt electrodes separated by 20-300 nm on a glass substrate at various levels of RH (30-60%). The results indicated that ionic transportation occurred through capillary (canicular) condensation near the deposited DNA molecules and the electrical resistance was approximately 1.9 TΩ in these humidity conditions.
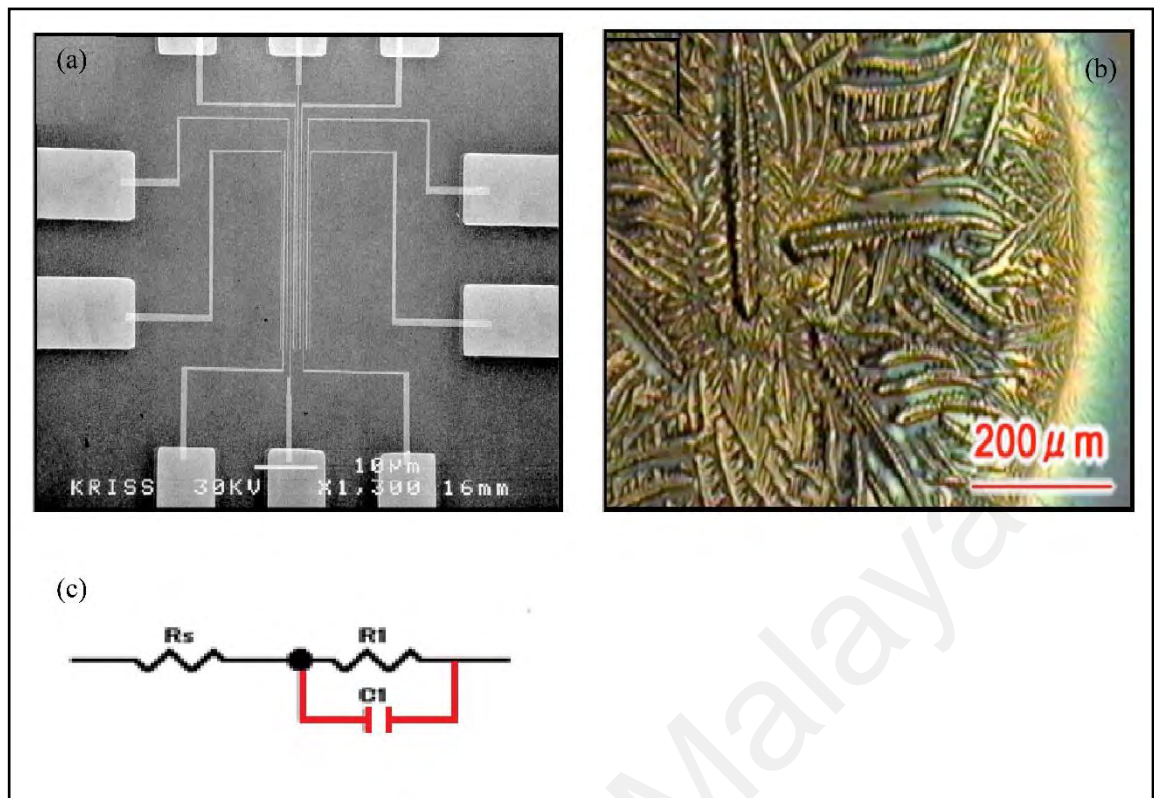
Figure 2.27: (a) SEM image of comb-shaped nanogap electrodes. The electrodes are separated by 100 nm. (b) Morphology of dried DNA films in which poly (dG)-poly (dC) DNA formed a dendrite structure, with the DNA concentration at 1.25 μg/μl. (c) The equivalent electrical circuit (Otsuka et al., 2002).

Terawaki meanwhile measured the electrical conductivity of a DNA network by utilizing Point-Contact Current Imaging Atomic Force Microscopy (PCI-AFM) under different humidities (Terawaki et al., 2005). This was achieved through the deposition of 10 μl of DNA on a mica substrate. The distributed DNA covered an area corresponding to a 1 cm diameter. Subsequently, a gold layer was deposited over half of the surface area; the gold acted as an electrode that was connected to the DNA network, while the height was 20 nm (**Figure 2.28**). Electrical conductivity was measured at humidities of 0% and 60%. The DNA network resistance was observed to be 500 GΩ higher than that of the mica substrate in the dry condition and the gap between the gold electrode and the AFM tip was approximately 100 nm. At high humidity, the current indicated that the conductivity of the DNA network was higher than that of the mica substrate because the current was 60 pA and 40 pA for the DNA network and mica,

respectively. Indeed, mica is an insulator and it could be estimated that DNA acted as a wire at high humidity.
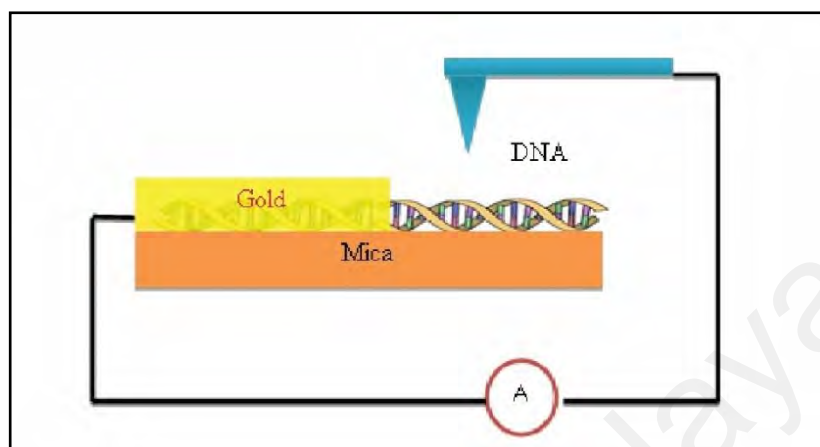
Figure 2.28: Design of the PCI-AFM measurement (Terawaki et al., 2005).

Yamahata and co-workes studied the electrical characteristics of DNA on a silicon-on-insulator (SOI) substrate (Yamahata et al., 2008). Investigation was performed by fabricating silicon nano-tweezers using silicon on insulator (SOI) or microelectro-mechanical system (MEMS). The λ-DNA solution was dropped on the microscope glass and the silicon nanotweezers were moved toward the surface of the droplet. A high frequency electric field (40 $V_{pk–pk}$, 1 MHz; 20 mm gap) was applied to the silicon nanotweezers and DNA for a few seconds. Consequently, the DNA became attached to the silicon nanotweezers and a DNA rope could form at the end of the tip by dielectrophoresis. To shield against electrical noise, all the electrical measurements of the DNA bundles were determined in a Faraday cage. I–V plots showed a nonlinear increase in the current with voltage for different bundles under conditions of 50-60% humidity and room temperature, as shown in **Figure 2.29**. The water adsorption on the molecule was calculated to have led to the conductivity in the DNA bundles. Permittivity also increased due to this adsorption, leading to an exponential relationship between the conductivity and the RH.
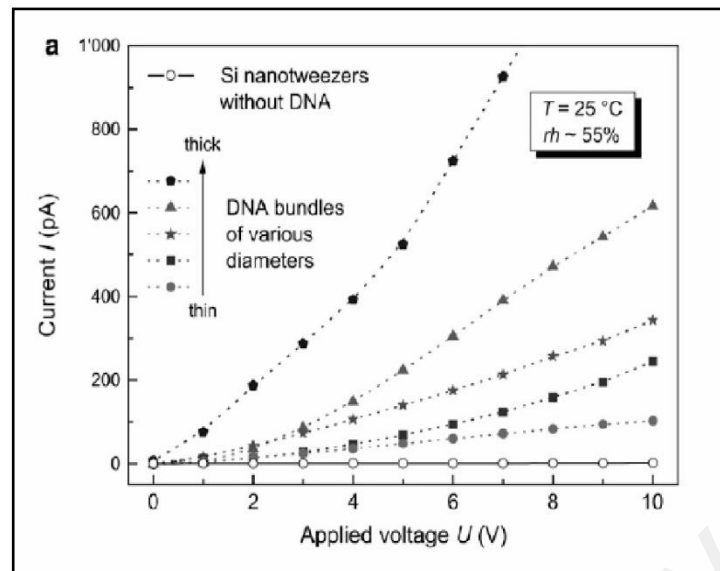
Figure 2.29: I–V curve at constant humidity for different sample thicknesses
(Yamahata et al., 2008).

Another research group, Paul and his team measured the difference in the
conductance of a DNA functionalized carbon nanotube (DFC) network at various values
of RH (Paul et al., 2013). The electrical characteristics were measured for a DFC
solution in Tris-EDTA buffer that was placed between two gold electrodes (150 nm
thickness) separated by a gap of 25 μm. Thermal evaporation was used to deposit the
solution on a SiO_2 (250 nm thickness) substrate that was generated using conventional
lithography, as shown in **Figure 2.30**(a). I–V curve was measured at various levels of
RH; the drain-source bias voltage (VDS) ranged from 0-1 V and the gate bias was zero.

Figure 2.30(b) shows that the current increased linearly with RH increases from
45-77 RH%. Furthermore, the conductance increased exponentially with increases in
RH%. Many factors cause the humidity-induced change in the conductance of the DFC
network. The variation in the conduction of the DFC network might occur through the
Grotthuss mechanism, in which the charge transport occurs through protonic conduction
through the aquatic layers physisorbed on the DFC network. Another explanation for
the change in conductance could be the fact that the electronic transitions that occur
between the energy stages of DFC correspond to various bias voltages, as shown in

Figure 2.30(c) Secondly; this non-steady conductance may also result from electronic noise, which is expected in such CNT-based sensors. Finally, short ssDNA strands were immobilized on the surface of SWNT. The relation between the current and temperature was also studied as a function of RH. Calibration curve shifted to a lower RH value with increases in the temperature.
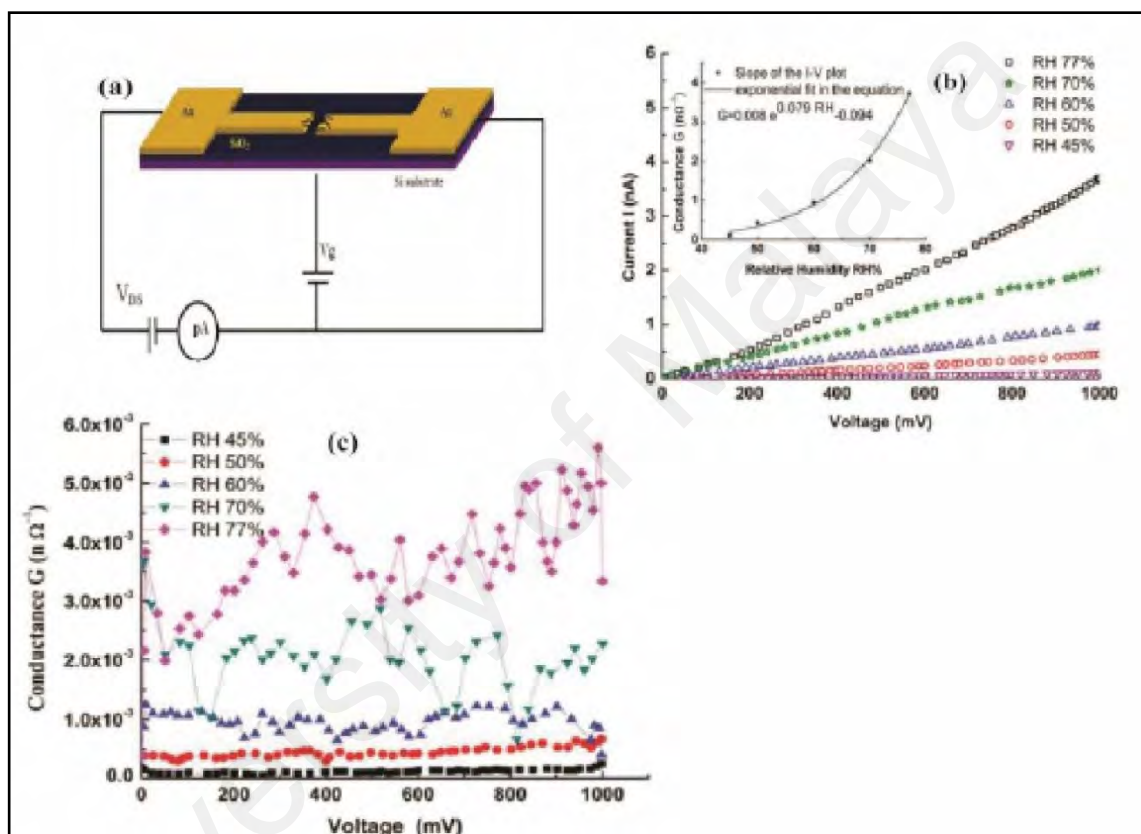
Figure 2.30: (a) Fabrication of the utilized device testing. (b) I–V curve for DFC network at various levels of humidity. (c)Relation between the conductance G and the bias voltage VDS, of the DFC network at various RH levels (Paul et al., 2013).

Paul and co-workers described these network as a function of RH and with different voltages by using microfluidic cantilevers as resistance-type humidity sensors (Paul et al., 2014). Measurements were obtained using a sensor built from a solution of DFC in Tris-EDTA buffer. Sensors were prepared by placing ssDNA and SWNTs between two (Cr)/(Au) electrodes of 100/150 nm thickness. The solution was deposited by the thermal evaporation method on the SiO_2 (250 nm thickness) substrate. Gaps were

varied (10, 15, 20 and 25 μm) and the substrate generated using conventional

lithography as shown in, **Figure 2.31**(a). The electrical characteristics of DFC at

humidity ranging from 40-80% are shown in **Figure 2.31**(b). Here, the current increased

exponentially with increases in the humidity. The length (L=25 μm) condition showed

greater variations than the L =10 μm condition. Sensitivity was calculated from

$\Delta I/\Delta RH\%$ and increased exponentially with increases in RH%. The DFC network

exhibited greater sensitivity at high humidity, as shown in **Figure 2.31**(b). However, the

sensitivity of device for values of L=15, 20 and 25 μm was higher than that at L=10 μm.

For 70-80 RH% values, the sensing area could be considered lower. Recovery time

decreased from 48-7 s as the voltage increased from 1.3-2.6 V. The potential energy of

interacting dipoles increased due to the parallel orientation of molecular dipoles along

the external field E, thus water molecules could be rapidly released from the surface of

the DFC.
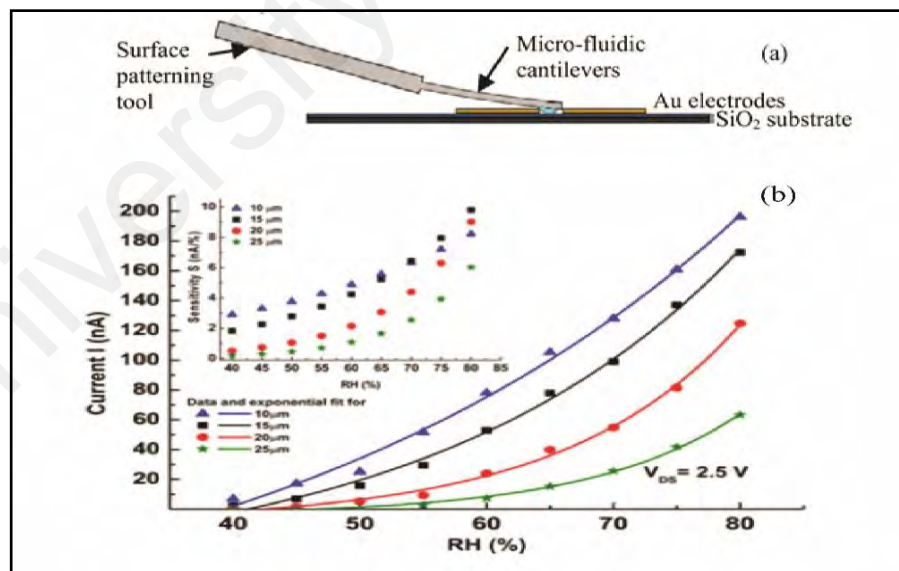
Figure 2.31: Relation between the current and RH for the DFC network with variation
in the electrode gap: L=10, 15, 20 and 25 μm. (Inset) Sensitivity, S against RH% curve
for the DFC devices(Paul et al., 2014).

2.8   Physics of Radiation Biology

The field related to the biological impact of non-ionizing and ionizing radiation in the full electromagnetic range is called radiology. Ionizing radiation consists of alpha particles (α), beta particles (β) and heavy charged ions.

Ionizing radiation refers to radiation that has sufficient energy to remove strongly bound electrons from the orbital of an atom when the radiation contacts the atom; making the atom becomes ionized. The same process can occur in the cells of living organisms because cells are made of organic matter.

Non-ionizing radiation involve microwaves, ultraviolet radiation, extremely low–frequency radiation, extremely energetic electromagnetic radiation (gamma rays, X-rays) and neutrons. Each type of ionizing and non–ionizing radiation has its own properties (Massey, 2005).

2.8.1   Alpha Particles (α)

Alpha particles are basically helium nuclei with two protons and two neutrons, as shown in **Table 2.1**. Decay of heavy radionuclides emits the alpha particles. These particles can penetrate less than a few centimeters in air and freely capture two electrons for conversion to ordinary helium. Due to their low penetration abilities and very high ionizing power, alpha particles are rarely utilized in radiation therapy since they do not penetrate very far into tissue, as shown in **Figure 2.32**. They interact very strongly with the atoms when they pass through materials because of the naturally high positive charge of alpha particles. Thus, alpha particles will deposit their energy over a smaller volume. Alpha particles post a significantly higher hazard than other types of radiation of equal strength if these particles are able to reach internal organs. They can transport large doses to internal organs, causing permanent damage. The source of these particles

are fission fragments from very heavy elements, such as uranium, thorium and radium (Ahmed, 2007).

2.8.2   Beta Particles (*β*)

Beta particles can be classified into two types, beta positive and beta negative but they have the same characteristics. These particles are smaller than alpha particles and will penetrate further into the body, which means they tend to damage more cells, but with less cell damage. Beta particles are emitted from the nucleus of an unstable radioactive atom whose neutron-to-proton ratio is too high. These particles have the ability to enter tissue to variable depths, as shown in **Figure 2.32**. As such the energy of a beta particle could pose an external radiation hazard. Any beta-emitting radionuclide is potentially hazardous when it enters the body in quantities exceeding those thought to be safe (Herman & Thomas 2009).

2.8.3   Gamma Rays (*γ*)
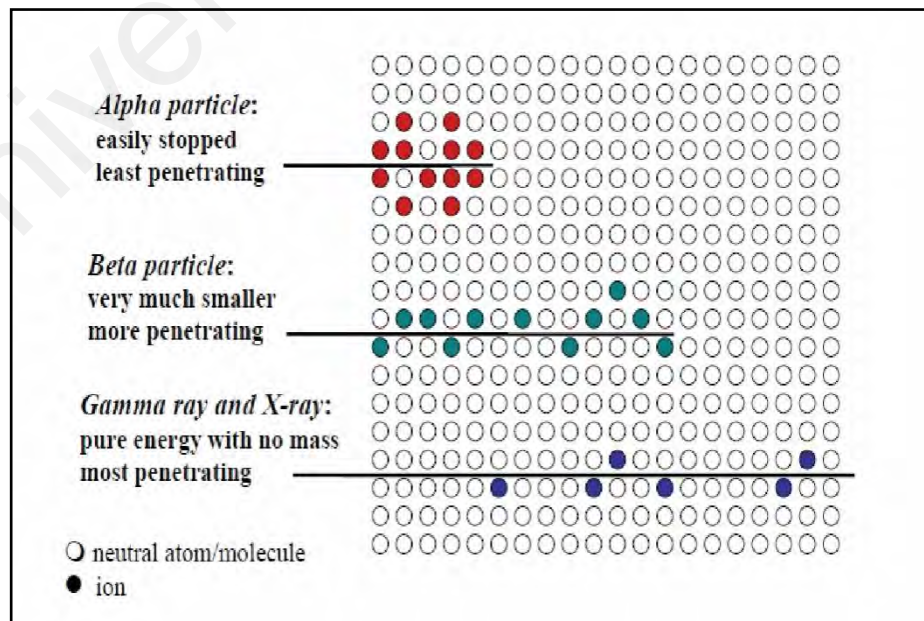
Figure 2.32: Interactions of (alpha particles, beta particles and gamma rays) with tissue or material (Holbert, 1995).

Gamma rays cause monochromatic electromagnetic radiation and are produced by the nuclei of excited atoms during radioactive transformations. They provide a mechanism for excited nuclei to eliminate their excitation energy without affecting either the atomic number or the atomic mass number of the atom. Gamma radiation is capable of moving several meters in air and several centimeters in human tissue (**Figure 2.32**). This radiation freely enters most materials and is sometimes called penetrating radiation. Gamma rays do not carry any charge and are thus pure energy and they do not have any mass. Gamma radiation is deeply penetrating and can easily pass completely through the body, but it may still interact with many atoms during its passage. Gamma rays spread the energy over a large volume, which causes less damage per collision compared with that of alpha particles. Gamma radiation can still cause a great deal of damage to tissues /materials. Because of their penetrating ability, gamma radiation can easily affect internal organs and bones, which explains why large doses can be used to damage cancer tissues (Alpen, 1997; Massey, 2005). **Table 2.1** lists the characteristics of alpha and beta particles and gamma rays.

Table 2.1: Characteristics of the different types of radiation (Holbert, 1995).

Characteristics	Radiation (E=1 MeV)				
	α	P	β or e	γ or X	N
Symbol	$^2\alpha^4$ or He^{+2}	$^1P^1$ or H^+	$^{-1}e^0$ or β	$^0\gamma^0$	$^0n^1$
Charge	+2	+1	-1	Neutral	Neutral
Ionization	Direct	Direct	Direct	Indirect	Indirect
Mass (amu)	4.00277	1.007276	0.000548	--	1.008665
Velocity (cm/sec)	6.944×10^8	1.38×10^9	2.82×10^{10}	$C=2.998 \times 10^{10}$	1.38×10^9
Speed of light (%)	2.3	4.6	94.1	100	4.6
Range in air (cm)	0.56	1.81	319	82.000*	39.250*

* Range based on a 99.9% reduction.

2.9 Radiation Properties

Energy is lost from the alpha particles as they pass through a medium due to a series of primary collisions with the negatively charged electrons of the atoms in the medium. These interactions result in ionization and excitation of the atoms in the medium. The energy lost by the moving alpha particles increases with deceleration.

In the same way, alpha particles can be created by stripping two electrons from helium atoms and acceleration to high energy. The latter method is utilized to produce a beam of high-energy alpha particles in particle accelerators such as in cyclotrons. Alpha particles energy obtained from the decay of radionuclides are in the range of 2–10 MeV; however alpha particles of up to a few hundreds of million electron volts (MeV) can be obtained by using an appropriately designed particle accelerator. Alpha particles lead to primary and secondary ionizations to atoms with which they interact and generate several ions and excited molecules within cells (Knapp & Dash, 2016).
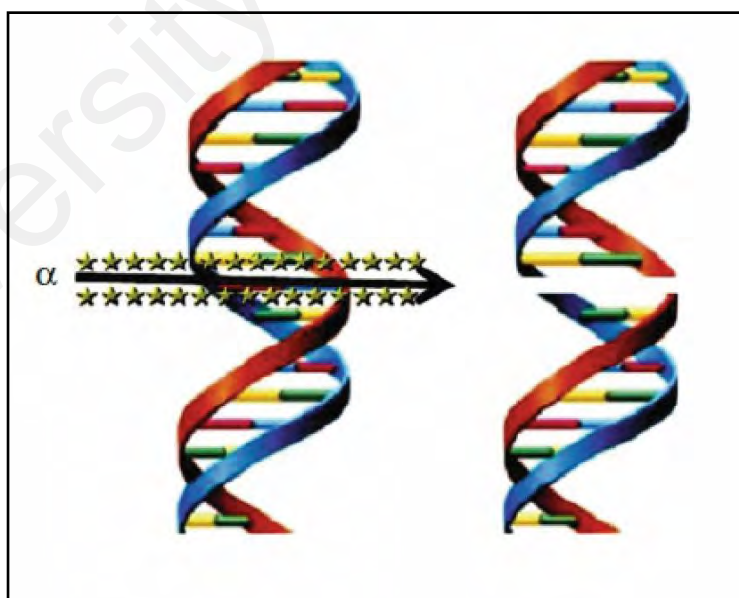
Figure 2.33: Alpha particle interacts with ssDNA molecule and the secondary double-strand disruption fractions (Knapp & Dash, 2016).

Owing to the high concentrated dose deposited along the path and short range in tissues on the order of cellular dimensions, alpha particles have a high possibility of

inducing damage to DNA (**Figure 2.33**) rendering them quite cytotoxic. By disparity radiation-induced cellular idle for low-Linear Energy Transfer (LET) radiation needs the accumulation of sub-lethal damage, realized only at much higher dose (Hofmann et al., 2004). This specific radiation quality of alpha particles, characterized by localized spatial distribution of the imparted energy and high density of ionization per unit path length, lead to direct DNA damage rather than indirect free radical mediated DNA damage (Loveland et al., 2006). There is an expected 20–40% possibility that an alpha particle interacting with the DNA molecule can ensure damage of the double strand leading to eventual cell death. On the other hand, internal depositions of alpha particles are of significance on a long term basis in terms of causing radiation damage which is of greater significance than from beta particles.

On the other hand, many alpha emitting materials also emit gamma radiation and this radiation might lead to important tissue damage, even though the total alpha energy exceeds the total gamma energy and the ratio of gamma emissions per alpha is very small. This follows from the information that the penetrating power of gamma radiation is many times greater than that for alpha radiation so that the total volume of tissue exposed to damaging radiation is many times greater (Loveland et al., 2006).

It can be summarized that the charge particles interaction with matter and these is common to all charged particles such as: All heavy charged particles mobile fundamentally straight paths in medium after that loses energy mostly through the ionization and excitation of atoms. However the Coulombic interactions between the particles and electrons in the medium impact to the slowing down of a moving charged particle. The moving charged particle uses electromagnetic forces on atomic electrons and imparts energy to them. The energy transferred may be sufficient to strike down an electron out of an atom and thus ionize it, or it may leave the atom in an excited, non-ionized state. Finally, a heavy charged particle could be transfer only a small fraction of

its energy in a single electronic collision. Its deflection in the collision is insignificant. (Coderre, 2007).

Gamma rays are considered as electromagnetic wave originating from nuclei. These rays are emitted from excited nuclei that change state. Compared with charged particles (e.g., alpha and beta particles), gamma rays react differently during the transition from an excited energy level to a lower energy level or to the ground state. Gamma rays have strong penetration power when interacting with materials and the energy of gamma rays is not lost because they indirectly ionize the medium. Gamma rays reacts with materials through three methods; the photoelectric effect, the Compton Effect and the production of electrons, as shown in **Figure 2.34**. The effects of gamma rays depend on the type of material, the material nature, the radiation quantity and the exposure time (Alpen, 1997; Holbert, 1995; Massey, 2005).
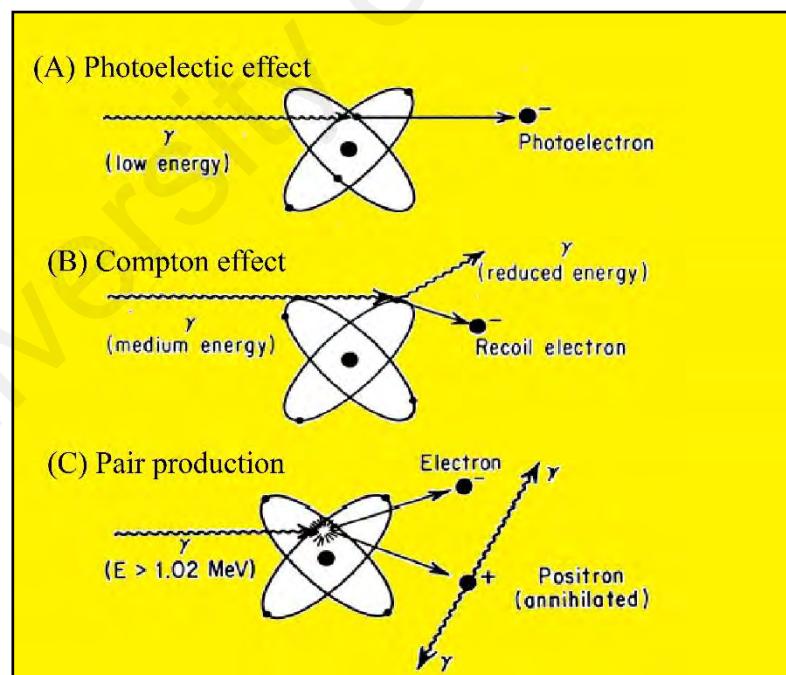
Figure 2.34: Three methods of interaction with matter (Loveland et al., 2006).

2.9.1 Mechanism Underlying the Radiation Effect on Materials

The reaction of ionizing radiation with materials leads to the storage of radiation energy and to the excitation or ionization of molecules and atoms and can thereby generate free radicals within 10^{-13}-10^{-15}s during the reaction between radiation and atoms. Free radicals are molecules that contain unpaired electrons, which can rapidly react with cellular molecules because of their short life. Free radicals interact with other molecules and generate secondary DNA, which also damages the cell. Free radicals are detected using methods such as flow electron spin resonance (ESR) and pulse radiolysis, which are considered quick measurements (Khaled & Held, 2012). The reactions of ionizing radiation and non-ionizing radiation with cells lead to subsequent molecular damage and free radicals by both direct and indirect effects (Holbert, 1995; Massey, 2005).

2.9.1.1 Direct Effect of the Radiation

In this case, ionizing radiation transfers its potential (energy) directly to the target structure (e.g., biological molecules), leading to ionization and excitation (**Figure 2.35**). This is the direct effect of radiation, which generates many changes. Ionizing radiation generates many free radicals, leading to the breaking of chemical bonds and energy deposition in molecules. These particles cause high linear energy transfer (LET) radiation, which is the domain of particles such as alpha and beta particles (Massey, 2005).

2.9.1.2 Indirect Effect of the Radiation

The interactions of radiation with matter, such as atoms or molecules, in the cell, especially in water or solution, leads to the creation of free radicals. H_2O is the most abundant molecule in active organisms; approximately 70-80% of the mass of a living

cell in water. Free radicals are capable of diffusing far enough to interact with the acute target and cause damage. This is called indirect effect of radiation, which can be caused by radiation such as gamma rays. The radiation loses energy through the ionization and excitation of H_2O particles (Alpen, 1997; Massey, 2005). Water can affect many complex chemical compounds. In irradiated cells, ionizing radiation can cause a process known as water radiolysis (**Figure 2.36**).
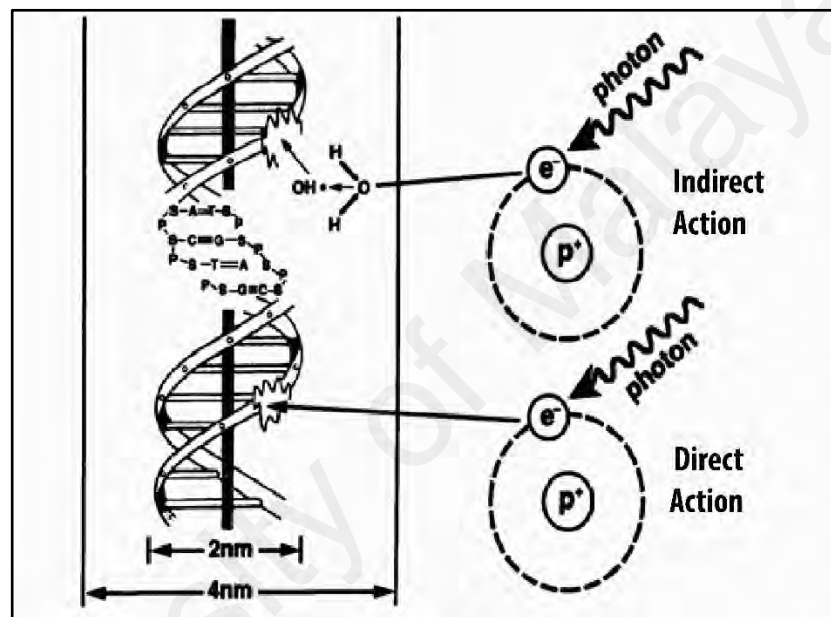
Figure 2.35: Direct and indirect effects on an organism (E. J. Hall & Giaccia, 2006).

The direct effect of ionizing radiation on DNA and other bioactive molecules in the cell are simply described as bond disruptions or radical generation at the location of energy deposition, leading to inactivation of the target molecule. Indirect effect through the products of water radiolysis are more complex and some probable reaction pathways have been identified (Alpen, 1997).
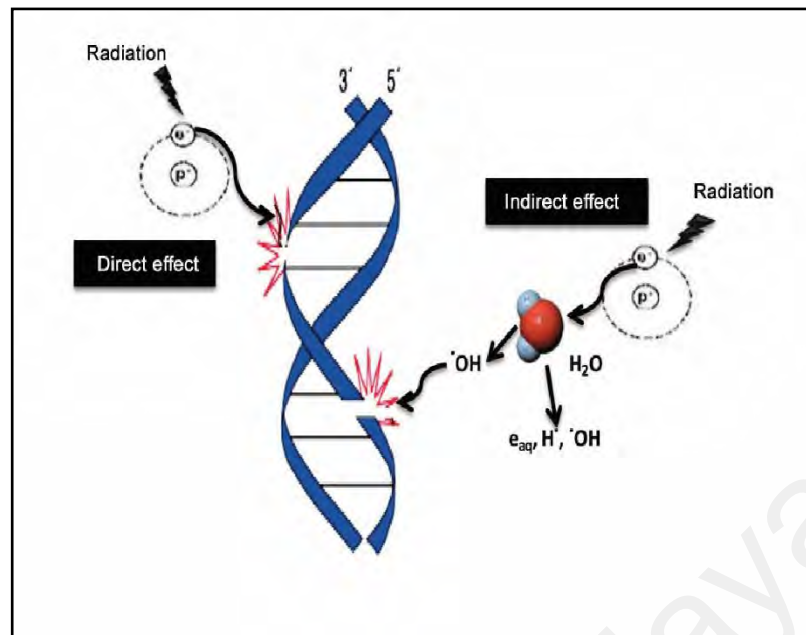
Figure 2.36: Direct and indirect impact on the interaction of ionizing radiation with DNA (Montoro, 2014).
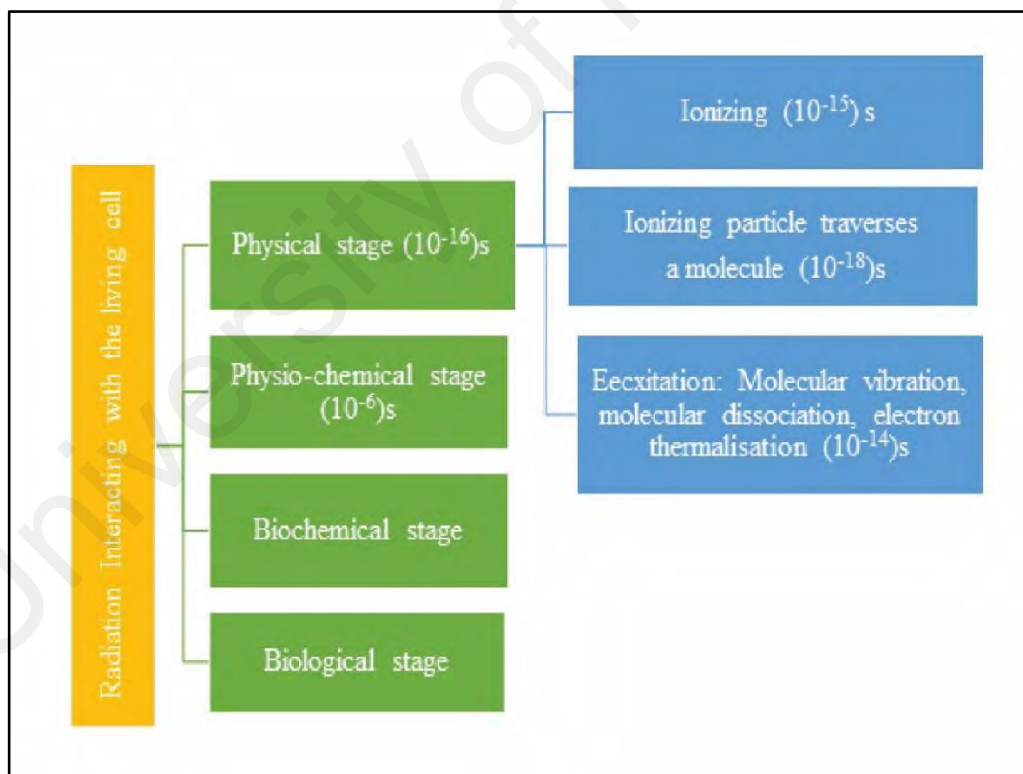
Figure 2.37: Radiation interacts with living cells.

2.9.2 Radiation Interacts with Living Cells

Radiation interaction can be generalized into four stages; physical, physio-chemical, chemical and biology stages (**Figure 2.37**). **Table 2.2** describes all the radiation stages. Physical stage occurs within a very short time (approximately 10^{-16} s). Ionization occurs, during which energy transfers from the radiation to the water molecule. This is preceded by the physio-chemical stage, which occurs in a very short time (approximately 10^{-6} s) after ionization. During this time, the positive ions and negative electrons interact with other water molecules from these reactions to create new compounds.

Table 2.2: Time scales of radiation actions (Nikjoo, 2003).

Time (s)	Event
Physical stage	Energy transfer
10^{-18}	Ionizing particle traverses a molecule
10^{-15}	Ionizing
10^{-14}	Excitation: molecular vibration, molecular dissociation, electron thermalization
Chemical stages	Formation of radical species and molecular product
10^{-12}	Diffusion of free radicals
10^{-10}	Free radical reactions with the solute
10^{-8}	Formation of molecular products
10^{-5}	Completion of chemical reactions
Biochemical stage	Energy transfer
1 s–1 hr.	Enzymatic reactions, repair processes
Biological stages	Genomic instability, aberration, mutation
1 hr–100 years	Killing of cells
Early effects, days – months	Killing of stem cell, normal-tissue damage and loss of cell proliferation
Late effects, days- years	Damage, blood vessel damage
Carcinogenesis, many years	Appearance of tumours and secondary tumours

The chemical stage follows as a result of the above stages, leading to hydrogen (H), hydroxide (OH) and hydrogen oxide, which will react with organic compounds found in the cell, such as chromosomes. This reaction leads to the breaking of long chains and compounds and occurs in several seconds.

Finally biology stage takes between a few minutes and tens of years. The effects of the cell changes begin to appear; some of these effects are the prevention or delay of cell division and an increase in the growth rate during cell division. Irreversible changes occur if genetic transformation occurs during cell division and during death.

2.10 Charge Transport Mechanisms
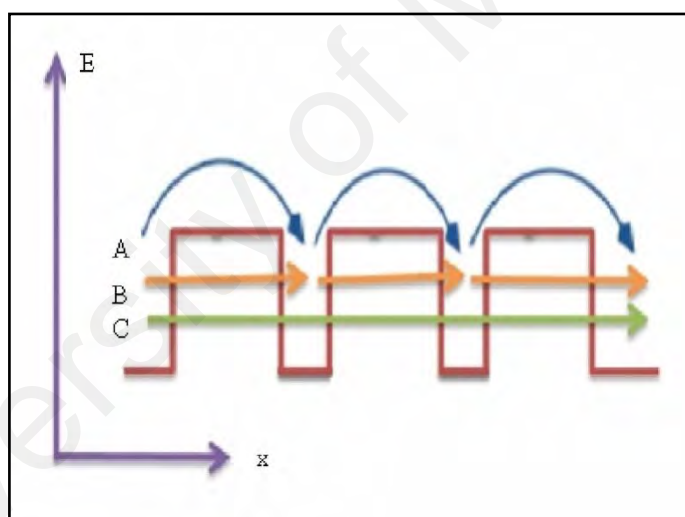
Figure 2.38: Illustration of three possible mechanisms for charge transfer in DNA, depicted as a series of energy barriers. (A) Thermal hopping, (B) sequential tunneling and (C) coherent or unistep tunneling (Di Ventra & Zwolak, 2004).

Charge transport phenomena in DNA have attracted much attention because of the potential to study damage and mutation in DNA. Understandingly these phenomena require the expansion of DNA-based molecular technologies, particularly electrochemical sequencing techniques (Berlin et al., 2001). In the last three decades, numerous transport mechanisms have been proposed to describe a variety of empirical

results. These useful results were expected due to the change in the conducting characteristics of DNA. The three famous transport mechanisms are sequential tunneling, thermal hopping and coherent tunneling, as shown in **Figure 2.38**.

2.10.1 Thermal Hopping Mechanisms (A)

In this mechanism, an electron passes some energy barriers through a multistep process called the thermal hopping mechanism, which involves transport from one position to another by thermal (phonon) activation. Local energy-reduction of dynamic structural biases produces a self-trapped state of finite degree (Schuster & Landman, 2004), as shown in **Figure 2.38**(A). This process can be expressed by a classical formula, known as the Arrhenius equation, for thermal active transport (Stubbe et al., 2003).

$$k_{ET} = k_{ET}^{o} \exp\left(\frac{-E_a}{KT}\right) \tag{2.1}$$

where k_{ET} is the electron transport rate, E_a is the activation barrier and K is the Boltzmann constant. The hopping method depends on the temperature, as indicated by Equation (2.1).

The hopping mechanism is responsible for the charge transport when a promising molecular structure is momentarily generated by nuclear motion. Sequence of transport actions between stable positions does not display an exponential dependence on transport length; instead the molecule length d is inversely proportional to the hopping current. Due to the larger length d, the thermal hopping method is more effective for transporting charges compared to coherent tunneling. Although molecules can attain a suitable structure for thermal hopping in solution, the thermal hopping mechanism does not apply for frozen molecules with a static structure (S. Lu, 2006).

A few researchers have suggested a phonon-assisted, polaron-like hopping mechanism for charge transfer (Henderson et al., 1999; Schuster, 2000). Because the structural instabilities of DNA are relatively fast (Borer et al., 1994; Brauns et al., 1999), the local structure around a charged base is likely to reorganize. Also, the distance and angle between base pairs would thus decline.

2.10.2 Incoherent Tunneling (B)

Tunneling has been proposed to describe the long-distance movement of electrons in molecules, even in the case of super exchange. The tunnel is only efficient for small distances, less than 4 nm. However, in the 1990s, electron transport over 4 nm was reported in a DNA helix (D. B. Hall & Barton, 1997).

In this model, a series of sites form potential wells that govern the molecular characteristics. The position of the charge changes for a limited time due to effect of each potential well, which also makes the phases of the electrons incoherent. Thus, the charge wave function lacks coherence due to the dephasing processes that occur after each tunneling event, such as the scattering by molecular vibrations (Zwolak & Di Ventra, 2005). This process consists of a series of detached stages and thus, there is as a multistep process. **Figure 2.38**(B) illustrates this phenomenon. Incoherent tunneling (inelastic scattering) does not depend on the molecular length (Bending & Beasley, 1985; S. Lu, 2006). One important difference between incoherent tunneling and thermal hopping is the role of nuclear motion, where the nuclei are the bodies that carry the charge like the thermal hopping. But one significant difference between the thermal hopping and incoherent tunneling was the part of nuclei (body carrying the charge) movement. The charge transport only occurred in the hopping method when a favorable molecular formation was produced by nuclei movement, but in incoherent tunneling the

electron tunnel through the energy barriers without nuclei movement. Finally, incoherent tunneling does not rely on the molecular length.

2.10.3 Coherent Tunneling (C)

In this process, the charge can tunnel from one side to the other side of the DNA length, such as during the fast single-step transport from donor to acceptor through a bridge of well-stacked DNA bases (Voityuk, 2011). The process is called coherent unistep tunneling because the charge wave function does not lose phase coherence. This mechanism has strong distance dependence. Coherent tunneling occurs for thin barriers. Quantum mechanics can be used to calculate the probability for the electron to tunnel through the barrier and retain its phase, as shown in **Figure 2.38**(C). The Simmons relation (Simmons, 1971) can be used to express the current density as,

$$J = \frac{Vq^2}{dh^2}(2m\Phi)^{1/2}\exp\left[\frac{-4\pi d}{h}\sqrt{2m\Phi}\right] \tag{2.2}$$

where q is the electron charge, h is the Plank's constant, d is the barrier thickness, m is the electron mass, Φ is the barrier height and V is the applied voltage.

In the case of DNA, many scientists have supposed that a charge coherently tunnels through the entire length of DNA, with a rate of charge transfer R or current density J.

$$J = \text{Re}^{-\beta d} \tag{2.3}$$

where β is the tunneling decay length and d is the length of the DNA (donor-acceptor separation). As the value of β increases, the rate of tunneling declines rapidly as the distance increases (Krider & Meade, 1998; Lewis & Letsinger, 1998; Priyadarshy et al., 1998; Turro & Barton, 1998).

In some experiments, the DNA configuration or empirical conditions exclude some of the famous mechanisms. For example, in fluorescence experiments, thermal fluctuations enable charges to leap among bases, as indicated in **Figure 2.38**(A).

Nonetheless, this process requires a considerable amount of thermal energy. Thus, this case is very improbable. Charges may move from one site to the next sequentially, as in **Figure 2.38**(B). Dephasing processes act to reduce the coherence of the charge wave function after each tunneling process through the scattering caused by molecular vibrations. None of these mechanisms depend on the DNA length (Di Ventra & Zwolak, 2004).

In the coherent tunneling mechanism, an electron tunnel along a potential barrier to travel from a donor to an acceptor site. For instance, an electron on a G base has a comparatively low energy and must tunnel to pass the barrier posed by a contiguous T or A base until it reaches another G base. The relation between transfer decays and distance becomes exponential. The electron still obeys conservation of energy and this process is frequently described as super exchange in the chemistry literature (Ratner, 1999). This mechanism is strongly dependent on the distance (Di Ventra & Zwolak, 2004). The vertical axis represents the energy, E and the horizontal axis represents the spatial position, *x*.

Berlin and colleagues examined the competition between hopping transport and coherent tunneling using a 1-dimensional tight-binding model (Berlin et al., 2002). In this case, the form (AT)m-GC-(AT)n-GC- (AT)m was chosen for the DNA sequence, where m indicates exposed or buried donor and acceptor groups and n is the number of AT pairs. The tunneling rate is calculated using Equation (2.4);

$$V_{tun} = e^{-\beta d} \tag{2.4}$$

where $d = (n+1)a$ is the space between the two GC pairs, a is the distance between base pairs, V_{tun} is a fitting parameter and β is the tunneling decay length derived from the tight-binding model. The rate of thermal transport is;

$$\nu_{therm} e^{g_G/TK_B}$$
(2.5)

where g_G represents the energy separation between the hole state of the G-C pair and the bottom of the A-T band. This value is derived from the tight-binding model. There is an acute value of n when these two rates are equal. At this value, the main mechanism will switch from tunneling to thermal hopping. Value of the transfer integral between close base pairs is expected to be between 3 and 5 using this model. The experimental work of Giese (Giese, 2002) is consistent with this model; this model predicted that the transfer rate would decrease exponentially for bridge lengths of up to three A-T pairs. This prediction also agrees with the experimental results suggesting that some charge is concentrated at the A-T bridge (Sartor et al., 2001; Williams et al., 2000). In this case, the characteristics of the structural deformation and fluctuations have also been investigated (Berlin et al., 2001; Grozema et al., 2002; Kelley et al., 1999; Wan et al., 1999; Y Zhang et al., 2002).

Finally, we necessarily indicate that in addition to the three discussed main transport methods, other methods such as soliton (Hermon et al., 1998; Lakhno, 2000) and polaron (Breslin et al., 1997; Gasper & Schuster, 1997; Henderson et al., 1999; Yoo et al., 2001) creation in DNA, have also been studied. The former concerns the coupling of the vibrational and electronic mode degrees of freedom, while the latter relates to the formation of domain walls in dimerized DNA bands. Published scientific papers utilizing DNA are listed in **Table 2.3**.

Table 2.3: Published scientific papers of measurements of the effects of radiation on I–V properties.

Year	Title and Summary	References
1997	Micro fabricated electrochemical sensor for the detection of radiation-Induced DNA damage. Wang et al fabricated an electrochemical biosensor that was dependent on several factors, such as wavelength, irradiation time and distance. They also observed the same results when measuring a bare strip of electrodes that were connected by an irradiated DNA solution.	(J. Wang et al., 1997)
2011	DNA immobilization on n-type silicon surface and electro-physical properties of Au-DNA-(n-Si) structures. A DNA molecule was strongly fixed to an n-silicon tip on the surface and the changes in the electrical characteristics of a gold–DNA- Si junction were determined. The Schottky diode containing a molecular mesh had the same ideality factor and the Fermi level controlled the charge in the semiconductor.	(Sokolov et al., 2011)
2013	A novel nonmetric DNA thin film as a sensor for alpha radiation. They observed the morphological changes and optical responses of artificially designed DNA thin films in response to exposure to alpha particle radiation using an AFM, Raman microscopy and a reflectance spectroscope. Significant changes in the reflected intensity of the exposed DNA thin film suggested that a thin film made of biomolecules can be a promising candidate for the development of online radiation sensors.	(Kulkarni et al., 2013)
2013	Real time biomechanical characterization of DNA damage under therapeutic radiation beams. The report was the first to directly detect the DNA damage caused by gamma rays and by therapeutic irradiation. Procedure involved the use of silicon nano-tweezers procedure. This information paved the way to studies of DNA damage caused by ionizing beams to optimize tumour treatment. The study was performed using microfluidics. During constant irradiation, the resonant frequency and the noise level were not safely (not significantly) modified under irradiation.	(Perret et al., 2013).
2014	RADAMOL tool: role of radiation quality and charge transfer in damage distribution along DNA oligomer. Effect of exposing DNA to 0.01, 1, 2, 5, 10 and 20 MeV energy of electrons, protons and alpha particles was predicted using the simulation tool RADAMOL. The simulation explained how hole and electron migration and	(Štěpán & Davídková, 2014)

Year	Title and Summary	References
	localization act to produce charges due to the direct ionization of DNA and bound water.	
2014	Dual detection of ultraviolet and visible lights using a DNA-CTMA/GaN photodiode with electrically different polarity. A DNA-CTMA/n-GaN photodiode provided a good solution for detecting both ultraviolet and visible light using photocurrents and differences in electrical polarity. The changed charge transport technique in the DNA-CTMA (rely on light wavelengths) and the charge reactions between DNA-CTMA and n-GaN lead to the distinct characteristics observed.	(M. S. P. Reddy et al., 2014)
2015	Electrical conduction and photo responses of gamma-ray-irradiated single-stranded DNA/single-walled carbon nanotube composite systems. This report investigated the electrical conductivity and photoresponse of ssDNA/SWNT composite films irradiated by gamma rays. Gamma radiation led to photodesorption and photoresponse. The measurements indicated changes in the photoexcited charge carrier generation in the composite systems and the creation of structural defects and radicals. Furthermore, the charge transportation fluctuated in a manner consistent with the tunneling model, indicating that the gamma rays modify the barrier to thermally activated conduction.	(Hong et al., 2015)

CHAPTER 3: EXPERIMENTAL SETUP

3.1 Introduction

This chapter explains the DNA preparation and the DNA sensor fabrication processes. The techniques for the electrical characterization and the description of the essential equipment were also discussed. Structural, optical and electrical properties of the DNA thin film were determined using several techniques. The structural properties of these materials were evaluated using Atomic Force Microscopy (AFM) and field Effect Scanning Electron Microscopy (FESEM) while thickness of the thin film was determined using a KLA TENCO P-6 Profilometer. Optical properties of the DNA were investigated using UV-Vis spectroscopy, micro-Raman and photoluminescence (PL) spectroscopy. Finally, the electrical characteristics were evaluated using a Keithley 236 Source Measurement Unit (SMU).

3.2 Materials

3.2.1 DNA Extraction

DNA was extracted from a common local Malaysian fungus, oyster mushroom or its scientific name *Pleurotus floridanus* (**Figure 3.1**). A simple preparation procedure to extract the mushroom DNA from colonies of the fruiting bodies was used for polymerase chain reaction (PCR) amplification (PTC-100TM, MJ Research Inc., U.S.A.). The procedure began with the collection of minute quantities of mycelium (0.1–1.0 gm) from a colony of the fruiting body (Stipe) of a mushroom species using sterilized tweezers. The mycelium was suspended in 100 µl of STL buffer in a 2 ml centrifuge tube and 100 µl of STL buffer was added. The specimen was later grinded and then another 100 µl of STL buffer was added. This step was followed by incubation at 55°C for 15 min. Every 2 min, the solution was vortexed to provide uniform mixing. Finally, the temperature was maintained at 60°C for another 45 min before the addition

of 25 µl of OB protease solution, followed by further vortexing. The sample was then incubated for 45 min at 60°C with occasional mixing.

A centrifuge was used to remove droplets from the lid of the centrifuge tube, which was spun at a speed of 8000 rpm× g for 30 seconds. Then, 225 µl of BL buffer was added and the sample was vortexed again to mix the contents. The next step was incubation at 60°C for 10 min, followed by a water bath temperature adjustment to 70°C. The sample was centrifuged again to further remove drops from the lid. Afterward, 225 µl of absolute ethanol was added to the centrifuge tube and then the mixture was vortexed. The sample was centrifuged to separate each component in the homogenous mixture. For Edmund preparation (solution), 100 µl of equilibration buffer was mixed into the column and allowed to rest for 4 min before spinning in the centrifuge at a speed of 13000 rpm ×g for 20 s. The entire sample was transferred to the column, including any precipitate that may have formed. Centrifugation speed was then maintained at 8000 rpm ×g for 1 min to obtain DNA molecules. After the collection tube was discarded, nitrogen gas was allowed to pass through the liquid to remove water.

During the preparation of the elution buffer, a water bath at 70°C was used. The columns were transferred to new 2 ml tubes. This step was preceded by washing by the pipetting of 500 µl HB buffer into the columns; centrifugation at a speed of 8000 rpm ×g for 1 min was used to remove the collection and flow through liquid. The collection tube was washed for reuse via pipetting 750 µl of DNA wash buffer into the columns and another centrifugation at 8000 rpm ×g for 1 min. A new collection tube was then used and the same procedure was performed a second time with DNA wash buffer. Afterward, the flow through liquid was discarded and the collection tube was stored. Centrifugation was then performed at a maximum speed of 13000 rpm ×g for 2 min to dry the columns and the sample was then placed into a 2 ml micro tube. Next, 50 µl of

elution buffer was added; the sample was mixed and then kept in the tube for 3 minutes at room temperature. Afterward, the sample was centrifuged at a speed of 8000 rpm ×g for 1 min for elution. The process was then repeated as above before the PCR process.

Figure 3.1: The oyster mushroom used in this work.

DNA samples in Eppendorf tubes were then stored in a -20°C freezer for future use. The DNA of all samples was amplified by PCR (PTC-100TM, MJ Research Inc., U.S.A.) using the following universal primers: ITS1 forward (5′-TCC GTA GGT GAA CCT GCGG-3′) and ITS4 reverse (5′-TCCTCCGCTT ATT GATATGC-3′). Amplification reactions were performed in a total volume of 50 μl containing 4 μl of 10x PCR buffer, 2.5 μl of dNTP mix, 2.5 μl of each primer, 1 μl of Taq polymerase (Cosmo, Korea), 4 μl of genomic template DNA and 26 μl of sterilized distilled water. The suitability of the DNA obtained using the extraction method was tested by PCR amplification with the specific primers ITS 1 and ITS 4. PCR conditions were 5 μl of MgC1$_2$, 1 μl of dNTP, 4 μl of each primer, 1 μl of Taq, 26 μl of ddH$_2$O and 4 μl of

DNA; for a 50 µl final volume, the cycling parameters were 30 cycles at 94°C for 30 min of denaturation, 50°C for 60 min of annealing and 72°C for 1 min of extension. The initial denaturing at 95°C was extended to 5 min and the final extension was at 72°C for 5 min (Cubero et al., 1999; Imtiaj et al., 2011).
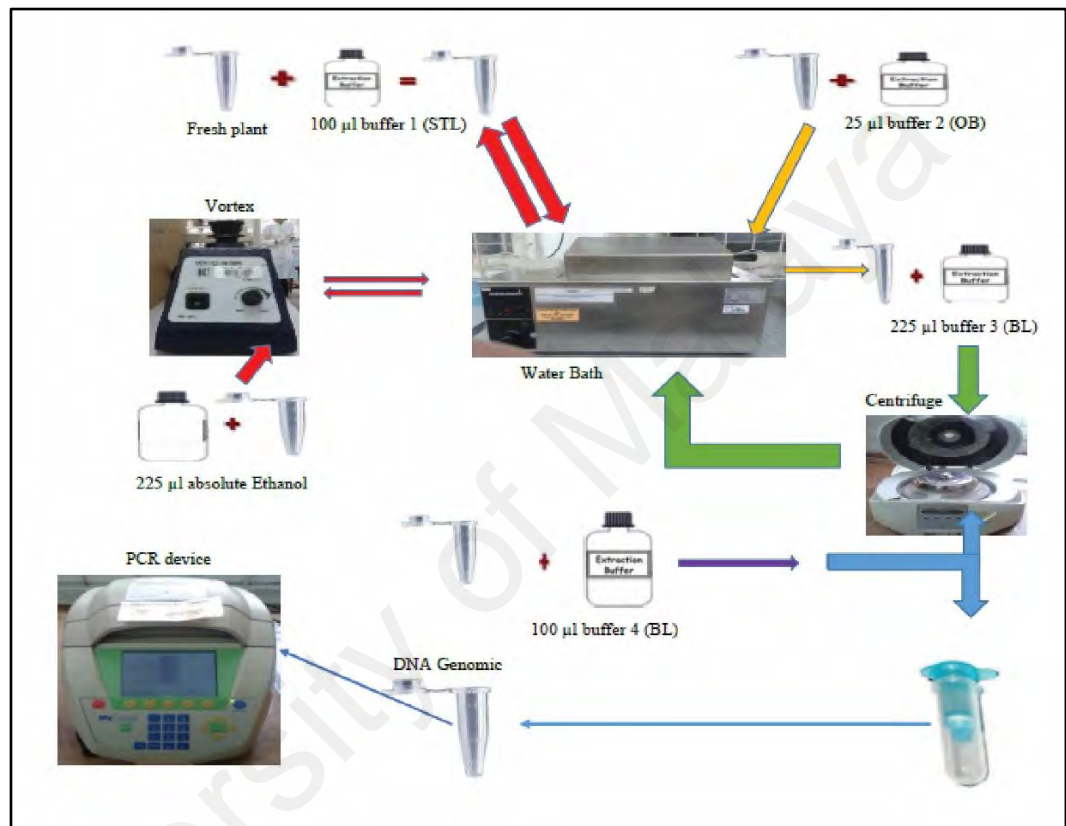
Figure 3.2: The DNA extraction steps.

Genomic DNA was tested using gel electrophoresis. A agarose gel was prepared by mixing 0.4 gm of agarose powder with 40 ml of Tris-Borate EDTA (TBE) buffer. The mixture was heated in a microwave to allow the agarose to melt. After the mixture formed a clear solution indicating that the agarose was fully melted, the solution was cooled using running tap water. Then, RedSafeTM nucleic acid staining solution (2 ml) was added to and mixed with the solution. The solution was then poured onto a mould, a comb was placed and the gel was left for approximately 20 min to cool and solidify. DNA (5.0 µl) was mixed with 3.0 µl of iNtRON loading dye before being loaded into

the well and $1 \times$ TBE buffer was used as the running buffer. Gel separation was carried-out for 60 min at 100 V. After electrophoresis, the gel was viewed under an autoradiograph machine (AlphaDigiDoc UV transilluminator). The general extraction steps are shown step by step in Error! Not a valid bookmark self-reference.

3.3 Fabrication Techniques

In this section, the fabrication methods utilized to make the devices are discussed. These steps include the substrate preparation (pre-fabrication) and the material deposition systems. The devices fabricated in this research were Schottky junction diodes or sensors for potential application in radiation and humidity detection. The steps are explained as follows.

3.4 Substrate Cleaning

3.4.1 Glass Substrate

Glass substrates were cleaned by immersion in soap solution, followed by an ultrasonic bath for 15 min to remove stubborn grease and dirt from the substrate surface. The substrates were then rinsed sequentially in deionized (DI) water, acetone solution, ethanol solution and DI water again. Finally, the glass substrates were dried using nitrogen gas. Glass substrates were utilized for the morphology and optical studies and to deposit the Al metal.

3.4.2 Silicon Substrate

Silicon was manually cut to dimensions of 1.0 cm × 1.0 cm using a diamond cutter. The standard RCA method was then used for cleaning. First step was a rinse in DI water and was followed by a simple cleaning process for removing contaminations. In this work, the p-Si substrates were cleaned using the following steps;

a) Standard RCA cleaning was performed using a mixture of 96% HCl and 32% H_2O_2 (Hydrogen Peroxide) and DI water solution in a 1:1:6 volume ratio for 10 min to remove firm ionic and metal surface impurities. This step was followed by a strong rinse in DI water.

b) After the standard RCA cleaning, the substrate was further cleaned using a mixture of 96% ammonium hydroxide (NH_4OH), 32% H_2O_2 (Hydrogen Peroxide) and DI water solution in a 1:1:5 volume ratio for 5 min, followed by a strong rinse in DI water.

c) To remove the native oxide layer and any impurities in the oxide from the wafer surface, the substrates were immersed for 5 min in 1:10 hydrofluoric acid (HF): DI water. This step was again followed by a strong rinse in DI water.

d) Nitrogen air was used to dry the substrates at the end of cleaning process.

3.4.3 Indium Tin Oxide

ITO is a conventional and transparent semiconducting oxide thin film utilized in morphology and optical studies. It is also used as the substrate in optoelectronics (Fan & Zavracky, 1976; Marikkannan et al., 2015; Saghaei et al., 2015), display and infrared (Kang & Guo, 2007; Kim, 1999) devices. ITO is known for its sensitivity to toxic gases, such as nitric oxide, suggesting its possible use as a sensor material (Vaishnav et al., 2005). Due to its wide electrochemical window and its low electrical resistivity, ITO is utilized as transparent electrodes for spectro-electrochemical studies.

The dimensions used in this work were 2.0 cm × 2.0 cm. Process of cleaning the ITO substrate is described here. Initially, the substrate was immersed in soap solution. It was then sonicated in an ultrasonic bath for 15 min. The substrate was then sequentially rinsed in DI water, acetone and isopropanol for 5 min. Finally, the substrate was blown

dry using nitrogen gas. All these cleaning procedures were carried out very carefully to ensure that the substrates were totally clean and free from any contaminations.

3.4.4   Quartz Slide

Quartz slides were utilized for UV-Vis absorption because they are highly transparent. Form a homogenous film and since they do not absorb in the UV range. The slides were cuts manually using a diamond cutter (using a regular cutter) into dimensions of 1.0 cm × 2.5 cm. Cleaning by immersing in Decon 90 solution followed this step and the slides were then placed in an ultrasonic bath for 15 min to remove stubborn grease and dirt. They were rinsed using DI water, acetone solution, ethanol solution and then DI water again. Finally, the slides were dried using nitrogen gas.

3.5   Thermal Metal Evaporator

An Al electrode was deposited on top of the organic (DNA) thin layer, silicon and glass using a thermal evaporator. A schematic diagram of the thermal evaporator system used is shown in **Figure 3.3**(a). The system consists of a glass vacuum chamber, a two-stage rotary pump, a diffusion pump, a penning gauge and two Pirani gauges. The diffusion pump was also cooled with flowing water for effective pumping. A base pressure of at least 10^{-5} mbar must be achieved before any deposition could be carried-out.

Figure 3.3(b) includes a picture of the vacuum chamber. The substrate was covered with an Al mask with the electrode pattern. Al wire (Kurt J. Lesker, Hudson Valley, PA, USA) of 99.999% purity was cut to approximately 1.5 cm in length and hooked to the tungsten wire. After the pressure inside the chamber was reduced to a vacuum level greater than 10^{-5} mbar, a current was applied through the tungsten wire filament (Function Technologies Company Kuala Lumpur).Current was increased

slowly to approximately 20-24 A to achieve evaporation. Sample for deposition was placed on the upper side of the chamber. After that the shutter was closed for 30 s upon melting of the Al to evaporate and obtain a high quality deposition. An electrical connection was then made using needles, a small crocodile clip and silver paste. The final fabricated device (Al/DNA/Si/Al) is shown in **Figure 4.1**(b).
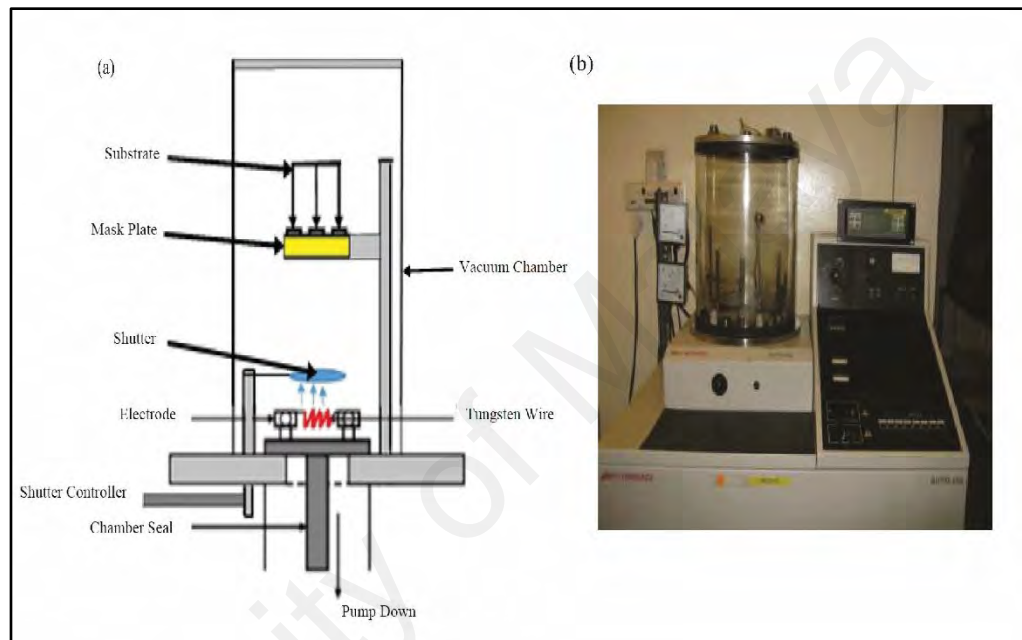
Figure 3.3: The schematic diagram of the thermal evaporator system belonging to the Department of Physics, University of Malaya, used in the present study.

3.6 Measuring Thickness

Thickness of the DNA thin films utilized for this study was measured using a KLA Tencor P-6 profilometer (**Figure 3.4**). The working principle of this device uses the greatest difference between the substrates and the thin films that it measures. For this reason, the films must be scratched very carefully in order to create a different layer between the substrate and the thin film. A small needle or diamond stylus is moved vertically through the thin film surface for a specific distance, as shown in **Figure 3.4**(a). The thin film thickness was measured from the step height difference between the substrate (base) and the thin film layer. In this work, the film was scratched at four

different places and the average value of the measured depths was the thin film thickness.
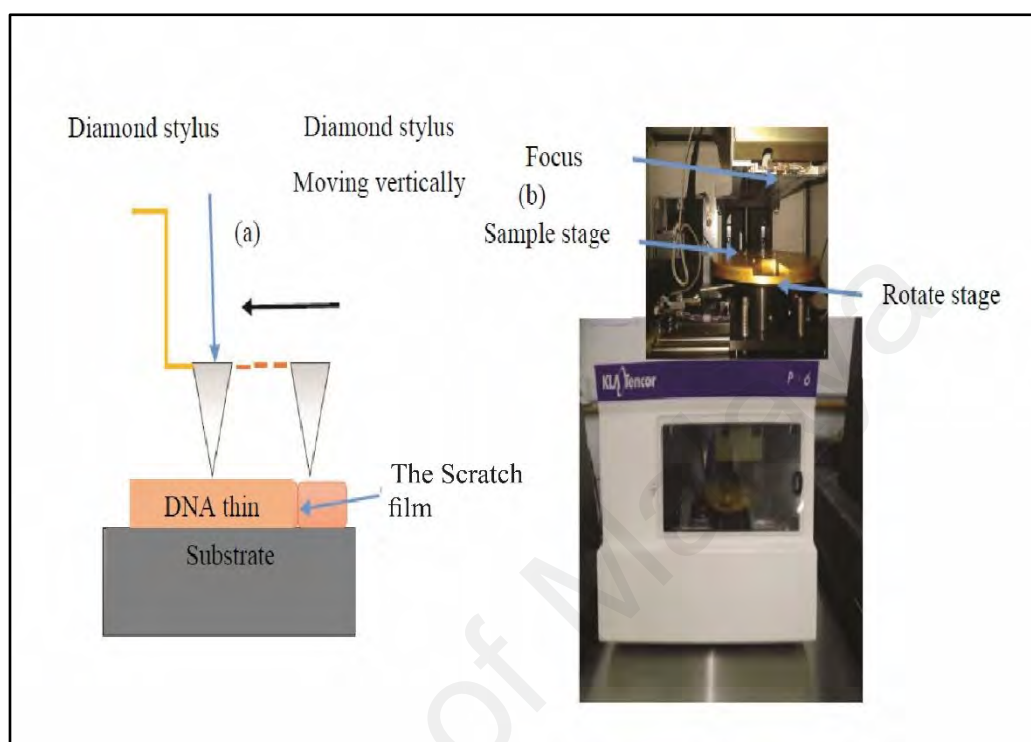
Figure 3.4: Photograph depicting the KLA TENCOR P-6 surface profilometer used to measure the thickness in this research.

3.7   Atomic Force Microscopy

Figure 3.5(a) is a scanning probe-imaging technique that characteristically images the surface structures on the basis of the surface topography. AFM has a limited range of scan area but has very high crosswise and height resolution in nm range. These features make AFM the most common instrument for studying the surface morphologies of thin films, such as organic layers. AFM can provide suitable means of examining the surface morphologies to optimize the DNA thin film or to observe the changes on the surface that result from irradiation.

A cantilever with a sharp tip was utilized to scan the sample surface and was part of the AFM device. The curvature radius of the cantilever tip is extremely small (~10-50 nm) and the tip is usually made from silicon or silicon nitride. The working principle

for this device involves the photodetector recording the laser deflection caused by the cantilever deflecting a laser beam from a laser diode, as shown in **Figure 3.5**(b). Tapping mode is the best mode. In this mode, the cantilever tip does not physically contact the surface tip; instead it vibrates at its resonant frequency. The amplitude of the vibrations was changed near the surface and this information can be transferred and recorded as a variation in the surface profile. Thus, this mode is comparatively less destructive than contact mode. Cantilever for small displacements was controlled according to Hooke's law. The laser spot was reflected from the top of the cantilever into the photodiodes, which were utilized to measure that deflection. In this work, AFM surface scans of DNA layers were obtained using a Q-Scope Series (Ambios Technology, Germany) scanning probe microscope.
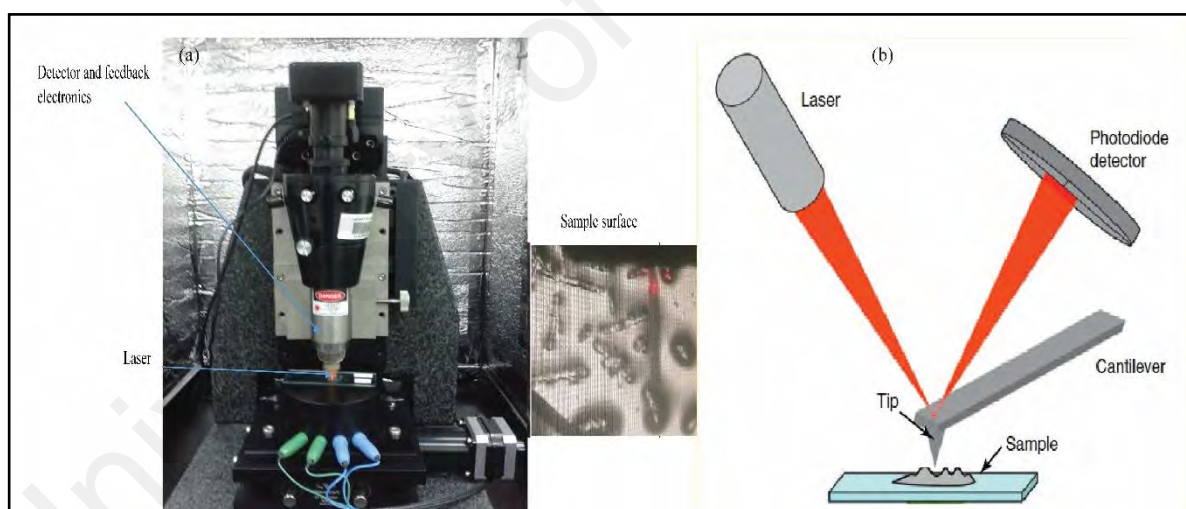
Figure 3.5: (a) AFM used in this work (Faculty of Dentist University of Malaya) and its (b) components (de Souza & Rocha, 2011).

3.8 Raman Spectroscopy

The optical properties of the DNA thin film were studied using a Raman spectroscopy (RENISHAW inVia Raman Microscope) shown in **Figure 3.6**. Raman spectroscopy is capable of providing several types of information regarding the molecular composition of both organic and inorganic materials. These data include the

chemical character and the crystallinity of materials. Raman spectroscopy is a method based on the inelastic and elastic scattering of monochromatic light by a molecule. Inelastic scattering or Raman scattering occurs when the molecule becomes excited to a different vibrational level relative to the original state. Elastic scattering or Rayleigh scattering takes place when a photon is re-emitted and has the same frequency and energy as the incident light; this process occurs when the molecule is excited to a virtual level and subsequently relaxes to the original vibrational region.

Figure 3.6: The Raman spectroscope (Department of Physics, University of Malaya) used in the present study.

Stokes Raman scattering occurs when the incident photon transfers energy to the sample. Anti-stokes Raman scattering occurs whenever the incident photon absorbs energy from the sample. **Figure 3.7** shows the different types of scattering (Lin-Vien et al., 1991; McCreery, 2005).

Absorption, emission and scattering phenomena can occur. All these phenomena occur on material surfaces due to incident light. A laser can pass through the surface of

the thin film, causing light to scatter with the same wavelength or with the incident frequency v_o and the laser light has the energy hv_o, where h is Planck's constant and v_o is the frequency of the laser beam that is incident on the surface of the material.

Differences in the energy of the incident and scattered laser light can be observed as a wavelength (or frequency) shift between the scattered light and the excitation light. When the light source emits photons onto a system, it increases the energy of the system instantly by inducing a polarization in the chemical species; For example, laser beams are capable of exciting electrons in molecules from the ground state to a virtual state.
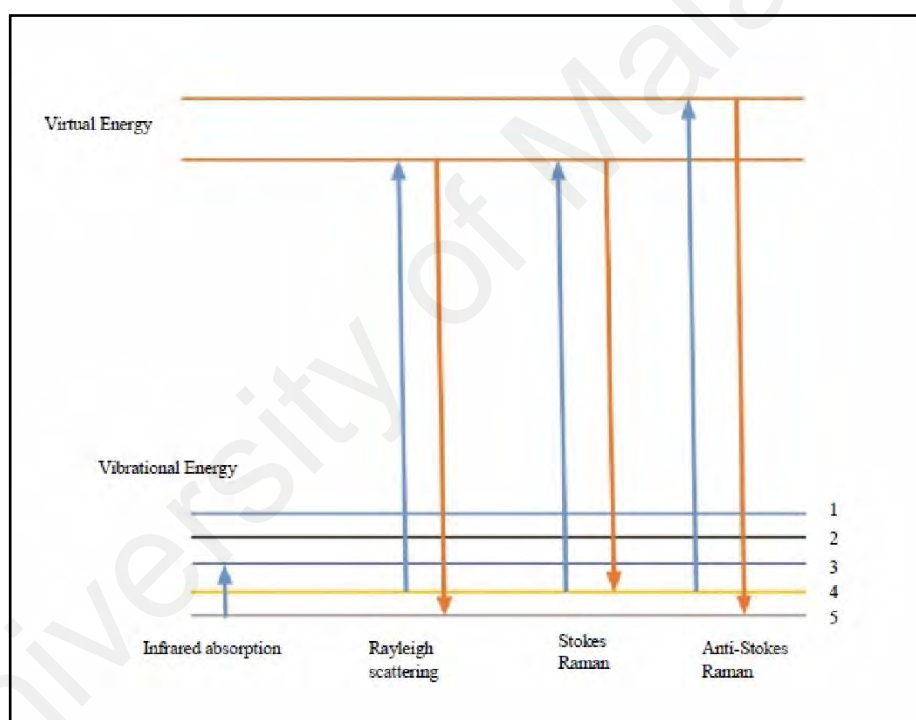
Figure 3.7: Energy states for infrared and Raman spectroscopy (McCreery, 2005).

The polarized condition is not a true energy state and is considered a virtual state. Relaxation from the virtual state occurs almost instantaneously, mainly with reversion back to the initial ground state. The molecule emits a photon and returns to a different vibrational or rotational state and the molecule gains or loses energy equivalent to ΔE (where E is the energy). For the Rayleigh scattering produced by this process, the

scattered light has the same wavelength as the excitation laser. Relaxation to the first excited vibrational level results in a Stokes-Raman shift. This shift scattered light has lower energy than the laser light. In most systems, at least a small population of molecules must initially be at an excited vibrational state.

3.9   Field Emission Scanning Electron Microscopy

An electronic beam (e-beam) is the foundation of the SEM, which is considered a high-magnification imaging instrument. Instead of the light in optical microscopes, an SEM is based on the scanning of a sample with a beam of high-energy electrons to observe the surface topography, chemical composition, crystalline structure and orientation.

The electron gun (cathode) placed at the top of the microscope ejects electrons and the anode accelerates the electrons, forming the e-beam. The instrument has a slit that only allows the vertically focused electrons to move downwards. A magnetic lens assists in the focusing of the beam into a small region.

Meanwhile in FESEM, a beam of electrons produced through a field emission source scans the sample surface. The electrons that are created in an electron gun are accelerated in a column by a high electrical field gradient. In general, the beam of electrons interacts with the electron shell of the sample. Back-scattered electrons, secondary electrons, light, heat, X-rays and transferred electrons are created. Backscattered electrons are the ones that rebound from the nuclei of the atoms in the sample, while secondary electrons are emitted from the sample and X-ray could be utilized for element analysis. An electronic signal is then generated by a detector, which detects the secondary electrons. The surface structure of a sample can be determined from the velocity and angle of the secondary electrons.

Finally, the signal is treated with amplifiers and an image is produced on the monitor based on the scanning of the sample with a beam of high-energy electrons to detect surface topography, crystalline construction, chemical composition and orientation. In this research, FESEM Model Jeol JSM 7600F from Japan was used (**Figure 3.8**).
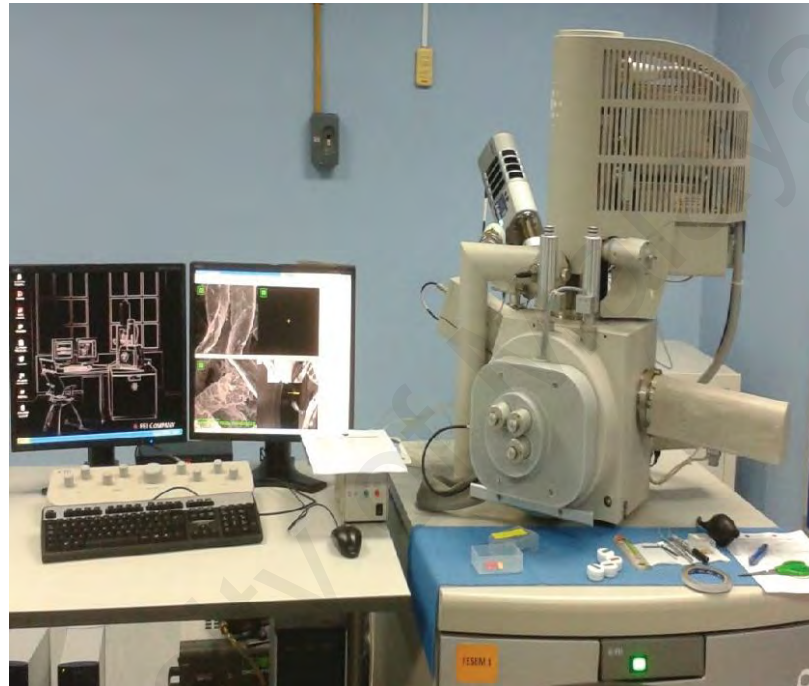
Figure 3.8: One of two FESEM used in this work (IPS, University of Malaya).

The advantage of utilizing FESEMs are as follows Firstly, field emission is one way of generating electrons that avoids thermionic emitters, which uses electrical current to heat up a filament as, in SEMs. A Field Emission Gun (FEG) called a cold cathode field, emitter does not heat the filament. The emission is reached by placing the filament in a huge electrical potential gradient. The FEG is usually a wire of tungsten fashioned into a sharp point. Secondly, the spot size (of electron beam) should be smaller to obtain better resolution. The spot obtained by FEG is much smaller than thermionic emission electron gun since its smaller dimension. Also the energy spread

(coherency) can be enhanced by utilizing FEG gun (Huggett & Shaw, 1997; Matthew & Drouin, 2010).

3.10 Preparation of the Experimental Setup

Sensors are devices that produce a measurable output variation in response to an identified input stimulus. This stimulus could be a physical stimulus, for example, temperature, pressure or a concentration of a specific chemical or biochemical material. The output signal is typically proportional to the input variable; for example, temperature sensors respond with a voltage, resistance, color, or other change when the temperature is varied (Setter et al., 2006). The effect of other radiation sources can be neglected when placing the sensor in a special box made from Palladium (Pd) metal when carrying out experiments. This ensures that the effects of gamma and background radiation and beta particles are removed.

3.10.1 Current-Voltage Characterization

A schematic of the electrical preparation used to measure the I–V features is shown in **Figure 3.9**. The I–V properties of the junction diodes were determined using a SIGNTONE Probe Station connected to a Keithley-SMU 236 I–V source multi-meter and LabVIEW graphical programming. To compute the different parameters of the Schottky diode, it was necessary to measure the I–V characteristics under dark condition for the alpha irradiation diode. The calculated parameters were the ideality factor (n), barrier height (Φ_b) and series resistance (R_S), as well as the defect states and transport properties of the material. To acquire I–V profiles, the following were needed: (1) a probe station with needles to probe very small devices, (2) a source meter to apply a voltage and measure the current or vice versa and (3) a computer with an appropriate

program to collect and analyze the data. The figure shows the schematic of our I–V setup. All these measurements were repeated three times to ensure reliability.
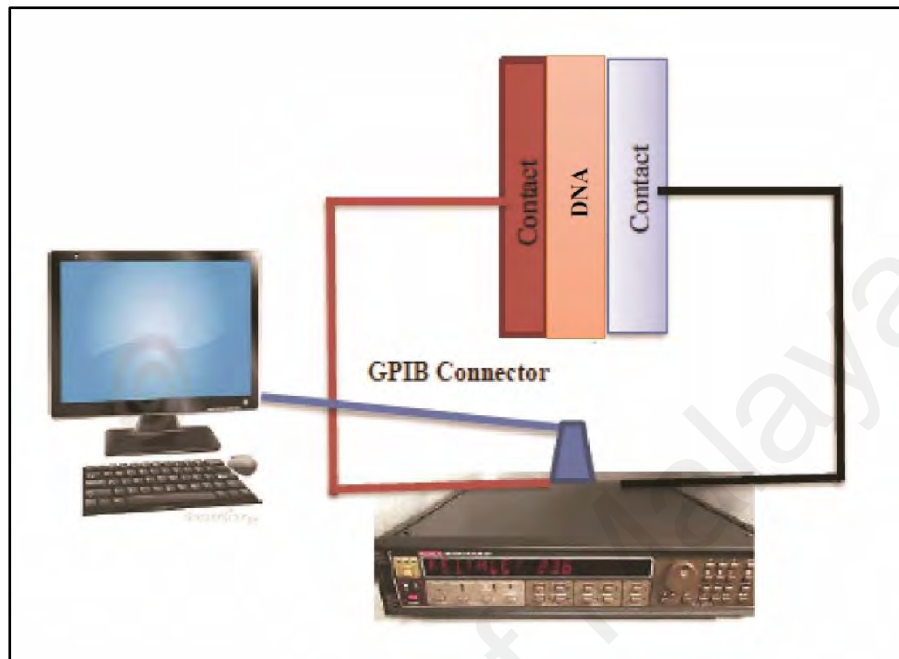
Figure 3.9: Electrical preparation utilized to determine the I–V features.

3.10.1.1 Preparation of Al/DNA/p-Si/Al Junctions

Junctions were prepared using a polished p-type Si wafer with [100] orientation with thickness and resistivity of $650 \pm 25,850 \pm 100$ μm and (1–10), (0.008–0.03) Ω·cm, respectively (Polishing Corporation of America, Santa Clara, CA, USA). The wafer was chemically cleaned using the RCA cleaning procedure; i.e., 10 min boil in $NH_4 + 6H_2O + H_2O_2$ followed by a 10 min boil in $HCl + H_2O_2 + 6H_2O$ solution. Then, a low-resistivity Ohmic back contact to the p-type Si wafer was made by using Al, followed by heat treatment at 570 °C for 3 min in N_2 atmosphere. The native oxide on the front surface of the Si wafer was removed by immersing in $HF + H_2O$ (1:10) solution before rinsing in DI water (18.2 MΩ-cm, Barnstead Nanopure II water system, Lake Balboa, CA, USA) for 30 s. Other necessary chemicals (NH_3, H_2O_2, HF, HCl and acetone) were supplied by Sigma Aldrich (St. Louis, MO, USA) and were used without further

purification. After which, formation of the organic DNA layer was carried-out by using a micro syringe (Hamilton) containing 10.0 µl DNA with concentration of 1.80 ng/µl from the pre-prepared DNA solution. Schottky metal contacts were then deposited onto the organic layer using a metal shadow mask by evaporating Al metal wire (Kurt J. Lesker, Hudson Valley, PA, USA) of 99.999% purity. The Al contacts had dimensions of 2.0 mm, 2000 Å and 3.14×10^{-2} cm^2 of diameter, thickness and area, respectively. All evaporation processes were carried-out in a vacuum thermal metal evaporator-coating unit (Edward Auto 306, West Sussex, UK) pressurized to about 10^{-7} mbar. The prepared DNA based devices were air-dried for 24 hr in a class 1000 (1K) clean room before carrying out the irradiation by alpha particles. Sample irradiation by alpha particles was achieved using ^{241}Am with an activity of 150 nCurie and $t_{1/2}$ of 457 years for periods of 2, 4, 6, 8, 10, 20, 30 and 40 min. It's corresponding I–V profiles were finally recorded in dark using an electrometer (SMU-236, Keithley, OH, USA) at room temperature as shown in **Figure 3.10**.
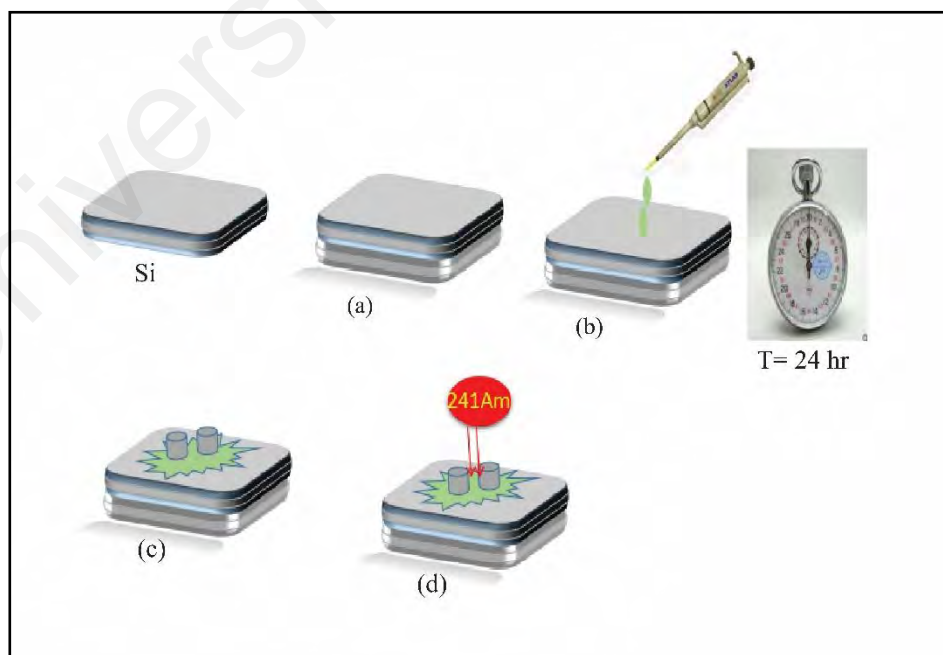
Figure 3.10: Preparation process of the sample (a) Al layer deposition, (b) drop of DNA solution was applied on the sample (c) Al layer deposition and (d) alpha particles bombardment on the sample.

3.10.2 Real-time Current-Voltage Measurement Setup
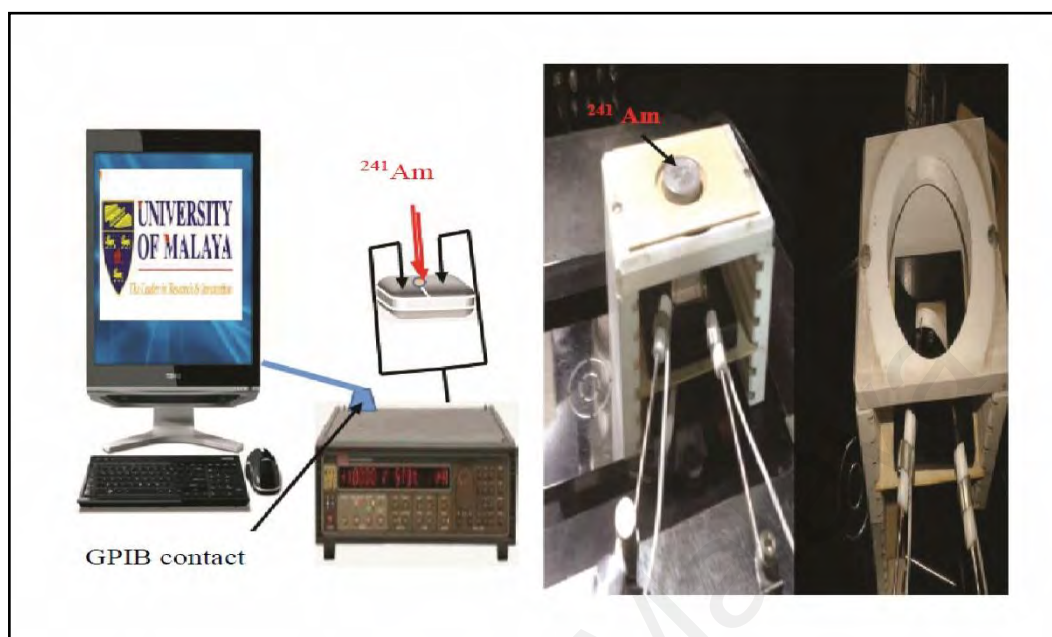
Figure 3.11: Setup of the real-time detection of alpha particles to determine the I–V features.

In this setup, we utilized a ^{241}Am source as an alpha radiation source for 0 to 40 min; these were equal to dosages of 0 – 0.24 Gy. For I–V measurements, the device was shielded with a proper contact, as shown in **Figure 3.11**. In our experimental, sensitivity was determined based on distance from source, which was about 4.1 cm. We observed that beyond 4.1 cm, there was no significant exposure on DNA. As such, the detection sensitivity was defined by length. However, the distance of the source from the DNA layer was maintained at 2 cm for the purpose of this work.

3.10.2.1 Fabrication of the Al/DNA/Al Sensor

Glass slides cleaned for 15 min using DI water (18.2 MΩ.cm, Barnstead Nanopure II water system, Lake Balboa, CA, USA) in an ultrasonic cleaner and later dried in a dust free environment were utilized as the substrates. Thin films of Al (thickness ≈325 nm) were deposited on the glass substrate using an Edward Auto 306

vacuum coater with a diffusion pumping system (Edward Auto 306, West Sussex, United Kingdom) and Al metal wire (Kurt J. Lesker, Hudson Valley, PA, USA) of 99.999% purity. While depositing the Al thin film, pressure inside the chamber was kept at 10^{-5} mbar, whereas the deposition rate was maintained at 0.1 nm/s. The gap between the electrodes was 30 µm, while the length of the gap was 25 mm, after which the formation of the organic DNA layer was carried-out by using a micro syringe (Hamilton concentration of DNA 1.80 ng/µL) containing 10 µl pre-prepared DNA solution. The fabricated device was then kept in a 1K-class clean room. Sample irradiation by alpha particles was achieved using ^{241}Am with an activity of 150 nCurie and $t_{1/2}$ of 457 years (The Radiochemical Centre. Amersham, England) for periods of 2-40 min. The thickness of the DNA layer was measured using two devices: Ellipsometer and Profilometer. For the nonradiated sample, the thickness was measured at 100 nm. Thickness increased with the increase in the irradiation time, as there is an increase in the number of tracks and therefore its roughness. The value for the effective area is 1.625×10^{-5} m^2 while the distance of the source from the DNA layer was maintained at 2 cm.

3.10.3 Fabrication of Humidity Sensor

Figure 3.12 show the setup utilized to conduct humidity measurements. The various components in the setup for characterizing the humidity sensors includes (i) an LCR meter (Instruments Instek LCR-829 LCR Meter) to measure the capacitance and resistance of the devices and (ii) a digital humidity meter (Testo 625-Thermohygrometer) to measure the humidity level with ±1% RH error. Both of these instruments were used to determine the electrical characteristics, which included the capacitance-humidity and resistance-humidity relationships and the hysteresis response, along with the response and recovery times. The humidity level was measured by the

flow of wet and dry nitrogen in the chamber required to achieve the desired RH level. All the measurements were conducted at room temperature and in triplicates for reliability purpose.
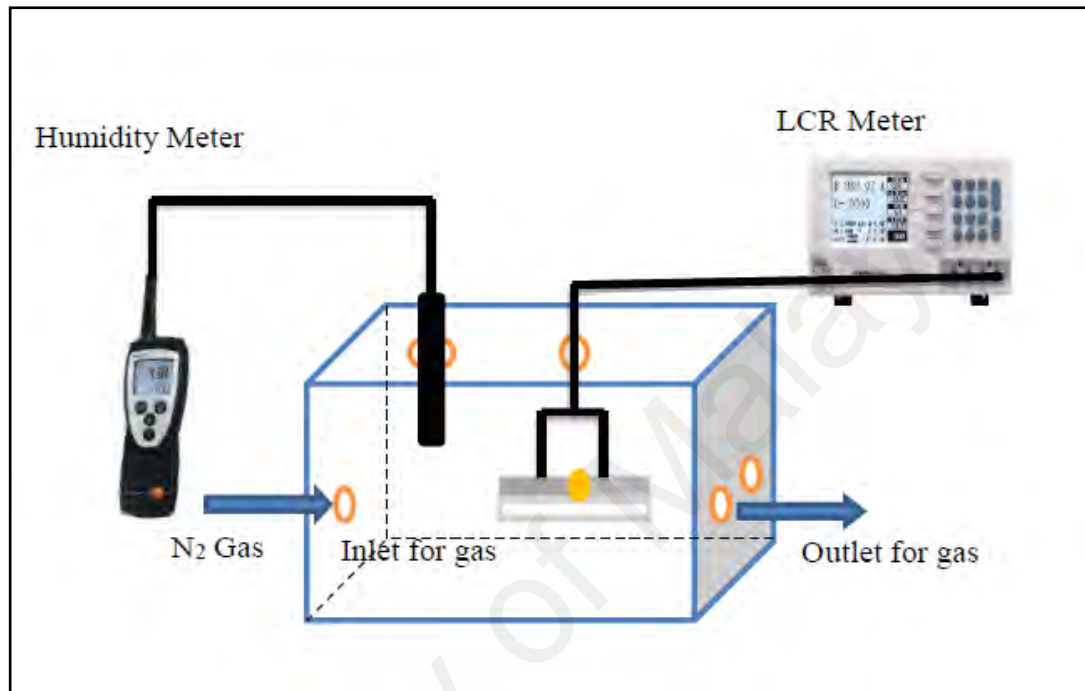
Figure 3.12: Schematic diagram of the characterization setup.

CHAPTER 4: RESULTS AND DISCUSSIONS

4.1 Introduction

Many types of materials such as inorganic semiconductors have been employed as detectors for nuclear radiation, the importance of which has increased significantly due to recent nuclear catastrophes. Despite the many advantages of this type of materials, the ability to measure direct cellular or biological responses to radiation might improve detector sensitivity. Semiconducting organic materials such as DNA have been studied in recent years. This was established by studying the varying electronic properties of DNA-metal or semiconductor junctions when exposed to radiation. DNA in particular is a polymorphic molecule strongly affected by the environment (H. M. J. Al-Ta'ii et al., 2015c).

4.2 Investigations of the Electrical Properties of Structures Al/DNA/ITO/Al Exposed to Alpha Particles

I–V characteristics of Al/DNA/ITO/Al, Al/DNA/Si/Al and Al/DNA/Al junction in forward and reverse bias measured at room temperature are shown in **Figure 4.1**(a-d). The forward bias corresponds to the positive potential to the Al with respect to ITO and Al electrode. I–V characteristics of the Schottky junction were nonlinear, asymmetric and show rectification behavior, which gives the clue of formation of the depletion region. Measurements were carried-out in the dark to remove possible contribution of the environmental light.

.
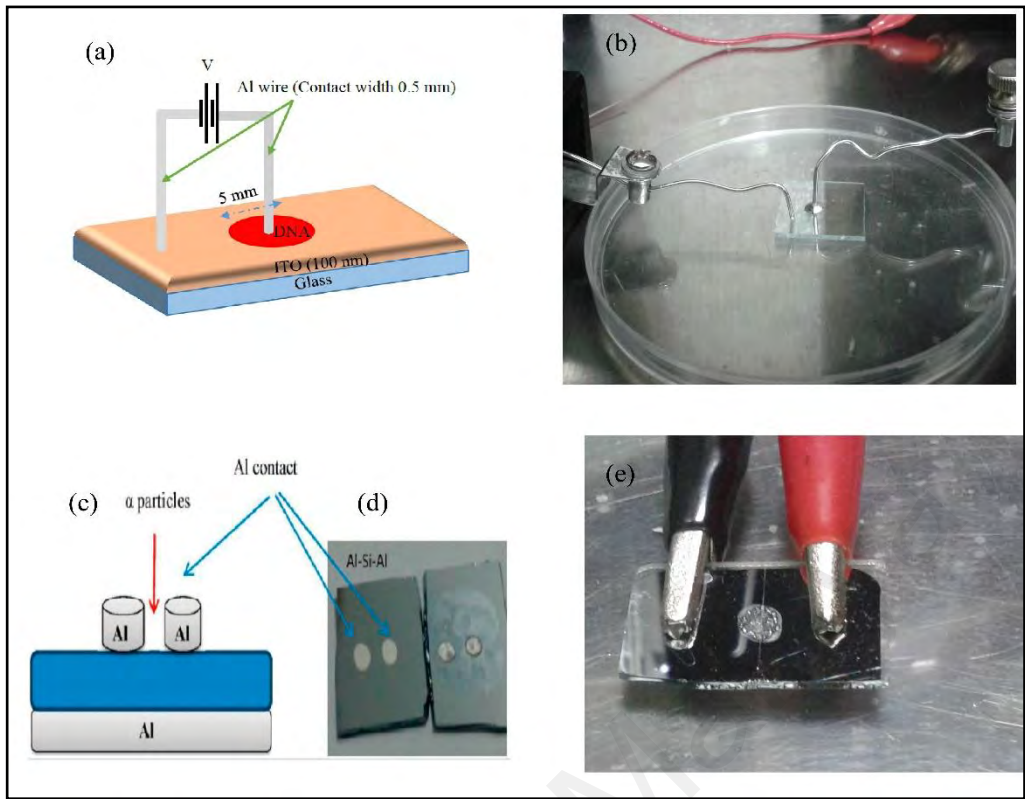
Figure 4.1: The device fabricated in this work.
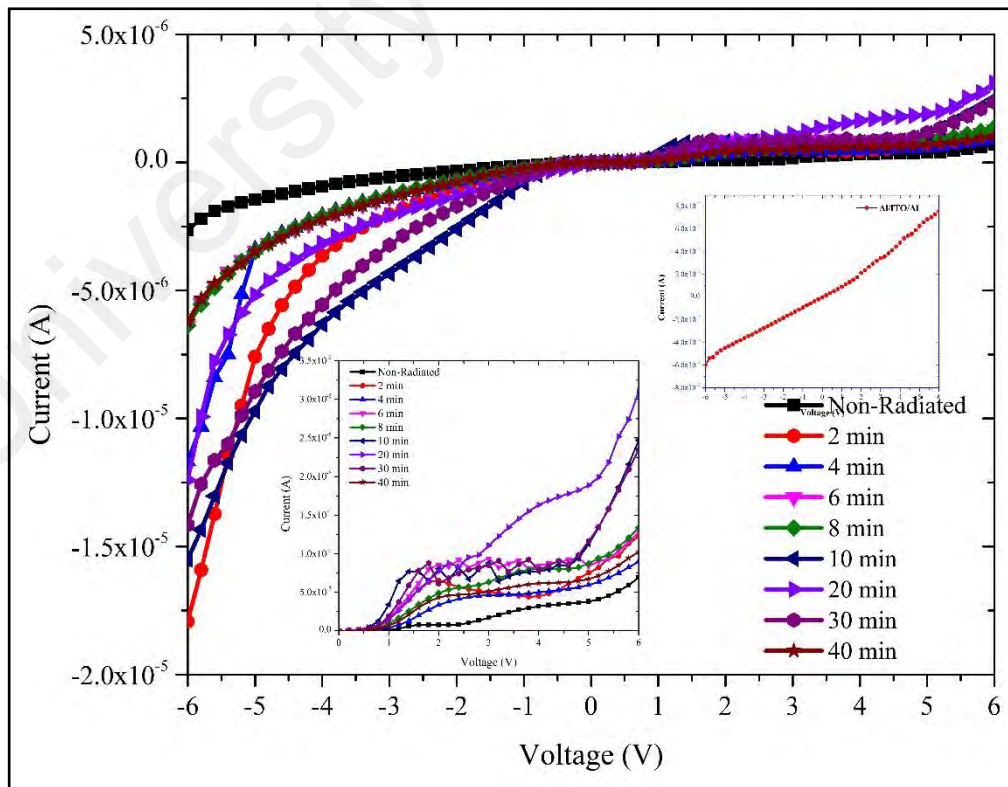
Figure 4.2: The relation between the current and voltage for forward and reverse regions.

The I–V characteristics of the DNA sensor at 300K (room temperature) are shown in **Figure 4.2**. I–V characteristics can be described by the following relationship (Ahmad & Sayyad, 2009; Karataş & Türüt, 2004; Kılıçoğlu & Ocak, 2011; Tuğluoğlu & Karadeniz, 2012):

$$I = I_o \exp\left(\frac{qV}{nkT}\right)\left[1 - \exp\left(\frac{-qV}{kT}\right)\right] \tag{4.1}$$

where

$$I_o = AA^*T^2\left(\frac{-q\Phi}{kT}\right) \tag{4.2}$$

where I_o is the saturation density, V is the definite forward-bias voltage, A is the effective diode area, k is the Boltzmann constant, q is the charge, T is the absolute temperature and A* is the Richardson constant ($A^*=1.3\times10^5$ Acm^{-2}K^{-2}) for ITO (Tahir et al., 2012). The barrier height was calculated using Equation (4.2) and the value of reverse saturation current was obtained from forward bias semi-(log(I)–V) graph for all cases. The value of the ideality factor (n) was calculated from the slope of the linear region of the forward bias of (ln(I)–V) plot as shown in **Figure 4.3** using the following relation (Yakuphanoglu, 2008);

$$n = \frac{q}{kT}\left(\frac{dV}{d\ln I}\right) \tag{4.3}$$

For an ideal Schottky barrier diode, n is equal to one. However, n usually has a value greater than unity, which shows the importance of the effect of the series resistance in the linear region. The high values of n may also be attributed to the non-homogenous thickness of the organic film (Karataş & Türüt, 2004), series resistance (Aydoğan et al., 2008), thickness (Okur et al., 2009) and temperature (Cheung & Cheung, 1986; V. S. Reddy et al., 2006). Using Equation (4.2), the barrier height, Φ can be derived and shown by;

$$\Phi = \frac{kT}{q} \ln\left(\frac{AA^*T^2}{I_o}\right) \qquad (4.4)$$

Using Equations (4.3) and (4.4), the values of the barrier height and ideality factor can be measured. The barrier height describes the potential barrier at the interface of the DNA and the Al wire. Higher Φ_b will constrain the flow of charge carriers in the device, to create non-uniform junctions at the interface. In addition, Φ_b relies on the interfacial layer thickness and state density along with series resistance (Karataş & Türüt, 2004; Schmitsdorf et al., 1997).
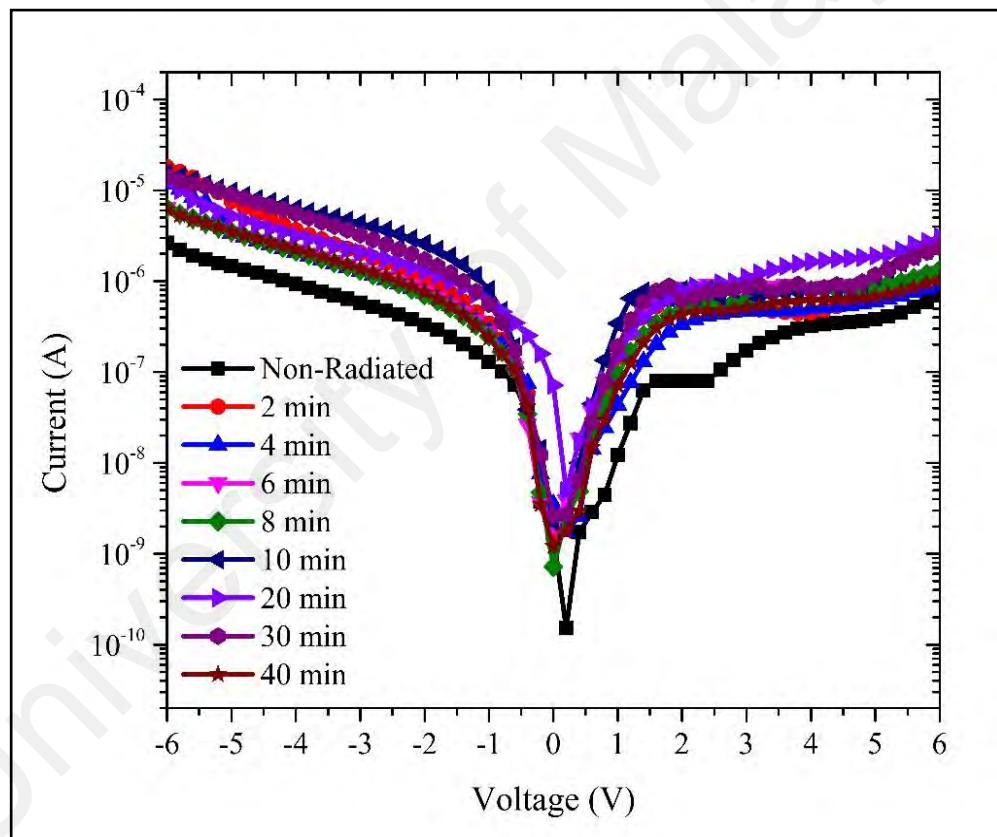
Figure 4.3: Semi-log I–V curves of the Al/DNA/ITO Schottky diode.

The values of series resistance are calculated from the junction resistance as $R_S = \partial V/\partial I$ based on the I–V properties of the diode. The resistance R_S versus voltage of the surface-type ITO/DNA/Al Schottky diode is demonstrated in **Figure 4.4**. From this figure, it can be seen that the R_S values were lowest at low voltages (>1.5 V) for all

periods of radiation except for the non-radiated sample. However, above 3.5 V, the R_S

value becomes insignificant for the latter sample. The highest R_S value occurs in the

non-radiated sample followed by samples radiated for 4 and 2 min.
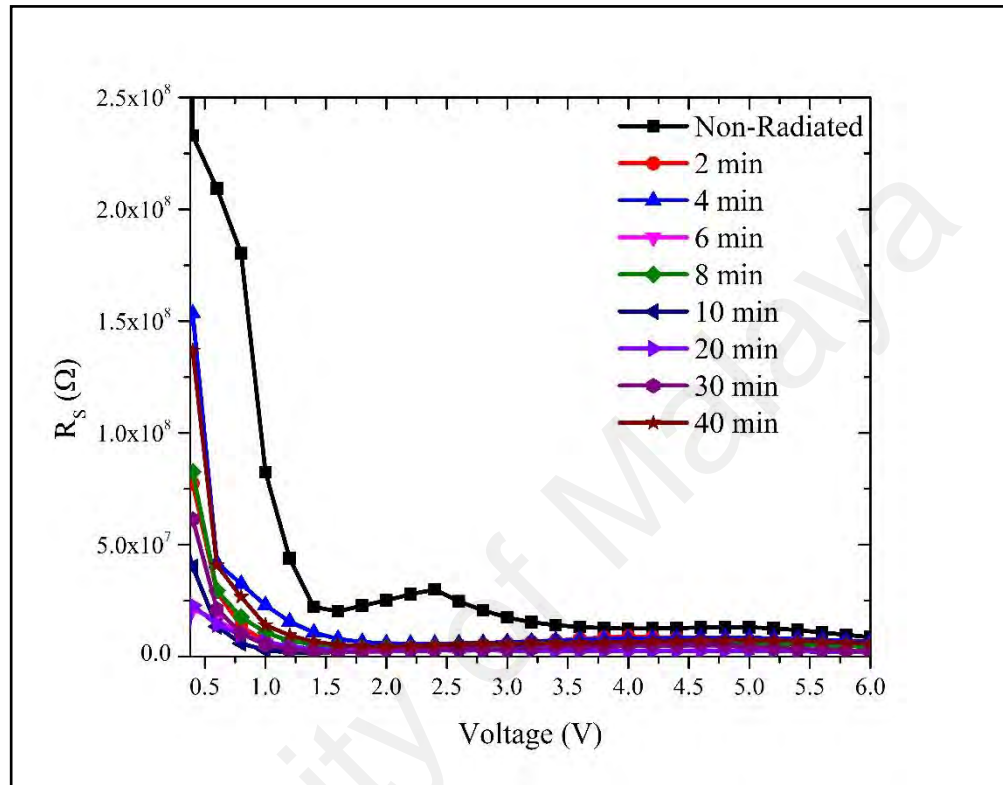
Figure 4.4: The relation between the series resistance and voltage using conventional method.

This study used the Cheung and Cheung's models, which is based on three

parameters. The first parameter is the resistance, which is essential for Schottky diodes.

Other parameters are the barrier height and ideality factor. Cheung and Cheung's

formula is shown as below (Cheung & Cheung, 1986);

$$\frac{dV}{d\left(\ln I\right)} = IR_S + n\frac{kT}{q} \tag{4.5}$$

$$H\left(I\right) = V - \left(\frac{kT}{q}\right)\ln\left(\frac{I}{AA^*T^2}\right) \tag{4.6}$$

therefore;

$$H(I) = IR_S + n\Phi_b \tag{4.7}$$

Figure 4.5(a) and (b) shows the experimental H(I) versus I and dV/d(lnI) versus I plots, respectively for the Al/DNA/ITO Schottky diode at room temperature. A plot of H(I) versus I (**Figure 4.5**(a)) shows a straight line with a y-axis intercept equal to nΦ. Φ was obtained by substituting the n value from Equation (4.5) and the data of the downward curvature region in the forward bias I–V features from Equation (4.7). The slope of this plot also limits R_S, which can be utilized to check the accuracy of Cheung and Cheung's method.

The Φ and R_S values were measured from the H(I) versus I plot presented in **Table 4.1** in column one and two using Cheung and Cheung's method. Equation (4.5) gives a straight line for the data of the downward curvature region with regard to the forward bias I–V properties. **Figure 4.5**(b) shows the plot of dV/d(lnI) versus I, from which the values of n and R_S were calculated **Table 4.1**, column four. As seen in the table, the values of R_S obtained from dV/d(lnI) and H(I) versus I plots are in close agreement with each other.
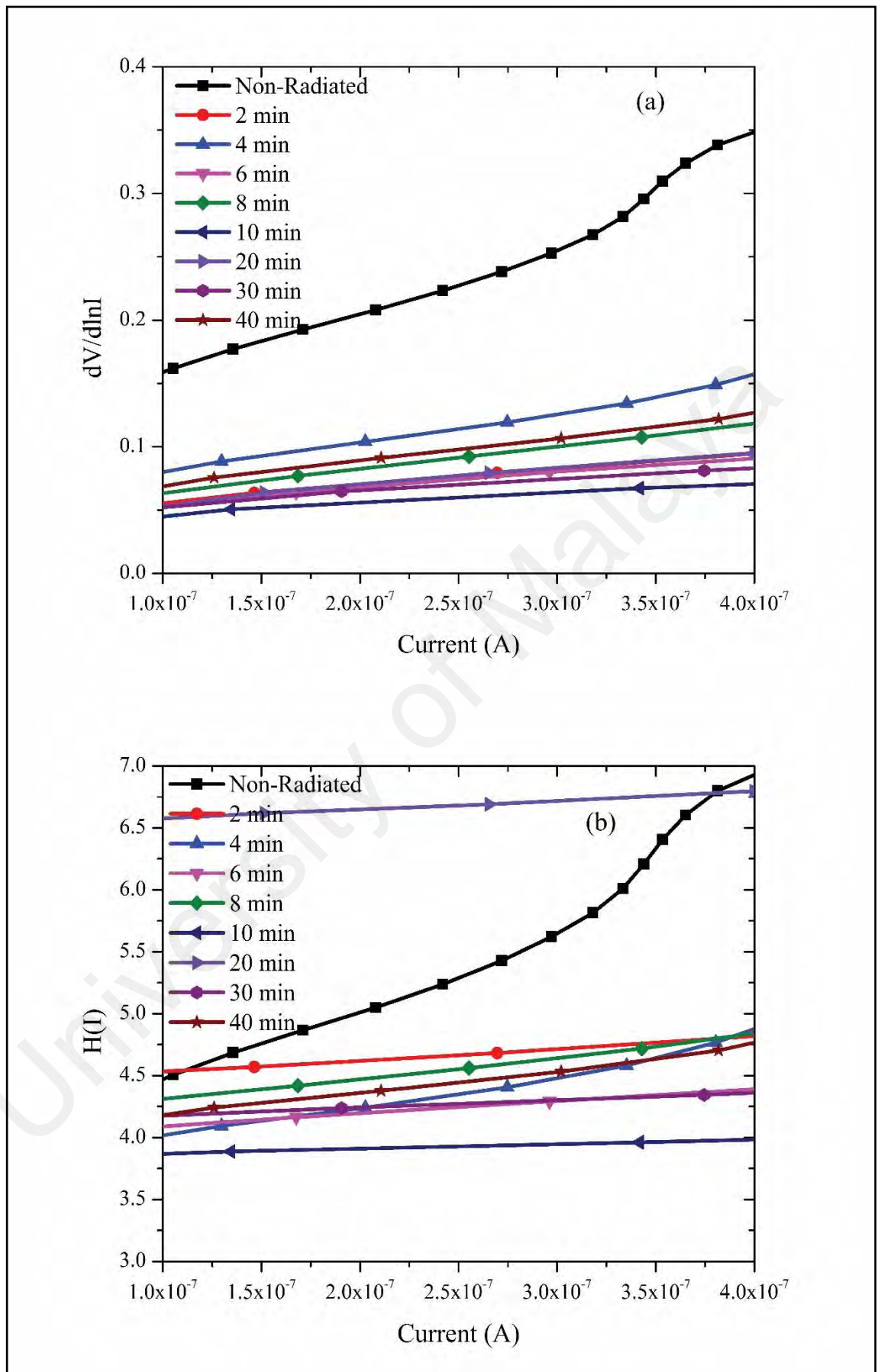
Figure 4.5: (a) H(I)-I and (b) (dV/ln (I)) plots of the Al/DNA/ITO Schottky diode.
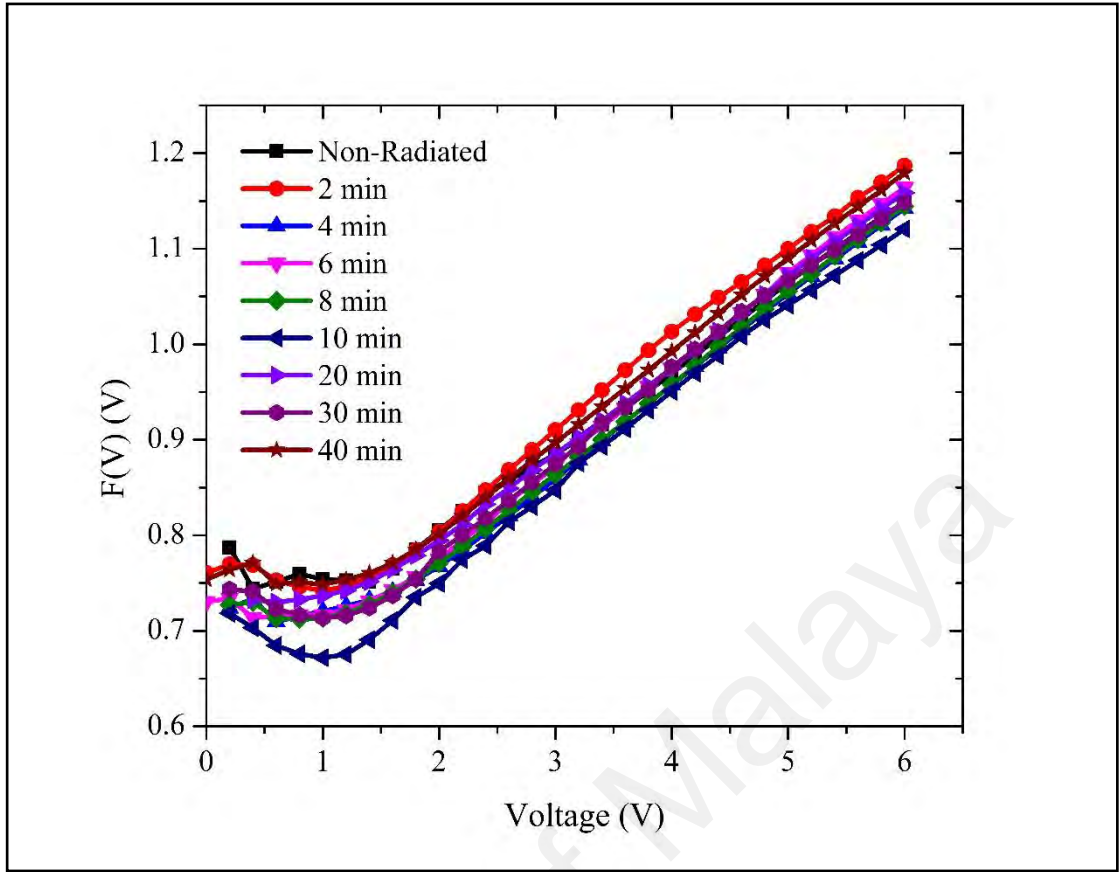
Figure 4.6: F(V)–V plot of the Al/DNA Schottky diode.

The Norde's method is an alternative method to calculate the series resistance and

barrier height (Norde, 1979);

$$F(V) = \frac{V}{\gamma} - \frac{kT}{q} \ln\left(\frac{I}{AA^*T^2}\right)$$ (4.8)

where (γ) is dimensionless (the first integer) having value more than n and the effective

Schottky barrier height is given by;

$$\Phi = F(V_{\min}) + \frac{V_{\min}}{\gamma} - \frac{kT}{q}$$ (4.9)

and

$$R_S = \frac{(\gamma - n)kT}{qI_o}$$ (4.10)

where I_o is the current at $V = V_{min}$.

Plot of F(V) versus V for the Al/DNA/ITO Schottky structure at room temperature is shown in **Figure 4.6**. From this plot, the values of Φ and R_s were determined and presented in **Table 4.1**.
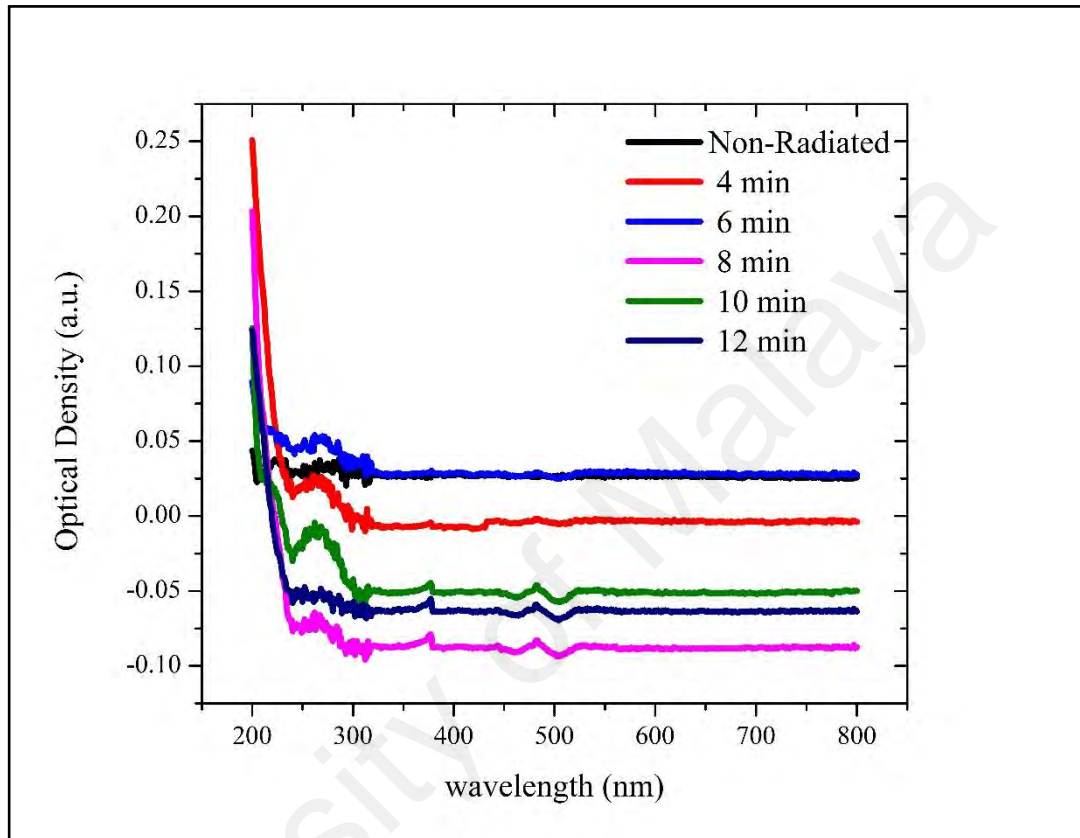
Figure 4.7: The absorption spectra of DNA on quartz.

Figure 4.7 shows the absorption spectra of DNA on quartz under different radiation periods. In this figure, observations generally illustrated strong DNA absorption peaks at < 300 nm, which are in the ultraviolet wavelength range. This is the strong absorption band that corresponds to π-π* transition of electrons of the C=C bond of DNA bases. This shows that visible (or infrared) light was unable to release an electron from the DNA (no photocurrent under visible and near-infrared illumination) because the photons at these wavelengths do not have sufficient energy (Grote & De Yu 2007). The second absorption band is seen at approximately 375 and 480 nm for irradiation times of 8, 10 and 12 min. Increasing the radiation time increases the

emission of the secondary electrons associated with crossovers and irritability occurring in the material.

Radiation dose, however does play an important role in changing resistance values. The resistance increases gradually at low doses, which therefore makes the DNA seek self-protection. Plots of Φ, n and R_S with the radiation time, as shown in **Figure 4.8** and **Figure 4.9** indicate the hypersensitivity phenomena of the DNA at low doses.
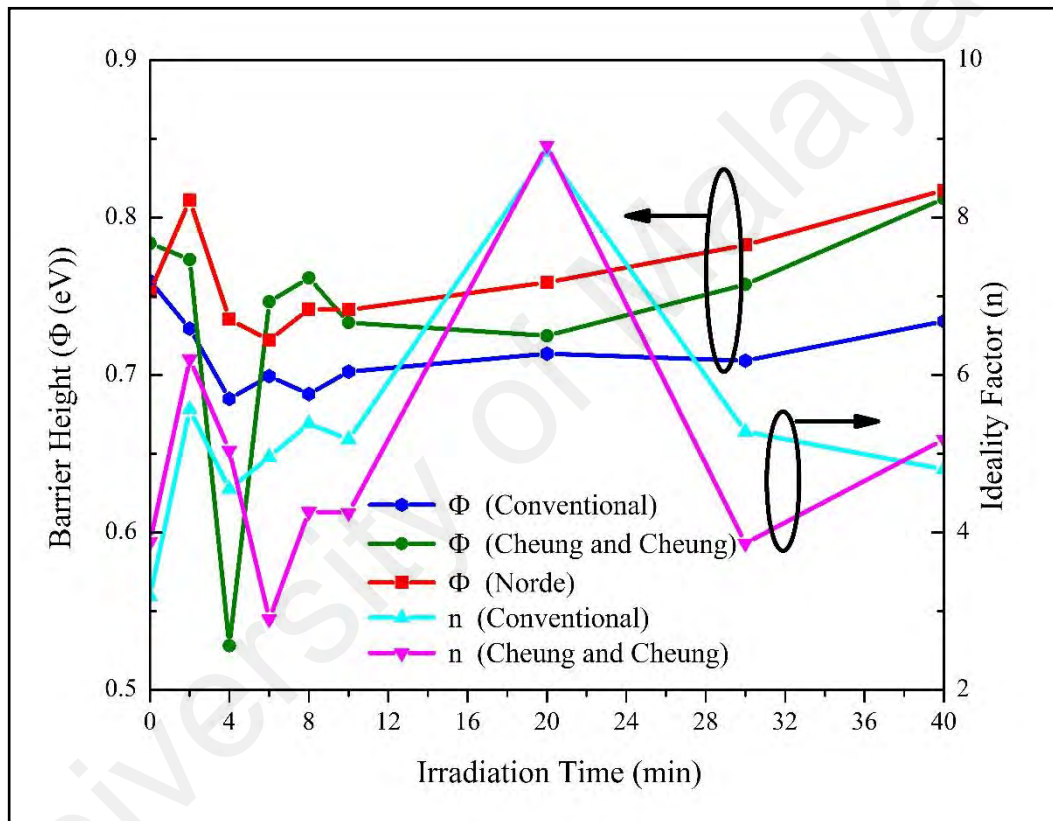
Figure 4.8: The relation of barrier height Φ and ideality factor versus radiation time for all methods.

Table 4.1: The measured values of ideality factor, barrier height and series resistance.

Irradiation time (min)	Conventional method			Cheung and Cheung's method				Norde's method		
	n	Φ (eV)	R_S (MΩ)	Φ (eV)	R_S (MΩ)	n	R_S (MΩ)	F(V) (V)	Φ (eV)	R_S (MΩ)
0	3.1901	0.7597	8.689	0.7837	11±0.293800	3.8760	5.2±0.03195	0.7387	0.7528	15.064
2	5.5609	0.7295	2.85	0.7733	1.2±0.072316	6.2016	0.26±0.02491	0.737	0.8112	0.1767
4	4.5493	0.6848	5.79	0.528	6.2±0.165347	5.0388	0.37±0.0288	0.7041	0.7353	1.8057
6	4.9565	0.6992	5.79	0.7465	1.2±0.165545	2.8958	0.13±0.00946	0.708	0.7222	1.3830
8	5.3833	0.6879	4.09	0.7616	1.8±0.183368	4.2636	0.29±0.01281	0.7076	0.7418	1.2778
10	5.1818	0.7021	1.1818	0.7333	0.4±0.025125	4.2471	0.055±0.00662	0.6671	0.7413	0.0757
20	8.8291	0.7135	1.93	0.7249	9.2±0.087327	8.9147	0.081±0.00708	0.7246	0.7588	0.6170
30	5.2806	0.7091	2.046	0.7575	8.2±0.07579	3.8610	0.06±5.02468E-6	0.7083	0.7825	0.1357
40	4.8029	0.7341	4.603	0.8120	2.0±0.04153	5.1814	0.3±0.02952	0.7431	0.8173	0.3647

Using data from **Table 4.1**, the relations of both the barrier height and the ideality factor versus radiation time were plotted (**Figure 4.8**) for all the methods used in this work. The gradual decrease in Φ and n can be observed very clearly within the period between 4 and 6 min. In contrast, a rapid decrease was seen in the R_s values during this period (**Figure 4.9**). This could point to the ability of DNA to protect itself against alpha particle radiation, but when radiation time increased, R_s values also increased gradually. However, beyond 20 min of exposure, the ideality factor was observed to decrease because the number of alpha particle tracks also increased with time.
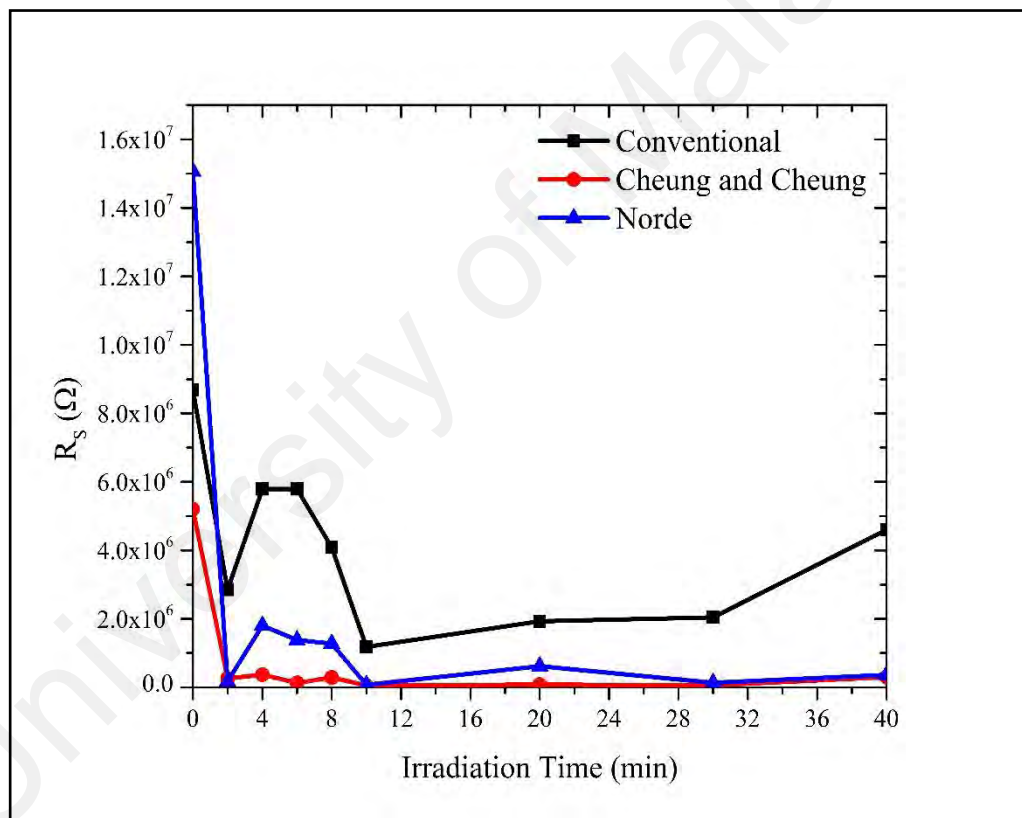
Figure 4.9: The relation between the R_s and radiation time for all methods.

As a result of this particle interaction, a penetration effect occurs; however, DNA traces remain on the substrate. Accordingly, by increasing the dose time and conducting similar experiments for periods of 0, 2, 4 and 14 min, images with different depths were

obtained. **Figure 4.10** shows AFM depth profiles linearly increasing from 9 to 400 nm for exposure periods of 2 and 14 min, respectively.

FESEM and SEM images confirm the formation of DNA strands on the ITO substrate. **Figure 4.11** illustrates close-up views of the DNA strands on the ITO substrate. Prior to electric field alignment, the DNA strands were aggregated as non-uniform groups of molecules (a). Upon radiation field alignment, it can be observed that the strands disperse and align themselves. Because the alpha particles have $2e^+$, their reactions with the material create electrons and holes, which participate in the ionization process under the influence of the electric field.

As seen from **Figure 4.12**, the bombardment of the DNA by alpha particles causes extensive damage with increasing radiation time. The particles can be observed to leave behind many holes or tracks with a range of diameters, as shown in **Figure 4.12**.
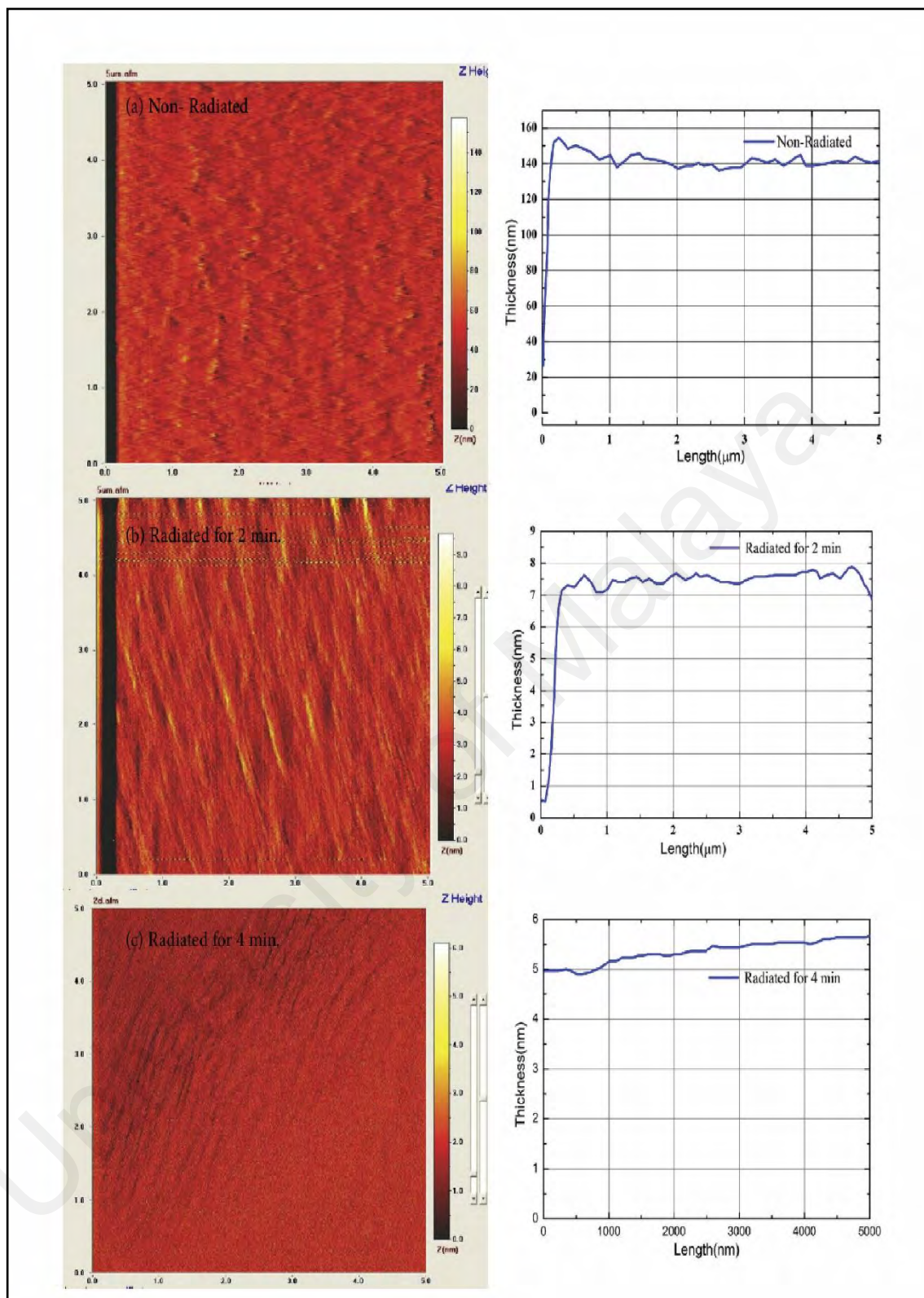
Figure 4.10: The depth of profiles of DNA strands remaining on ITO surface of (a) non-radiated, (b) radiated 2 min and (c) radiated for 4 min.
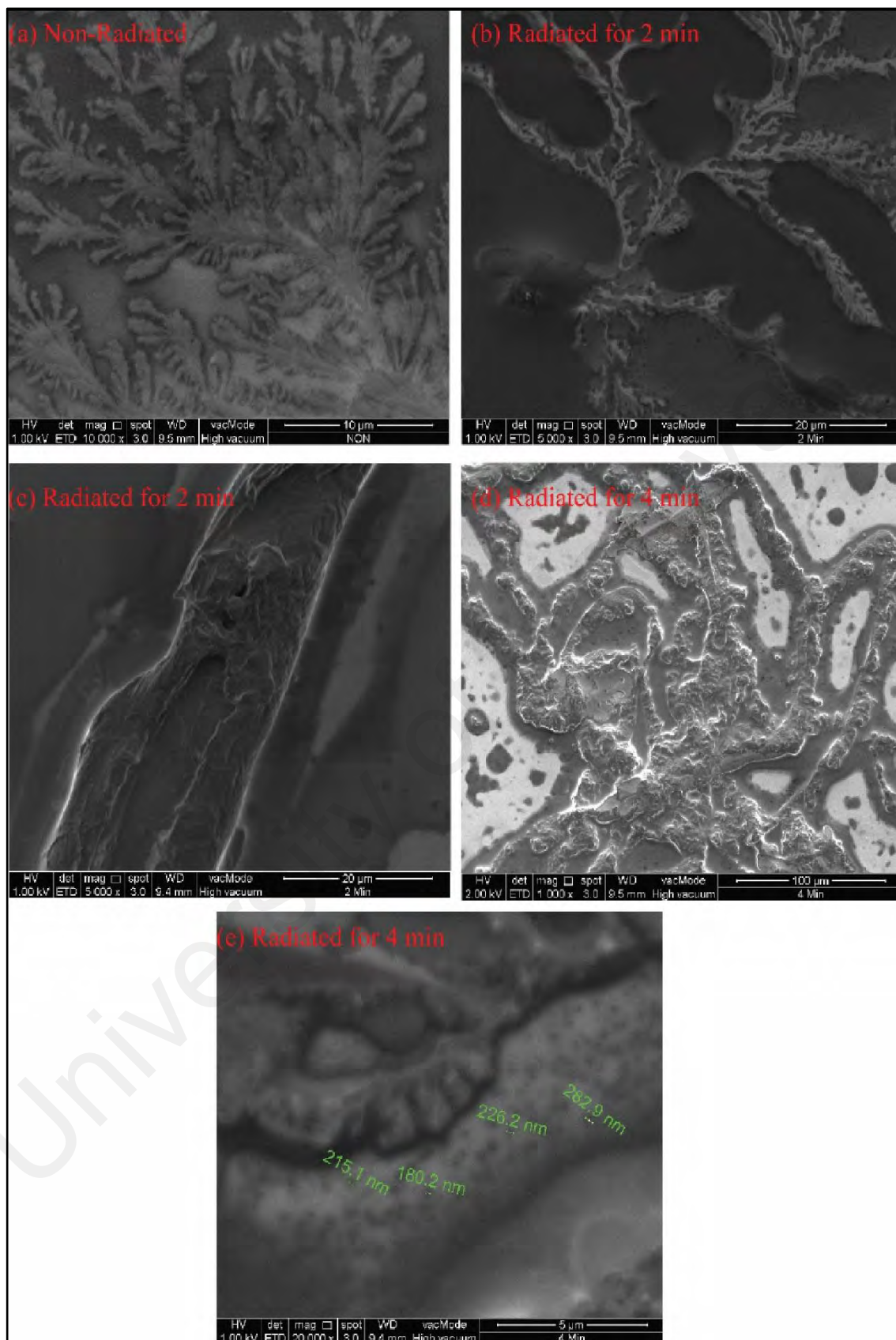
Figure 4.11: FESEM images for non-radiated (a) and radiated (b)-(c) DNA samples.
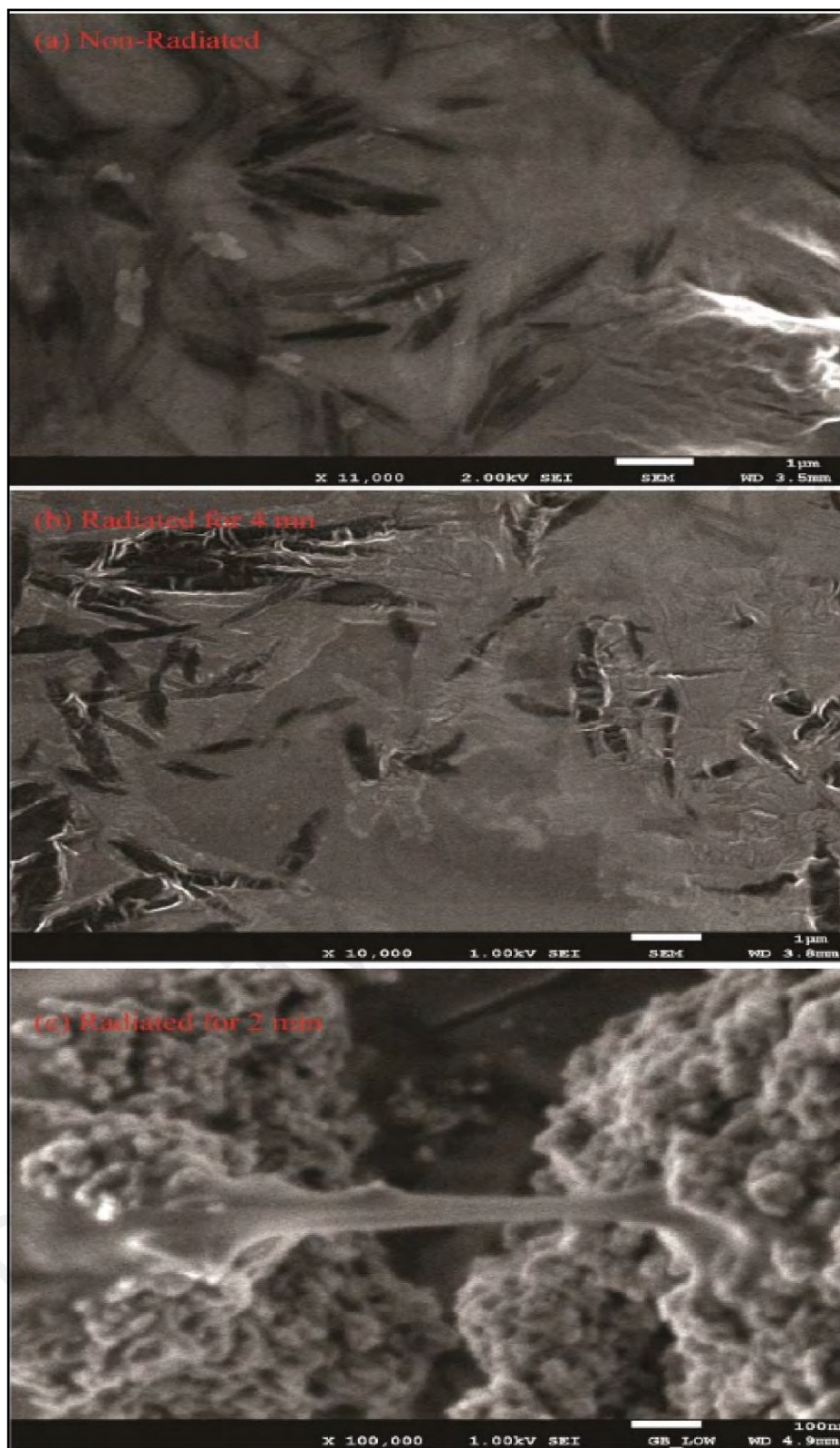
Figure 4.12: SEM images of non-radiated (a) and radiated (b)-(c) DNA samples.

4.3 Calculation of the Electronic Parameters of an Al/DNA/p-Si Schottky Barrier Diode

The forward and reverse bias I–V characteristics of the Al/DNA/p-Si/Al junctions at room temperature were given in **Figure 4.13**. As can be observed, the I–V characteristics of the device clearly demonstrate a rectifying behavior.
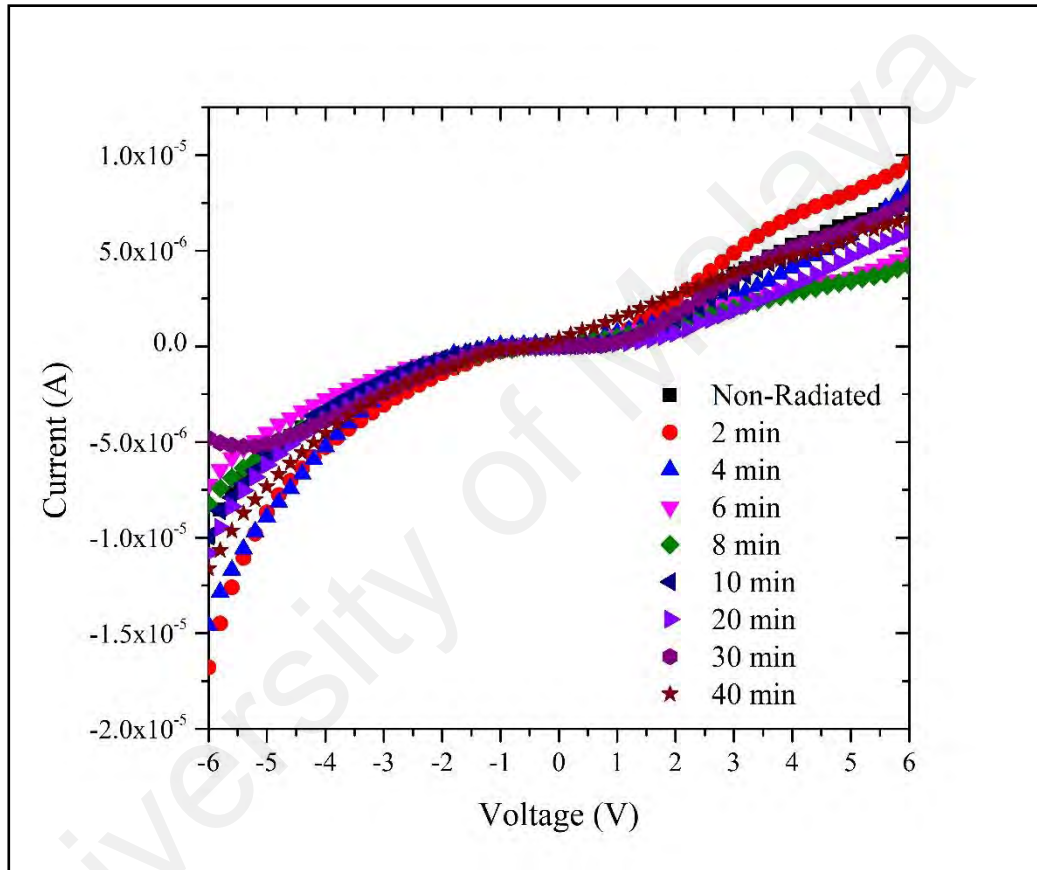
Figure 4.13: Graphs demonstrates the relationship between current and voltage for forward and reverse biases.

According to the thermionic emission theory, the I–V characteristic of a diode is given by Equation (4.3) for values of $V > 3kT/q$, the ideality factor from Equation (4.1) can be re-written as Equation (4.3). The ideality factor determined from the slope of the linear region of the forward bias ln(I)-V characteristics through the relation in Equation(4.3) is a measure of conformity of diode to pure thermionic emission (R. K. Gupta & Yakuphanoglu, 2012; V. R. Reddy et al., 2011). **Figure 4.14** shows the

ideality factor fluctuations of the Al/DNA/p-Si/Al based junctions fabricated in this work calculated using Equation (4.3).
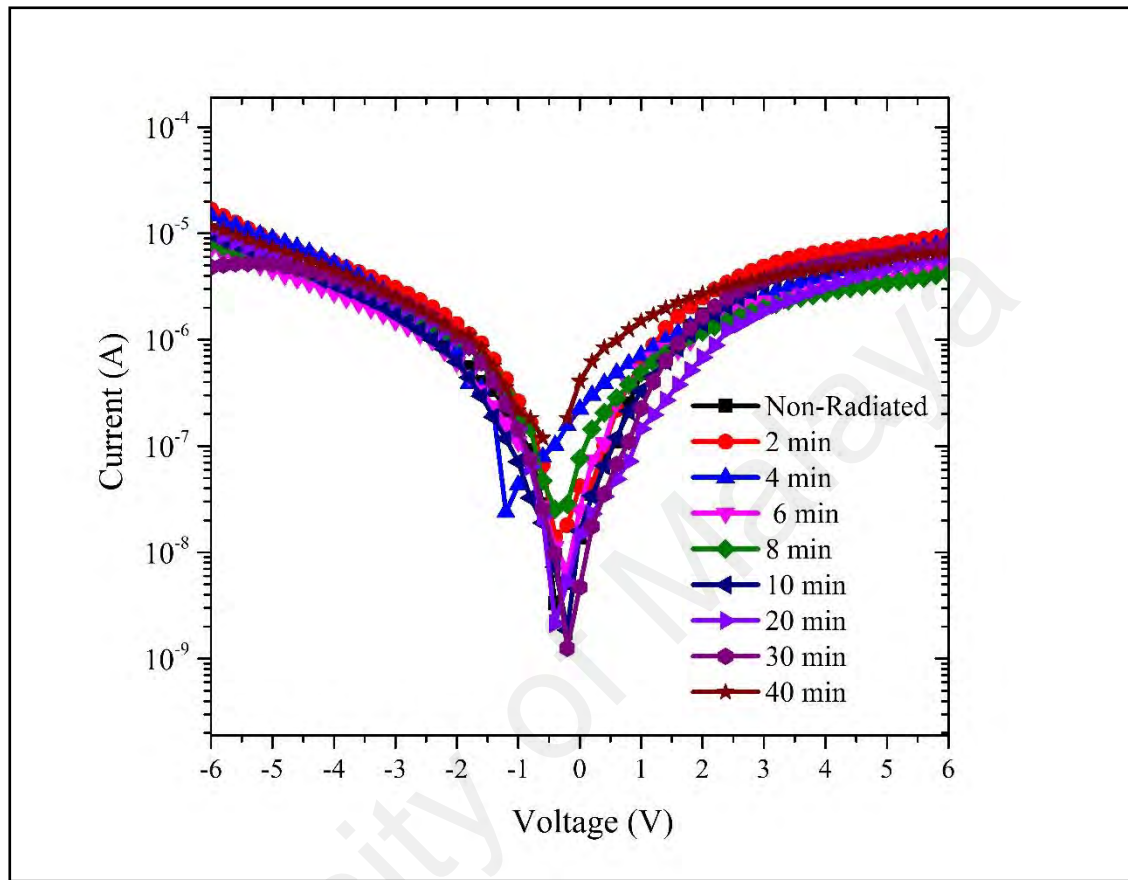
Figure 4.14: Curves show the I–V characteristics of Al/DNA/p-Si Schottky diode at room temperature.

For both the radiated and non-radiated samples, the linear region of the forward bias I–V plots indicates that the effect of the series resistance in this region is not important. The value of the barrier height of the Al/DNA/p-Si/Al Schottky diode was 0.7468 eV before irradiation. Values before and after irradiation (**Table 4.2**) was calculated from the y-axis intercepts of the semi log-forward bias I–V plots using Equation (4.4). It ought to be noted that Φ is the connection potential barrier that exists at the interface between inorganic and organic layers, i.e., at the DNA/p-Si interface.
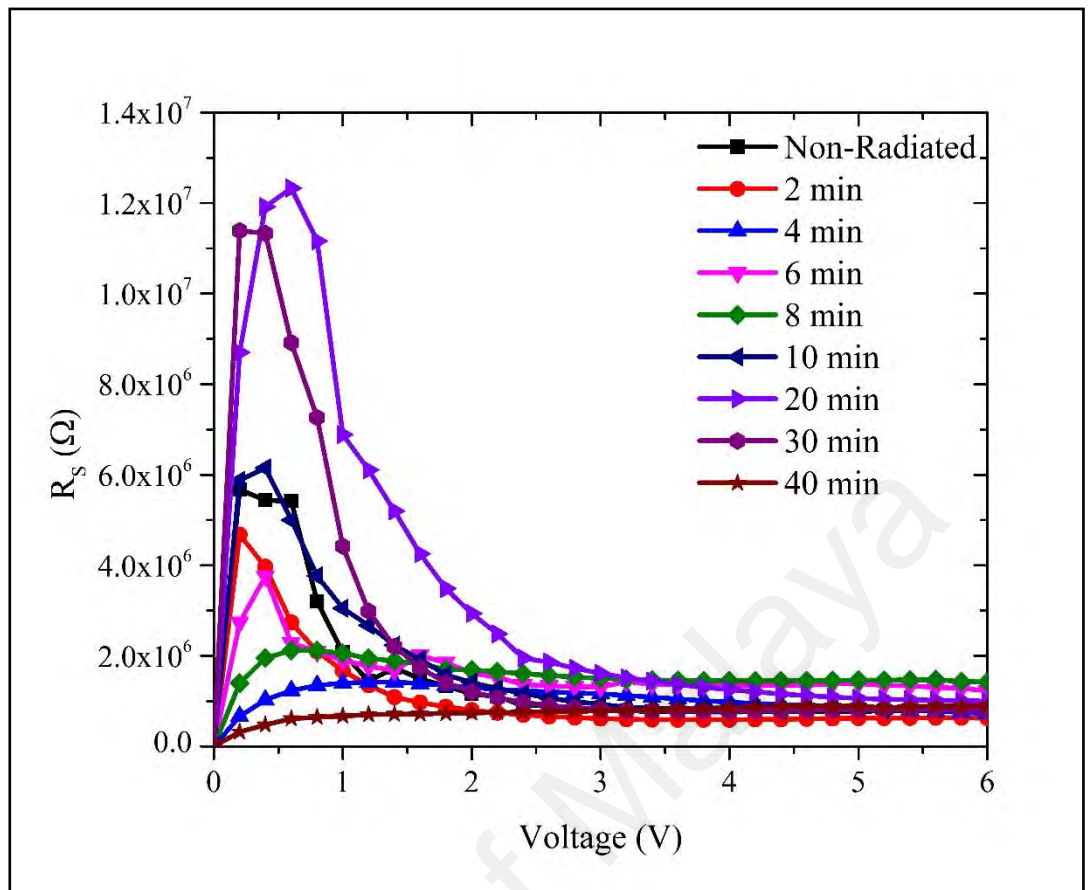
Figure 4.15: Relation between series resistance and voltage measured using the conventional method.

Table 4.2: Values of ideality factor, barrier height and series resistance measured.

Radiation time (min)	Conventional method			Cheung and Cheung's method				Norde's method		
	n	Φ (eV)	R_S(MΩ)	Φ (eV)	R_S(MΩ)	n	R_S(MΩ)	F(V)(V)	Φ (eV)	R_S(MΩ)
0	8.2643	0.7486	0.7772	0.6050	0.81±0.0391	0.6202	0.066±6.22×10-4	0.7541	0.7482	0.7342
2	9.0139	0.7553	0.5889	0.6213	0.56±0.01921	0.2481	0.046±3.28×10-4	0.7471	0.7612	0.2567
4	7.2683	0.6876	0.7263	0.6742	0.66±0.01825	1.1628	0.053±6.039×10-4	0.699	0.6931	0.0861
6	8.5814	0.7429	1.228	0.6409	1.2±0.08275	0.2984	0.093±5.44×10-4	0.7353	0.7294	0.3544
8	12.2826	0.7127	1.423	0.6758	1.1±0.05372	1.4341	0.086±5.085×10-4	0.718	0.7121	0.1804
10	10.1212	0.7582	0.7985	0.6225	0.84±0.02063	0.3178	0.067±6.87×10-4	0.755	0.7491	0.7601
20	10.9747	0.7594	0.9995	0.6834	0.92±0.05833	1.3566	0.071±8.52×10-4	0.765	0.7591	1.1257
30	7.6935	0.7872	0.7872	0.9878	0.90 ±0.0001	0.8915	0.073±5.41×10-4	0.772	0.7661	1.4733
40	18.2579	0.6720	0.3217	0.6025	0.76±0.01868	0.2636	0.06±4.86×10-4	0.6803	0.6744	0.0416

The values of series resistance was calculated from the junction resistance formula $R_S = \partial V / \partial I$ from the I–V properties of the diode. The resistance R_S versus voltage of the surface-type Schottky diode is demonstrated in **Figure 4.15**. From the figure, it can be concluded that at low voltages (≤ 2.0 V), R_S values were the highest for 20, 30 and 10 min in reducing order, followed by the non-radiated sample. However above 2.0 V, the R_S values become insignificant.

At high currents, there is always a deviation of the ideality that has been obviously shown to rely on bulk series resistance and the interfacial state density, as one would expect. The lower the series resistance and the interface state density, the better is the range over which ln I(V) does in reality yield a straight line. Schottky diode factors such as the barrier height, Φ_{bo}, the series resistance R_S and the ideality factor n were also determined using the technique advanced by Cheung and Cheung (Cheung & Cheung, 1986). The method's functions can be written as Equations (4.5), (4.6) and (4.7).

Figure 4.16(a ,b) shows the experimental H(I) versus I and dV/d(ln I) versus I plots for the Al/DNA/Si Schottky diode at room temperature, respectively. A plot of H (I) versus I (**Figure 4.16**(a)) shows a straight line with intercept at y-axis equal to nΦ. Φ was obtained by substituting the n value from Equation (4.5) and the data of the downward curvature region in the forward bias I–V graph from Equation (4.7). The slope of this plot also limits R_S, which can be utilized to check the accuracy of Cheung and Cheung's method. From H (I) versus I, the Φ and R_S values were measured and presented in **Table 4.2**. Equation (4.5) gives a straight line for the data of the downward curvature region in the forward bias I–V graph.
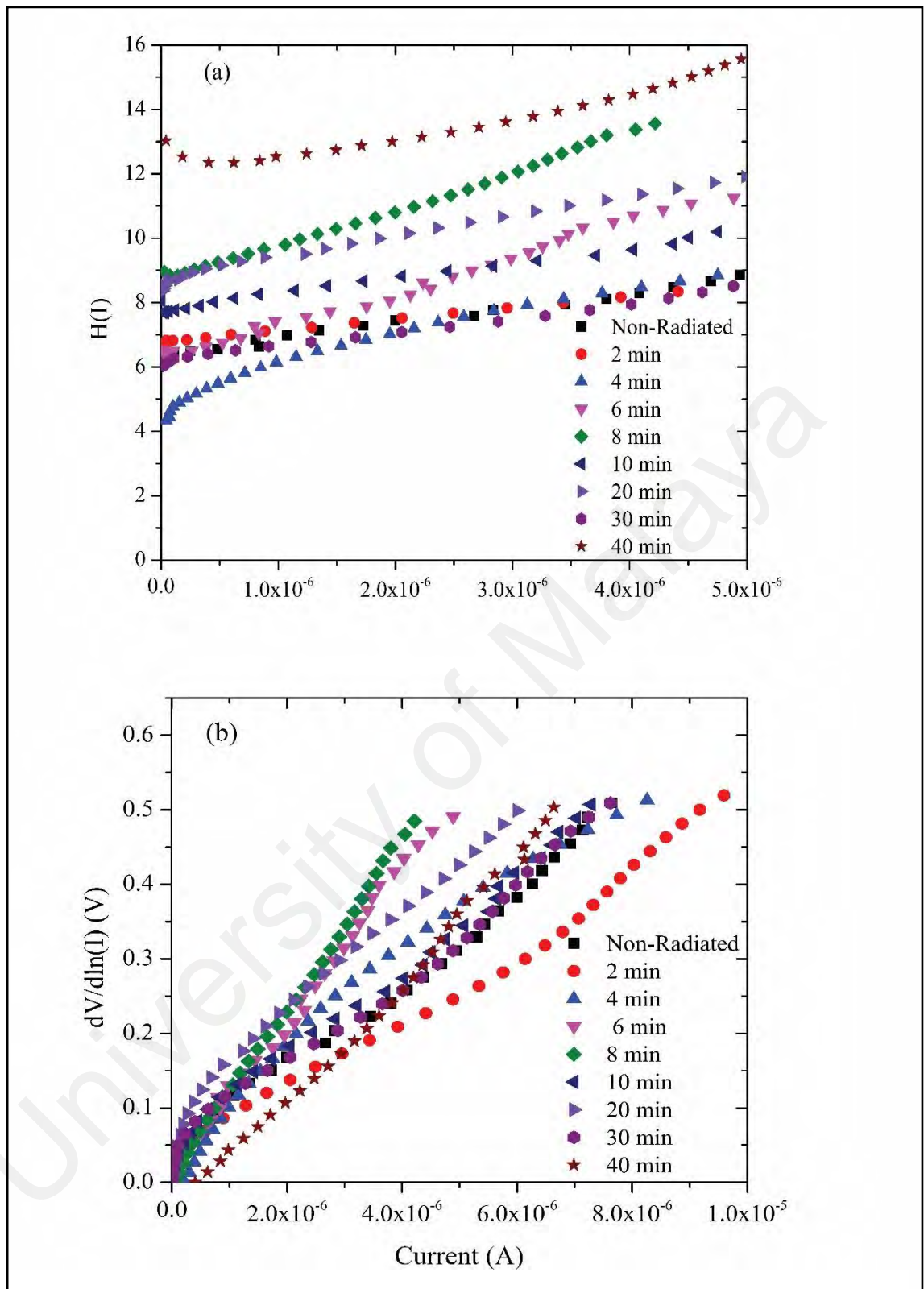
Figure 4.16: H(I) and dV/d(ln I) versus I graphs obtained from forward bias I–V characteristics of Al/DNA/Si/Al Schottky junction diode.

Figure 4.17(b) shows the plot of dV/d(ln I) versus I, from which the values of n and R_S were calculated shown in (**Table 4.2**). As can be seen in the table, the values of R_S

obtained from dV/d(ln I) versus I and H(I) versus I plots were in near agreement with each other. Radiation dose however does play an important role in changing the series resistance values, thus the resistance increases gradually at low doses, which therefore enables the DNA to seek self-protection. Plots of Φ, n and R_S with radiation periods as shown in **Figure 4.17** and **Figure 4.18** therefore indicate the hypersensitivity phenomena of the DNA at low doses.
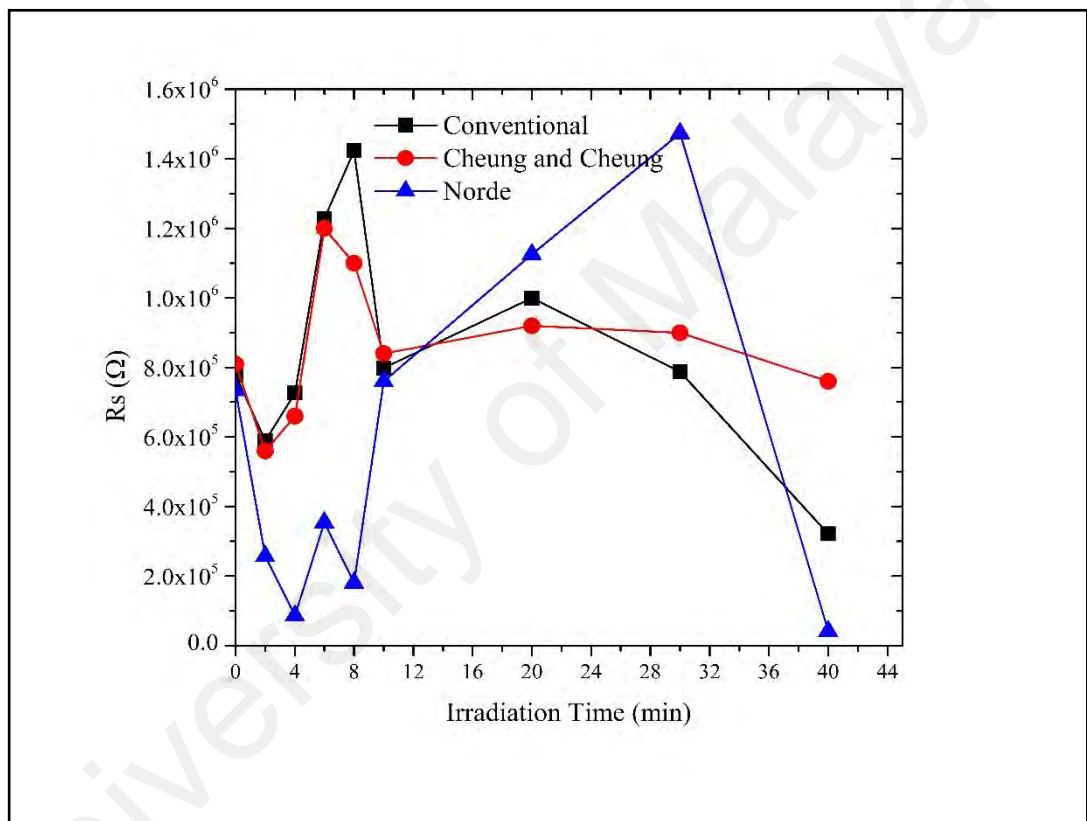
Figure 4.17: Graphs explaining the relationship between series resistance and alpha radiation time.

Φ_b is the real barrier height derived from the low-voltage part of the forward I–V characteristics. The series resistance was obtained from the straight-line region seen in **Figure 4.16**. Using Equation (4.7), the values of barrier height and the series resistance were then obtained and the results presented in **Table 4.2**. The table lists values of n, Φ_b and R_S obtained from both the conventional and the Cheung and Cheung's models.
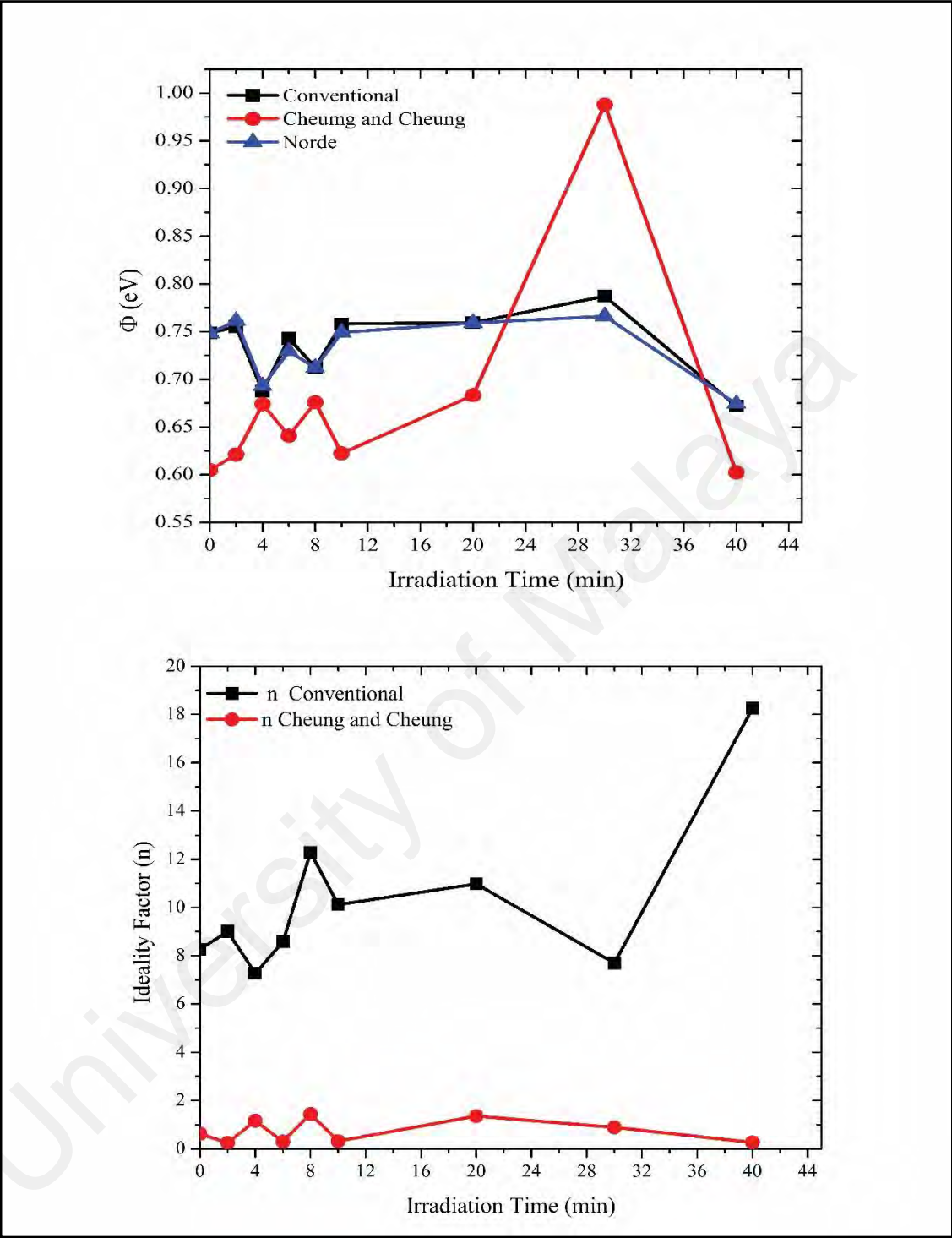
Figure 4.18: Graphs demonstrating the relationship between ideality factor and barrier height with the radiation time.

Generally, values of n obtained from the $dV/d(\ln I)$ versus I curve is lower than that of the forward bias $\ln(I)$ versus V plot. This can be attributed to the effect of the series resistance, interface states and voltage drop across interfacial layers (Bazlov et

al., 2013; Farag et al., 2010; Karadeniz et al., 2013) and radiation effect (Çınar et al., 2010). Norde's method is an alternative method to calculate the series resistance and barrier height (L. M. Martin et al., 2013; Norde, 1979). The following function has been derived in the modified Norde's method: as shown by the Equations (4.8), (4.9) and (4.10). Where F (V_{min}) is the minimum point in the F(V) versus V curve, while V_{min} and I_o are the corresponding voltage and current, respectively.
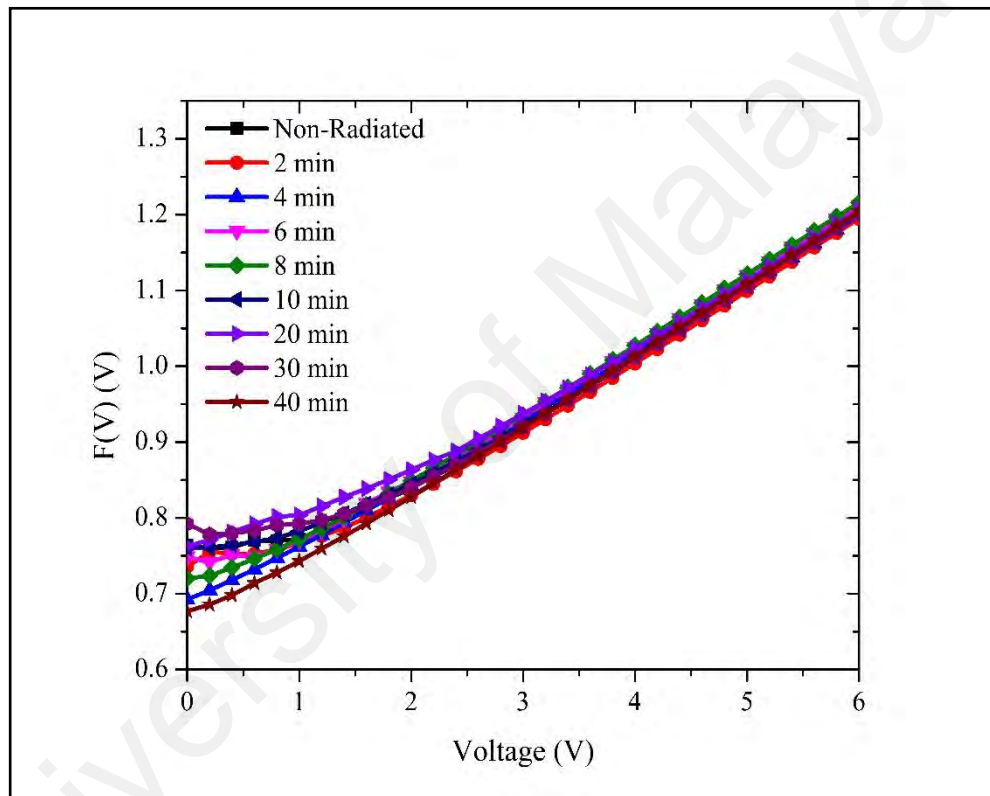
Figure 4.19: F(V) versus V plots of the radiated and non-radiated Al/DNA/Si Schottky diodes.

A plot of F(V) versus V at room temperature is shown in **Figure 4.19**. The values of Φ and R_S from the plot F(V) versus V are listed in **Table 4.2**. Norde's method demonstrates that the values of R_S diverge close to non-radiation values when calculated using the conventional method. At lower radiation doses, a significant decrease in series resistance was observed. However, an increase is seen within 10 to 30 min of radiation, registering a drop again at 40 min. The increase may be attributed to the decrease in free

119

carrier concentration and charge mobility. Higher barrier height values denote lower reverse currents (S. Gupta et al., 2009). Furthermore, the hypersensitivity phenomenon was responsible for the increase in the Φ and R_S values. In all the methods, values of the barrier heights were observed to converge. The series resistance initially decreased and later increased with increasing radiation time (**Figure 4.17**) as a result of the increasing number of alpha particle tracks. At lower dosages, the ideality factor dropped dramatically demonstrating the hypersensitivity phenomena of the DNA molecules (**Figure 4.18**(b)), which may act to protect against harmful alpha radiation. This phenomenon seems to be similar to the relationship observed between survival curves and radiation dosage (H. M. Al-Ta'ii et al., 2009; H. M. Al-Ta'ii & Mohenned A., 2012; L. M. Martin et al., 2013). Schottky barrier height on the other hand has an inverse proportionality relationship with the ideality factor as seen in **Figure 4.18**(a).

Radiation effect on DNA thin films were also studied using Raman spectroscopic analysis to determine the influence of exposure time. DNA without radiation exposure shows Raman bands of adenine, cytosine, guanine and thymine bases and phosphate backbone groups with different modes of DNA. The Raman bands observed are 1244 cm^{-1} bending of C-H and stretching of C-N bonds; 1418 cm^{-1} stretching of adenine; 1290 cm^{-1} C-C stretching; 1345 cm^{-1} stretching of C-N and C=C in cytosine; 1576 cm^{-1} C-N-C =C stretching in guanine; 1290 cm^{-1} C-C stretching; 1465 cm^{-1} stretching of C-N bonds in thymine; 1068 cm^{-1} symmetric stretching and 1146 cm^{-1} stretching mode of the phosphate backbone.
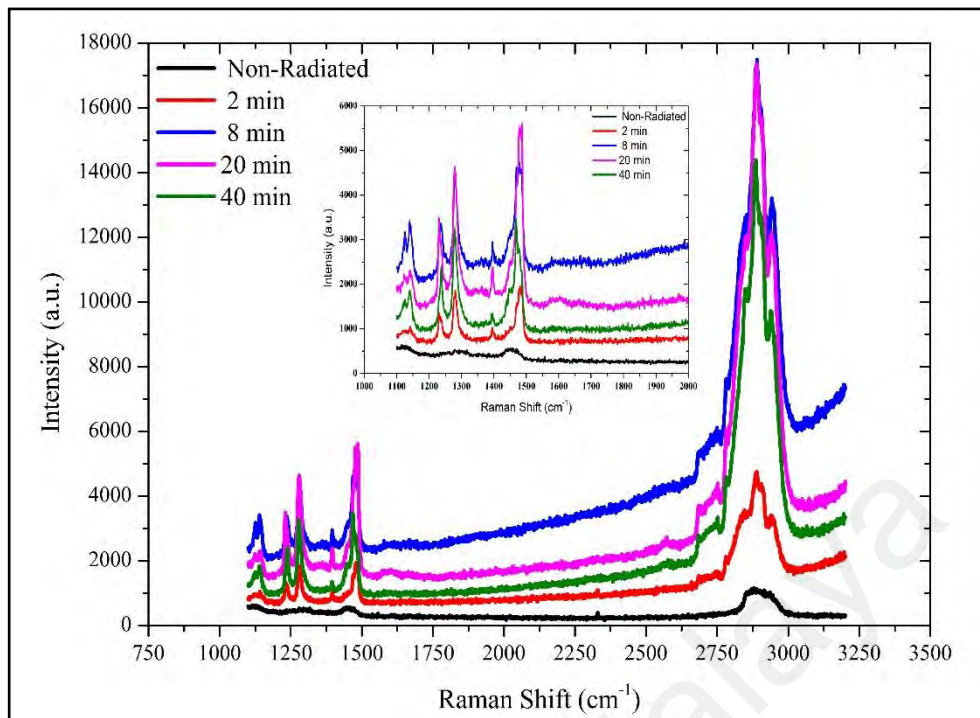
Figure 4.20: Raman spectra of Al/DNA/p-Si/Al junctions with and without alpha exposure. The insert figure shows the larger view of the peaks to the left of the spectrum.
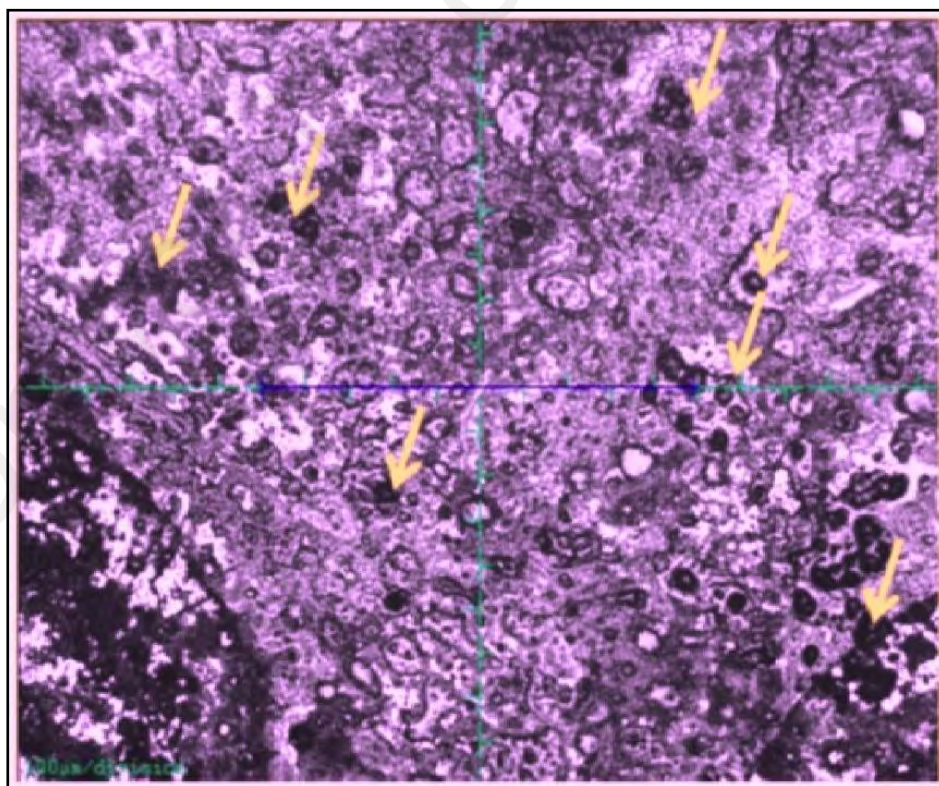
Figure 4.21: Alpha particle tracks as indicated by the yellow arrows can be clearly observed on the DNA film samples.

Alpha particle tracks as indicated by the yellow arrows can be clearly observed on the DNA film samples. Our results are similar with those reported by (Kulkarni et al., 2013). In the irradiated sample, clear shifting of these peaks can be observed due to the alpha exposures (**Figure 4.20**). This is caused by structural damage as a result of absorption of the radiation energy. The peak intensities gradually increased with increasing exposure time (and therefore the dosage) to the ^{241}Am radiation source. Increase in the alpha particle irradiation time leads to the linear increase of the number of tracks (**Figure 4.21**) and the significant intensity changes observed in the Raman spectrum (**Figure 4.20**).

PL spectra of irradiated DNA were obtained. A red shift occurs at a range of 610 to 750 nm higher than the green wavelength (500-570 nm) due to the irradiation effect. The intensity of these peaks increases with an increase in the radiation dose. Luminescence phenomena involve subsequent light emission and energy absorption. Phosphors are luminescent materials that produce light after excitation by radiation, thin films or micro-crystalline powders, which usually produce visible color emission. This confirms that the purified DNA has a five-component linear triple complex consisting of green, orange and red dots in the prepared. According to Tikhomirov et al. in 2011 the complex exhibits pure red luminescence and is substantially devoid of the green and orange luminescence that was present before hybridization and the linear ternary complex after cleavage by DNase, displaying the reversibility of complexation (Tikhomirov et al., 2011). It is known that the emission spectrum of the nucleic acid bases (adenine, guanine, cytosine, thymine, uracil) is in the range of 400–600 nm, which indicates that the major contribution to the DNA PL spectrum are caused by these bases (Gorelik & Sutula, 2010; Kwon et al., 2012). The homogeneous and specific bindings to DNA against intercalation between base-pairs and binding on phosphate backbones lead to the enhancing of the intensity of the PL (Dugasani et al., 2015).
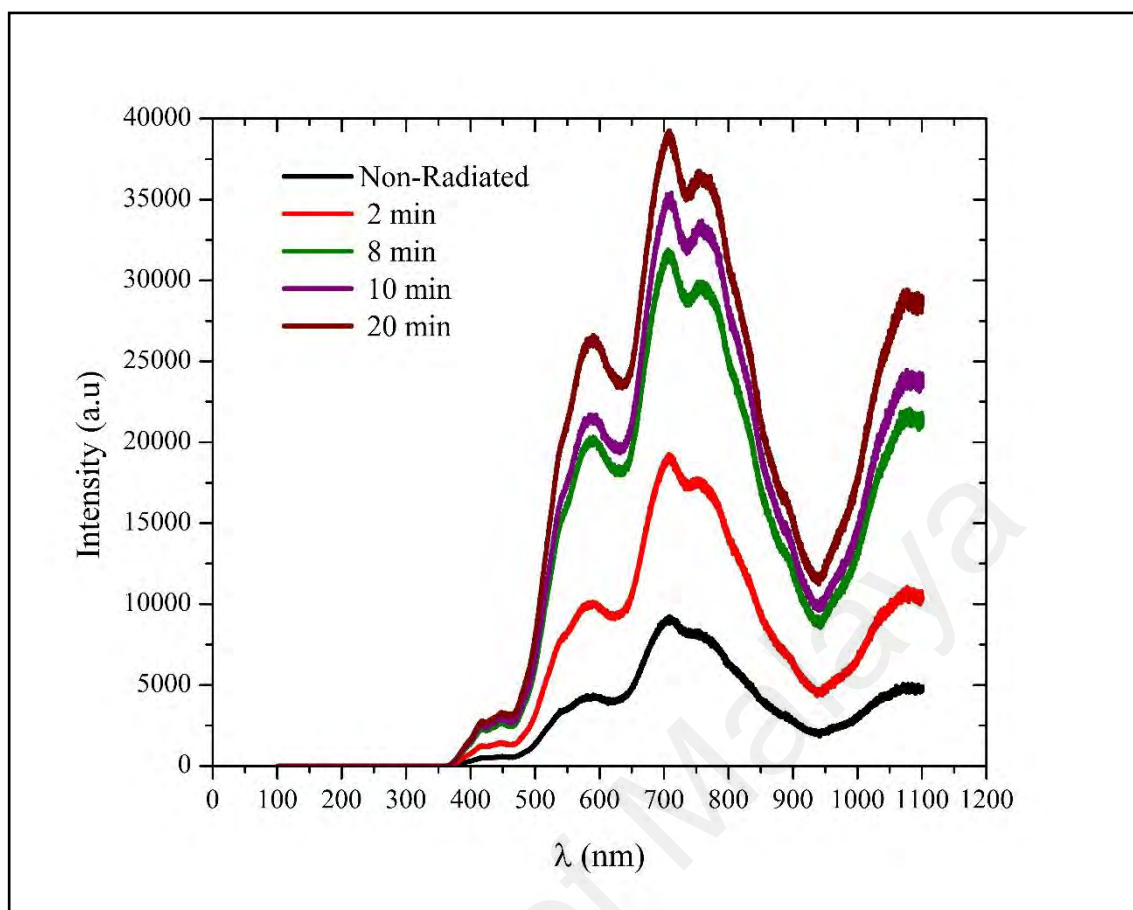
Figure 4.22: Photoluminescence spectra of DNA irradiated by alpha particles.

Generally, excitation and emission are considered significant processes in phosphors luminescence. Different types of energy could excite the phosphors, such as photon (often ultra-violet) that acts to excite the PL, an electric voltage to excite electroluminescence (EL) or chemiluminescence excited by the energy of a chemical reaction and so on. The process of emission is a release of energy in the form of photon (Shinde et al., 2012). Therefore, the results demonstrated in this current work may suggest utilization as light emitting structures based on DNA diodes (**Figure 4.22**).

4.4 Electronic Properties of DNA-Based Schottky Barrier Diodes in Response to Alpha Particles

The reverse and forward bias I–V features of the Al/DNA/p-Si/Al and Al/Si/Al contacts at room temperature were given in **Figure 4.23** together with the former junction's response after 24 hr. As apparent from the figure, the I–V properties demonstrate a rectifying behavior. According to the thermionic emission theory, the I–V features of a junction follow the Equations (4.1-4.3) (Tuğluoğlu & Karadeniz, 2012). For values of V more than 3 kT/q, the ideality factor from Equation can be re-written as Equation (4.3).

The ideality factor can be determined from the slope of the linear region of the forward bias (ln(I)–V) characteristics, which is a measurement of the conformity of the junction to pure thermionic emission (V. R. Reddy et al., 2011). n values for the samples Al/DNA/p-Si/Al Schottky diode was calculated using Equation (4.3). From the linear zone of the forward bias (**Figure 4.24**), for before and after irradiation, the I–V graph indicates that the affected series resistance was not significant. Values of the barrier height of Al/DNA/p-Si/Al in the two cases and Al/Si/Al Schottky junction were 0.4780 and 0.5078 eV, respectively. The values for the former junction are shown in **Table 4.3**, together with the ones measured after 24 hr.
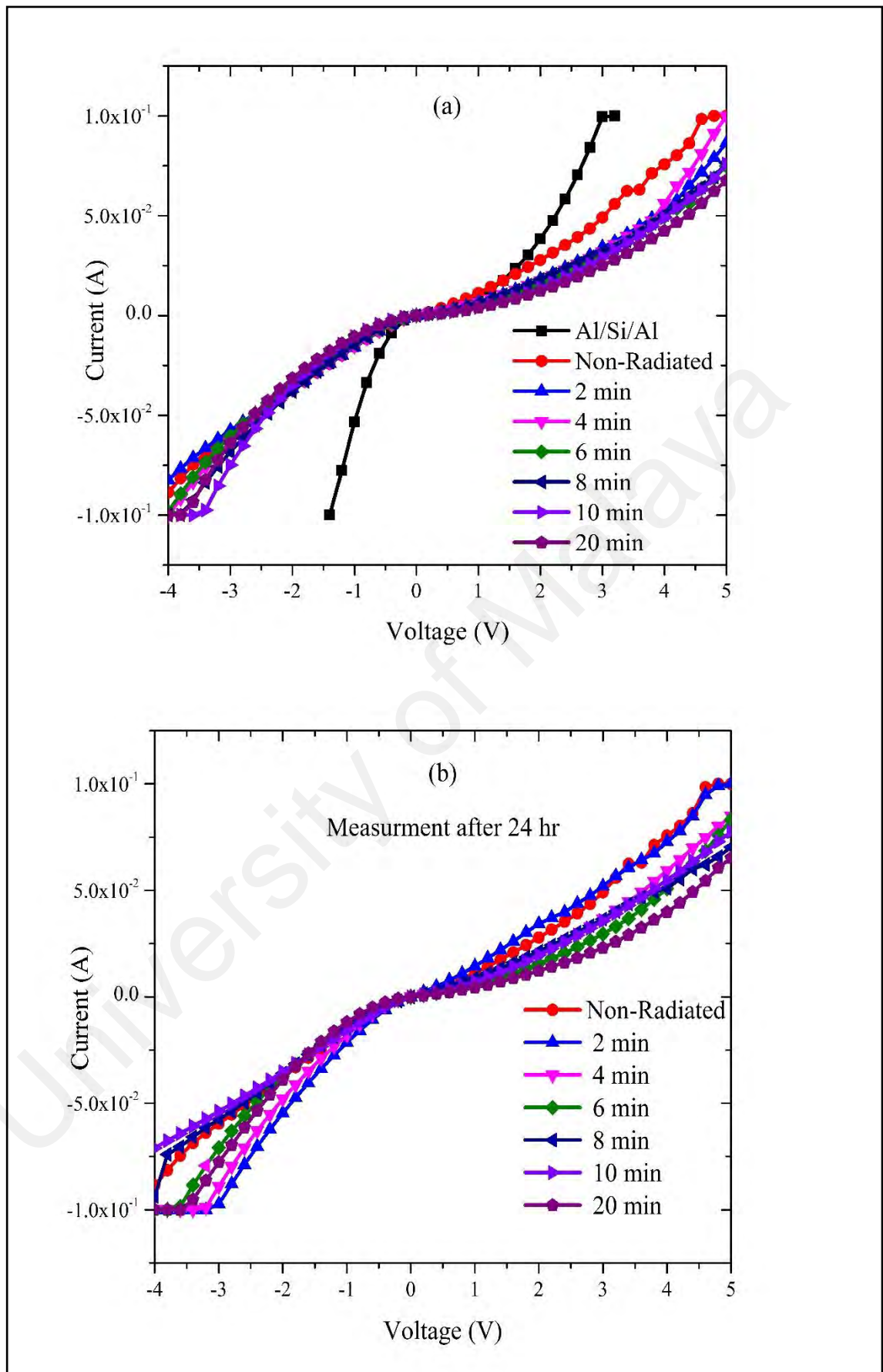
Figure 4.23: The relationship between I and V for forward and reverse biases at (a) 2, 4, 6, 8, 10 and 20 min and (b) measured after 24 hr.
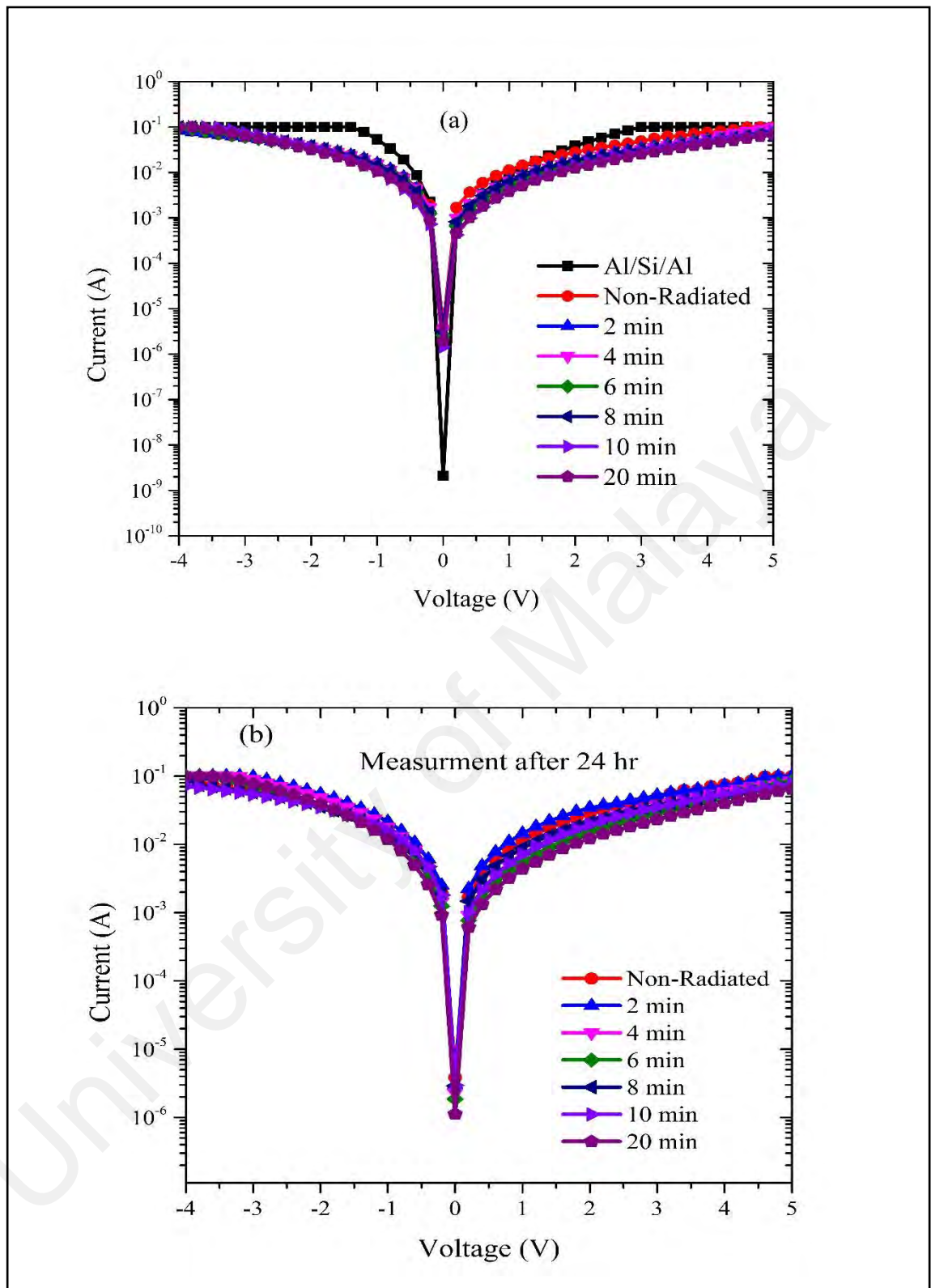
Figure 4.24: ln(I)–V characteristics of the Al/DNA/p-Si Schottky diode at room temperature (a) before and after (b) 24 hr.

The barrier height was calculated based on the y-axis intercepts of the semi log-forward bias I–V plots using Equation (4.4). It should be noted that the barrier height is

related to the potential barrier at the interface between the inorganic and organic layers, i.e. at the DNA/p-Si interface. The values of series resistances were calculated from the junction resistance ($R_S = \partial V / \partial I$) obtained from the I–V properties of the diode. Resistance, R_S versus voltage on the surface-type (Al/DNA/Si/Al) Schottky diode is shown in **Figure 4.25**. From the figure, it can be concluded that at low voltages (≤1.5 V), R_S values were the lowest except for the non-radiated samples, radiated for 10 and 20 min and for the Al/Si/Al junction. For irradiation periods beyond 24 hr, the lowest values occur before radiation and at 2 and 8 min. However, above 2.0 V, the R_S value becomes insignificant for the latter sample. The highest R_S values occur in the sample radiated for 20 min followed by samples irradiated for 10 and 6 min. In the cases for after 24 hr, the same trend was observed for samples radiated for 20, 6 and 4 min. This may refer to the phenomenon of DNA protecting itself by increasing its' series resistance (H. M. J. Al-Ta'ii et al., 2015d; Sawant et al., 2002).

At high currents, there is always a deflection of the duality that relies on bulk series resistance and the interface state density (Güllü et al., 2010; Gunduz et al., 2012). The lower the series resistance and the interface state density, the better is the range over which ln I(V) yield a straight line. The Schottky diode factors such as the ideality factor, n, the series resistance, R_S and barrier height, Φ_{bo} were also measured using the technique developed by Cheung and Cheung's (Cheung & Cheung, 1986). Cheung and Cheung's functions can be written as Equations (4.5-4.7).

Table 4.3: Values of ideality factor, barrier height and series resistance.

Irradiation time (min)	Al/DNA/Si/Al and Al/Si/Al									
	Conventional method			Cheung-Cheung's method				Norde's method		
	n	Φ (eV)	R_S (Ω)	Φ (eV)	R_S (Ω)	n	R_S (Ω)	F(V)(V)	Φ (eV)	R_S (Ω)
Al/Si/Al	7.7478	0.5078	30.12	0.4259	41±0.3389	1.5372	19.4057±0.6747	0.497	0.3634	15.3107
0	9.9719	0.4780	46.304	0.4914	35±0.7793	3.0217	20±0.12813	0.4773	0.3632	15.4018
2	9.7934	0.5041	54.31	0.5208	42.±1.29643	2.3643	24±0.28975	0.495	0.3654	14.1393
4	10.5587	0.5004	62.81	0.5304	49±1.46054	2.8682	27±0.2054	0.4959	0.3685	12.5607
6	9.7301	0.5026	58	0.5241	46±1.64446	1.5891	25±0.23108	0.4984	0.3598	17.6020
8	9.7510	0.4982	57.38	0.5538	43±1.14544	4.6512	25±0.16048	0.5105	0.3653	14.2170
10	9.1727	0.5190	58.56	0.5560	43±1.33531	3.5271	25±0.24622	0.511	0.3493	26.3337
20	9.5912	0.5063	63.69	0.5526	48±1.75847	4.6512	26±0.2963	0.51	0.3503	25.3676
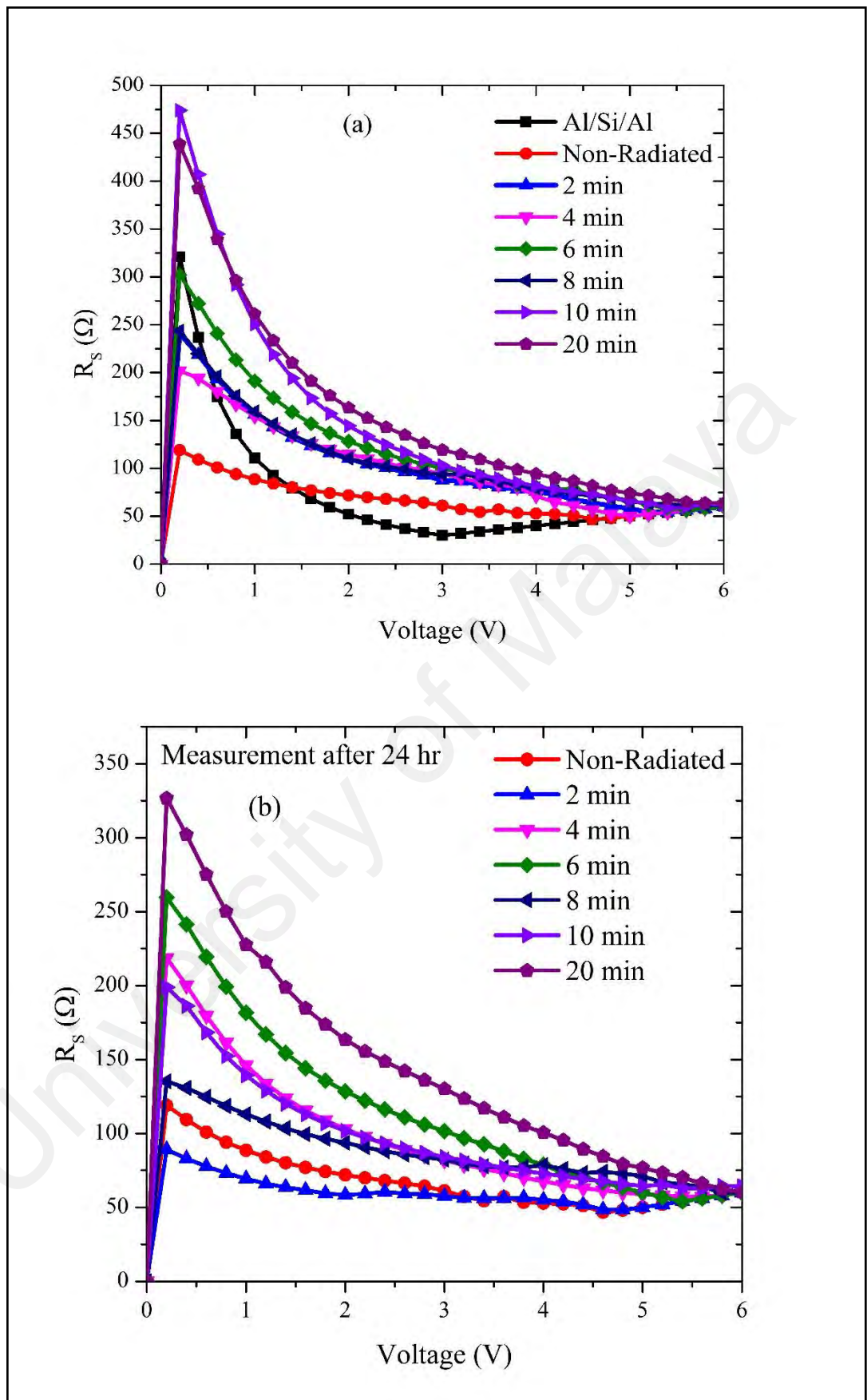
Figure 4.25: The relation between the series resistance and voltage generated using conventional method (a) before and (b) after 24 hr.

Figure 4.26 shows the experimental H(I) and dV/d(ln I) versus I for the Al/DNA/Si Schottky diodes at room temperature. H(I) versus I (**Figure 4.26**(a, c)) shows a straight line with the intercept at y-axis equal to $n\Phi$. Φ was obtained by substituting the n value from Equation (4.5) and the data of the downward curvature region in the forward bias I–V features from Equation (4.7). The slope of this plot also limits R_S, which can be used to check the accuracy of Cheung and Cheung's method. From H(I) versus I, the Φ and R_S values were measured and presented in **Table 4.3** and **Table 4.4**. Equation (4.5) gives a straight line for the data of the downward curvature region in the forward bias I–V properties. **Figure 4.26**(b), **Figure 4.26**(d) show the plots of dV/d(ln I) versus I, from which the values of n and R_S were calculated. As can be seen in the tables, the values of R_S obtained from both dV/d(ln I) versus I and H(I) versus I plots were in near agreement with each other. Radiation dose, however, does play an important role in changing series resistance values, thus the resistance increases gradually at low doses, self-protecting the DNA.

Norde's method meanwhile is an alternative method to calculate the series resistance and barrier height (Bazlov et al., 2013; Farag et al., 2010; Karadeniz et al., 2013). The following function has been known in the modified Norde's technique; where $F(V_{min})$ is the minimum point in the F(V) versus V curve, V_{min} and I_o are the corresponding voltage and current, respectively. Graphs of F(V) versus V for Al/DNA/Si before and after 24 hr of radiation at room temperature is as displayed in **Figure 4.27**. From the plot F(V) versus V, the values of Φ and R_S were determined (**Table 4.3** and **Table 4.4**).
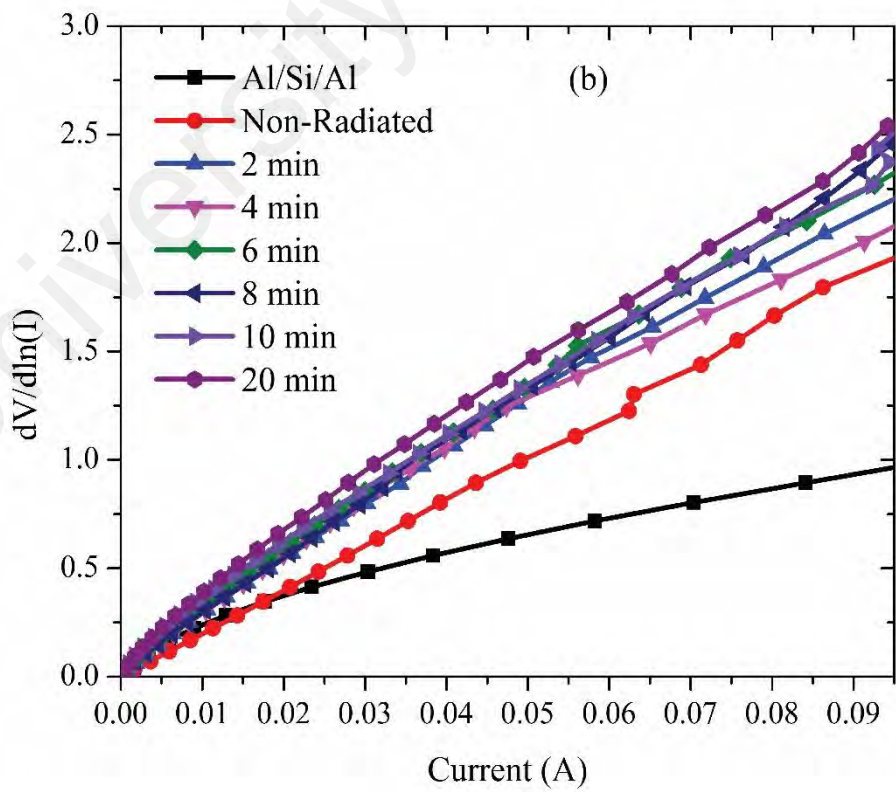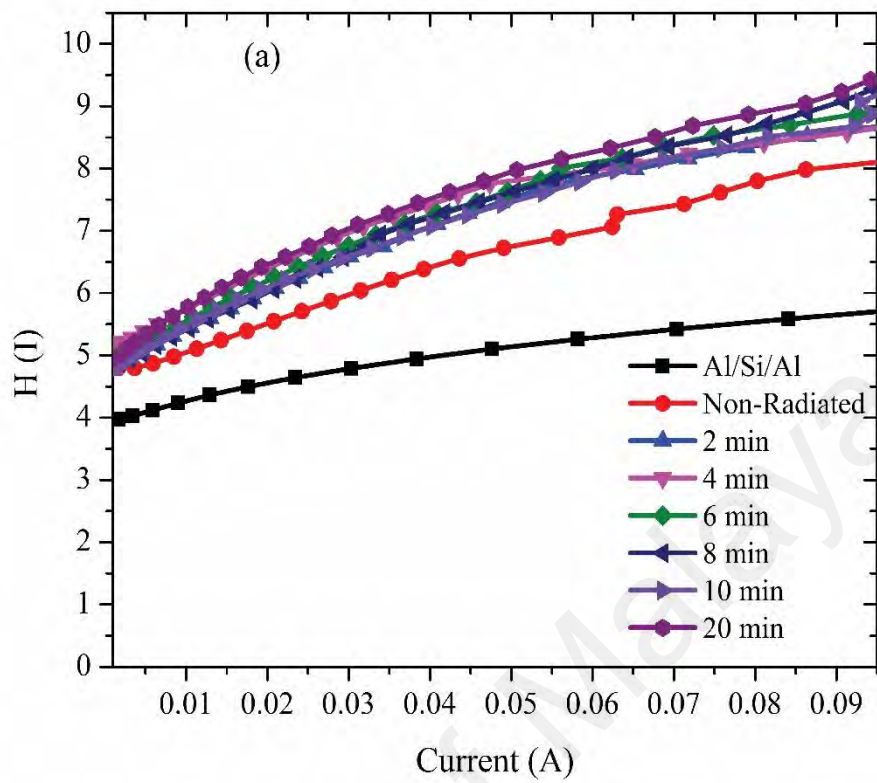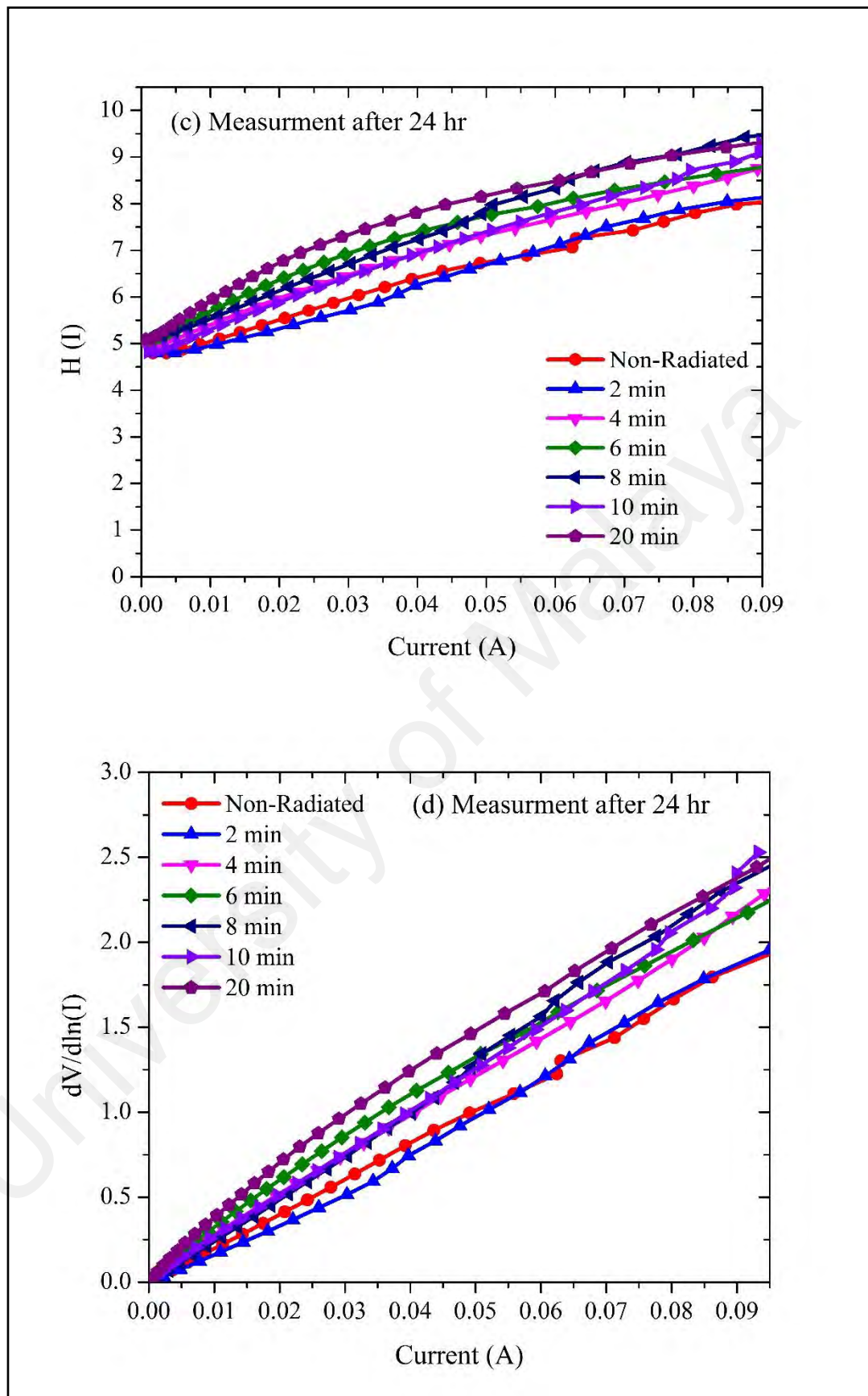
Figure 4.26: H(I) and dV/d(ln I) versus I obtained from forward bias I–V properties of Al/DNA/Si/Al Schottky junction diode (a,b) before and (c,d) after 24 hr.
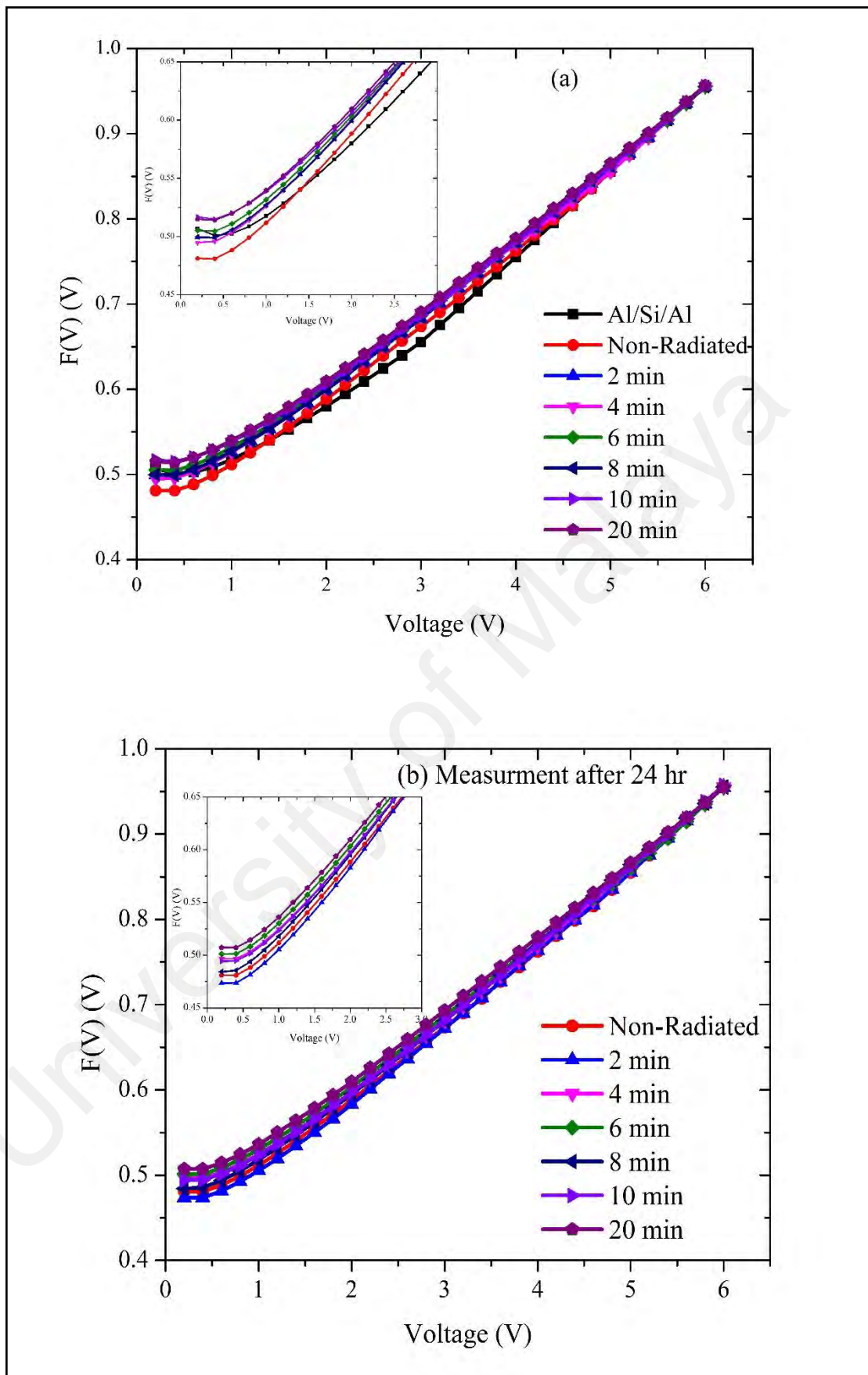
Figure 4.27: F(V) versus voltage plots of non-radiated and radiated Al/DNA/Si Schottky diodes (a) before and (b) after 24 hr.

Table 4.4: Values of ideality factor, barrier height and series resistance measured after 24 hr.

Irradiation time (min)	Al/DNA/Si/Al after 24 hr									
	Conventional method			Cheung-Cheung's method				Norde's method		
	n	Φ (eV)	R_S (Ω)	Φ (eV)	R_S (Ω)	n	R_S (Ω)	F(V)(V)	Φ (eV)	R_S (Ω)
0	9.9719	0.4780	46.72	0.4713	38±0.8092	3.3721	20±0.12813	0.4772	0.3834	7.0697
2	10.1446	0.4736	48.41	0.4534	41±0.794	3.3333	22±0.35064	0.4697	0.3308	11.5000
4	9.9168	0.4982	57.28	0.5042	43±0.9192	1.3178	24±0.1577	0.4927	0.3677	12.9375
6	10.1190	0.4982	54.11	0.5336	41±1.4499	3.8760	23±0.34179	0.4972	0.3030	33.5838
8	10.6707	0.4780	59.83	0.4779	52±0.8308	1.3566	27±0.19048	0.4805	0.3199	17.4831
10	9.7510	0.4982	62.52	0.4923	49±0.5774	0.1899	26±0.23352	0.4903	0.3100	25.6188
20	10.0429	0.5078	60.22	0.5477	47±2.1368	5.0388	26±0.41278	0.5031	0.2971	42.2497

According to the Norde's method, the values of R_S were two orders of magnitude less when compared to the conventional method. From **Figure 4.28**, the series resistance was observed to have increased in all the methods with increasing irradiation time. This could be attributed to the increasing number of alpha particle tracks (Çınar et al., 2010). Also the increasing R_S of the material results in reduction in the reverse current as shown in **Figure 4.23** and **Figure 4.24**, but series resistance measured using the conventional method remains the highest.
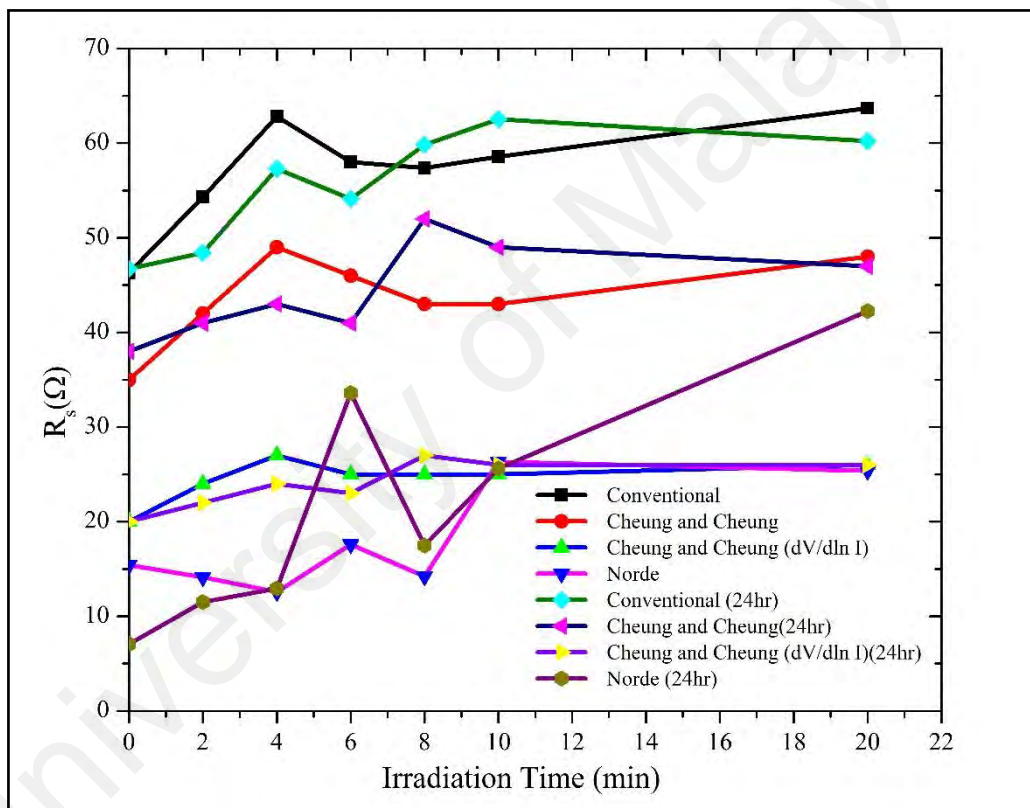
Figure 4.28: The relation between the series resistance and irradiation time.

Plots of Φ, n and R_S with radiation time are shown in **Figure 4.28** and **Figure 4.29**, which clearly indicates the hypersensitivity phenomena of the DNA at low doses. Φ_b is the real barrier height taken from the low-voltage region of the forward I–V graph. The series resistance was obtained from the straight-line region observed in **Figure 4.27**. After which, the values of barrier heights and the series resistances were

calculated from Equation (4.7) (**Table 4.3** and **Table 4.4**). Results show that the values calculated are very close to each other. The values of n, Φ_b and R_S were obtained from conventional and Cheung-Cheung's model. It indicates the values of n obtained from the dV/d (ln I) versus I curve to be lower than the values obtained from the forward bias ln (I) versus V plot. This can be attributed to the effect of the series resistance, interface states and voltage drop across the interfacial layer (Hsiung et al., 2012; L. M. Martin et al., 2013; Norde, 1979) and the irradiation effect (H. M. J. Al-Ta'ii et al., 2015a).

Ideality factor equals one for an ideal diode, which means that the resulting current is only due to thermionic emission. In this work, the n values demonstrated greater than unity values when operated in the voltage range between -1 and +1 V (Güllü et al., 2008). When operated between -4 and +5 V, high values of n give rise to a wide distribution of low barrier height Schottky diodes and interfacial thin layer (Aydoğan & Türüt, 2011). This is due to an increase of defect density at the interface with irradiation or lateral inhomogeneous barrier height (Ö Güllü et al., 2008; Tung, 1992; Umana-Membreno et al., 2003). In this aspect, the effects of alpha particle with higher mass (4×) and charge (2×) compared to an electron, becomes greater than that of the electron and gamma rays (Hsiung et al., 2012).

At low doses, the ideality factor drops dramatically, which demonstrates the hypersensitivity phenomena of the DNA (**Figure 4.29**) and its self-protection. Again this phenomenon is similar to the behavior observed between survival curve and dosage (H. M. Al-Ta'ii et al., 2009; H. M. Al-Ta'ii & Mohenned A., 2012; Bazlov et al., 2013). Schottky barrier height on the other hand has an increased proportional relationship with the ideality factor as shown in **Figure 4.29**. From **Figure 4.29**(b), barrier height values increases dramatically after 24 hr of exposure as measured from Cheung and Cheung's method and fluctuates according to conventional and Norde's methods. This may arise due to the DNA oligonucleotides ability to resist the alpha radiation (**Figure 4.29**(a)).
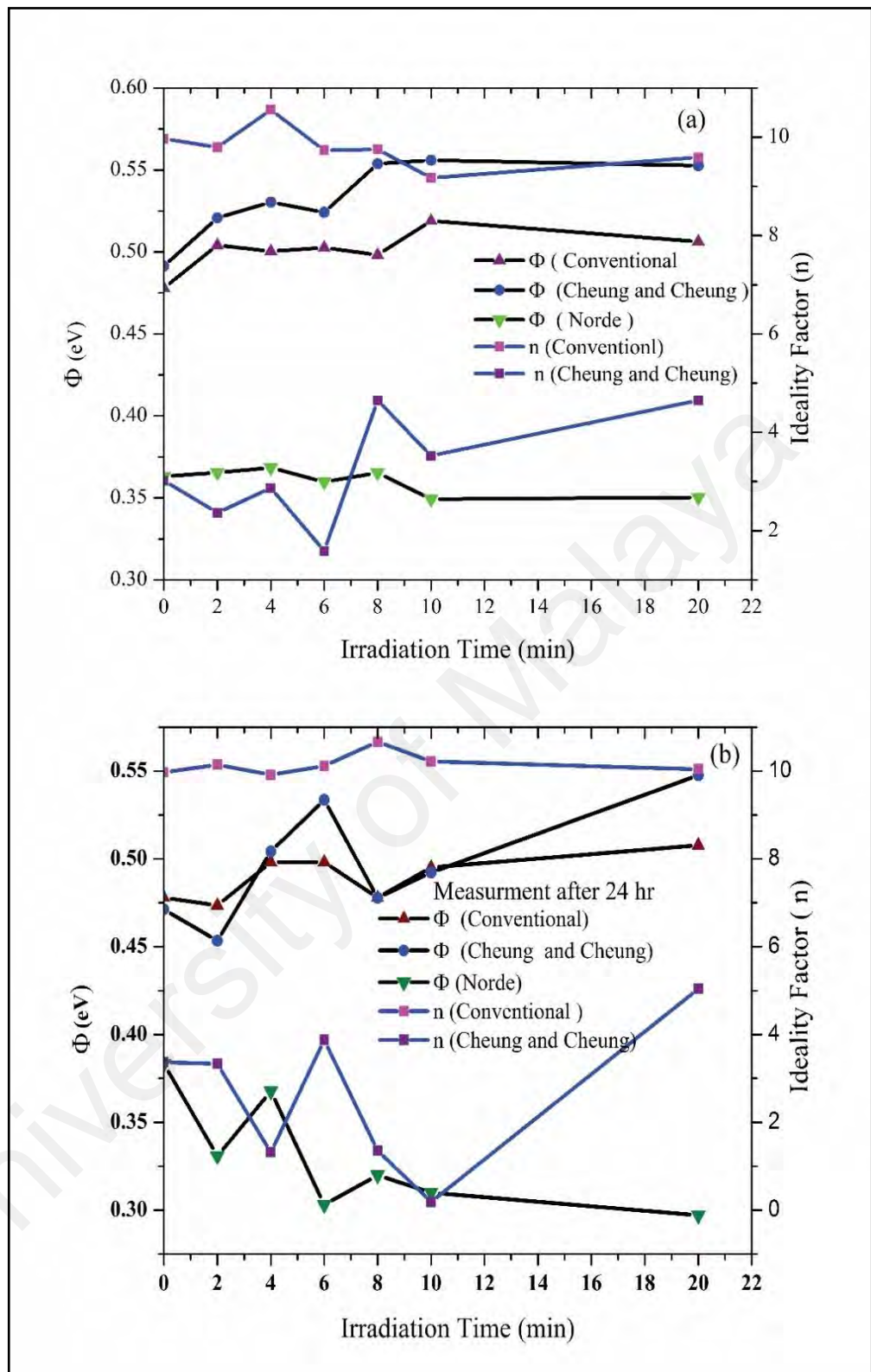
Figure 4.29: The relation between the ideality factor and barrier height with irradiation time (a) before and (b) after 24 hr.

Figure 4.30 displays the dual logarithmic plot of forward bias I–V properties of the Al/DNA/Si/Al junction. The log(I)–log(V) graphs clearly shows the power law

behavior of the I–V curve. Space-charge-limited current (SCLC) affecting the diode and its charge transport can be shown through the $I = V^m$ rule where m is the slope of each region, which corresponds to Ohmic and SCLC. The m values of the region shown in **Table 4.5**, portrays two linear regions of the log(I)–log(V) plot of the forward bias I–V properties. Region (I) shows an Ohmic region, while region (II) demonstrates the presence of the SCLC mechanism controlled by the traps.

Figure 4.31 shows the I–V curve for the contact of Al/Si/Al sandwich structure in the absence of DNA, which generates a resistance of about 22.5 Ω and radiation effect induced current of about 10^{-1} A. This means that the radiation does not have any effect on the sample and the diode behaves as a good rectifier. **Figure 4.32** shows the relation between saturation current under direct irradiation and after 24 hr. In the first case, the saturation current was clearly lower than the non-radiated ones. However after 24 hr, some of these irradiated samples generated higher currents. This observation of a decline in saturation current can be attributed to the rise of carrier resistance and potential barrier (Mtangi et al., 2009).

Figure 4.33 demonstrates that the Richardson constant is very sensitive to the radiation effect. The Richardson constant was measured from the I–V curve and it increases with irradiation time. Ionizing radiation process leads to energy sedimentation in the metal, appearing as thermal heat and changing the material properties (Holbert, 1995). Work function of the metal/semiconductor junction changes, which provides sufficient energy for the charge carriers to get over the binding potential. Increasing number of alpha particles tracks also leads to increase in the number of holes thereby increasing the effective mass, which causes a lower rate of carriers to break through the potential barrier, reducing the current.
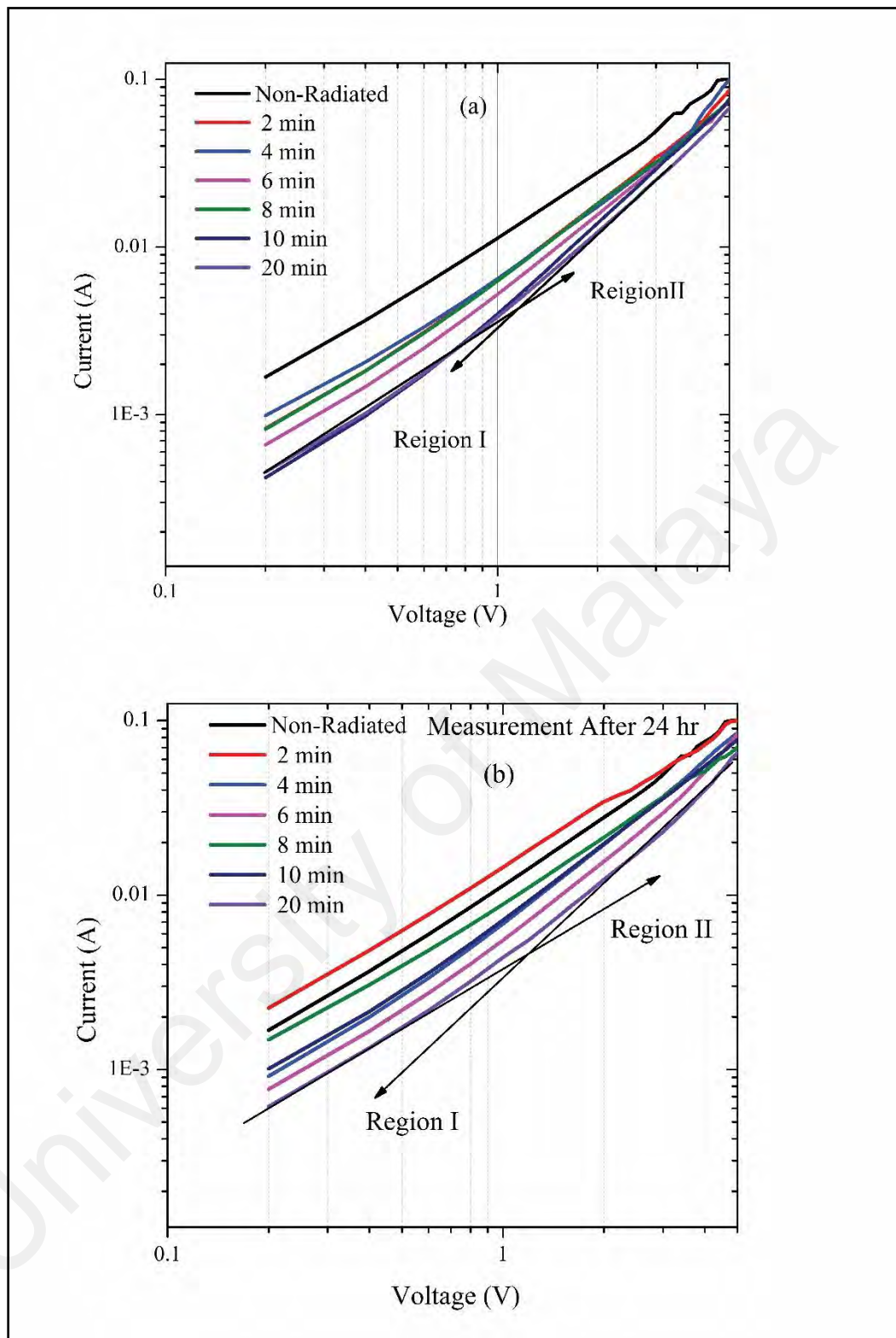
Figure 4.30: Double logarithmic plots of the Al/DNA/p-Si/Al junctions (a) before and (b) after 24 hr.

Due to the excitation of the material by ionizing radiation, such as by the alpha particles, a huge number of excited atoms are produced along its path, thereby

increasing the number of electrons and R_S. The number of electrons also decreases through the collision between the MSM electrodes. This results in increase in the barrier heights as in **Table 4.6**, followed by a decline in the current.

Table 4.5: Values of m for regions (I) and (II) of the power law for Al/DNA/Si/Al measured before and after 24 hr.

Irradiation time (min)	Al/DNA/Si/Al		Al/DNA/Si/Al after 24 hr	
	Region (I)	Region (II)	Region (I)	Region (II)
0	1.16746	1.42133	1.1481	1.4343
2	1.38448	1.71641	1.22538	1.27533
4	1.35663	1.84725	1.33968	1.5977
6	1.38282	1.68783	1.35636	1.74065
8	1.31927	1.59468	1.18727	1.28848
10	1.47493	1.82395	1.3137	1.48376
20	1.3539	1.85096	1.15171	1.77029
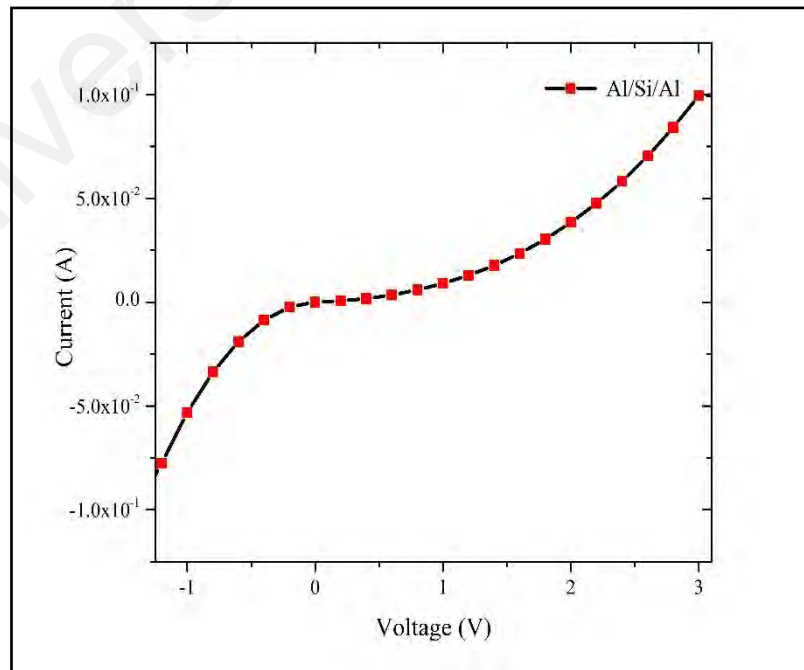
Figure 4.31: I–V curve of the Al/Si/Al junction in the absence of the DNA molecule.
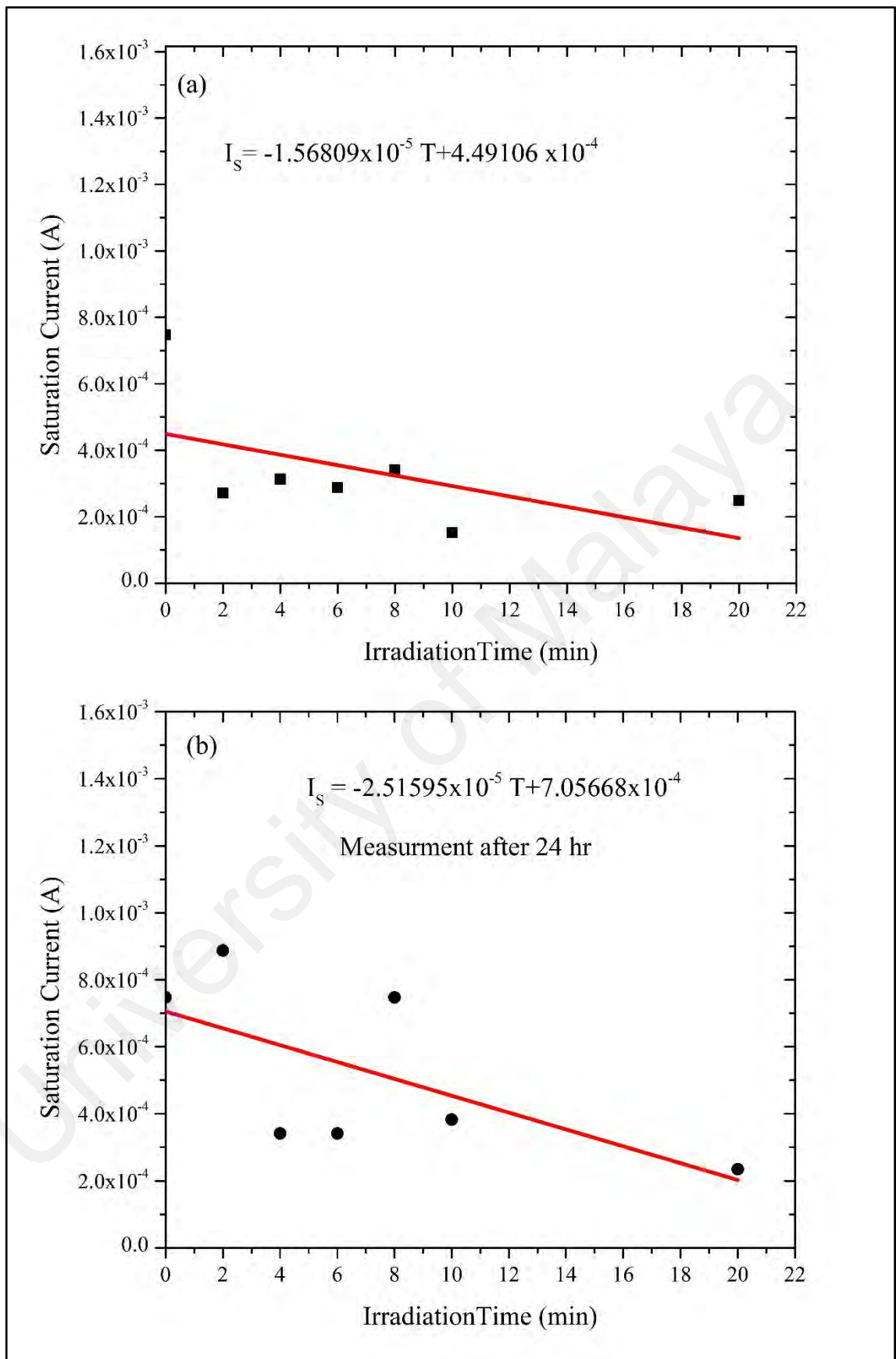
Figure 4.32: The relation between the saturation current and irradiation time (a) before and (b) after 24 hr.
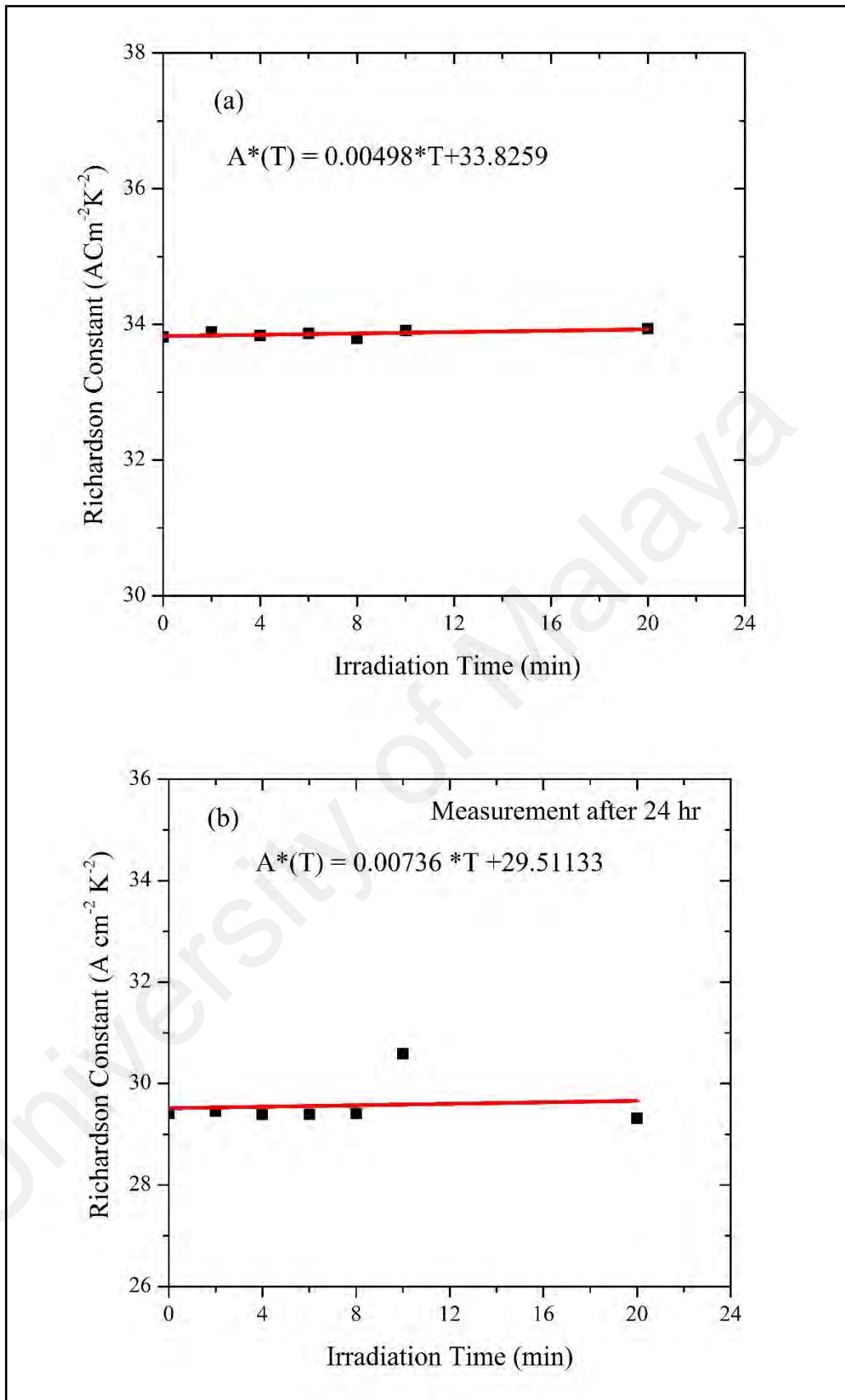
Figure 4.33: Irradiation time dependent Richardson constant for the MDM design (a) before and (b) after 24 hr.

Table 4.6: Barrier height and Richardson constant against irradiation time in Al/DNA/Si/Al structures.

Irradiation time (min)	Φ (eV)	A*(A.cm^{-2}K^{-2})	Φ (eV) (After 24 hr)	A* (A.cm^{-2}K^{-2}) (After 24 hr)
0	0.4816	33.80976	0.4780	29.40648
2	0.5078	33.88901	0.4736	29.45637
4	0.5041	33.83585	0.4982	29.38977
6	0.5063	33.86438	0.4982	29.38978
8	0.5018	33.79057	0.4780	29.40648
10	0.5228	33.90649	0.4982	30.59743
20	0.5101	33.93433	0.5078	29.30825

4.5 Detection of Alpha Particles using DNA/Al Schottky Junctions

The forward and reverse bias I–V characteristics of the Al/DNA/Al junctions at room temperature are given in **Figure 4.34**(a) and I–V–T in **Figure 4.34**(b). As can be observed, the I–V characteristics of the device demonstrate a rectifying behavior. **Figure 4.34**(a) demonstrates the relation between the I–V, showing good rectifying trend for the current. **Figure 4.34**(b) meanwhile shows the three-dimensional relationship between I–V and irradiation time.

According to the thermionic emission theory, the I–V characteristic of a diode is given by the Equations (4.1) and (4.2) (Khatir et al., 2012). For values of V > 3kT/q, the ideality factor from Equation (4.1) can be re-written as Equation (4.3).
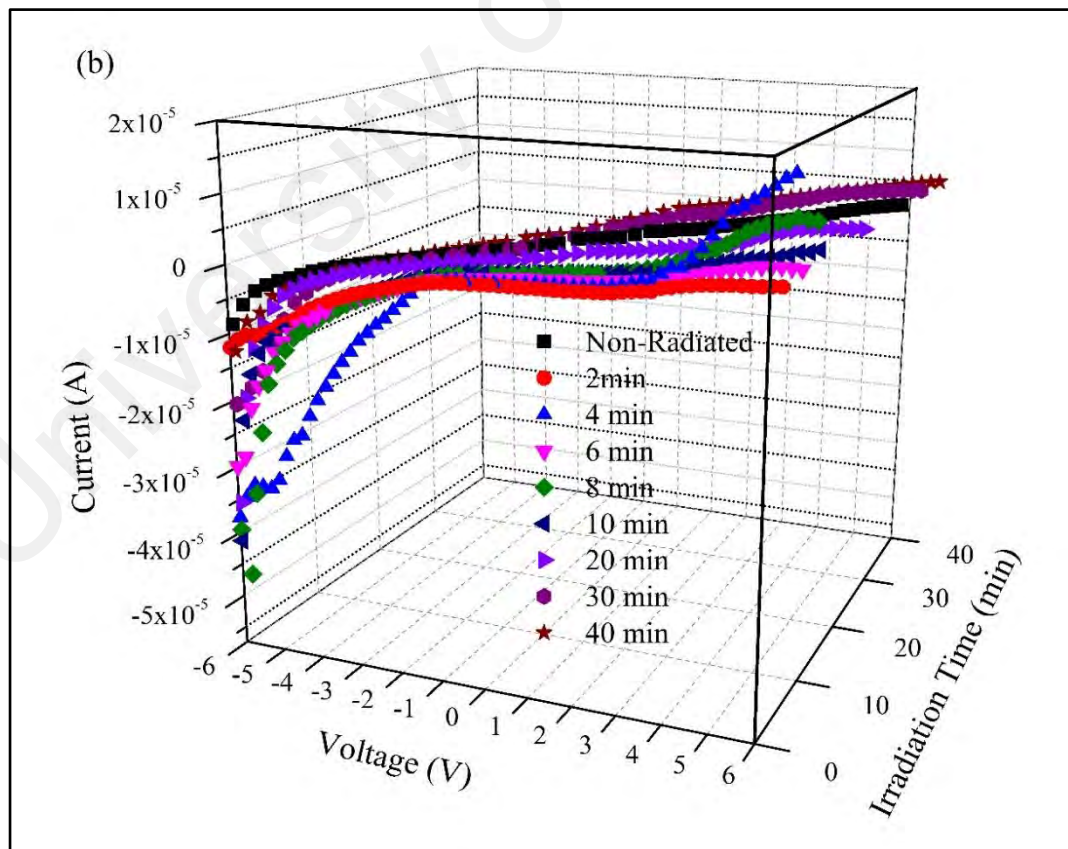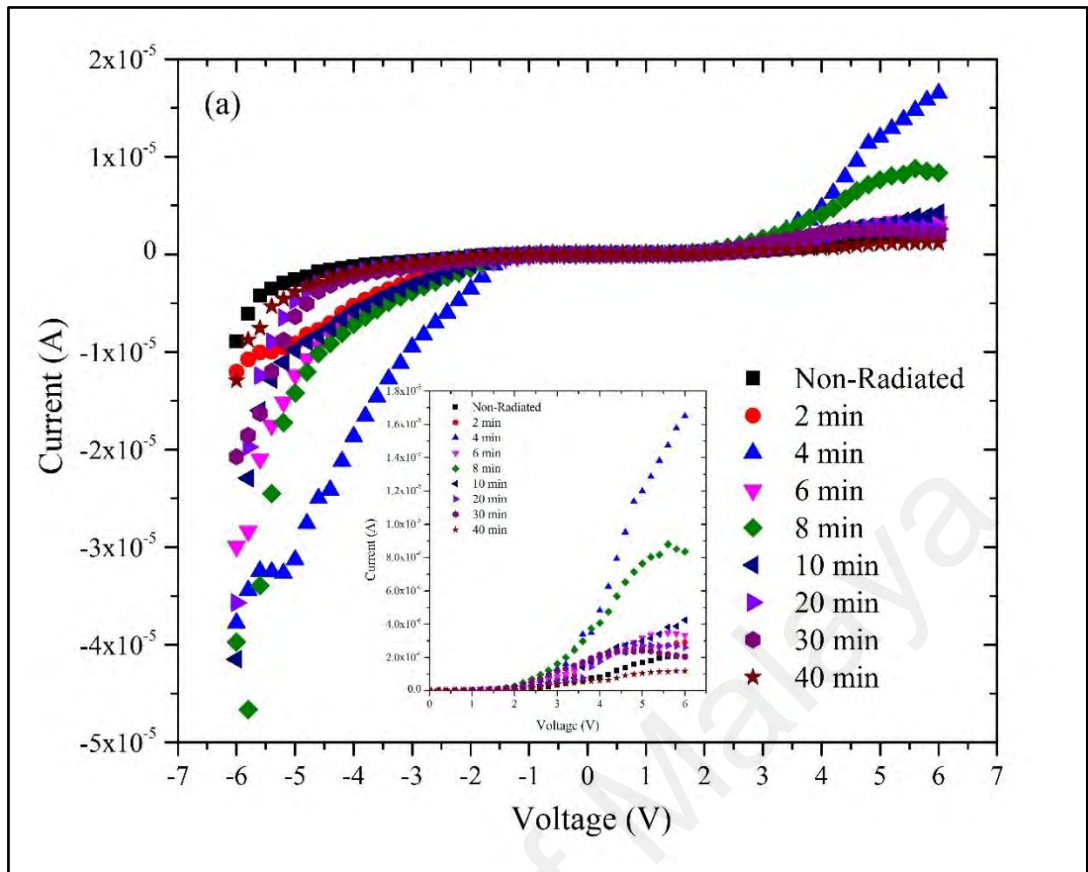
Figure 4.34: Graphs demonstrate the relationship between (a) current and voltage, (b) I–V–T for forward and reverse biases in real time.
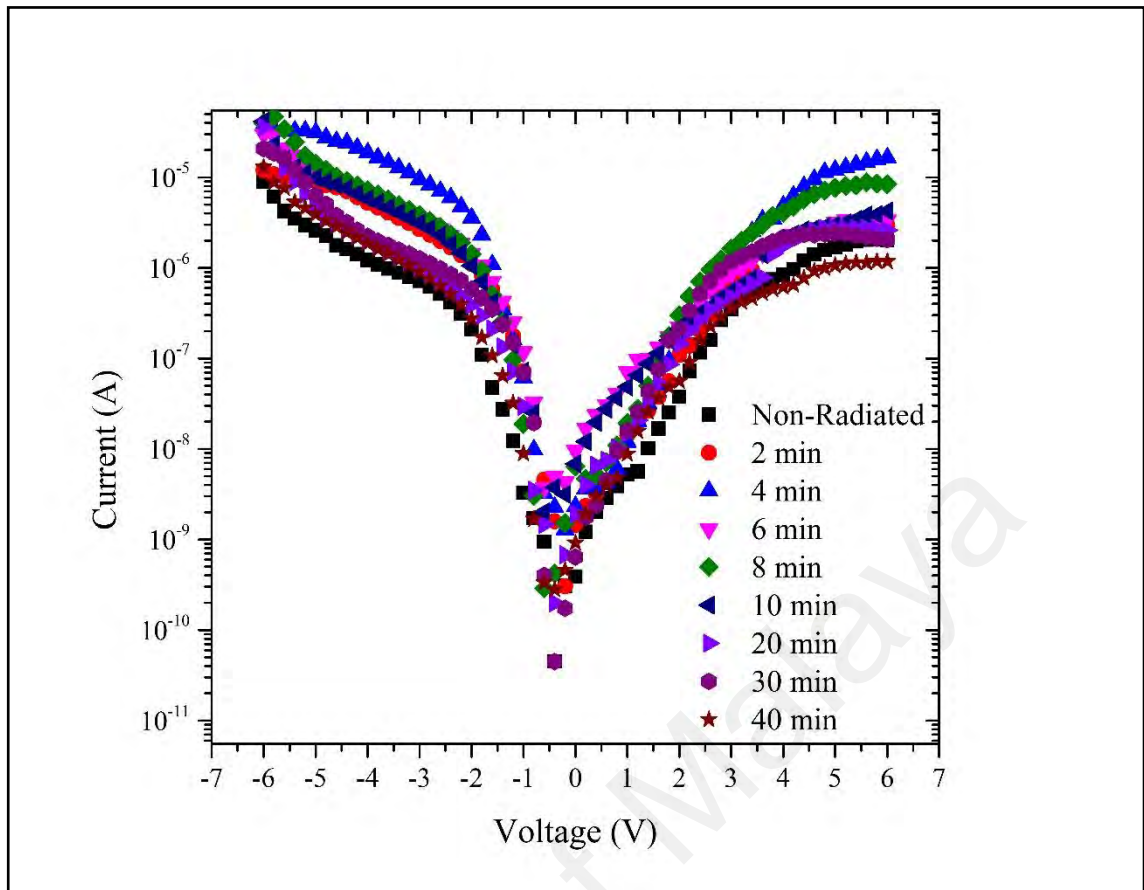
Figure 4.35: Profiles show the real time log I–V characteristics of Al/DNA/p-Si Schottky diode at room temperature.

The ideality factor determined from the slope of the linear region of the forward bias (ln(I)-V) characteristics through the relation in Equation (4.3) is a measure of conformity of diode to pure thermionic emission (R. K. Gupta & Yakuphanoglu, 2012; V. R. Reddy et al., 2011). As discussed earlier, n equals to 1 for an ideal diode but here, it demonstrates higher values. These high values of n can be attributed to the presence of interfacial thin film, a huge distribution of low Schottky barrier height (SBH) patches (or barrier inhomogeneity), rearrangement of electrons and holes in the depletion regions and bias dependence of voltage of SBH (Sze & Ng, 2006). **Figure 4.35** shows the ideality factor fluctuations of Al/DNA/Al based junctions fabricated in this work calculated using Equation (4.3).

For both the radiated and non-radiated samples, the linear region of the forward bias I–V plots indicates that the effect of the series resistance in this region is not

important. The value of the barrier height (Φ) of the Al/DNA/Al Schottky diode was 0.7149 eV before irradiation. Values before and after irradiation (**Table 4.7)** was calculated from the y-axis intercepts of the semi log-forward bias I–V plots using Equation (4.4). It should to be noted that Φ is the connection potential barrier that exists at the interface between inorganic and the values of series resistance are calculated from the junction resistance formula $R_S = \partial V / \partial I$ from the I–V properties of the diode. The resistance R_S versus voltage of the surface-type Schottky diode is demonstrated in **Figure 4.36**. From the figure, it can be concluded that at low voltages (≤ 2.0 V), R_S values were the highest for non-radiated, 30 and 4 min of irradiation in reducing order, followed by the sample radiated for 2 min. However above 2.0 V, the R_S values become insignificant.

At high currents, there is always a deviation of the ideality factor that has been obviously shown to rely on bulk series resistance and the interface state density, as one would expect. The lower the series resistance and the interface state density, the better is the range over which ln I(V) does in reality yield a straight line. The Schottky diode factors such as the barrier height Φ_{bo}, the series resistances and the ideality factor n were also determined using the technique advanced by Cheung and Cheung (Cheung & Cheung, 1986). The method's functions can be shown in Equations (4.5-4.7) and **Figure 4.37**, respectively for the Al/DNA/Al Schottky diode at room temperature.
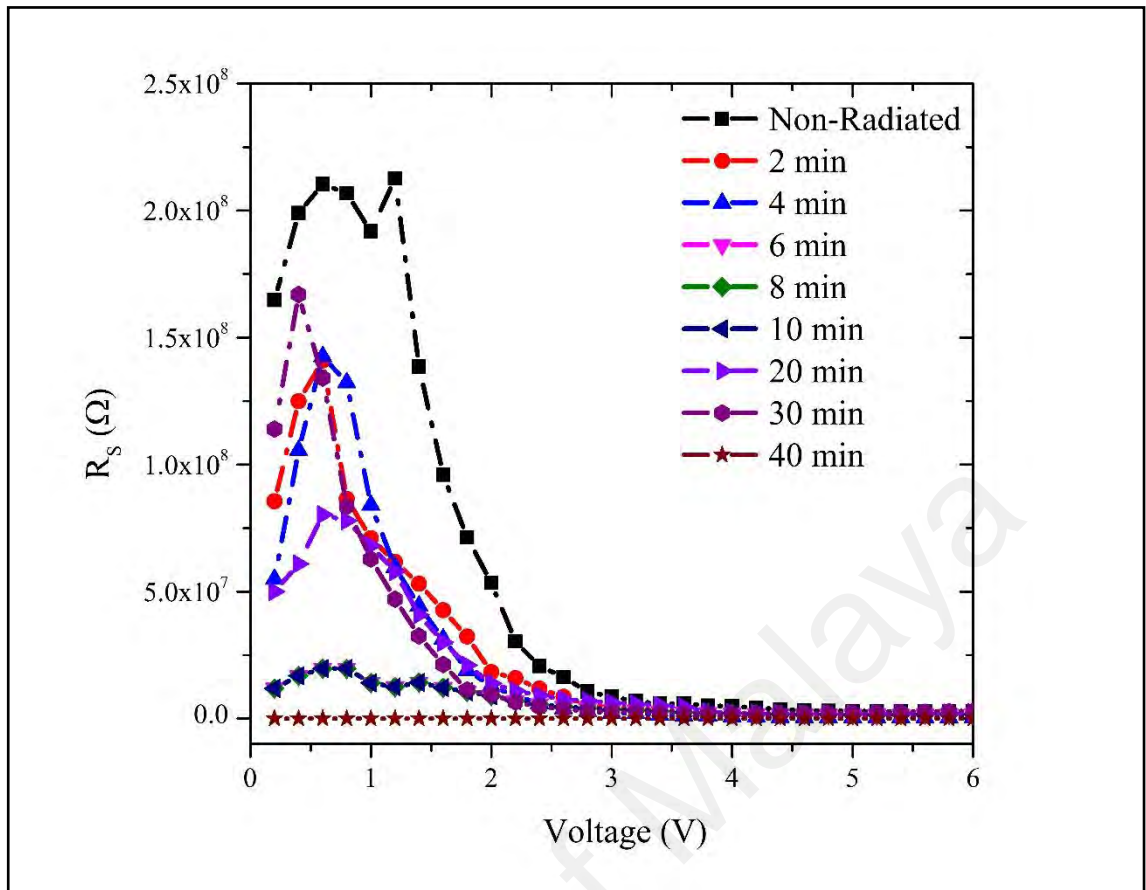
Figure 4.36: Real time plots of the bias-dependent resistance Rs =dV /dI versus applied voltage for the Al/DNA/Al junction.

A plot of H(I) versus I (**Figure 4.37**(a)) shows a straight line with intercept at y-axis equal to $n\Phi$. Φ was obtained by substituting the n value from Equation (4.5) and the data of the downward curvature region in the forward bias I–V graph from Equation (4.7). The slope of this plot also limits R_S, which can be utilized to check the accuracy of Cheung and Cheung's method. From H(I) versus I, the Φ and R_S values were measured and presented in **Table 4.7**. Equation (4.5) gives a straight line for the data of the downward curvature region in the forward bias I–V graph.
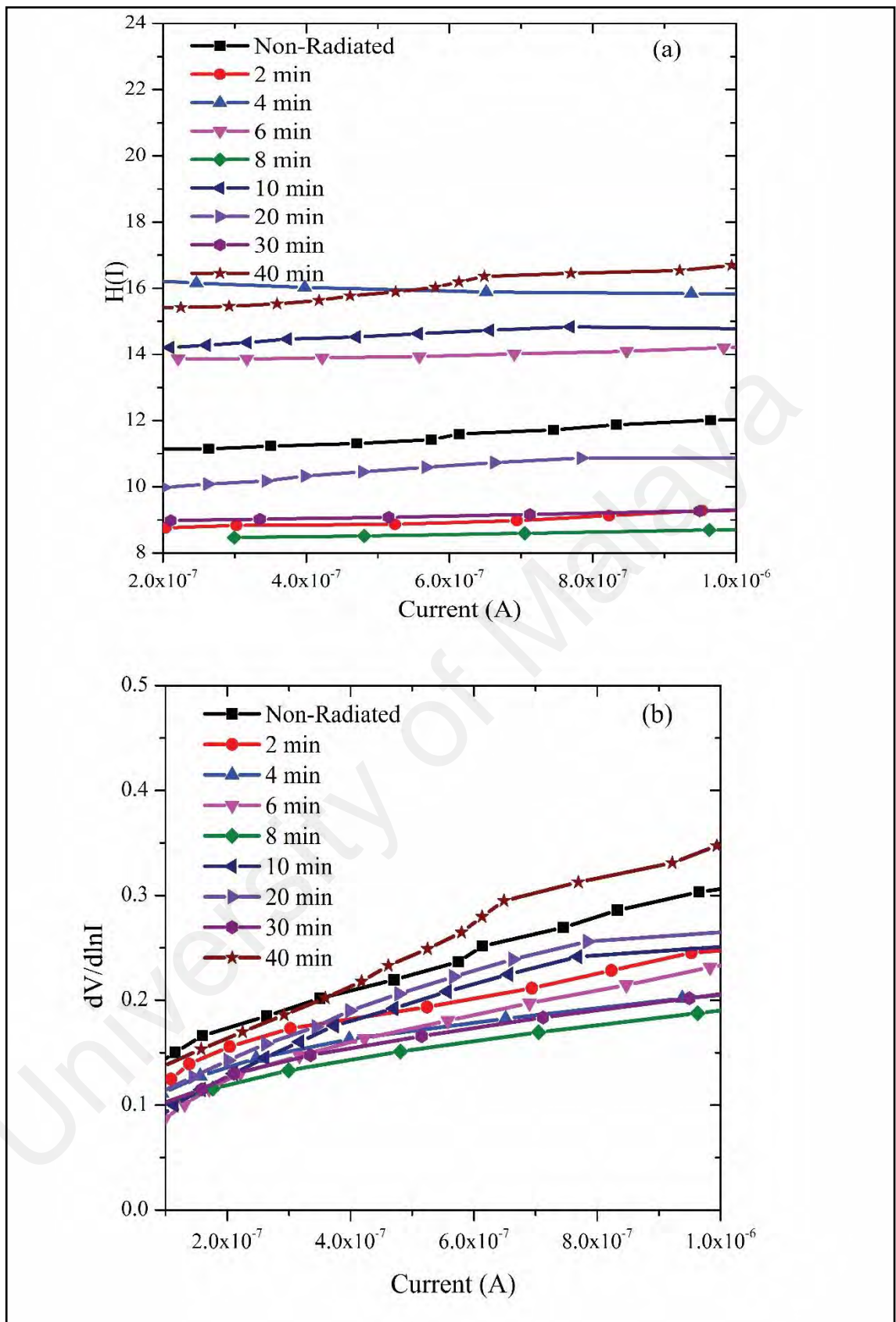
Figure 4.37: H(I) and dV/d(ln I) versus I graphs obtained from forward bias I–V characteristics of Al/DNA/Al Schottky junction diode.

Table 4.7: Values of ideality factor, barrier height and series resistance.

Irradiation time (min)	Conventional thermionic emission model			Cheung-Cheung's method			
	n	Φ(eV)	R_S (MΩ)	n	R_S (MΩ)	Φ(eV)	R_S (MΩ)
0	15.6814	0.7149	2.743	3.4109	0.180±0.03321	0.6983	0.9694±0.01078
2	11.3911	0.7286	1.896	3.0233	0.130±0.06352	0.7528	0.301±0.00635
4	26.4286	0.7367	0.3637	4.2636	0.028±0.0105	0.6124	0.0144±0.00208
6	22.3706	0.6704	1.547	2.9457	0.110±0.0142	0.6124	0.4828±0.00676
8	12.3710	0.7129	0.6362	3.5271	0.048±0.00529	0.6867	0.2560±0.00339
10	22.9404	0.7009	1.413	3.4109	0.100±0.01121	0.6114	1.06804±0.00599
20	14.5968	0.8481	1.764	3.3333	0.120±0.03097	0.6945	0.5132±0.01294
30	13.1230	0.7680	1.845	2.2868	0.140±0.02572	0.6650	0.6444±0.00778
40	24.1728	0.7164	0.4665	2.6744	0.300±0.16596	0.6265	1.55188±0.02045

R_S was obtained from both the Conventional and the Cheung and Cheung's models, but the values calculated using the former method was higher than the ones derived from the latter one (**Figure 4.38**). Generally, values of n obtained from the dV/d(ln I) versus I curve is higher than that of the forward bias ln I versus V plot. This can be attributed to the effect of the series resistance, interface states and voltage drop across interfacial layers (Bazlov et al., 2013; Farag et al., 2010; Karadeniz et al., 2013) and radiation effect (Çınar et al., 2010).

Figure 4.39 displays the dual logarithmic plot of forward bias I–V properties of the Al/DNA/Al junction. The log(I)–log(V) graphs clearly shows the power law behavior of the I–V curve. SCLC effecting the diode and its charge transport can be shown through the $I=V^m$ rule where m is the slope of each region, which corresponds to Ohmic and SCLC. m values of the region shown in **Table 4.8**, portrays three linear

regions of the log(I)–log(V) plot of the forward bias I–V properties. Region (I) shows an Ohmic region, while region (II) demonstrates the presence of the SCLC mechanism controlled by the traps. The second region of this graph having a slope of 2.47-5.2 up to a transition voltage of about 2.7 V is similar to the SCLC with the exponential distribution of traps in the band gap of the organic material. The third region of double logarithmic forward bias curve has a slope value of 1.1 to 2.5 except for the sample with 20 min of radiation. This region shows that at higher voltage the slope of the curve decreases because the device approaches the trap filled limit.
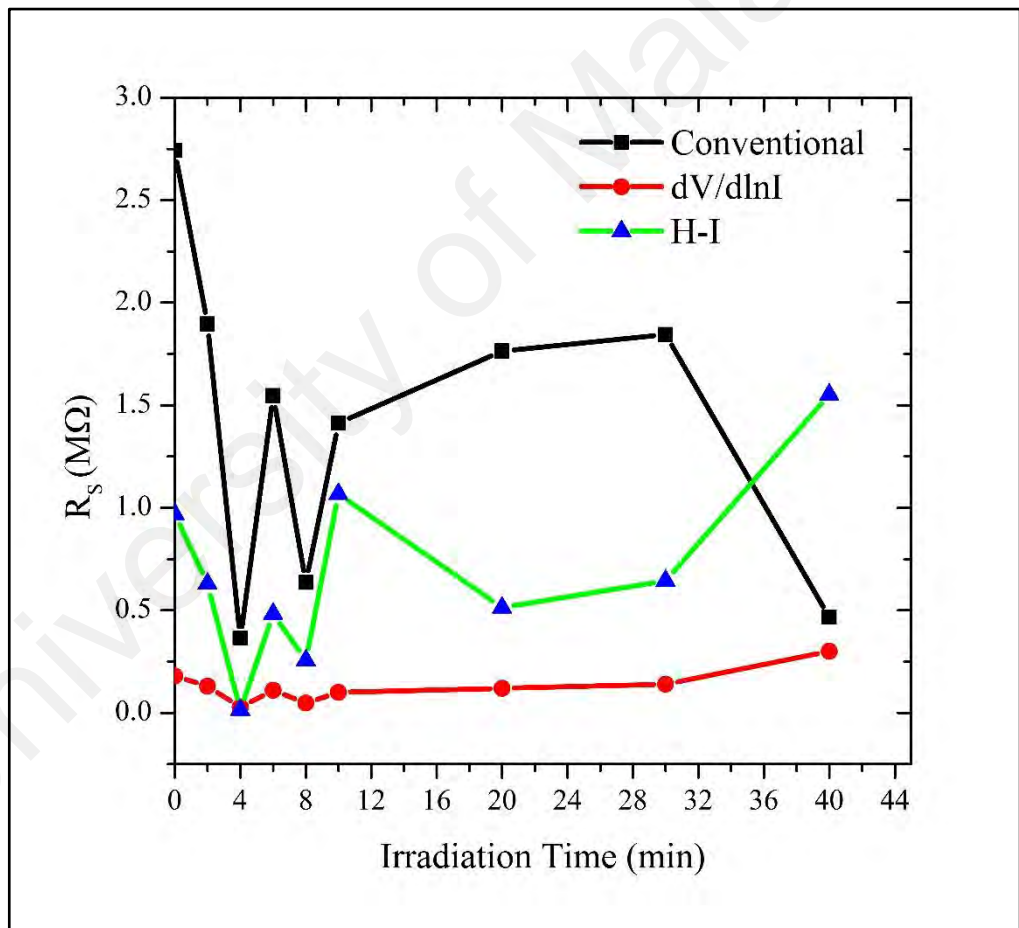
Figure 4.38: Diagrams demonstrate the relationship between R_S and alpha radiation time.
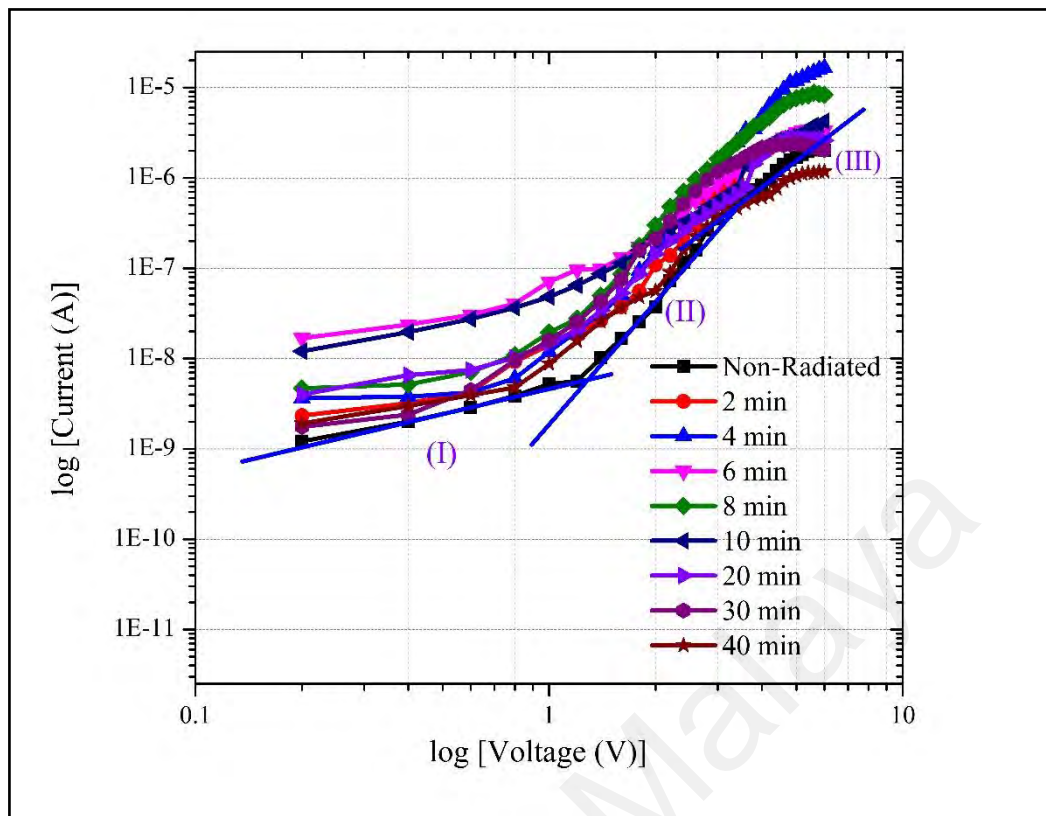
Figure 4.39: Double logarithmic plots of the Al/DNA/Al junctions.

In this work, the n values demonstrated greater than unity values when operated in the voltage range between -1 and +1 V (Güllü et al., 2008). However, when operated between –6 and +6 V, high values of n gives rise to a wide distribution of low barrier height Schottky diodes and interfacial thin layer (Aydoğan & Türüt, 2011). This is due to an increase of defect density at the interface with irradiation or lateral inhomogeneous barrier height (Ö Güllü et al., 2008; Tung, 1992; Umana-Membreno et al., 2003). In this aspect, the effects of alpha particle with higher mass ($4m_p$) and charge (+2e) compared to an electron, becomes greater than that of the electron and gamma rays (massless) (Holbert, 1995).

Table 4.8: Values of m for regions (I), (II) and (III) of the power law Al/DNA/Al.

Irradiation time (min)	Al/DNA/Al junction (slope gradient, m)		
	Region (I)	Region (II)	Region (III)
0	0.88799	5.03999	2.51623
2	0.53536	4.73327	1.68588
4	0.12278	5.2034	1.73042
6	0.61435	3.27404	1.80156
8	0.35643	4.53009	1.26685
10	0.84715	2.47782	1.58914
20	0.64404	3.83097	0.69162
30	0.80862	4.65787	1.02202
40	0.65955	5.03193	1.11818

At low doses, the ideality factor drops dramatically, demonstrating the hypersensitivity phenomena of the DNA (**Figure 4.40**) and its self-protection. This phenomenon is similar to the behavior observed between survival curve and dosage (H. M. Al-Ta'ii et al., 2009; H. M. Al-Ta'ii & Mohenned A., 2012; L. M. Martin et al., 2013). Schottky barrier height on the other hand has an increased proportionality in relationship with the ideality factor as shown in **Figure 4.40**. This may arise due to the DNA oligonucleotides ability to resist the alpha radiation and the ideality factor from Cheung-Cheung's method registers lower values compared to the conventional method. On the other hand, the Φ_b value using the conventional method becomes higher than Φ_b from Cheung-Cheung's method. The hypersensitivity phenomenon was observed in that the cells obtain some resistance after irradiation to about ≤ 0.5 Gy, where the typical response exhibited an exponential form of the survival curve. It begins to rise at about

0.5 Gy to an upper survival limit as the irradiation dose rises before eventually decreasing in a normal manner as observed earlier (H. M. Al-Ta'ii et al., 2009; Böhrnsen et al., 2002; Marples et al., 1994; Schettino et al., 2001).

Figure 4.41 demonstrates that the Richardson constant is very sensitive to the radiation effect. Richardson constant was measured from the I–V curve and it increases with irradiation time. The ionizing radiation process leads to energy sedimentation in the metal, appearing as thermal heat and changing the material properties (Holbert, 1995). The work function of the metal/semiconductor junction changes, which provides sufficient energy for the charge carriers to get over the binding potential. Increasing number of alpha particles tracks also leads to increase in the number of holes, thereby increasing the effective mass, which causes a lower rate of carriers to break through the potential barrier, reducing the current.
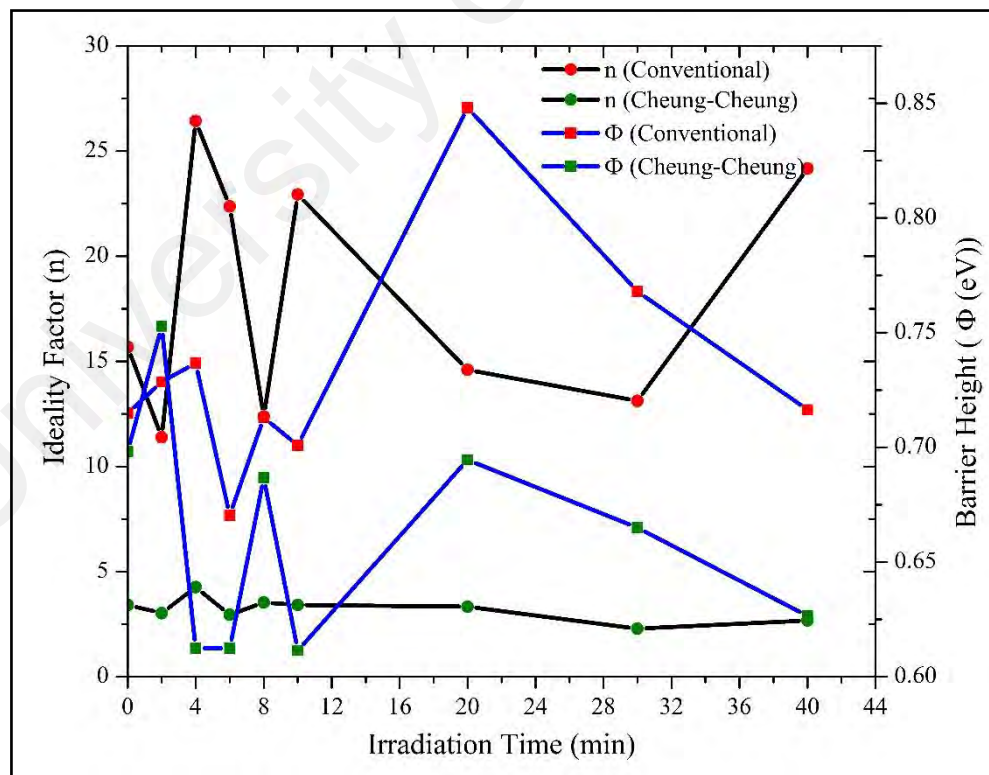
Figure 4.40: Graphs demonstrate the relation between the ideality factor and barrier height by irradiation time.
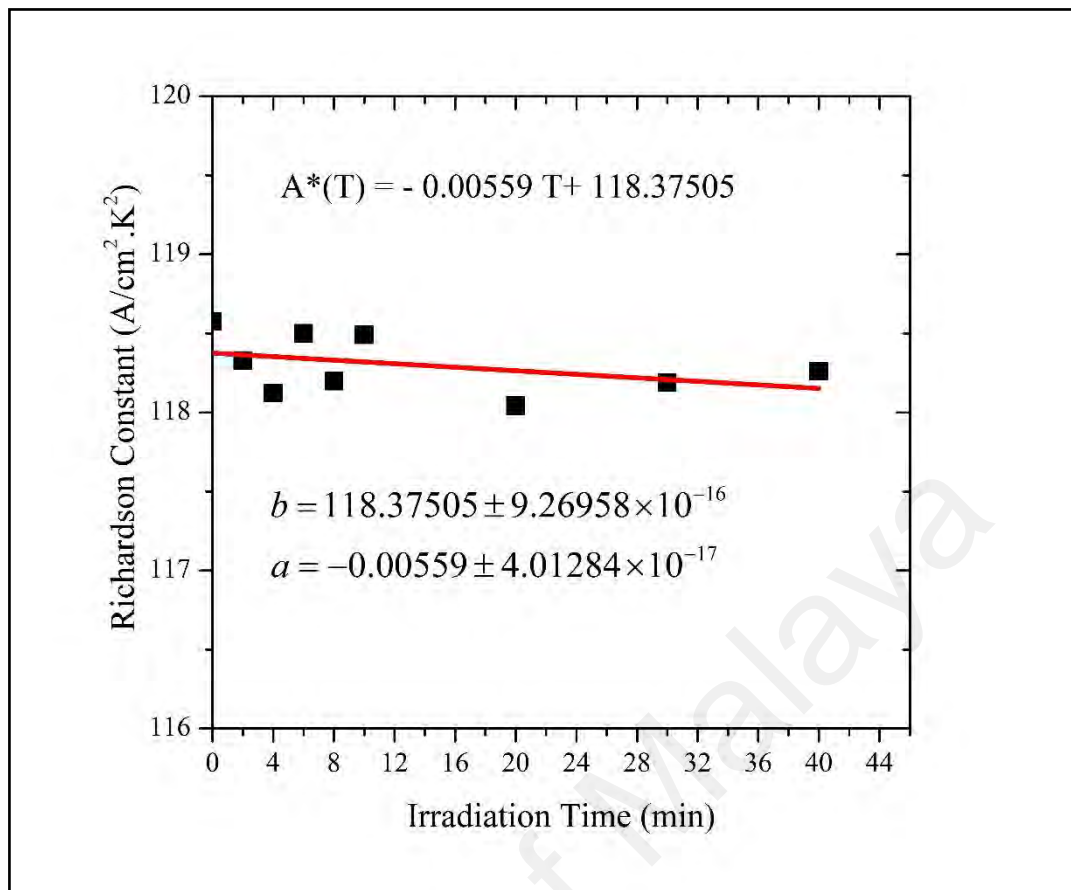
Figure 4.41: Irradiation time dependent Richardson constant for the MDM structure.

Due to the excitation of the material by ionizing radiation such as by alpha particles, a huge number of excited atoms are produced along its path, thereby increasing the number of electrons. Further, a decrease in the number of electrons was observed as a result of collisions between the MDM electrodes and the increase in resistance due to the number of traps in DNA preventing internal charge movement and hence increases the electrical resistance (Borhani et al., 2007; Sabet et al., 2012). This results in an increase in the barrier heights as listed in **Table 4.9**, followed by a decline in the current.

In these experiments, we measured the current with increasing irradiation for all the samples for the same time periods. Electrical field increases due to the I–V response through the circuit and the alpha particle charge incident on the DNA layer, which increases the number of electron transfer from the valance to conductance band. This

can be explained as after the traversal of the alpha particles to the DNA layer, a large number of excited atoms along the alpha particles tracks were produced. Thereby the holes left in the valence band and electrons in the conduction band could be important in increasing the electrical conductivity of both semiconductors and insulating materials. This phenomenon is well known as radiation-induced conductivity. Thus, electron-hole pairs are created (electron in the conduction and hole in the valence band) due to this irradiation event. On the other hand, irradiation also creates secondary electron charge carriers, which affects the electrical properties. The relaxation time in semiconductors, such as in the DNA strands becomes longer than compared to metals causing more permanent damage (Holbert, 1995).

Table 4.9: Barrier height and Richardson constant against irradiation time in Al/DNA/Al structures.

Irradiation time (min)	Richardson constant A^* $(A.cm^{-2}.K^{-2})$	Barrier height Φ (eV)
0	118.57569	0.7149
2	118.32802	0.7286
4	118.12141	0.7367
6	118.49909	0.6704
8	118.19823	0.7129
10	118.4912	0.7009
20	118.04117	0.8481
30	118.18911	0.7680
40	118.2611	0.7164

4.6 Humidity Influenced Capacitance and Resistance of Al/DNA/Al Schottky Diode Irradiated by Alpha Particles

The quantity of water vapour in the atmosphere is called humidity, which affects all environmental biological and chemical processes. Humidity also negatively affects various industrial-manufacturing methods if proper steps are not taken. As such, humidity level in terms of RH are closely monitored to reveal fluctuations in situations ranging from high to low temperatures or in mixtures with other gases (Stetter et al., 2003). RH equals to the ratio between the quantity of wetness or content of air to the extreme (saturated) moisture level that the air can hold at a given pressure and temperature (Farahani et al., 2014). Therefore, RH values are recorded and studied extensively as it has many applications that includes improving indoor air quality for comfortable and healthy living conditions (Kulwicki, 1991).

Humidity sensors are important for the determination of environmental conditions in many manufacturing applications due to the negative impacts of water vapor or humidity in an industrial environment (Anjaneyulu et al., 2007). Generally, humidity sensors can be classified by their measuring parameter, which may involve resistive, hydrometric, optical, gravimetric or capacitive either separately or integrated together (Chen & Lu, 2005; C.-Y. Lee & Lee, 2005). Compared to the rest, capacitive-type humidity sensors have numerous advantages, including low power consumption and large output signals (Kh S Karimov et al., 2012).

Generally, humidity sensors can be divided into resistive, thermo elemental capacitive, oscillating and mechanical types using sensitive organic materials (Huang et al., 2007; Ramaprasad & Rao, 2010). There are several factors that act to determine the performance and the advantage of the humidity-measuring instrument. These include properties such as fast reaction time, physically and chemically stable active compounds, linear behavior, suitable detection range, good strength, resistance against

pollution and cheaper fabrication cost (Azmer et al., 2015; Rittersma, 2002; Traversa, 1995; S. Wang et al., 2013).

The humidity meter and the Al/DNA/Al diode placed in a closed chamber were exposed to irradiation of alpha particles in a controlled humidity environment. The chamber has built-in input and output valves for gas flow. Nitrogen gas was then passed through water and then channeled into the chamber to control and maintain a certain humidity level within the chamber. LCR meter (Instruments Instek LCR-829 LCR Meter) was used to measure the capacitance of the sensor. The in-situ capacitance and resistance values versus RH measurements of the Al/DNA/Al sensor at ambient temperature (25±1°C) were carried-out by placing the device in the hermetically sealed humidity chamber capable of providing a humidity range of 20–99.9% RH. **Figure 3.12** illustrates the experimental setup used for the measurements.

4.6.1 Humidity at Low Doses of Alpha Radiation

Figure 4.42(a) shows the relationship between capacitance and RH within the range from 20 to 99.9%. Measurements were taken for the Al/DNA/Al humidity sensor for non-radiated samples (2, 4, 6 and 8 min of irradiation) at 0.8 KHz and 1 V. We chose the mid-frequency at 0.8 KHz since capacitance decreased with increase in frequency corresponding to the operating parameters of the LCR meter used from the experimental results, the capacitance was observed to increase with higher humidity, which demonstrates sensitivity to humidity in the studied range. Higher water molecule content at high humidity levels increases the dielectric permittivity constant, thereby acting to improve the capacitance of the device (Ahmad et al., 2008; Yamahata et al., 2008). This in turn increases conductivity as a result of the rise in electron transport along the dsDNA helix (Armitage et al., 2004).
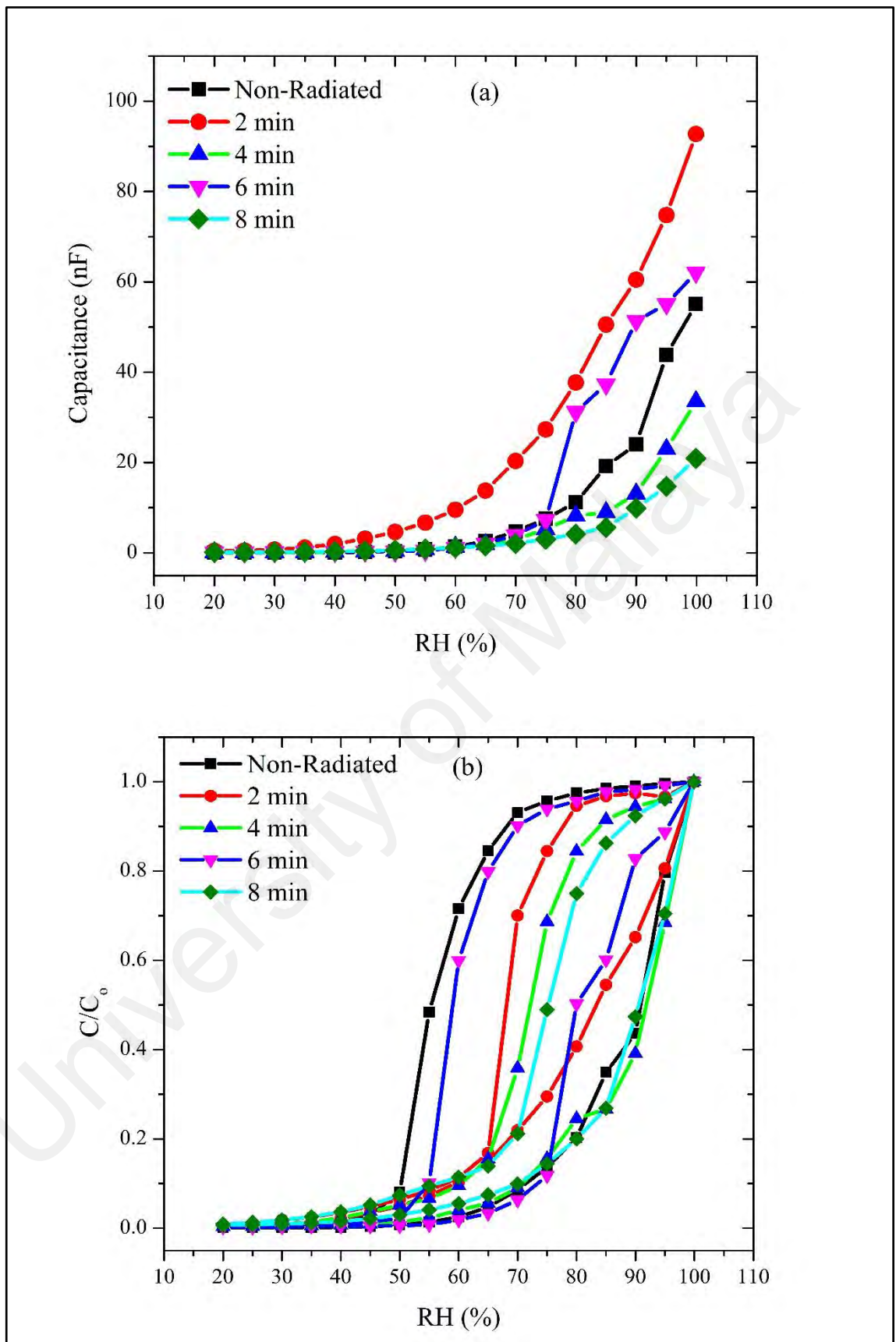
Figure 4.42: Capacitance versus relative humidity for the Al/DNA/Al humidity sensor.

In the case of decreasing humidity, a deviation was observed instead. **Table 4.10** shows the capacitance values in three distinct parts. At 99.9%, the highest capacitance values were 92.736, 62.103 and 55.102 nF for 2 min, 6 min and in non-radiated samples, respectively. For RH of 45%, 2 min registers the highest value (3.1506 nF) followed by 8 min (0.44304 nF) and 4 min (0.30054 nF). This trend changes again at RH value of 20%, where 2 min is the highest followed by 6 and 8 min (0.46463, 0.14945 and 0.1425 nF, respectively). In the last two cases, the non-radiated samples registered the lowest capacitance values contrary to the highest RH environment.

Table 4.10: Capacitance and resistance values registered under different relative humidity.

Irradiation time (min)	Capacitance (nF)			Resistance (KΩ)		
	20%	45%	99%	20%	45%	99%
Non-radiated	0.05894	0.20463	55.102	1678	379.4	6.526
2	0.46463	3.1506	92.736	1512	153.3	1.801
4	0.103	0.30054	33.549	980.3	344.4	9.194
6	0.14945	0.29634	62.103	619.6	287.5	4.017
8	0.1425	0.44304	20.938	905.2	235.1	11.1

At high humidity levels, water molecules play an important role towards improvement in conductivity in which case, the increase in electron transfer along the dsDNA helix may lead to the improvement in charge conduction. The charge transfer phenomena may therefore play an important role in the sensing mechanism, which could have primarily lead to the insignificant base-line shift and faster recovery time. This change in the electrical properties of the Al/DNA/Al structure due to the change in RH may therefore be generally attributed to the absorption of water molecules and the

increase of the number of holes due to tracks made by the alpha particles upon bombardment.

In is known that alpha particles lead to primary and secondary ionizations in atoms upon interaction. These processes in turn produce several types of ions and excited molecules in cells ultimately causing intermolecular bond biomolecule cleavage. Cleavage occurs within the cytoplasm and other intracellular components besides the cell nucleus. As such, the DNA molecule being double stranded in nature, exhibits cleavage in one or both the strands. The DNA molecule has characteristic capability to repair single-strand damage; but a scission in double-stranded DNA repair to its original form is not trivial. However repair of double-stranded scission of the DNA molecule may cause gene mutations as a result of the exposure to radiation (Knapp & Dash, 2016).

Figure 4.42(b) shows the relationship between capacitance-RH within the range of 20 to 99.9%. The non-radiated samples showed a significant increase with increasing humidity with a maximum at 75%. After which, the values begins to drop dramatically and the irradiated samples now register higher capacitance values. The sample irradiated for 2 min (92.736 nF) registers higher value compared to 6 min (62.103 nF) and 4 min (33.549 nF).

The relationship between humidity and the resistance within the range from 20 to 99.9% RH is demonstrated in **Figure 4.43**(a). Here the resistance decreases with increasing humidity, which clearly depicts the sensitivity to humidity in the studied range. Generally, the highest value was observed in the non-radiated samples in the 20 to 45% RH range, followed by samples irradiated for 2 and 4 min. In the case of decreasing RH environment (99.9-20%), the non-radiated samples still record the highest values until 30% RH. However, samples radiated for 8 min registers a higher resistance value in the 35-99.9% range. All other irradiated samples demonstrate higher

values compared to the non-radiated samples in the 50-75% range. **Figure 4.43** demonstrates the trend for the resistance with RH, which shows a clear variation between the range 45-75% RH. The trend in the resistance and capacitance can also be observed clearly above 45% RH as shown in **Table 4.11**.The readout of the resistance values obtained from the device in response to the RH values was also achieved (**Figure 4.43**(a)), which demonstrated the exponential decrease in the resistance values relative to the increasing RH. The ionic dissociation of the water molecules may have led to this phenomenon that acts to increase the film conductivity. Capacitance values initially increased gradually within the range 20-40% RH, followed by rapid rise within 45-99.9% range as shown in **Figure 4.43**(b) depending on irradiation time (**Table 4.10**).

As discussed, the resistance in general decreased exponentially (**Figure 4.43**(a)), while the capacitance increased following a S-shape demonstrated in **Figure 4.43**(b). This could be attributed to the charge transfer mechanism between the DNA and the water molecules. The observed changes in the mechanism results from the decrease in resistance in response to increase in H_2O molecule concentration and displacement currents and the concentration of charge carriers doped by water molecules (Kh S Karimov et al., 2012), which causes an exponential variation of conductance of the DFC nanotube networks with the RH. This is in contrast to observation by Paul et al. in 2013, who in their work indicated that the reason for the low output signal current from the networks may be due to it being unsuitable for use in low RH sensors (Paul et al., 2013) . Since the output signal current of the detector rises exponentially with increase in RH, the device display elevated sensitivities especially at higher RH.
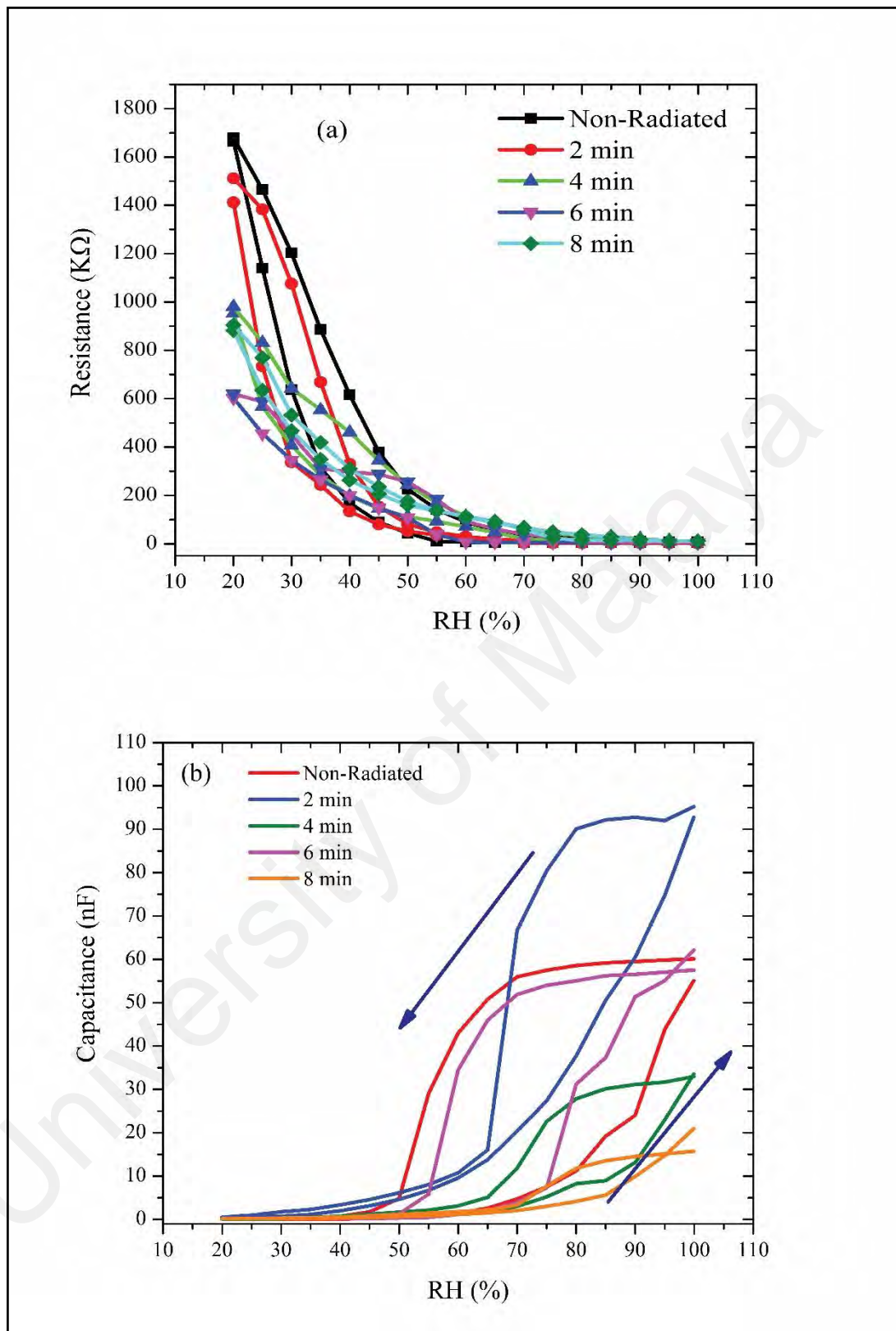
Figure 4.43: Relation between the capacitance and resistance with humidity for the Al/DNA/Al junctions.

Table 4.11: Sensitivity values and other parameters measured for the Al/DNA/Al Schottky barrier diode type humidity sensor.

	Non-radiated	2 min	4 min	6 min	8 min
Slope a (arbitrary)	0.02773	0.04214	0.03356	0.03889	0.03068
b (1/RH%)	−2.8779	−4.12762	−3.40147	−3.81196	−2.90167
Adjusted R-square	0.99023	0.99199	0.98588	0.93011	0.98775
Sensitivity (nF/RH%)	0.6889	1.15484	0.4112	0.77539	0.26027

The resistance meanwhile decreased exponentially and was attributed to adsorption of water molecules by the DNA. This change can again be explained as follows. Consisting of three portions; which are the bases, sugars and phosphoric acids, the hydrophilic phosphoric acid around the base pairs of DNA caused the water molecules to be easily absorbed and form hydrogen bonds between the phosphoric acid and the water molecules. Resistance values quickly decline as the RH increases and tend to saturate for humidity above 99.9%. These phenomena agree with ionic conduction at higher humidity scale. The decline of resistance with increasing humidity meanwhile displays sensitivity to humidity within the studied range. Electronic instrument features are significantly affected by adsorption of water molecules on the surface of the DNA film being the active layer. Water molecules adsorbed on the surface of the Al/DNA/Al film have great dipole momentum, which leads to the increase of the charge carrier density (Aziz et al., 2011). Number of alpha particle tracks acting as micro scale pores shown in **Figure 4.44** also plays a vital role in the charge conduction upon easy absorption of water molecules, which in turn decreases the resistance of the device.
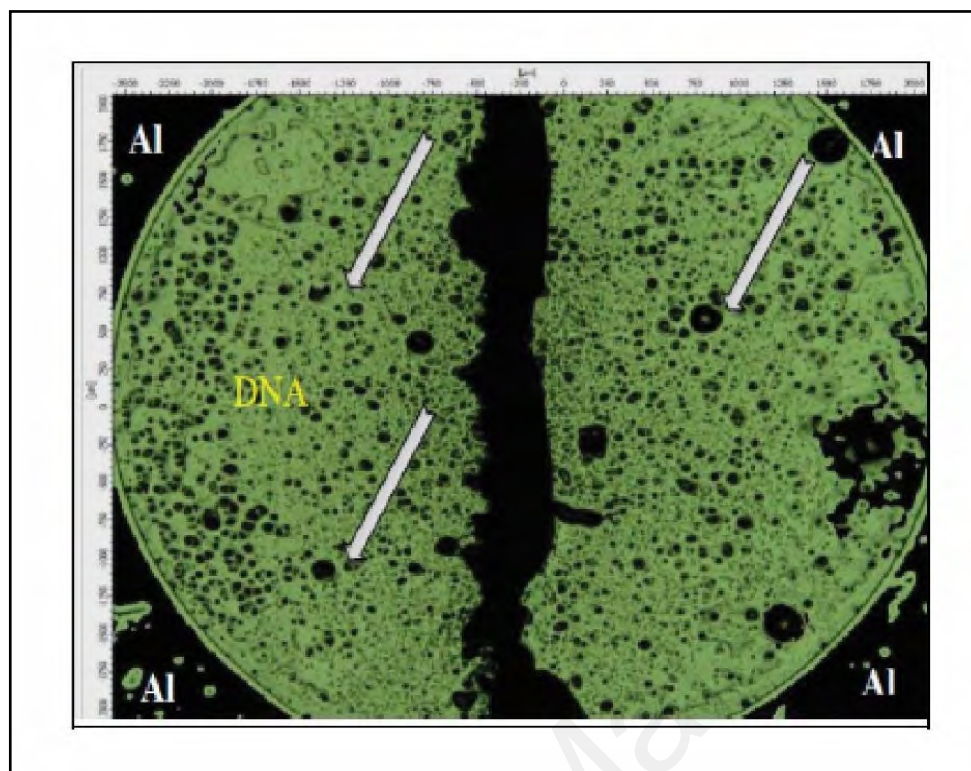
Figure 4.44: Optical microscope (Infinite Focus, Alcona, Austria) image showing the number of alpha particle tracks on the Al/DNA/Al sensor after irradiation.

Otsuka and colleagues studied the humidity influence on the electrical conductivity of DNA thin film (Otsuka et al., 2002). They observed that the ionic conduction was overcome by the electrical conduction. The capacitance values increasing with the increase in RH% indicated the proton transfer through the physically adsorbed layer of water, which improved with increasing humidity. At higher RH, the proton conductivity dominates the ionic conduction. As RH increases, intermolecular conductivity was increased rapidly mainly due to the increase of local dielectric constant (Ha et al., 2002). In the latter case, the exponential dependence of the conductivity was attributed to the adsorption of water molecules on the nanostructured film surfaces. As a result of the current increasing with humidity, it is believed that the charge carriers are the H^+ and OH^- species produced by water adsorption. The ions separate and recombine according to the Grotthus mechanism, which describes the

passing of protons through the cooperation of neighboring water molecules (Kumemura et al., 2007).

Figure 4.45(a) demonstrates the sensitivity of the pre and post-radiated Al/DNA/Al junctions in the RH range of 20-99.9%. The sensitivity showed an exponential behavior upon increase in the RH value. Highest value was observed at 2 min, while significant increase in sensitivity was observed for 6 min under 75% RH. Humidity detecting capabilities of this type of capacitive device rely on factors such as the gap between the electrodes and the area of the electrodes (Farahani et al., 2014). The Al/DNA/Al device can be considered as a surface plate capacitor, assuming that the face edges of the electrodes act as parallel layers. As such, the capacitance of the sensor can be measured using the following method (Azmer et al., 2015; Karimov et al., 2015; Yaworski & Detlaf, 1968).

$$C_{eq} = C_o = A\varepsilon\varepsilon_o/d \tag{4.11}$$

where C_o is the initial capacitance, ε represents the relative dielectric constant, ε_o the absolute permittivity, A is equal to the area of the surface and d the distance between the electrodes. Equation (4.12) meanwhile expresses the capacitance influenced by the humidity effect. This equation can also be obtained by fitting the sensor under higher humidity levels;

$$C = A\varepsilon\varepsilon_o\left(1+m_1H\right)/d\left(1-m_2H\right) \tag{4.12}$$

where H is the relative humidity level and m_1 and m_2 are the constants. In the case of relative capacitance, Equation (4.12) can be rewritten as;

$$C/C_o = \left(1+m_1H\right)/\left(1-m_2H\right) \tag{4.13}$$

From Equation (4.13), the following simple equation can be derived;

$$C/C_o = aH + b \tag{4.14}$$

Figure 4.45(b) shows the experimental and simulated results where the latter results were calculated using Equation (4.14). Table 4.11 lists the sensitivity and value

(*a*) of the slope in **Figure 4.45**(b) and the value *b* from Equation (4.14) for both the non-radiated and radiated structures (2, 4, 6 and 8 min).
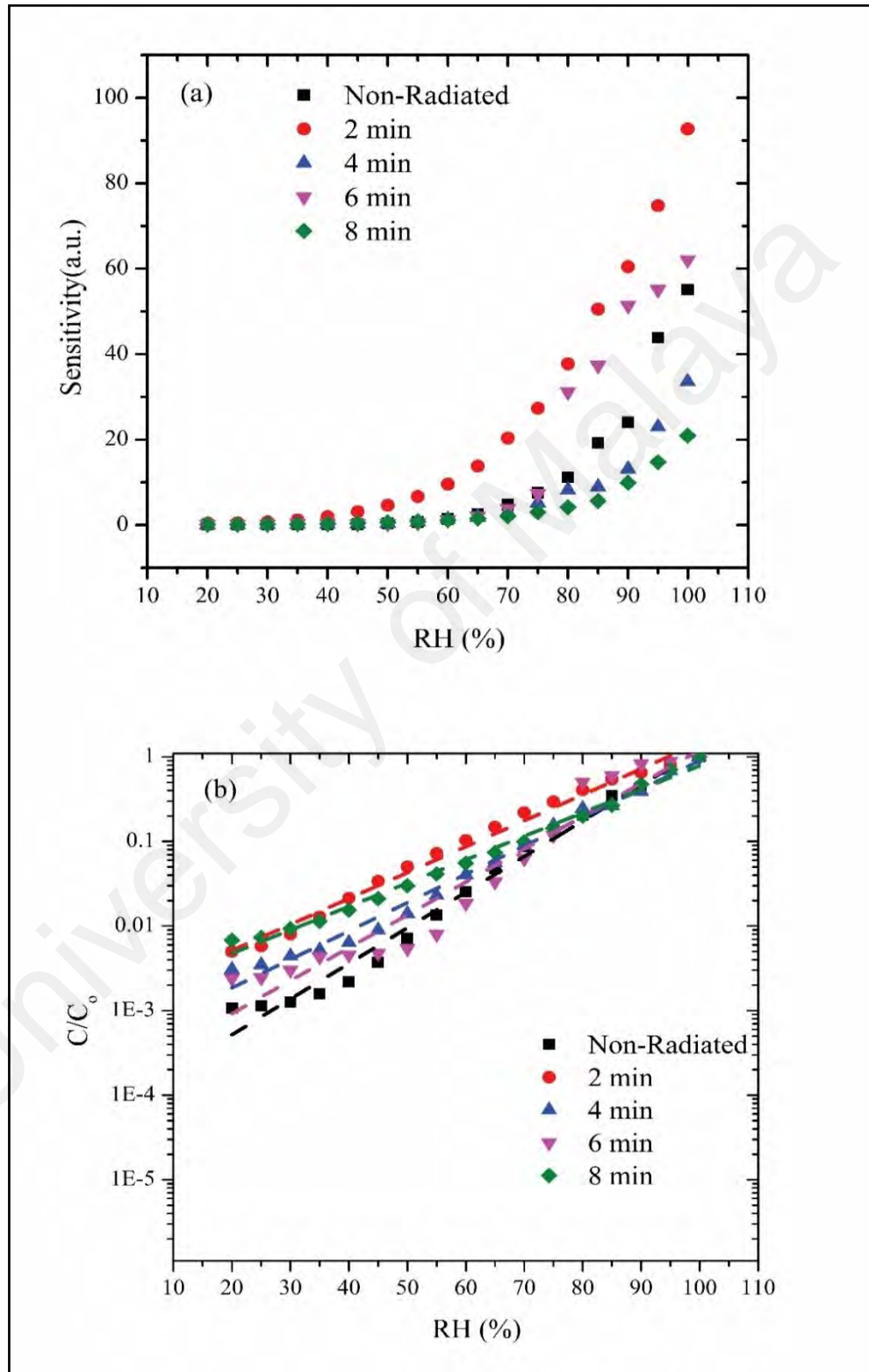
Figure 4.45: Graph (a) demonstrates the sensor's sensitivity and (b) shows the results for the capacitance-humidity relationship of the Al/DNA/Al humidity sensor.
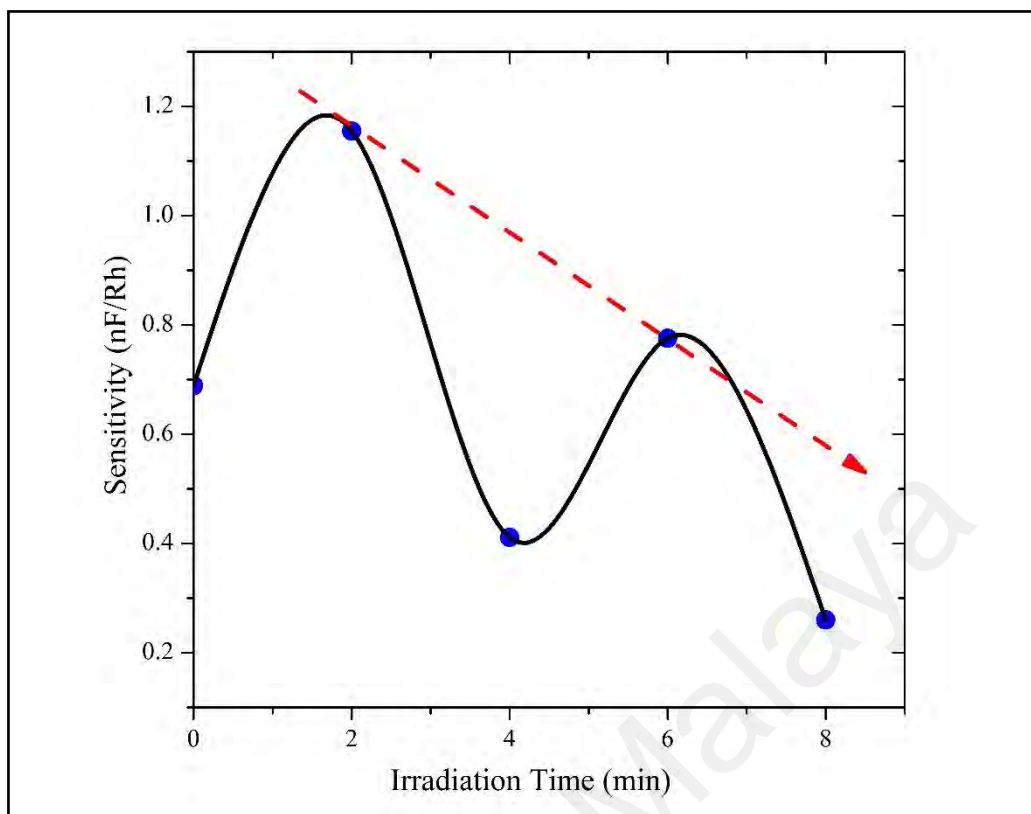
Figure 4.46: Graph demonstrates the relationship between sensitivity and irradiation time.

Figure 4.46 demonstrates the relationship between sensitivity and irradiation time. It shows that sensitivity fluctuates with alpha radiation time and possibly the occurrence of the hypersensitivity phenomena indicated by the drop in sensitivity at 4 min. At this point, the DNA seeks to self-protect itself against the radiation and humidity effects probably as depicted by the survival curve phenomena demonstrated by Ta'ii et al (H. M. Al-Ta'ii et al., 2009) and others (Chiu et al., 1982; Joiner et al., 1996).

The dielectric constant from the fits made from Equation (4.14) was calculated and tabulated in **Table 4.12**. Values for the dielectric constant were calculated at RH=50% for all the samples (Leveritt et al., 2009), which was observed to peak at irradiation times of 2 and 6 min. It is expected that upon initial exposure to alpha particles, a deviation from the general dielectric constant value (in this case, about 5.73) could be observed. A maximum value of 8.21 is calculated at irradiation time of 2 min,

which indicates the onset of DNA damage. It is understood that tracks are formed upon bombardment of alpha particles. These tracks involve an increase in the number of charges due to the linear energy transfer (LET) from the alpha particle (H. M. J. Al-Ta'ii et al., 2015; H. M. J. Al-Ta'ii et al., 2015b; Knapp & Dash, 2016). As a result of a large number of material excitation by these particles along its path, an increase in the number of charges can be expected. This in then increases the dielectrical constant as shown at 2 min of irradiation. Further irradiation however may initiate the self-repair mechanism within the DNA structure, effectively undergoing recombination. This is calculated as a decrease in the dielectric constant at 4 min of irradiation. These processes were continued accordingly with further irradiation until 8 min, where the dielectric constant becomes almost the same as with the non-radiated DNA (**Figure 4.47**).
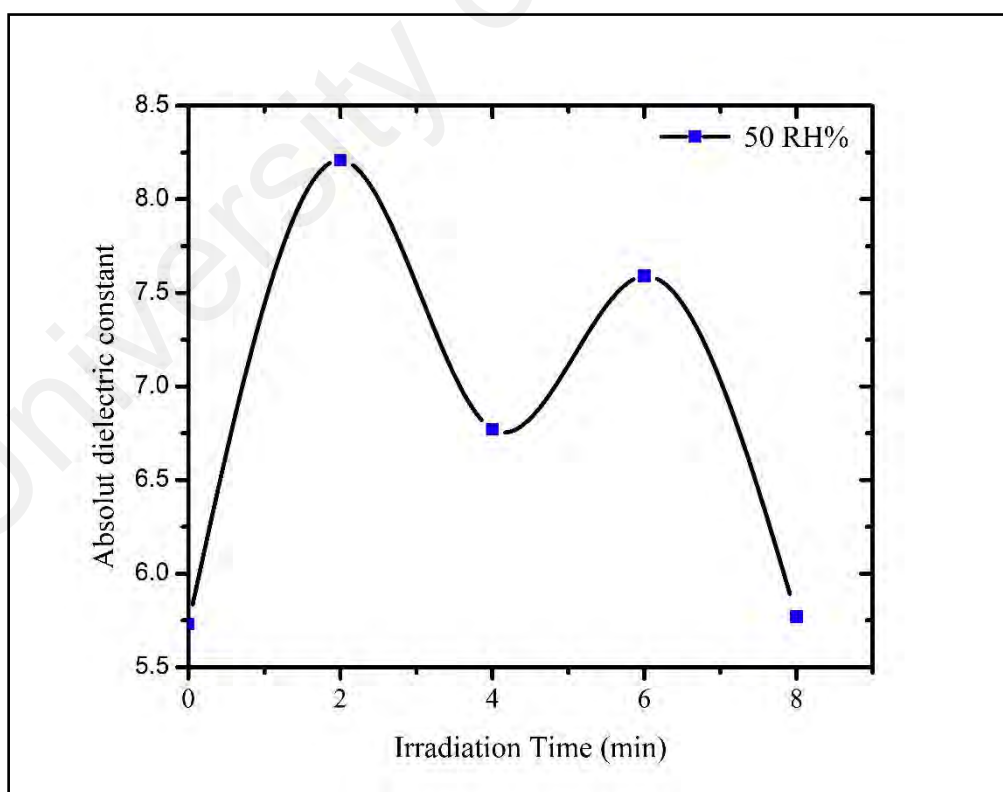
Figure 4.47: Variations in the dielectric constant of DNA with irradiation time.

Table 4.12: Dielectric constant for DNA exposed to different irradiation time.

Irradiation time (min)	Slope (arbitrary)	Absolute dielectric constant	Log (dielectric constant)
0	0.02771	5.73	0.75800
2	0.04214	8.21	0.914
4	0.03356	6.77	0.8305
6	0.03889	7.59	0.8799
8	0.03068	5.77	0.76

Surface morphology of the Al/DNA/Al thin films was examined using AFM and shown in **Figure 4.48**. The "spongy" looking film surface consists of water molecules due to absorption and numerous tracks resulting from the alpha particle irradiation. This also ensures efficient distribution of the water molecules and therefore increases electrical response to the humidity. To evaluate the performance of the Al/DNA/Al sensor, its response and recovery behavior can be examined experimentally, which is considered one of the most significant features for evaluating any type of sensors (Azmer et al., 2015; Bi et al., 2013; Yanyan Zhang et al., 2008).

The profiles in **Figure 4.48** demonstrate the capacitive response of the Al/DNA/Al structure exposed to a fast variation of humidity (5-95% RH), which was observed to be rapid. Electrical response of the sensor becomes unstable when exposed to a RH value of 95%, followed by a rapid and sharp change back to its unique values within 5 s upon replacing the tested vapor condition. Response and recovery time characteristics of the Al/DNA/Al sensor were measured at a frequency of 800 Hz under a RH condition of 5%. According to the graphs in **Figure 4.49**, the sensor response time (humidification from 5% to 95% RH) was 26 s. The relative capacitance of the sensor increased from 4.0 (5% RH) to 1188 nF (95% RH). When exposed to the maximum humidity of 95% RH, values observed were 106, 420, 34, 55 and 1188 nF for the non-radiated, 2, 4, 6 and 8 min, respectively, while the recovery time (drying effect, 95 to

5% RH) was 78 s. Both types of responses (humidification and drying) illustrates obvious changes due to some hysteresis effect (Li et al., 2004). These changes are highly dependent on the thickness of the structure (Chani et al., 2012) and may also be attributed to permanent structural defect due to the alpha irradiation.
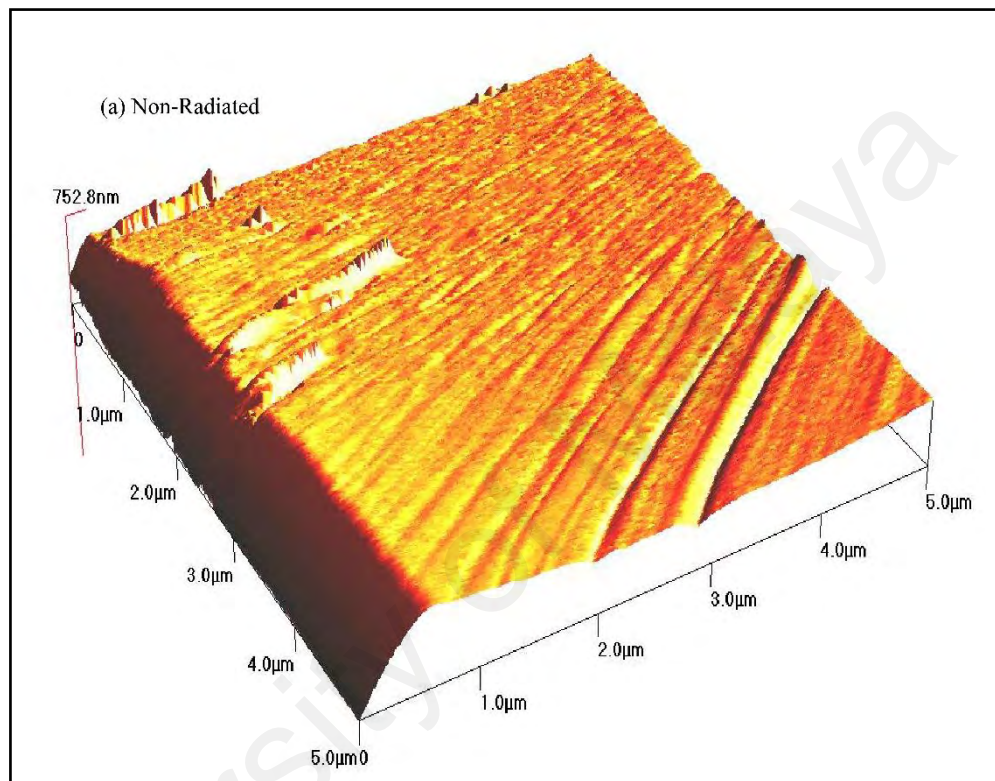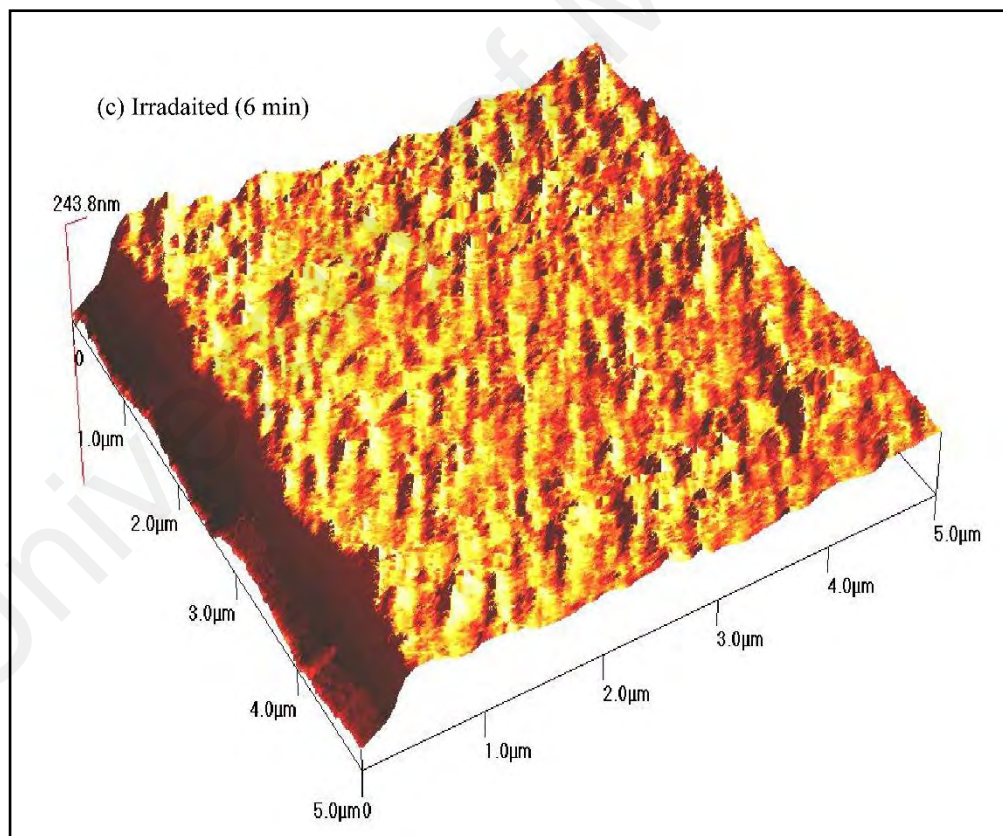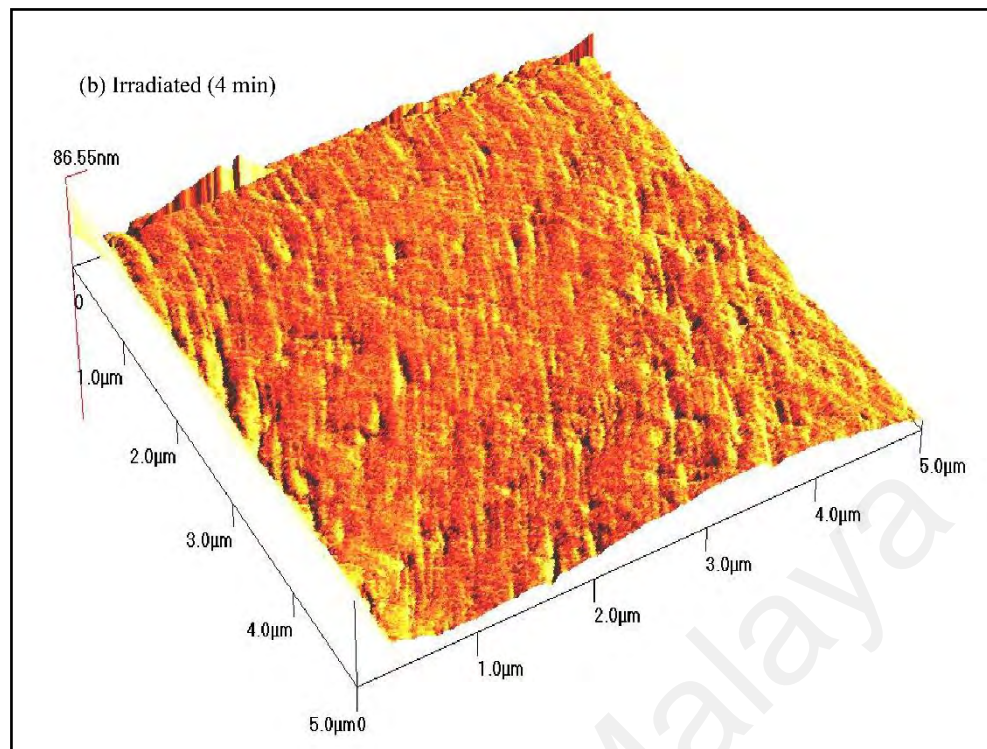
Figure 4.48: AFM images of (a) non-radiated and (b), (c) radiated Al/DNA/Al sensors.
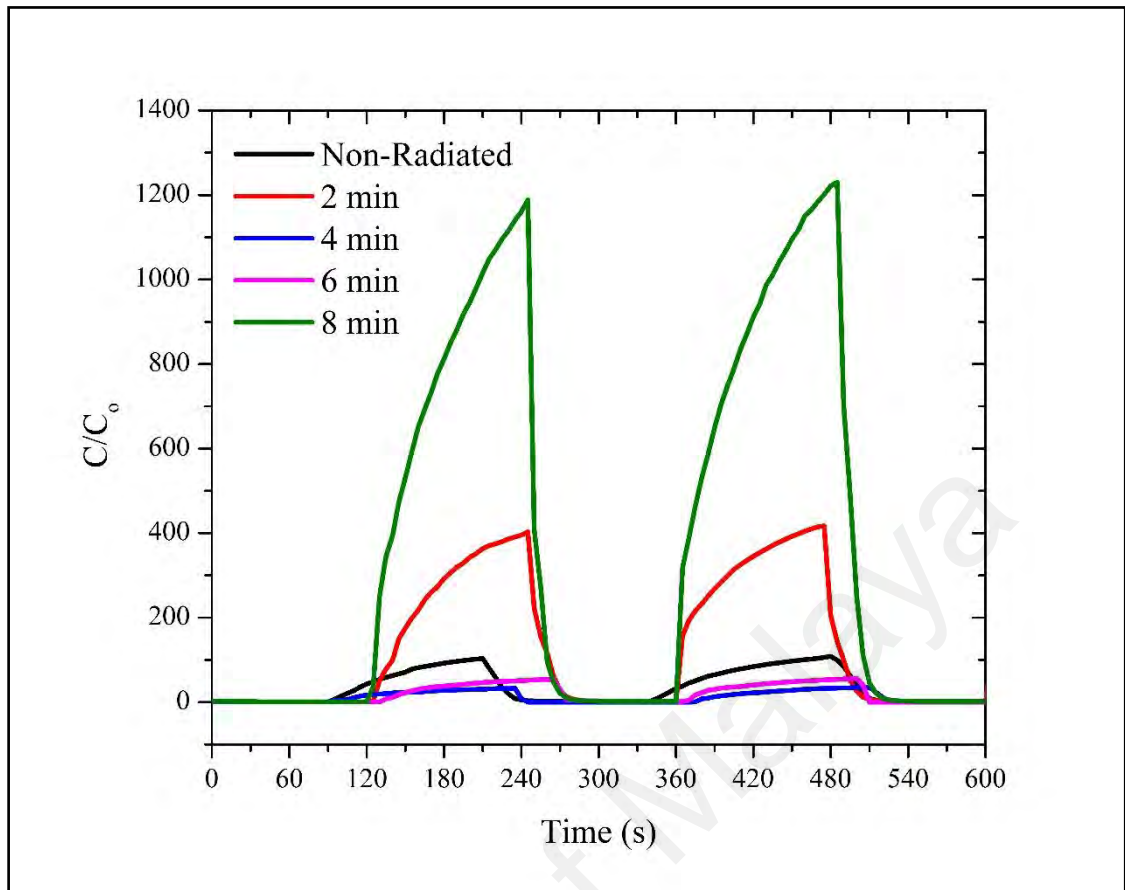
Figure 4.49: Response-recovery graph for the Al/DNA/Al humidity sensor.

The electrical characteristics of the Schottky barrier height connections are very sensitive to the features of the metal-semiconductor (MS) interface. As such, the I–V characteristics of the connection are suitable displays of the interface features. For a Schottky barrier diode, the thermionic emission theory predicts that the I–V characteristics at forward bias V are given by Equations (4.1) and (4.2) (Tuğluoğlu & Karadeniz, 2012).

Figure 4.50 provides the I–V characteristics of the fabricated Al-Al and Al/DNA/Al Schottky barrier diodes under normal (a) and high (b) humidity conditions. The profiles demonstrate highly rectifying behaviors with the presence of the DNA as observed from all the profiles. Al-Al structures clearly show an Ohmic behavior further confirming the rectifying nature of the DNA layer.

The ideality factor determined from the slope of the linear region of the forward bias (ln(I)–V) characteristics through the relation in Equation.(4.3) is as already discussed, a measure of conformity of diode to pure thermionic emission (R. K. Gupta & Yakuphanoglu, 2012; V. R. Reddy et al., 2011). The ideality factor of the Al/DNA/Al junctions was larger than unity in the present work. An ideality factor greater than unity can be generally attributed to the same reason as discussed earlier. These includes the presence of a bias dependent distribution of low SBH patches (or barrier inhomogeneity), re-arrangement of electrons and holes in the depletion regions and bias dependence of voltage of SBH (Sze & Ng, 2006), the thickness of organic film (Karataş & Türüt, 2004), series resistance (Aydoğan et al., 2008) and temperature (Cheung & Cheung, 1986). **Figure 4.50** demonstrates the fact that DNA is the sensing element and not the Al metal. The ideality factor shows fluctuations of Al/DNA/Al based junctions fabricated in this work under the humidity condition calculated using Equation (4.3).

Figures 4.50 and **4.51** represent the forward and reverse I–V characteristics of the Al/DNA/Al Schottky diode before and after alpha irradiation under different humidity conditions (76, 99.9% RH). It is found that both forward and reverse current generally increases after the irradiation. The results of **Figure 4.50** agrees with another previous work (Jo et al., 2003) obtained under different humidity conditions. Highly rectifying curve and inverted S shape in this work at high RH are clearly attributed to water molecules adsorbed by the DNA. Dielectric constant increases lead to the increase of the ionic conduction and enhances the dissociation of water to H^+ and OH^- and the different mobility between H^+ and OH^- (Ha et al., 2002). The formation of electrical double layer through the redistribution of ions at the contacts between DNA molecules and electrodes leads to the highly nonlinear behavior seen on the I–V plots. Increasing RH also acts to increase the hysteresis (Ha et al., 2002), which can be attributed to the increase in reverse current with dose as a result of generation of carriers in the bulk

depletion region. Lattice defects are also induced due to the reverse current, which is proportional to the concentration of minority carriers near the junction.

The values of series resistance are calculated from the junction resistance formula $R_S = \partial V/\partial I$ from the I–V features of the diode. The series resistance (R_S) versus voltage of the surface type Schottky diode is demonstrated in **Figure 4.52**. From the figure, it can be concluded that at low voltages (≤ 2.0 V), R_S values were the highest for 8, 2 and 6 min, respectively in reducing order, followed by the sample radiated for 4 min and non-radiated at 76% RH. At 99.9% RH meanwhile, the series resistance values were the highest for 8 min, non-radiated and 2 min in reducing order followed by the sample radiated for 4 and 6 min. However above 2.0 V, the series resistance values become insignificant as shown in the **Table 4.13.**

From **Figure 4.52**(a,b), the shunt resistance becomes the highest at 1.0 V for all the samples and under the humidity condition. However, from **Figure 4.52**(c), the series resistance at 99.9% RH reduces compared to at 76% RH due to the increase in H_2O molecules.
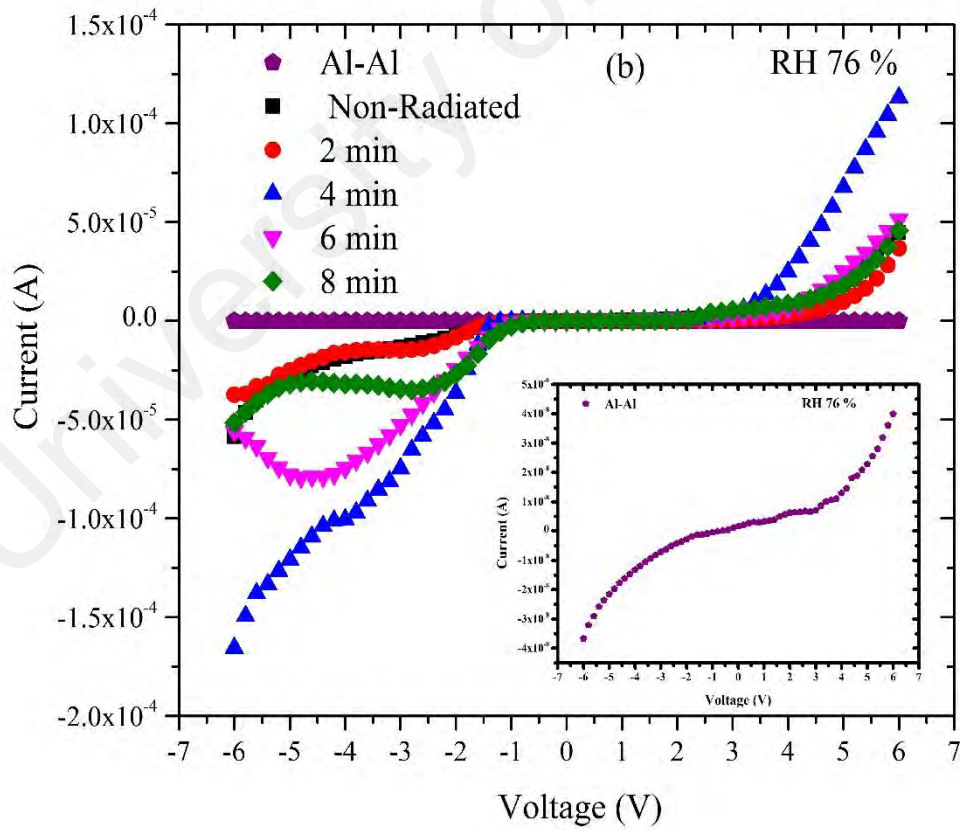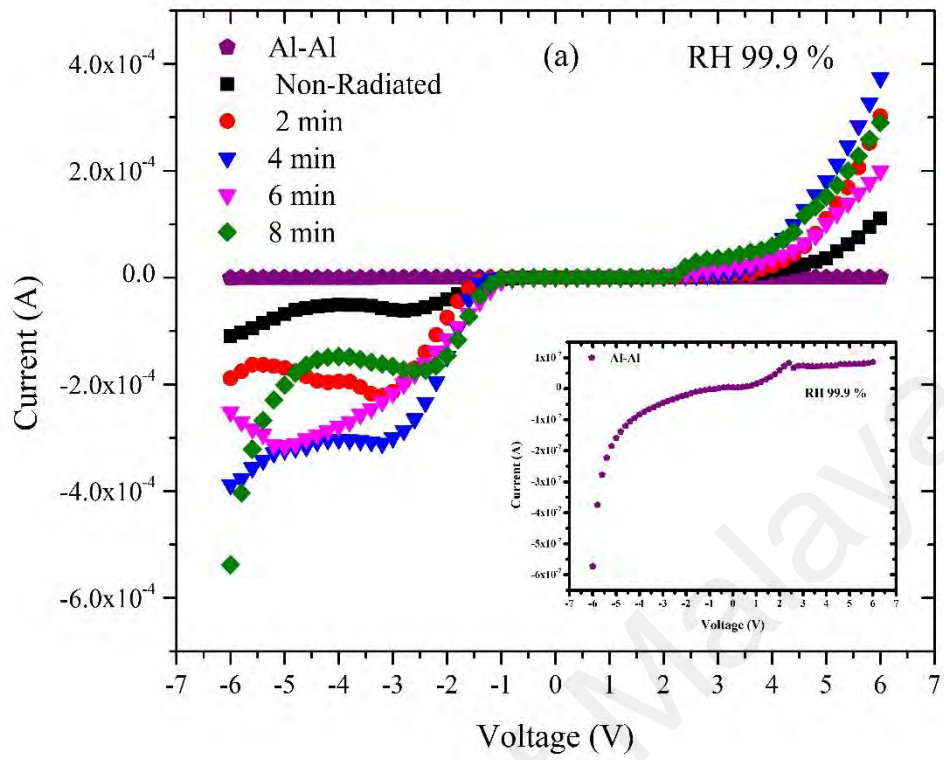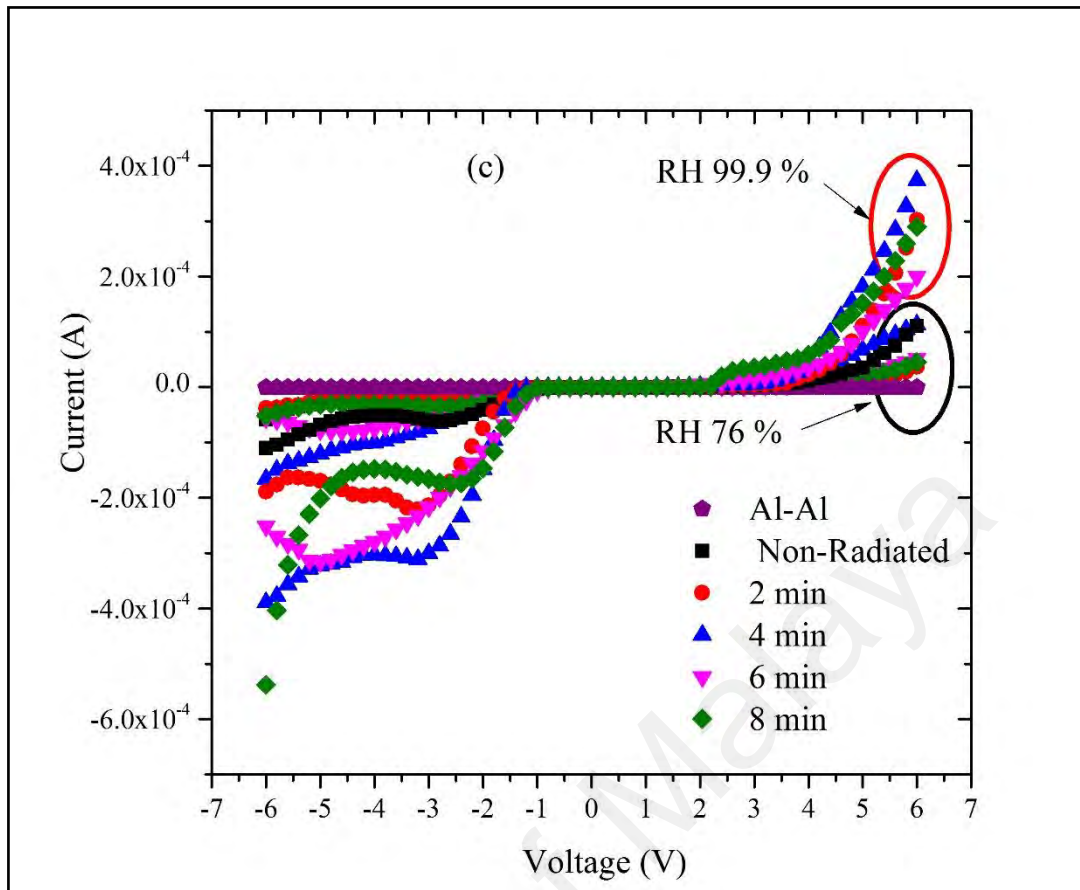
Figure 4.50: Graphs demonstrate the relationship between current and voltage under different humidity conditions; (a) RH 99.9%, (b) RH 76% and (c) RH 99.9 and 76%.
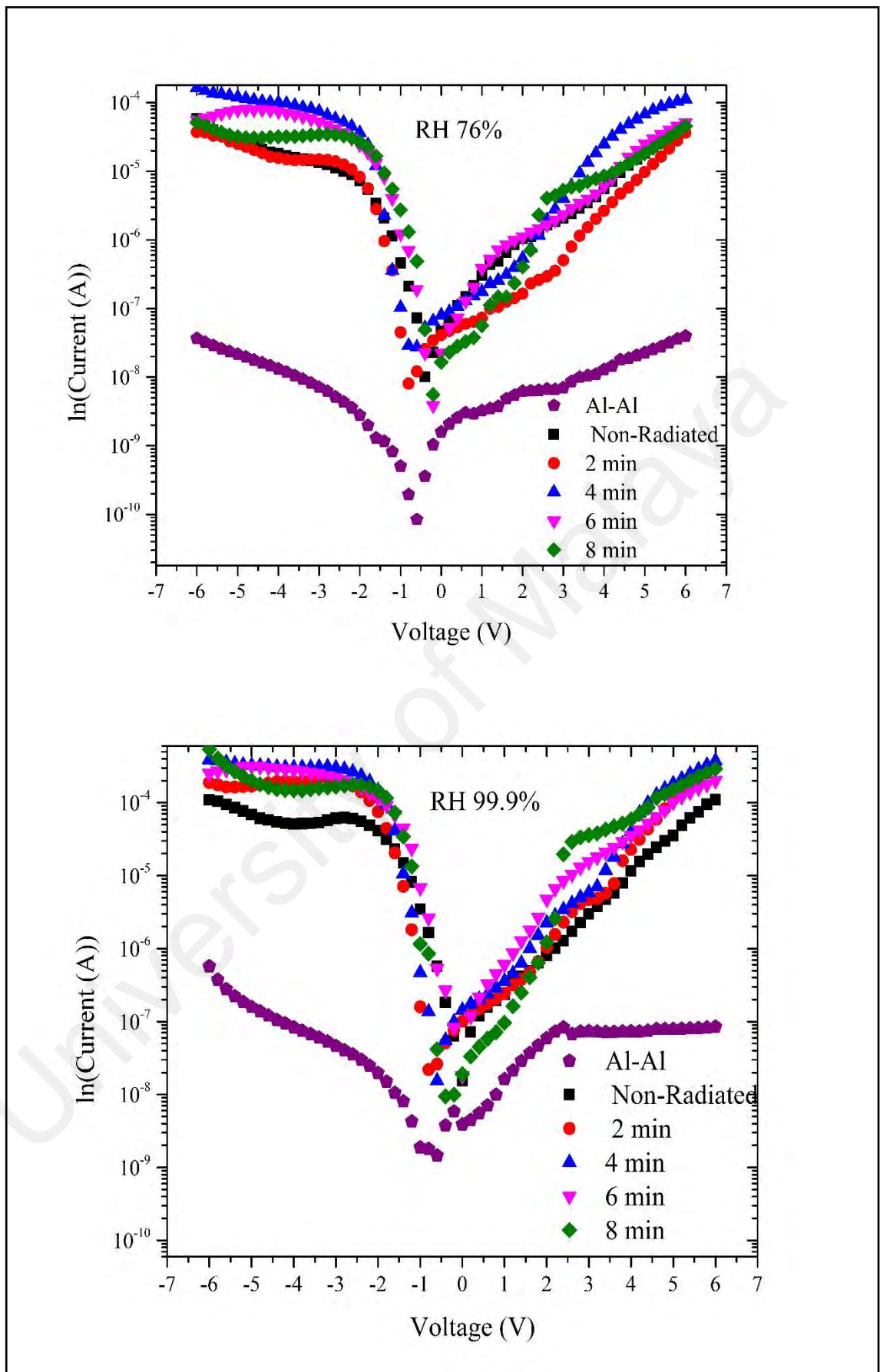
Figure 4.51: Profiles demonstrate the relation between the ln I–V under the irradiation effect and humidity condition.

According to Ha et al, the electronics properties of DNA such as the I–V profiles are generally influenced by the contact, bulk (DNA channel) and intermolecular features under humidity effect (Ha et al., 2002). It could be also assumed that the majority of response is initiated by the Schottky metal (Al)-semiconductor (DNA) contact.

Figure 4.53 shows the tracks of alpha particles on the DNA film irradiated for 2 min using a FESEM. The tracks seen in the image are similar to pores, agreeing well with the honeycomb structure that has been demonstrated for its' potential applications in electronic, optical and micromechanical devices (Masuda & Fukuda, 1995; Varghese & Grimes, 2003).
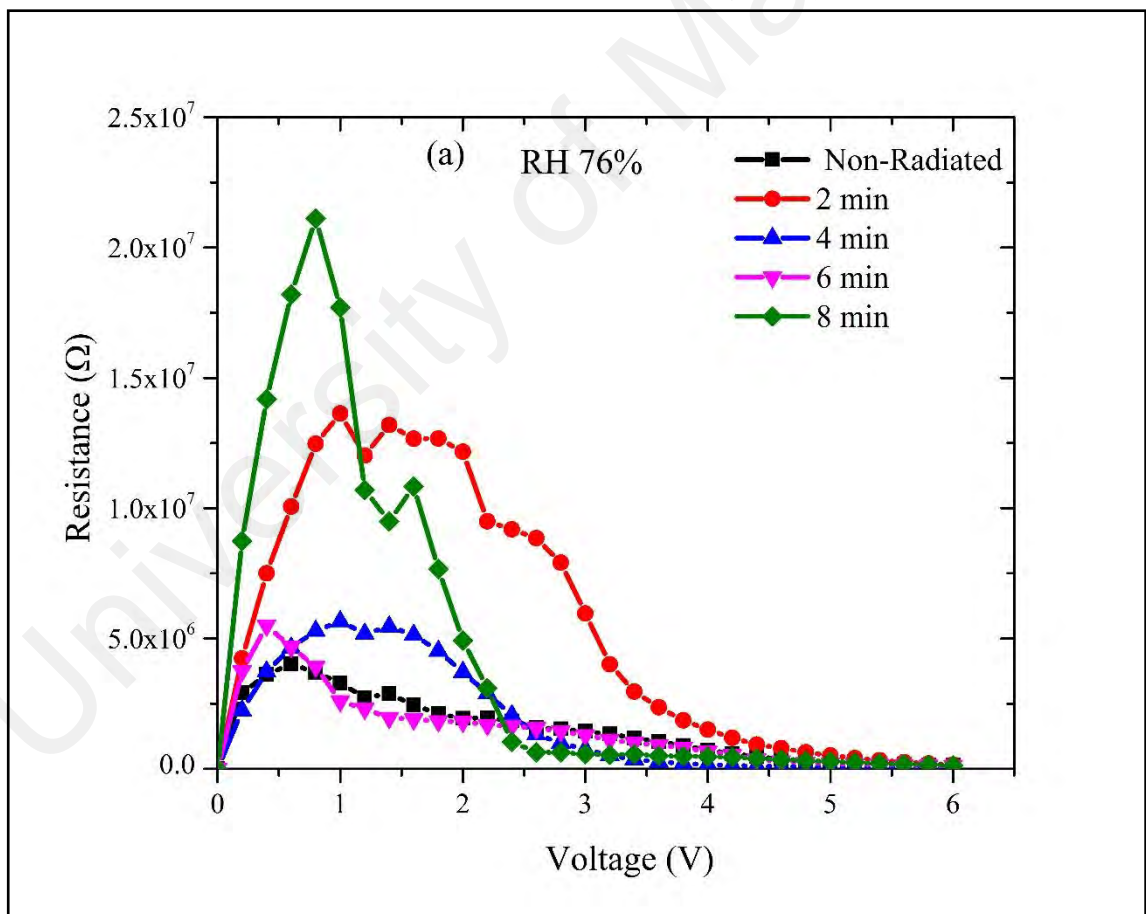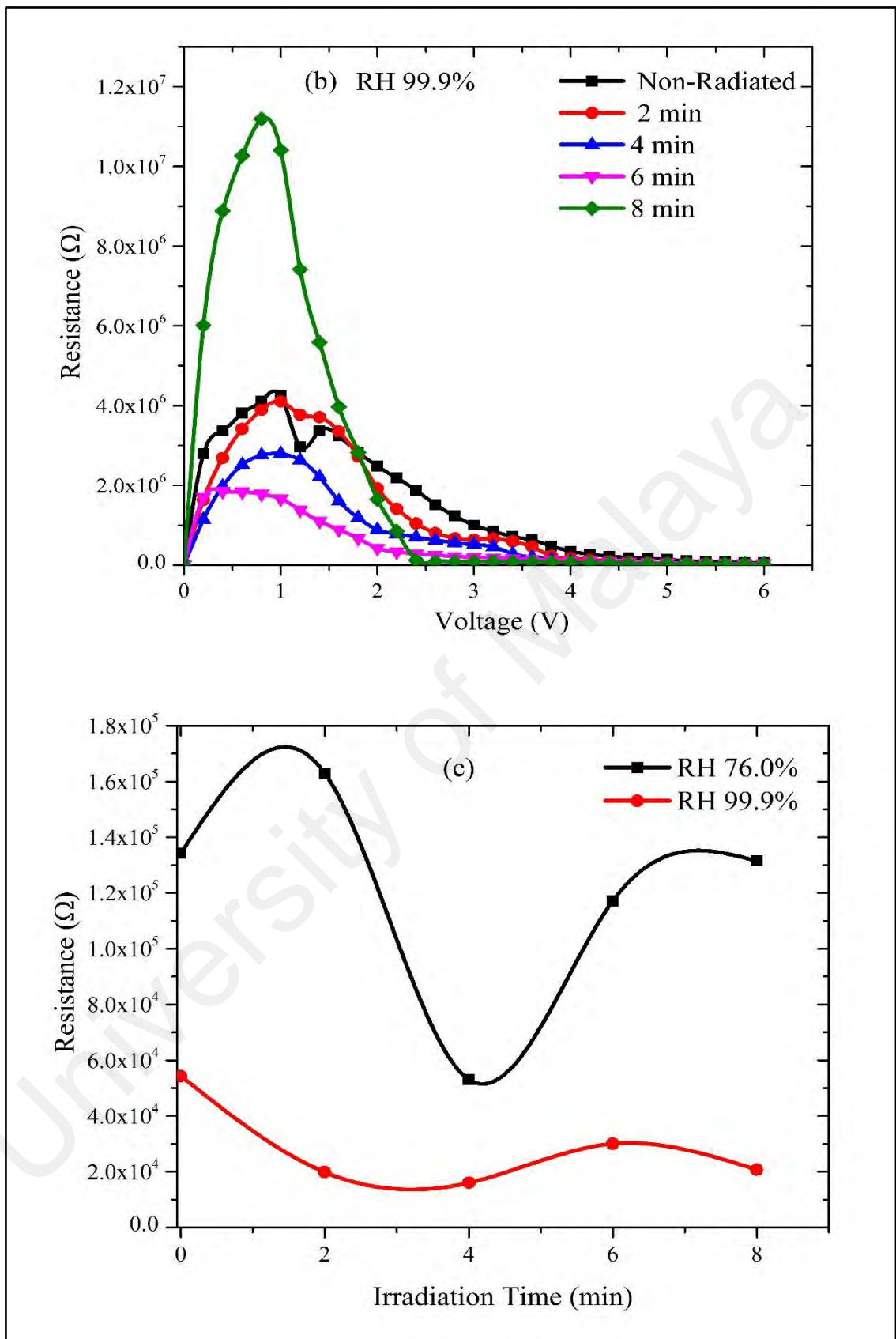
Figure 4.52: Profiles in (a) shows the relationship between the resistance and the voltage at 76% RH, (b) demonstrates the behavior of resistance against voltage at 99.9% RH and (c) the relation between the series resistance and irradiation time for 76 and 99.9% RH.

Table 4.13: Table lists the values of the Schottky diode parameters calculated for the Al/DNA/Al fabricated in this work.

Irradiation time (min)	n		Φ (eV)		Rs (KΩ)	
	RH76%	RH 99.9%	RH76%	RH 99.9%	RH76%	RH 99.9%
0	1.041	1.096	0.581	0.581	134.237	54.333
2	1.001	1.170	0.715	0.647	162.947	19.862
4	1.030	1.306	0.633	0.603	53.076	16.049
6	1.120	1.233	0.609	0.586	117.129	30.034
8	1.893	1.252	0.729	0.631	131.489	20.682
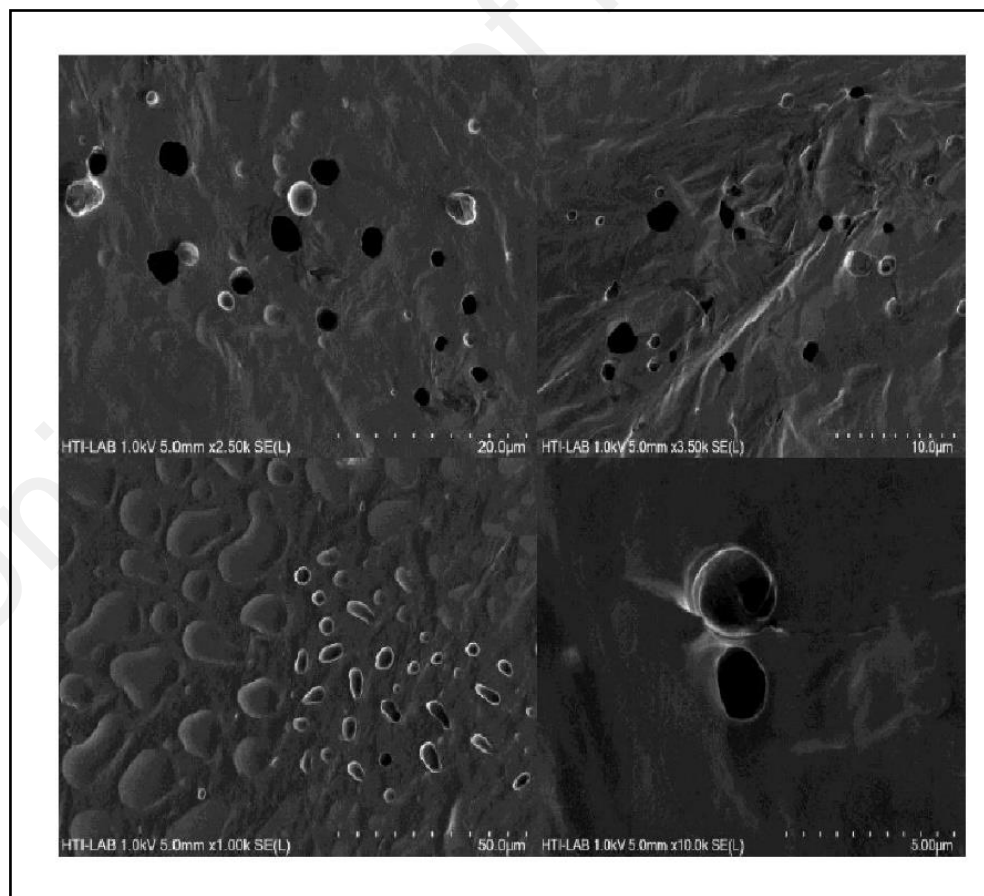
Figure 4.53: The alpha particle tracks on DNA film irradiated for 2 min.

4.6.2 Humidity at High Doses of Alpha Irradiation

Figure 4.54(a) shows the relationship between capacitance and RH within the range from 20 to 99.9%. Measurements were taken for the Al/DNA/Al humidity sensor for non-radiated and radiated (10, 20, 30 and 40 min) samples at 0.8 KHz and 1.0V. From the experimental results, the capacitance was observed to increase with higher humidity, which demonstrates sensitivity to humidity in the studied range. Higher water molecule content at high humidity levels increases the dielectric permittivity constant, thereby acting to improve the capacitance of the device (Ahmad et al., 2008; Yamahata et al., 2008). This in turn increases conductivity as a result of the rise in electron transport along the dsDNA helix (Armitage et al., 2004).

Table 4.14: Capacitance and resistance values registered under different relative humidity.

Irradiation time (min)	Capacitance (nF)			Resistance (KΩ)		
	20%	45%	99%	20%	45%	99%
0	0.059	0.205	55.102	1678	380	6.526
10	0.029	0.119	16.357	2949	525	10.210
20	0.028	0.156	28.071	2813	470	6.684
30	0.032	0.056	9.466	9999	2004	17.030
40	0.097	0.905	31.617	692.5	103	5.383

In the case of decreasing humidity, a deviation was observed instead. **Table 4.14** shows the capacitance values in three distinct ranges. In the range 99.9%, the highest capacitance values were 55.102, 31.617 and 28.071 nF for non-radiated, 40 and 20 min samples, respectively. For RH of 45%, 40 min registers the highest value (0.90475 nF) followed by non-radiated (0.20463 nF) and 20 min of radiation (0.15522 nF). This trend changed again at the RH value of 20%, where 40 min is the highest followed by non-

radiated and 30 min (0.09613, 0.05894 and 0.03142 nF, respectively). In the last two cases, the 30 min samples registered the lowest capacitance values contrary to the highest RH environment. This deviation occurred during the decline in the RH% level, whereas the capacitance of the device reduced due to desorption of water molecules. The results presented in **Figure 4.54(**b) demonstrate that during the reversal, the capacitance does not follow the same behavior causing the hysteresis cycle.

The hysteresis is common in adsorption based humidity sensors. Some factors contributing to this effect are porous structure and surface morphology of the sensing layer (Islam & Saha, 2006). As a result of this deviation, the hypersensitivity phenomena can be indicated. The occurrence of the hypersensitivity phenomena results in the DNA gaining some resistance or self-protection after irradiation. The effect involves additional breaks in the sugar-phosphate molecular chains. These breaks might also result in further separation to occur in the DNA chains, threatening the life of the cell.

Hysteresis occurs as a result of the ratio between the response observed during increasing and decreasing (reversal) RH values. This factor is considered significant to establish the absorption principle for the humidity sensor. The formation of clusters of absorbed water, pores size, film thickness and the deviation in pores geometry with RH leads to the hysteresis. Sensitivity and response time were found to decline due to the large pore size (Li & Yang, 2002; Sakai et al., 1996).
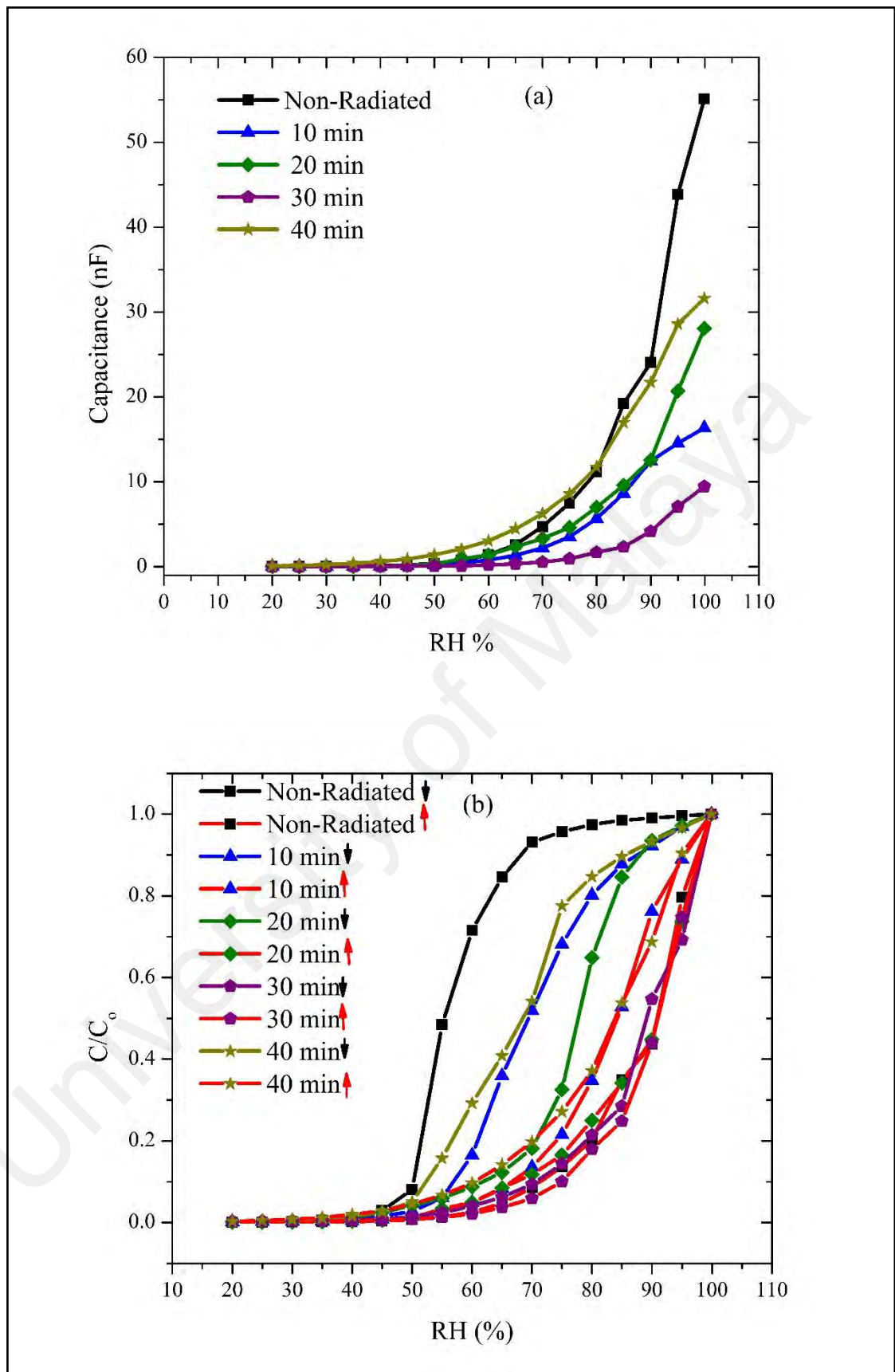
Figure 4.54: Graphs (a) capacitance versus relative humidity, (b) hysteresis curve for the Al/DNA/Al humidity sensor while the arrows refer to either increase in the RH% (↑) or reduction in the RH% (↓).

The results presented in **Figure 4.54**(b) shows that reversal RH profile for capacitance does not match the increasing RH profile driving the formation of the hysteresis loop. Hysteresis fluctuates with increasing irradiation time with values of 4.665, 4.1475, 9.4362, 7.3834 and 4.2893 for non-radiated, 10, 20, 30 and 40 min samples, respectively. A sharp increase was observed for the 30 min sample. The high hysteresis may be due to the fact that the film is thick and has a rough surface caused by the irradiation impact.

Capacitance and resistance were observed to increase with decreasing humidity. The capacitance increases exponentially together with the humidity, which follows the S-shape as shown in **Figure 4.55**(b). This could be due to the decrease in resistance in response to the increase in H_2O molecule concentration and displacement currents and the concentration of charge carriers doped by water molecules (Kh S Karimov et al., 2012). Leveritt et al. (2009) found that increasing the humidity results in the corresponding dramatic increase in the DNA conductance where the electrical field confinement inside water molecules induced the ion binding energy (Leveritt et al., 2009). Ajore et al. observed that the humidity also lead to structural distortion phenomena, which is considered a significant parameter responsible for DNA nanowire conductivity properties (Ajore et al., 2013). They reported quantitative changes in the conductivity values corresponding to the humidity conditions Humidity impact on the resistance and capacitance of the samples can be attributed physically to the absorption and adsorption of water molecules and therefore the organic material permittivity leading to the increase of capacitance. Furthermore, the resistance decreases due to the displacement of current, which is linked to the motion-bound charges of the water molecules (K. S. Karimov et al., 2015).
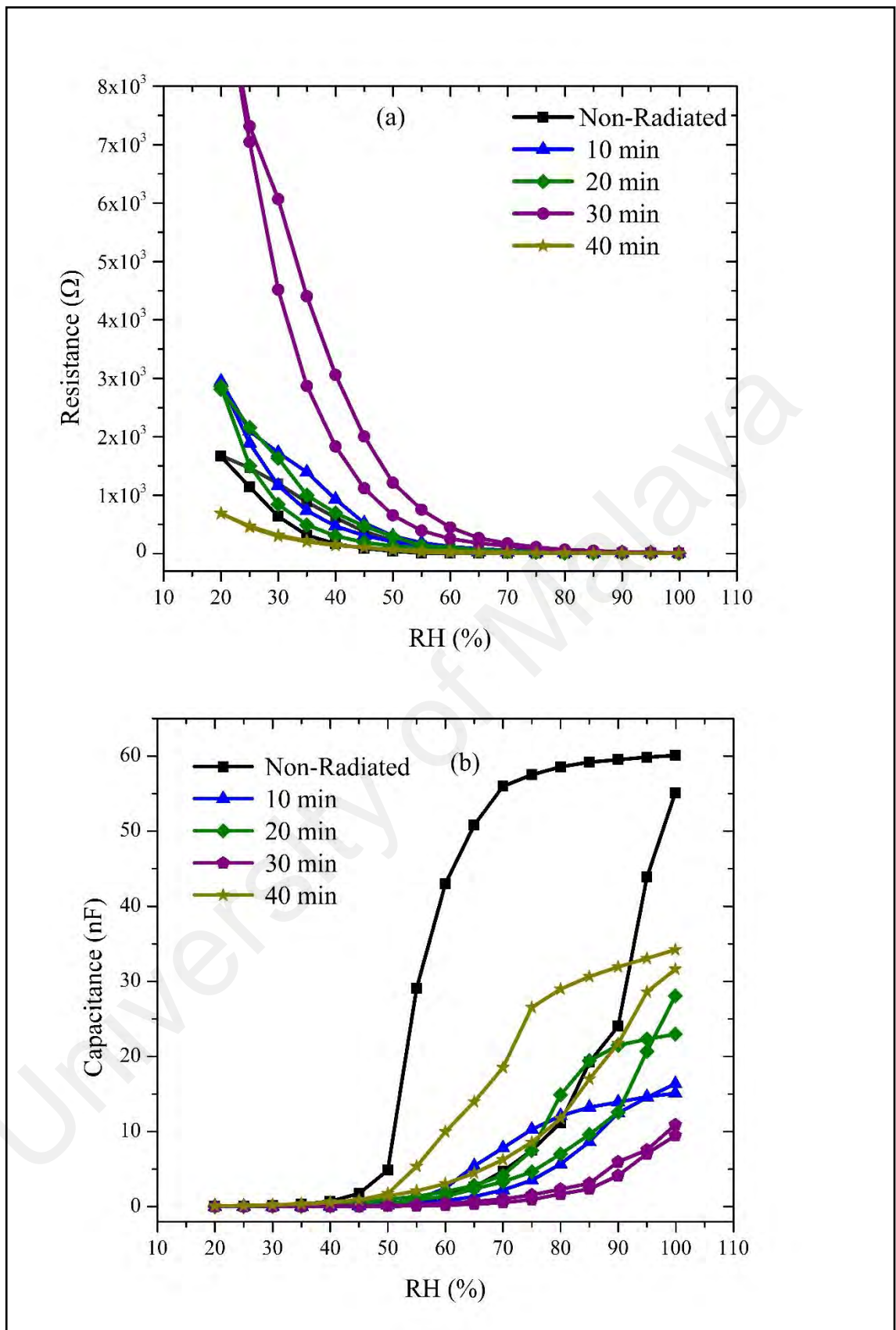
Figure 4.55: Relation between the resistance and capacitance with humidity for Al/DNA/Al junctions.

As shown in **Figure 4.55**(a), the resistance declines exponentially with increasing RH. Specifically, it decreases rapidly by about four orders of magnitude at a RH of 60~99.9%. Overall, the resistance drops dramatically from 1678, 2949, 2813, 9999 and 692.5 KΩ at 20% RH to 6.526, 10.21, 6.684, 17.03 and 5.383 KΩ at 99.9% RH for the non-radiated, 10, 20, 30 and 40 min, respectively. The resistance decreased exponentially and was attributed to adsorption of water molecules by the DNA. Hydrophilic phosphate group around the base pairs of DNA causes the water molecules to be easily absorbed by forming hydrogen bonds between them.

The sensitivity versus RH curve for all the fabricated devices plotted in **Figure 4.56**(a) agrees well with a previous work (Paul et al., 2014). As the sensitivity rises exponentially with RH, it was observed that the device was more sensitive at higher RH compared to lower RH% values. This could probably be attributed to the increase in the DNA conductance with increasing humidity and the ionic conduction (Paul et al., 2014), which leads to change in the electronic relocation in the nucleobases (Berashevich & Chakraborty, 2008). The protons tunnels or transfers from one water molecule to the other and was able to create hydrogen bondings with the water molecules (Chen & Lu, 2005). Humidity sensing ability of this type of capacitive device rely on elements such as the area of the electrodes and the distance between the electrodes (Farahani et al., 2014). The Al/DNA/Al device can be considered as a surface plate capacitor, assuming that the face edges of the electrodes act as parallel layers. As such, the capacitance of the sensor can be measured using the method employed by previous researchers (Azmer et al., 2015; Karimov et al., 2015; Yaworski & Detlaf, 1968) shown in Equation (4.11). Equation (4.12) has meanwhile, expressed the capacitance affected by the humidity effect. This equation can also be obtained by fitting the sensor under higher humidity levels, In the case of relative capacitance, Equation. (4.12) can be rewritten as Equation (4.13) and (4.14).

Figure 4.56(b) shows the experimental and simulated results where the latter were calculated using Equation (4.14). **Table 4.15** lists the sensitivity and value (*a*) of the slope in **Figure 4.56**(b) and value (*b*) from Equation (4.14) for both the non-radiated and radiated structures (10, 20, 30 and 40 min).

AFM images were examined to study the surface morphology of the Al/DNA layer (**Figure 4.57**). The absorption and numerous tracks resulting from the alpha particle irradiation lead to the "spongy" looking film surface, which consists mostly of water molecules. Electrical response also increases with the humidity due to efficient distribution of the water molecules. The surface morphology of the DNA films was also investigated using FESEM as shown by the images in **Figure 4.58**. The porous nature of the film's surface can be clearly seen in the surface morphology images. This porosity endorses the diffusion of water molecules, which enhances the electrical response to humidity.
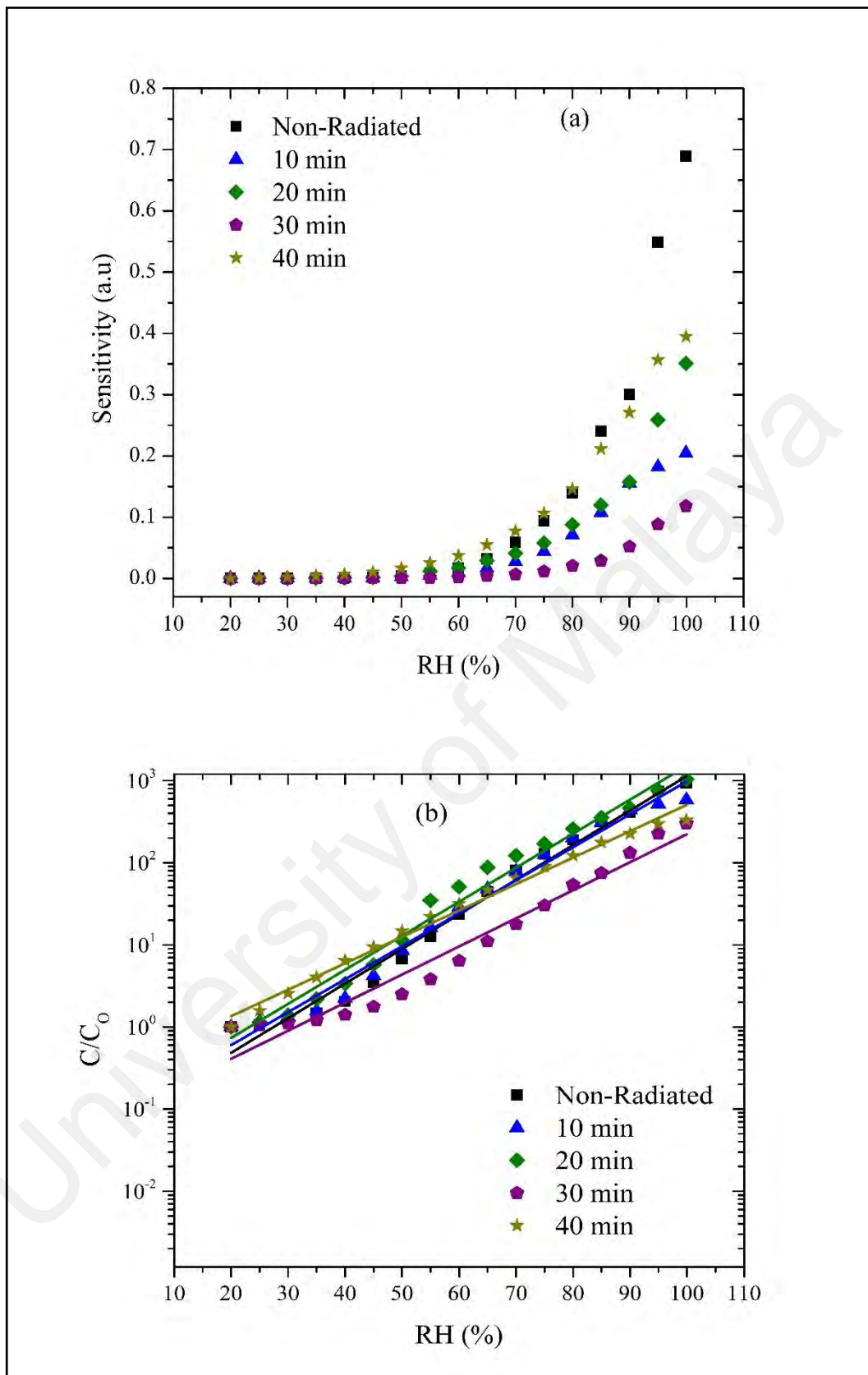
Figure 4.56: Graph (a) demonstrates the sensitivity of the sensor and (b) simulated results for the capacitance-humidity relationship for the Al/DNA/Al humidity sensor.

Table 4.15: Sensitivity values and other parameters measured from the Al/DNA/Al Schottky barrier diode-type humidity sensor.

	Non-radiated	10 min	20 min	30 min	40 min
Slope a (arbitrary)	0.042	0.0401	0.0414	0.034	0.03217
b (1/RH%)	-1.156	-1.023	-0.961	-1.068	-0.5116
Adjusted R-square	0.98297	0.98084	0.98095	0.95635	0.98932
Sensitivity (nF/RH%)	0.6889	0.20437	0.35099	0.11808	0.3945
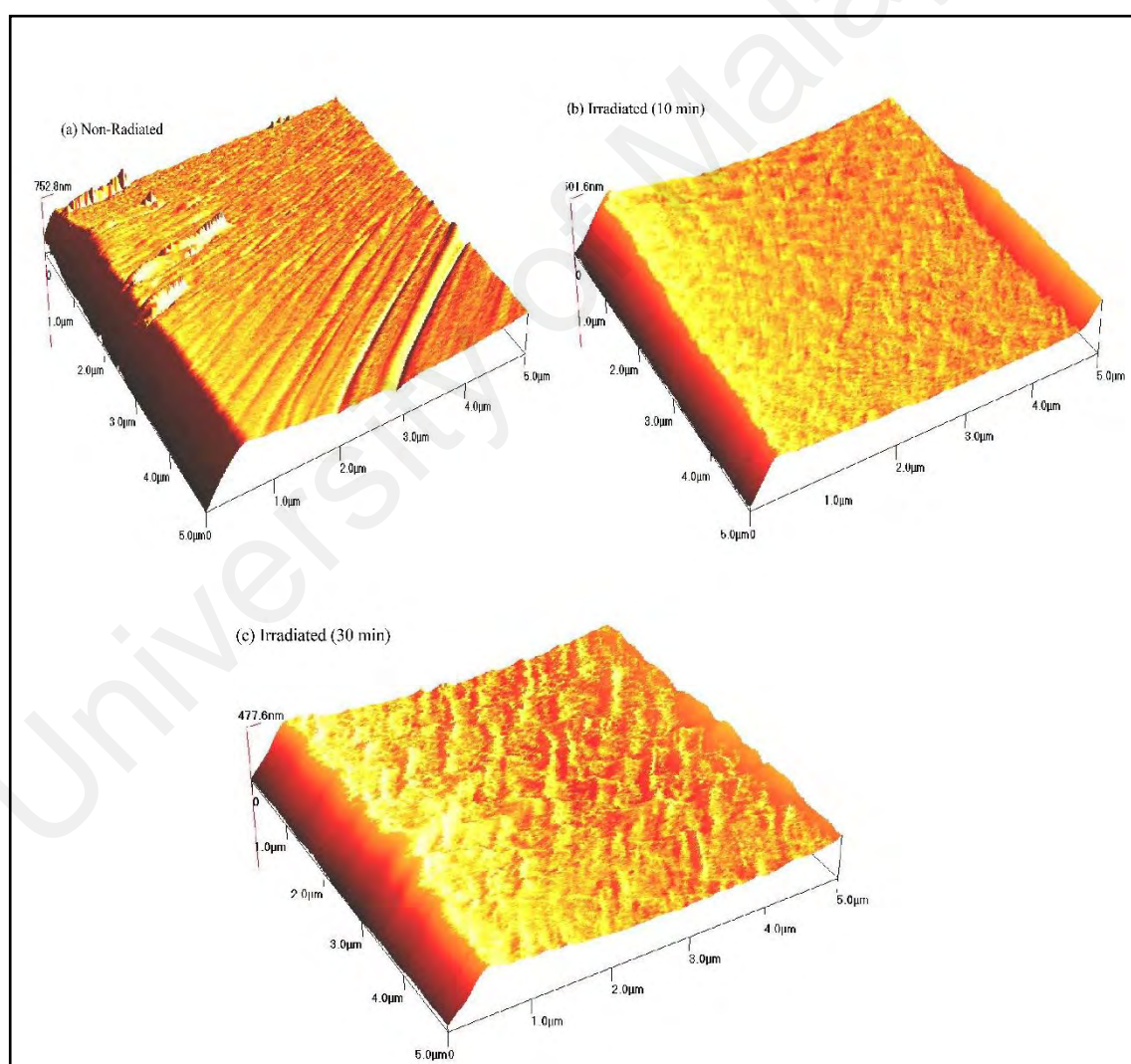
Figure 4.57: AFM images of non-radiated and radiated Al/DNA/Al sensors.

189
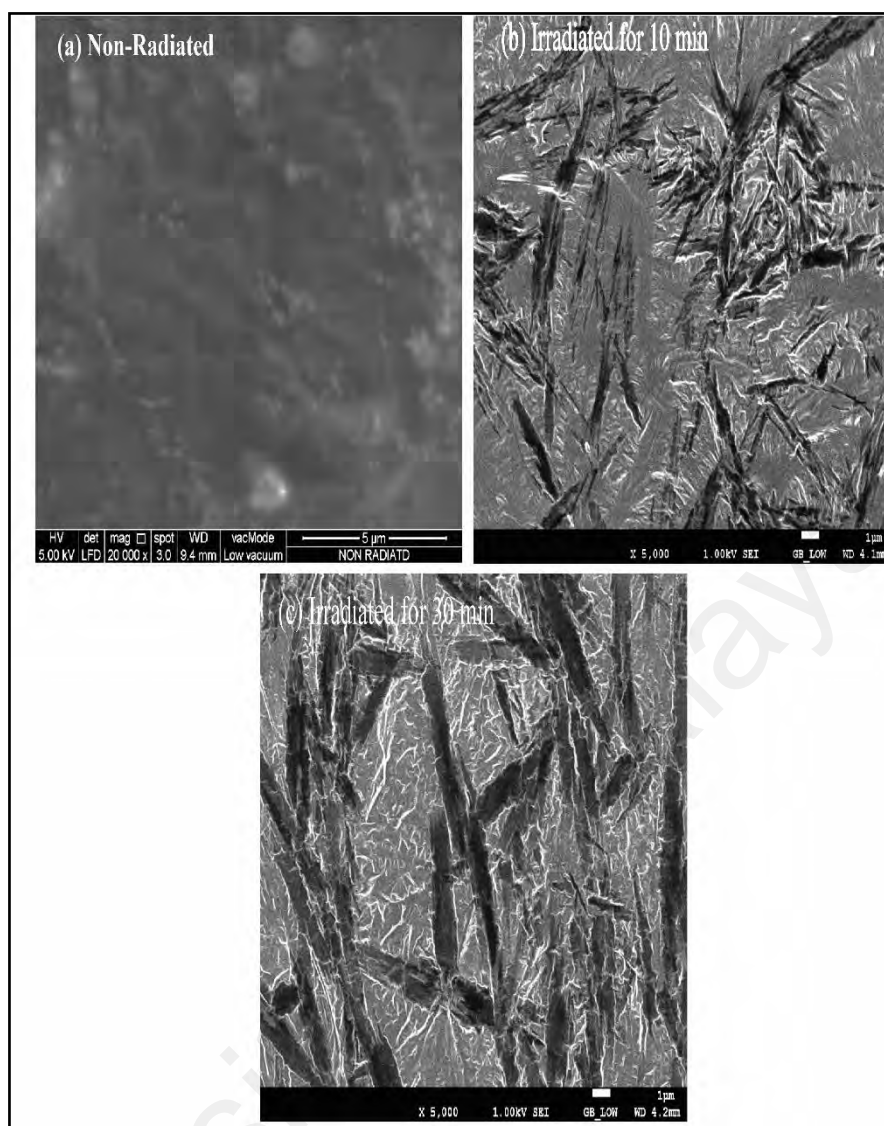
Figure 4.58: FESEM micrographs of DNA films before and after irradiation.

Profiles in **Figure 4.59** demonstrate the capacitive response of the Al/DNA/Al structure exposed to a fast variation of humidity (5-95% RH). The electrical response of the sensor becomes unstable when exposed to a RH value of 95%, followed by a rapid and sharp change back to its unique values within 5 s upon replacing the tested vapor condition. Response and recovery time characteristics of the Al/DNA/Al sensor were measured at a frequency of 800 Hz under a RH condition of 5%.
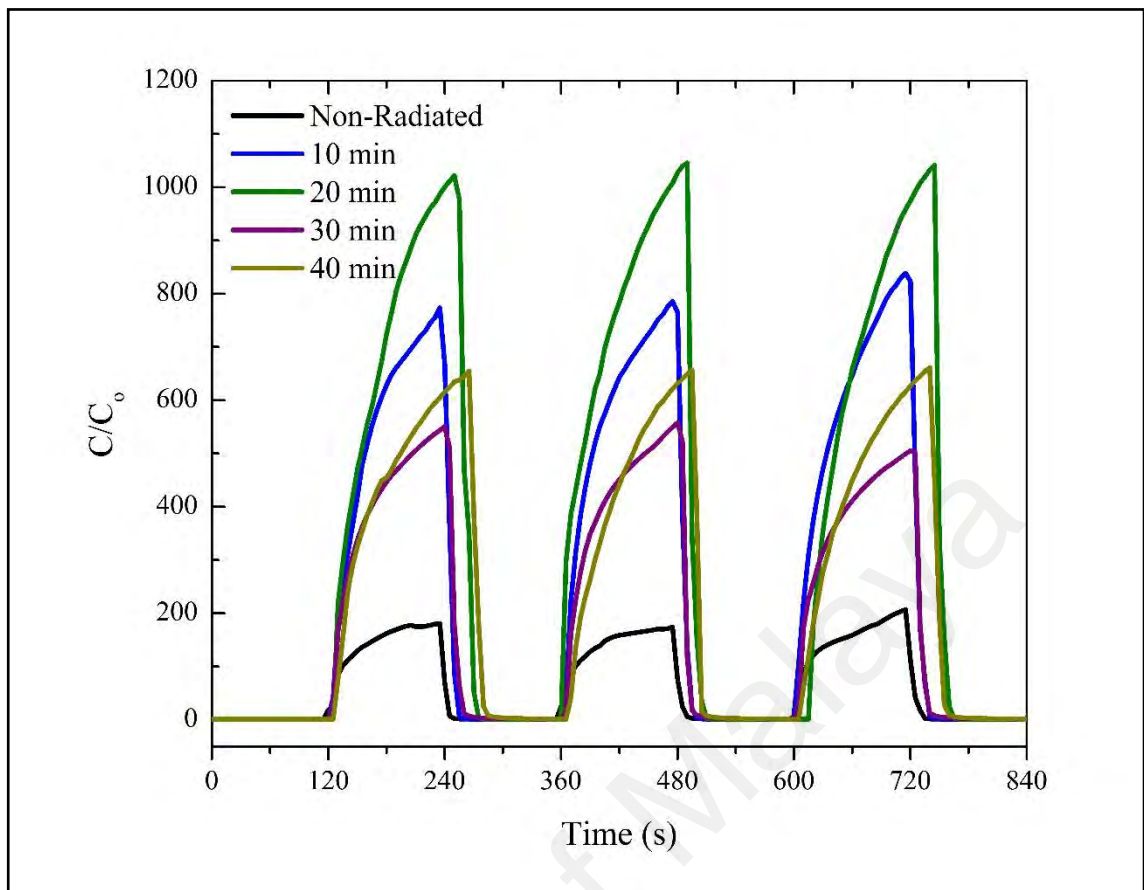
Figure 4.59: Response-recovery graph for the Al/DNA/Al humidity sensor.

Figure 4.59 also demonstrates the sensors' response time (humidification from 5% to 95% RH), which was at 88.701, 94.831, 105.168, 95.913 and 96.995 s for the non-radiated, 10, 20, 30 and 40 min, respectively. The relative capacitance of the sensor increased from 4.0 (5% RH) to 1035 nF (95% RH). When exposed to the maximum humidity of 95% RH, values observed were 175, 780, 1035, 550 and 650 nF for the non-radiated, 10, 20, 30 and 40 min, respectively, while the recovery time (drying effect, 95 to 5% RH) was 107.331, 113.461, 125.8413, 108.293 and 118.5096 s for the non-radiated, 10, 20, 30 and 40 min, respectively. Both types of responses (humidification and drying) illustrates obvious changes due to some hysteresis effect (Heilemann et al., 2004). These changes are highly dependent on the thickness of the structure (Chani et al., 2012) and may also be attributed to permanent structural defect due to the alpha irradiation. **Figure 4.60** demonstrates the relation between the

sensitivity of the Al/DNA/Al sensor with the irradiation time. From this figure, the sensitivity was observed to fluctuate with irradiation period, which can be attributed to the hypersensitivity phenomena of the DNA and the increasing number of alpha particle tracks.
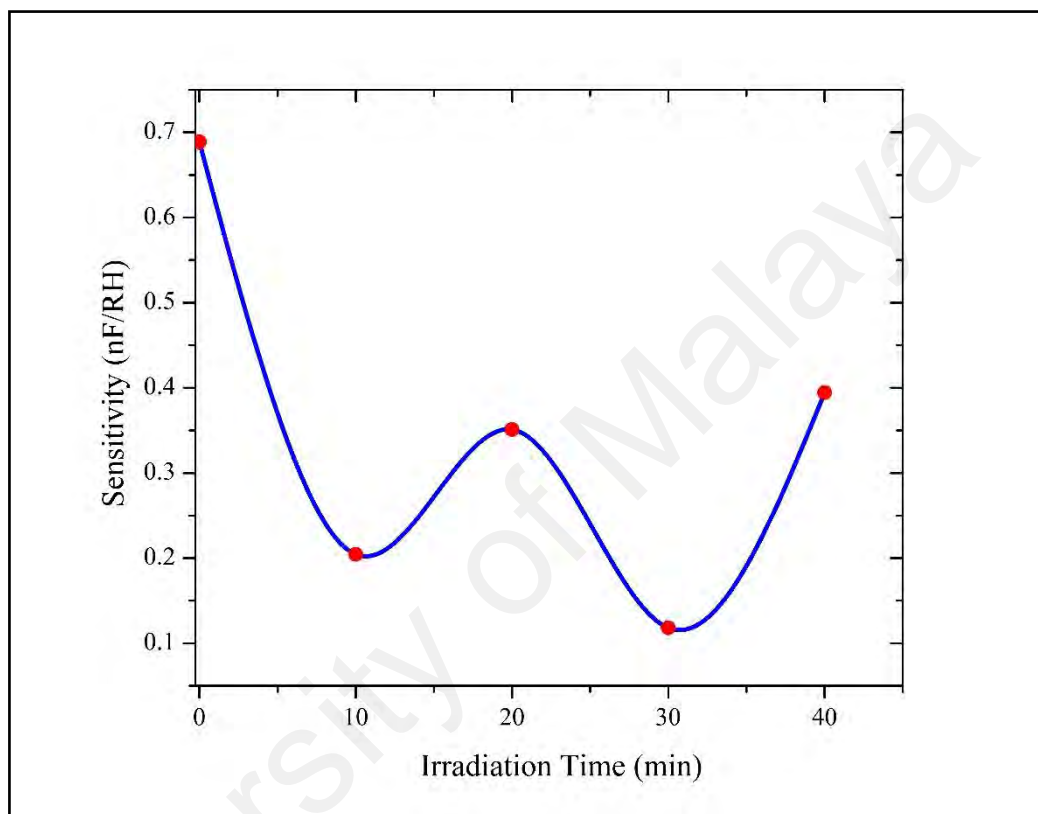
Figure 4.60: Relation between sensitivity and irradiation time with humidity between 20-99.9% RH for the Al/DNA/Al junctions.

CHAPTER 5: CONCLUSIONS AND FUTURE WORKS

5.1   Introduction

The aims of these studies were based on electrical characterization of Al/DNA/ITO/Al, Al/DNA/Si/Al and Al/DNA/Al structures in the presence and absence of radiation. DNA is abundant so it is cheaper, not polluting since it's all organic and not toxic when disposed. The present work was investigated in three parts;

1. The fabrication of MDM structures and the effect of radiation on the electrical characteristics of using three methods (thermionic emission or conventional, Cheung and Cheung's and Norde's methods).

2.   The detection of radiation effect on the DNA structures by utilizing the real time method.

3. DNA employed as a humidity sensor. As a result of these studies, it was observed that bombardment of alpha particles created the surface porosity on all the metal surfaces used in this study. The device was also found to be highly sensitive to the effect of alpha radiation. Therefore it can be suggested that there is a possibility of utilizing these devices as radiation and humidity sensors.

5.2   Summary of Findings

5.2.1   DNA as Radiation Sensor in MDM Structures

Al thin film evaporated with thermal evaporation technique utilized a MDM construction consisting of Al/DNA/Al and Al/DNA/Si/Al structures. Non-radiated and radiated samples (2, 4, 6, 8, 10, 20, 30 and 40 min) were investigated and their electric conduct ion properties studied using their I–V curve properties. Acquisition of the I–V graphs demonstrated that DNA exhibited diode behavior in the MDM structure. The results in summary are as below;

1. The DNA-Al interface potential barrier or Schottky barrier height of the samples show major difference with Irradiation time of alpha particles. It decreased with the increase of the irradiation time whereas the ideality factor increases with irradiation time. As such, the samples show significant changes in non-Ohmic and rectifying electrical behavior.

2. The ideality factor from the ln I–V graph was observed to increase with increase in the irradiation time. The phenomenon that causes deviations from this ideal diode conduction is due to current generated because of recombination carriers, non-homogenous and increase in the charge carriers or decrease in the series resistance.

3. All structures fabricated demonstrate that the series resistance R_S decreased with the increase in the irradiation time. This increase in the current may be caused by increase of the holes that occur as a result of interaction by alpha particles relating to the changes in the DNA structure. This also damages the hydrogen bonds between base pairs.

4. Richardson constant was observed to vary under the radiation impact, increasing with increasing irradiation time for the structure Al/DNA/p-Si and also after 24 hr. It has direct relationship with the carrier effective mass while passing through the electric field. Carrier effective mass increases and therefore results in the reduction of mobility. This only allows the charge carriers to penetrate through the potential barrier at a lower rate. On the other hand it fluctuate a little with increase in the irradiation time for Al/DNA/Al structure due to the current effect and the alpha particle effects.

5. Generally, the saturation current for most of the MDM structures demonstrated decrease with increase in the irradiated time, which can be attributed to the rise of carrier resistance and potential barrier.

6. DNA as radiation sensor can be used to detect low doses of alpha radiation utilized in medical field. The conventional (thermionic emission) model could be the best and most practical for estimating the diode parameters.

7. The hypersensitivity phenomena can be demonstrated using the Schottky diode parameters such as the series resistance, ideality factor and barrier height when irradiated especially at low doses.

8. Charge transport and conduction mechanism investigated suggested the behavior to be influenced by SCLC phenomena. The forward bias double log I–V features show three distinct linear regions parted by transition segments.

9. PL intensity of the DNA was increased with increasing irradiation time or dose. Results demonstrated from this result may suggest utilization as light emitting structures based on DNA diodes.

5.2.2 DNA as Humidity Sensor in MDM Structure

Characterization of DNA as a function of RH% was carried-out for Al/DNA/Al sensor at low and high doses. The sensors presented short response and recovery time and good sensitivity to humidity. In summary, the experimental results are below display that;

1. Capacitance of the Al/DNA/Al sensor raised by 935, 200, 326, 416, 147, 581, 1035, 301 and 329 nF times for non-radiated, 2, 4, 6, 8, 10, 20, 30 and 40 min, respectively. Whereas the resistance of the film reduced by 257, 840, 107, 154, 82, 289, 421, 587 and 129 KΩ times for non-radiated, 2, 4, 6, 8, 10, 20, 30 and 40 min, respectively. The variety in capacitance value is due to the difference between the dielectric constants of DNA and water molecule where the conductivity increases due to protons and ions in a thin layer of absorbed water.

2. Response time (humidification from 5% to 95% RH), was at 88.701, 94.831, 105.168, 95.913 and 96.995 s for the non-radiated, 10, 20, 30 and 40 min, respectively. The recovery time (drying effect, 95 to 5% RH) was about 107.331, 113.461, 125.8413, 108.293 and 118.5096 s for the non-radiated, 10, 20, 30 and 40 min, respectively. Both types of responses (humidification and drying) demonstrate obvious changes due to some hysteresis effect. So it can be concluded from the experimental results that the DNA capacitive sensor was more sensitive and quick to response than the resistive type sensor.

3. The sensitivity for the sensor was about 0.6889, 1.15484, 0.4112, 0.77539, 0.26027, 0.20437, 0.3509, 0.11807 and 0.39450 nF/RH% for the non-radiated, 2, 4, 6, 8, 10, 20, 30 and 40 min, respectively. From these results, it can be shown that the sensitivity at low doses was higher than at the high doses.

4. DNA/Al interface potential barrier (Schottky barrier height) for all samples show major differences with irradiation time under different humidity condition. It decreased with the increase in the humidity whereas the ideality factor increased with humidity. The series resistance reduced with increase in the irradiation under different RH%. In summary, it could be concluded that with increasing dosage. The DNA structures show significant changes in electrical behavior.

The main feature of this sensor is its cheap and easy to fabricate design utilizing the drop cast method. Besides this, the surface type humidity sensor is technologically much simpler and easy to fabricate compared to conventional sandwich type sensors.

5.3   Future Works

Application of DNA electronics as elements in micro to nano scaled devices has influenced recent works in many different fields such as in Physics and Biology. Results obtained in this work therefore have provided a new window toward employing DNAs

as smart materials in various applications, especially in radiotherapy. DNAs can be utilized as the active or sensing materials for magnetic field, temperature, RH and as photo sensors. It can also contribute towards for the development of some interesting applications in micro-array and chip fabrications especially in biotechnology and medical diagnosis.
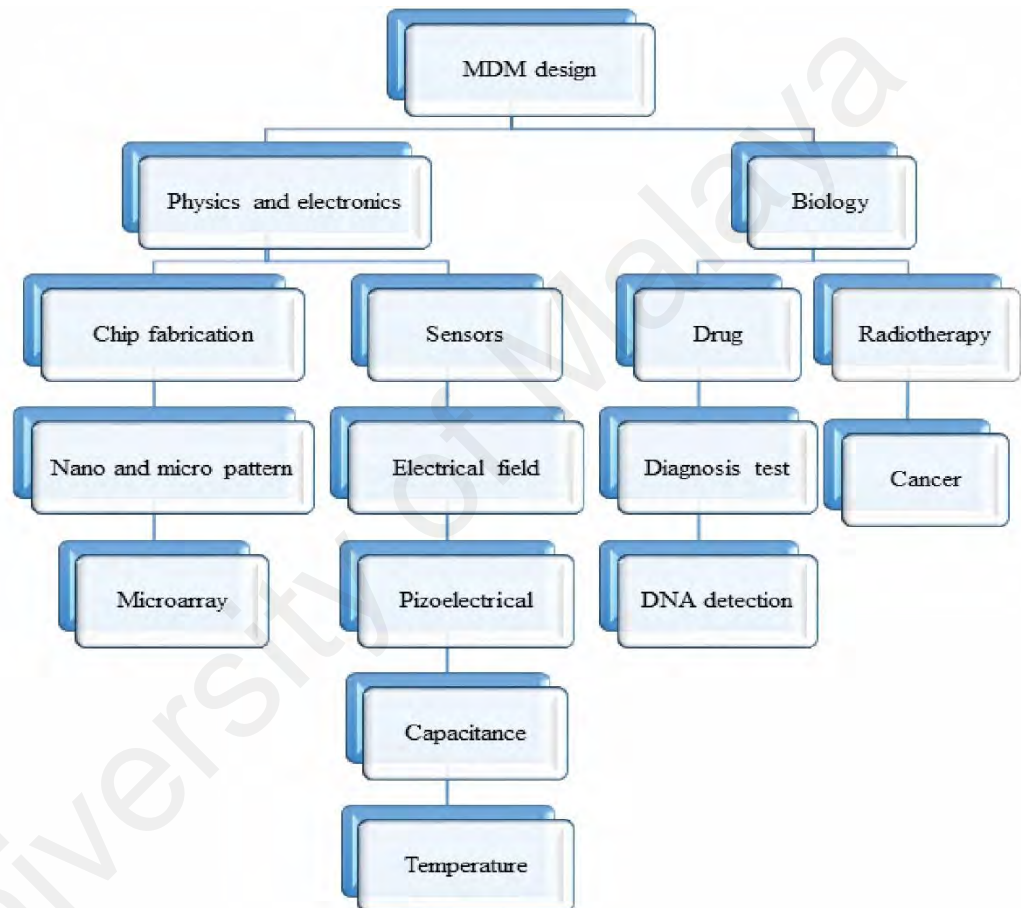
Figure 5.1: Summary of the probable applications of MDM structures that can be fabricated in the future.

Figure 5.1 summarizes the various probable applications of MDM structures in Physics and Biology that can be studied in future. Potential applications of this material are in electronic devices such as sensors, arrays and other hybrid materials. The biological applications of DNA can be further improved and promoted to extend the capability of this material.

REFERENCES

Adleman, L. M. (1994). Molecular computation of solutions to combinatorial problems. *Science, 266*(5187), 1021-1024.

Ahmad, Z., Sayyad, M., Saleem, M., Karimov, K. S., & Shah, M. (2008). Humidity-dependent characteristics of methyl-red thin film-based Ag/methyl-red/Ag surface-type cell. *Physica E: Low-dimensional Systems and Nanostructures, 41*(1), 18-22.

Ahmad, Z., & Sayyad, M. H. (2009). Extraction of electronic parameters of Schottky diode based on an organic semiconductor methyl-red. *Physica E: Low-dimensional Systems and Nanostructures, 41*(4), 631-634.

Ahmed, S. N. (2007). *Physics and engineering of radiation detection*. MA, USA: Academic Press.

Ajore, R., Kaur, I., Kaur, H., & Bharadwaj, L. M. (2013). Effect of Humidity on Structural Distortion and Conductance of DNA Nanowire. *Journal of Nanomaterials & Molecular Nanotechnology, 2*(7 (1000132)), 1-4.

Al-Ghamdi, A., Al-Hartomy, O., Gupta, R., El-Tantawy, F., Taskan, E., Hasar, H., & Yakuphanoglu, F. (2012). A DNA Biosensor Based Interface States of a Metal-Insulator-Semiconductor Diode for Biotechnology Applications. *Acta Physica Polonica A, 121*, 673-677.

Al-Hinai, M., Hassanien, R., Watson, S. M., Wright, N. G., Houlton, A., & Horrocks, B. R. (2016). Metal-conductive polymer hybrid nanostructures: preparation and electrical properties of palladium–polyimidazole nanowires. *Nanotechnology, 27*(9), 095704-095717.

Al-Ta'ii, H. M., Faika A , A., & Ahmad, K. D. (2009). Observation of Hypersensitivity Phenomena in E-Coli Cells after Irradiation by Alpha Particles. *Journal Rafidain of Science, 20*(2), 113-120.

Al-Ta'ii, H. M., & Mohenned A., A. S. a. (2012). Hypersensitivity phenomenon in hydatid protoscolices irradiated by alpha particles. *Journal of Kerbala Universitiy, 10*, 41-44.

Al-Ta'ii, H. M. J., Amin, Y. M., & Periasamy, V. (2015a). Calculation of the Electronic Parameters of an Al/DNA/p-Si Schottky Barrier Diode Influenced by Alpha Radiation. *Sensors, 15*(3), 4810-4822.

Al-Ta'ii, H. M. J., Amin, Y. M., & Periasamy, V. (2015). Detection of alpha particles using DNA/Al Schottky junctions. *Journal of Applied Physics, 118*(11), 1145021-1145027.

Al-Ta'ii, H. M. J., Amin, Y. M., & Periasamy, V. (2015b). Electronic Characterization of Au/DNA/ITO Metal-Semiconductor-Metal Diode and Its Application as a Radiation Sensor. *PloS one, 11*(1), e0145423-e0145440.

Al-Ta'ii, H. M. J., Amin, Y. M., & Periasamy, V. (2015c). Electronic Properties of DNA-Based Schottky Barrier Diodes in Response to Alpha Particles. *Sensors, 15*(5), 11836-11853.

Al-Ta'ii, H. M. J., Amin, Y. M., & Periasamy, V. (2015d). Investigations of electrical properties of structures Al-DNA-ITO-Al exposed to alpha particles. *Radiation Measurements, 72*, 85-94.

Allen, M. W. (2008). *Schottky Contact Formation to Bulk Zinc Oxide.* (PhD), Canterbury, Christchurch, New Zealand.

Alpen, E. L. (1997). *Radiation biophysics* (2 ed.). California - USA: Academic Press.

Anjaneyulu, Y., Jayakumar, I., Bindu, V. H., Rao, P. M., Sagareswar, G., Ramani, K., & Rao, T. (2007). Real time remote monitoring of air pollutants and their online transmission to the web using internet protocol. *Environmental monitoring and assessment, 124*(1-3), 371-381.

Armitage, N., Briman, M., & Grüner, G. (2004). Charge transfer and charge transport on the double helix. *Physica Status Solidi (b), 241*(1), 69-75.

Artacho, E., Machado, M., Sánchez-Portal, D., Ordejón, P., & Soler, J. M. (2003). Electrons in dry DNA from density functional calculations. *Molecular Physics, 101*(11), 1587-1594.

Aydoğan, Ş., Güllü, Ö., & Türüt, A. (2008). Fabrication and electrical properties of Al/aniline green/n-Si/AuSb structure. *Materials Science in Semiconductor Processing, 11*(2), 53-58.

Aydoğan, Ş., & Türüt, A. (2011). Influence of 12MeV electron irradiation on the electrical and photovoltaic properties of Schottky type solar cell based on Carmine. *Radiation Physics and Chemistry, 80*(8), 869-875.

Aziz, F., Sayyad, M. H., Sulaiman, K., Majlis, B., Karimov, K. S., Ahmad, Z., & Sugandi, G. (2011). Influence of humidity conditions on the capacitive and

resistive response of an Al/VOPc/Pt co-planar humidity sensor. *Measurement Science and Technology, 23*(1), 014001-014007.

Azmer, M. I., Ahmad, Z., Sulaiman, K., & Al-Sehemi, A. G. (2015). Humidity dependent electrical properties of an organic material DMBHPET. *Measurement, 61*, 180-184.

Bazlov, N., Vyvenko, O., Sokolov, P., Kas'yanenko, N., & Petrov, Y. V. (2013). Charge-controlled fixation of DNA molecules on silicon surface and electro-physical properties of Au–DNA–Si interface. *Applied Surface Science, 267*, 224-228.

Bending, S., & Beasley, M. (1985). Transport processes via localized states in thin a-Si tunnel barriers. *Physical Review Letters, 55*(3), 324-327.

Bensimon, A., Simon, A., Chiffaudel, A., Croquette, V., Heslot, F., & Bensimon, D. (1994). Alignment and sensitive detection of DNA by a moving interface. *Science, 265*(5181), 2096-2098.

Berashevich, J., & Chakraborty, T. (2008). How the surrounding water changes the electronic and magnetic properties of DNA. *The Journal of Physical Chemistry B, 112*(44), 14083-14089.

Berlin, Y. A., Burin, A. L., & Ratner, M. A. (2001). Charge hopping in DNA. *Journal of the American Chemical Society, 123*(2), 260-268.

Berlin, Y. A., Burin, A. L., & Ratner, M. A. (2002). Elementary steps for charge transport in DNA: thermal activation vs. tunneling. *Chemical Physics, 275*(1), 61-74.

Bethe, H. A. (1942). *Theory of the boundary layer of crystal rectifiers*. United kongdom: (Cambridge,Mass.) Radiation Laboratory, Massachusetts Institute of Technology.

Bhalla, V., Bajpai, R. P., & Bharadwaj, L. M. (2003). DNA electronics. *EMBO reports, 4*(5), 442-445.

Bi, H., Yin, K., Xie, X., Ji, J., Wan, S., Sun, L.,.Dresselhaus, M. S. (2013). Ultrahigh humidity sensitivity of graphene oxide. *Scientific Reports, 3*(2714), 1-7.

Böhrnsen, G., Weber, K., & Scholz, M. (2002). Low dose hypersensitivity and induced resistance of V79 cells after charged particle irradiation using 100 MeV/u carbon ions. *Radiation Protection Dosimetry, 99*(1-4), 255-256.

Borer, P. N., LaPlante, S. R., Kumar, A., Zanatta, N., Martin, A., Hakkinen, A., & Levy, G. C. (1994). 13C-NMR relaxation in three DNA oligonucleotide duplexes: model-free analysis of internal and overall motion. *Biochemistry, 33*(9), 2441-2450.

Borhani, M., Mirjalili, G., Ziaie, F., & Bolorizadeh, M. (2007). Electrical properties of EVA/LDPE blends irradiated by high energy electron beam. *Nukleonika, 52*(2), 77-81.

Boutry, C. M. (2010). DNA conductive properties (pp. 1-19). ETH Zurich - Switzerland: swiss federal Institute of Technology Zurich.

Braun, E., Eichen, Y., Sivan, U., & Ben-Yoseph, G. (1998). DNA-templated assembly and electrode attachment of a conducting silver wire. *Nature, 391*(6669), 775-778.

Braun, E., & Keren, K. (2004). From DNA to transistors. *Advances in Physics, 53*(4), 441-496.

Brauns, E. B., Madaras, M. L., Coleman, R. S., Murphy, C. J., & Berg, M. A. (1999). Measurement of local DNA reorganization on the picosecond and nanosecond time scales. *Journal of the American Chemical Society, 121*(50), 11644-11649.

Breslin, D. T., Coury, J. E., Anderson, J. R., McFail-Isom, L., Kan, Y., Williams, L. D.,.Schuster, G. B. (1997). Anthraquinone photonuclease structure determines its mode of binding to DNA and the cleavage chemistry observed. *Journal of the American Chemical Society, 119*(21), 5043-5044.

Cai, L., Tabata, H., & Kawai, T. (2000). Self-assembled DNA networks and their electrical conductivity. *Applied Physics Letters, 77*(19), 3105-3106.

Carr-Brion, K. (1986). *Moisture sensors in process control*. USA and Canada Elsevier Science Pub. Co.: Elsevier Applied Science

Chan, Z., Ahgilan, A., Sabaratnam, V., Tan, Y. S., & Periasamy, V. (2015). Rectification of DNA films self-assembled in the presence of electric field. *Applied Physics Express, 8*(4), 0470021-0470026.

Chani, M. T. S., Karimov, K. S., Khalid, F. A., Raza, K., Farooq, M. U., & Zafar, Q. (2012). Humidity sensors based on aluminum phthalocyanine chloride thin films. *Physica E: Low-dimensional Systems and Nanostructures, 45*, 77-81.

Chatzandroulis, S., Tserepi, A., Goustouridis, D., Normand, P., & Tsoukalas, D. (2002). Fabrication of single crystal Si cantilevers using a dry release process and

application in a capacitive-type humidity sensor. *Microelectronic Engineering, 61-62*, 955-961.

Chen, Z., & Lu, C. (2005). Humidity sensors: a review of materials and mechanisms. *Sensor Letters, 3*(4), 274-295.

Cheung, S., & Cheung, N. (1986). Extraction of Schottky diode parameters from forward current-voltage characteristics. *Applied Physics Letters, 49*(2), 85-87.

Chiang, P.-T. (2014). *Real-time Measurement of DNA Degradation by Silicon Nanotweezers Coupled with Microfluidic Cavity: Effect of Radiation Damage and Restriction Enzyme Digestion.* (PhD), Tokyo, Japan.

Chiu, S.-M., Oleinick, N. L., Friedman, L. R., & Stambrook, P. J. (1982). Hypersensitivity of DNA in transcriptionally active chromatin to ionizing radiation. *Biochimica et Biophysica Acta (BBA)-Gene Structure and Expression, 699*(1), 15-21.

Çınar, K., Coşkun, C., Aydoğan, Ş., Asıl, H., & Gür, E. (2010). The effect of the electron irradiation on the series resistance of Au/Ni/6H-SiC and Au/Ni/4H-SiC Schottky contacts. *Nuclear Instruments and Methods in Physics Research Section B: Beam Interactions with Materials and Atoms, 268*(6), 616-621.

Coderre, J. (2007). Principles of Radiation Interactions Retrieved 07 Jul, 2010.

Coffer, J. L., Bigham, S. R., Li, X., Pinizzotto, R. F., Rho, Y. G., Pirtle, R. M., & Pirtle, I. L. (1996). Dictation of the shape of mesoscale semiconductor nanoparticle assemblies by plasmid DNA. *Applied Physics Letters, 69*(25), 3851-3853.

Cubero, O. F., Crespo, A., Fatehi, J., & Bridge, P. D. (1999). DNA extraction and PCR amplification method suitable for fresh, herbarium-stored, lichenized, and other fungi. *Plant Systematics and Evolution, 216*(3-4), 243-249.

Cui, Y., Wei, Q., Park, H., & Lieber, C. M. (2001). Nanowire nanosensors for highly sensitive and selective detection of biological and chemical species. *Science, 293*(5533), 1289-1292.

De Pablo, P., Moreno-Herrero, F., Colchero, J., Herrero, J. G., Herrero, P., Baro, A.,.Artacho, E. (2000). Absence of dc-Conductivity in λ-DNA. *Physical Review Letters, 85*(23), 4992-4995.

de Souza, W., & Rocha, G. M. (2011). Atomic force microscopy: a tool to analyze the structural organization of pathogenic protozoa. *Trends in parasitology, 27*(4), 160-167.

Deng, Z., Chen, Y., Tian, Y., & Mao, C. (2006). A fresh look at DNA nanotechnology *Nanotechnology: Science and Computation* (pp. 23-34): Springer Berlin Heidelberg.

Dewarrat, F. (2002). *Electric characterization of DNA.* (PhD), Basel Germany.

Di Ventra, M., & Zwolak, M. (2004). DNA electronics. *Encyclopedia of Nanoscience and Nanotechnology, 2*, 475-493.

Dittmer, W. U., & Simmel, F. C. (2004). Chains of semiconductor nanoparticles templated on DNA. *Applied Physics Letters, 85*(4), 633-635.

Doi, K., Nishioka, Y., & Kawano, S. (2012). Theoretical study of electric current in DNA base molecules trapped between nanogap electrodes. *Computational and Theoretical Chemistry, 999*, 203-214.

Dugasani, S. R., Park, B., Gnapareddy, B., Pamanji, S. R., Yoo, S., Lee, K. W.,.Kim, C. (2015). Tunable near white light photoluminescence of lanthanide ion (Dy 3+, Eu 3+ and Tb 3+) doped DNA lattices. *Royal Society of Chemistry Advances, 5*(69), 55839-55846.

Dulić, D., Tuukkanen, S., Chung, C.-L., Isambert, A., Lavie, P., & Filoramo, A. (2009). Direct conductance measurements of short single DNA molecules in dry conditions. *Nanotechnology, 20*(11), 115502-115509.

Dyakonov, V., & Sariciftci, N. (2003). *Organic photovoltaics: concepts and realization.* verlag berlin heidlberg GmbH: Springer, New York.

Eichen, Y., Braun, E., Sivan, U., & Ben-Yoseph, G. (1998). Self-assembly of nanoelectronic components and circuits using biological templates. *Acta Polymerica, 49*(10-11), 663-670.

Esfandyarpour, R., Yang, L., Harris, J. S., & Davis, R. W. (2016). Nanoelectronic three-dimensional (3D) nanotip sensing array for real-time, sensitive, label-free sequence specific detection of nucleic acids. *Biomedical microdevices, 18*(1), 1-10.

Fan, J. C., & Zavracky, P. M. (1976). Selective black absorbers using MgO/Au cermet films. *Applied Physics Letters, 29*(8), 478-480.

Farag, A., Gunduz, B., Yakuphanoglu, F., & Farooq, W. (2010). Controlling of electrical characteristics of Al/p-Si Schottky diode by tris (8-hydroxyquinolinato) aluminum organic film. *Synthetic Metals, 160*(23), 2559-2563.

Farahani, H., Wagiran, R., & Hamidon, M. N. (2014). Humidity sensors principle, mechanism, and fabrication technologies: A comprehensive review. *Sensors, 14*(5), 7881-7939.

Feldman, A. K., Steigerwald, M. L., Guo, X., & Nuckolls, C. (2008). Molecular electronic devices based on single-walled carbon nanotube electrodes. *Accounts of Chemical Research, 41*(12), 1731-1741.

Fink, H.-W., & Schönenberger, C. (1999). Electrical conduction through DNA molecules. *Nature, 398*(6726), 407-410.

Förch, R., Schönherr, H., & Jenkins, A. T. A. (2009). *Surface design: Applications in bioscience and nanotechnology*. Strauss GmbH, Mçrlenbach, Germany: John Wiley & Sons.

Gasper, S. M., & Schuster, G. B. (1997). Intramolecular photoinduced electron transfer to anthraquinones linked to duplex DNA: The effect of gaps and traps on long-range radical cation migration. *Journal of the American Chemical Society, 119*(52), 12762-12771.

Gates, E. P., Dearden, A. M., & Woolley, A. T. (2014). DNA-templated lithography and nanofabrication for the fabrication of nanoscale electronic circuitry. *Critical Reviews in Analytical Chemistry, 44*(4), 354-370.

Giese, B. (2002). Long-distance electron transfer through DNA. *Annual review of biochemistry, 71*(1), 51-70.

Gorelik, V., & Sutula, I. (2010). Photoluminescence of nucleic bases, DNA, and biological objects. *Bulletin of the Lebedev Physics Institute, 37*(5), 159-161.

Grote, J. G., & De Yu , Z. (2007). *Photoelectrical effect and current-voltage characteristics in DNA-metal Schottky barriers.* Paper presented at the Integrated Optoelectronic Devices.

Grozema, F. C., Siebbeles, L. D., Berlin, Y. A., & Ratner, M. A. (2002). Hole mobility in DNA: Effects of static and dynamic structural fluctuations. *ChemPhysChem, 3*(6), 536-539.

Gu, J., Cai, L., Tanaka, S., Otsuka, Y., Tabata, H., & Kawai, T. (2002). Electric conductivity of dye modified DNA films with and without light irradiation in various humidities. *Journal of Applied Physics, 92*(5), 2816-2820.

Gu, Q., Cheng, C., Gonela, R., Suryanarayanan, S., Anabathula, S., Dai, K., & Haynie, D. T. (2006). DNA nanowire fabrication. *Nanotechnology, 17*(1), R14-R25.

Gu, Q., Cheng, C., & Haynie, D. T. (2005). Cobalt metallization of DNA: toward magnetic nanowires. *Nanotechnology, 16*(8), 1358-1363.

Güllü, Ö., Aydoğan, Ş., Şerifoğlu, K., & Türüt, A. (2008). Electron irradiation effects on the organic-on-inorganic silicon Schottky structure. *Nuclear Instruments and Methods in Physics Research Section A: Accelerators, Spectrometers, Detectors and Associated Equipment, 593*(3), 544-549.

Güllü, Ö., Cankaya, M., Barış, Ö., Biber, M., Özdemir, H., Güllüce, M., & Türüt, A. (2008). DNA-based organic-on-inorganic semiconductor Schottky structures. *Applied Surface Science, 254*(16), 5175-5180.

Güllü, Ö., Çankaya, M., Barış, Ö., & Türüt, A. (2008). DNA-based organic-on-inorganic devices: Barrier enhancement and temperature issues. *Microelectronic Engineering, 85*(11), 2250-2255.

Güllü, Ö., Kilicoglu, T., & Türüt, A. (2010). Electronic properties of the metal/organic interlayer/inorganic semiconductor sandwich device. *Journal of Physics and Chemistry of Solids, 71*(3), 351-356.

Güllü, Ö., Pakma, O., & Türüt, A. (2012). Current density-voltage analyses and interface characterization in Ag/DNA/p-InP structures. *Journal of Applied Physics, 111*(4), 0445031-0445036.

Güllü, Ö., & Türüt, A. (2011). Electronic properties of Al/DNA/p-Si MIS diode: Application as temperature sensor. *Journal of Alloys and Compounds, 509*(3), 571-577.

Gunduz, B., Yahia, I., & Yakuphanoglu, F. (2012). Electrical and photoconductivity properties of p-Si/P3HT/Al and p-Si/P3HT: MEH-PPV/Al organic devices: Comparison study. *Microelectronic Engineering, 98*, 41-57.

Guo, X., Gorodetsky, A. A., Hone, J., Barton, J. K., & Nuckolls, C. (2008). Conductivity of a single DNA duplex bridging a carbon nanotube gap. *Nature nanotechnology, 3*(3), 163-167.

Gupta, R., Al-Ghamdi, A., Al-Hartomi, O., Hasar, H., El-Tantawy, F., & Yakuphanoglu, F. (2012). Series resistance controlling photosensor of Ag/DNA/p-Si/Al diode. *Synthetic Metals, 162*(11), 981-987.

Gupta, R. K., & Saraf, V. (2009). Nanoelectronics: tunneling current in DNA–single electron transistor. *Current Applied Physics, 9*(1), S149-S152.

Gupta, R. K., & Yakuphanoglu, F. (2012). Photoconductive Schottky diode based on Al/p-Si/SnS 2/Ag for optical sensor applications. *Solar Energy, 86*(5), 1539-1545.

Gupta, R. K., Yakuphanoglu, F., Hasar, H., & Al-Khedhairy, A. A. (2011). p-Si/DNA photoconductive diode for optical sensor applications. *Synthetic Metals, 161*(2011), 2011-2016.

Gupta, S., Muralikiran, M., Farmer, J., Cao, L., & Downing, R. (2009). The effect of boron doping and gamma irradiation on the structure and properties of microwave chemical vapor deposited boron-doped diamond films. *Journal of Materials Research, 24*(04), 1498-1512.

Ha, D. H., Nham, H., Yoo, K.-H., So, H.-m., Lee, H.-Y., & Kawai, T. (2002). Humidity effects on the conductance of the assembly of DNA molecules. *Chemical Physics Letters, 355*(5), 405-409.

Hahm, J.-i., & Lieber, C. M. (2004). Direct ultrasensitive electrical detection of DNA and DNA sequence variations using nanowire nanosensors. *Nano Letters, 4*(1), 51-54.

Hall, D. B., & Barton, J. K. (1997). Sensitivity of DNA-mediated electron transfer to the intervening π-stack: a probe for the integrity of the DNA base stack. *Journal of the American Chemical Society, 119*(21), 5045-5046.

Hall, E. J., & Giaccia, A. J. (2006). *Radiobiology for the Radiologist* (6 ed.). California-USA: Lippincott Williams & Wilkins.

Hartzell, B., McCord, B., Asare, D., Chen, H., Heremans, J., & Soghomonian, V. (2003). Comparative current–voltage characteristics of nicked and repaired λ-DNA. *Applied physics letters, 82*(26), 4800-4802.

Heckman, E. M., Aga, R. S., Rossbach, A. T., Telek, B. A., Bartsch, C. M., & Grote, J. G. (2011). DNA biopolymer conductive cladding for polymer electro-optic waveguide modulators. *Applied Physics Letters, 98*(10), 1033041-1033043.

Heilemann, M., Tinnefeld, P., Sanchez Mosteiro, G., Garcia Parajo, M., Van Hulst, N. F., & Sauer, M. (2004). Multistep energy transfer in single molecular photonic wires. *Journal of the American Chemical Society, 126*(21), 6514-6515.

Henderson, P. T., Jones, D., Hampikian, G., Kan, Y., & Schuster, G. B. (1999). Long-distance charge transport in duplex DNA: the phonon-assisted polaron-like hopping mechanism. *Proceedings of the National Academy of Sciences, 96*(15), 8353-8358.

Herman, C., & Thomas , E. J. (2009). *Introduction to Health Physics* (4 ed.). the United States: The McGraw-Hill Companies.

Hermon, Z., Caspi, S., & Ben-Jacob, E. (1998). Prediction of charge and dipole solitons in DNA molecules based on the behaviour of phosphate bridges as tunnel elements. *EPL (Europhysics Letters), 43*(4), 482-487.

Hoa, P. T. M., Binh, N. T., Ha, N. T. T., & An, D. K. (2000). Some investigation results of the instability of humidity sensors based on alumina and porous silicon materials. *Sensors and Actuators B: Chemical, 66*(1), 63-65.

Hofmann, W., Fakir, H., Aubineau-Laniece, I., & Pihet, P. (2004). Interaction of alpha particles at the cellular level—implications for the radiation weighting factor. *Radiation protection dosimetry, 112*(4), 493-500.

Holbert, K. E. (1995). Radiation Effects and Damage (pp. 1-10). United state-Arizona Arizona State University Education.

Hong, W., Lee, E., Kim, D., & Lee, C. E. (2015). Electrical conduction and photoresponses of gamma-ray-irradiated single-stranded DNA/single-walled carbon nanotube composite systems. *Nuclear Instruments and Methods in Physics Research Section B: Beam Interactions with Materials and Atoms, 349*, 103-105.

Hsiung, C.-M., Chou, C.-S., & Chiang, T.-L. (2012). A generalized Norde plot for reverse biased Schottky contacts. *International Journal of Minerals, Metallurgy, and Materials, 19*(1), 54-58.

Huang, J.-R., Li, M.-Q., & Liu, J.-H. (2007). A novel conductive humidity sensor based on field ionization from carbon nanotubes. *Sensors and Actuators A: Physical, 133*(2), 467-471.

Huang, Y., Duan, X., Cui, Y., Lauhon, L. J., Kim, K.-H., & Lieber, C. M. (2001). Logic gates and computation from assembled nanowire building blocks. *Science, 294*(5545), 1313-1317.

Huggett, J., & Shaw, H. (1997). Field emission scanning electron microscopy; a high-resolution technique for the study of clay minerals in sediments. *Clay Minerals, 32*(2), 197-203.

Hughes, M. E. (2008). *Studies of DNA-carbon nanotube interactions* (Vol. 69-05): ProQuest Dissertations and Theses; Thesis (Ph.D.)-Harvard University.

Imtiaj, A., Lee, T., & Ohga, S. (2011). Collected from Eastern Asia. *Micología Aplicada Internacional, 23*(1), 1-10.

Ingram, J. M., Greb, M., Nicholson, J. A., & Fountain, A. W. (2003). Polymeric humidity sensor based on laser carbonized polyimide substrate. *Sensors and Actuators B: Chemical, 96*(1), 283-289.

Islam, T., & Saha, H. (2006). Hysteresis compensation of a porous silicon relative humidity sensor using ANN technique. *Sensors and Actuators B: Chemical, 114*(1), 334-343.

Jianrong, C., Yuqing, M., Nongyue, H., Xiaohua, W., & Sijiao, L. (2004). Nanotechnology and biosensors. *Biotechnology Advances, 22*(7), 505-518.

Jo, Y.-S., Lee, Y., & Roh, Y. (2003). Effects of humidity on the electrical conduction of lambda-DNA trapped on a nano-gap Au electrode. *Journal-Korean Physical Society, 43*(2), 909-913.

Joiner, M., Lambin, P., Malaise, E., Robson, T., Arrand, J., Skov, K., & Marples, B. (1996). Hypersensitivity to very-low single radiation doses: its relationship to the adaptive response and induced radioresistance. *Mutation Research/Fundamental and Molecular Mechanisms of Mutagenesis, 358*(2), 171-183.

Kang, M. G., & Guo, L. J. (2007). Nanoimprinted Semitransparent Metal Electrodes and Their Application in Organic Light-Emitting Diodes. *Advanced Materials, 19*(10), 1391-1396.

Karadeniz, S., Barış, B., Yüksel, Ö., & Tuğluoğlu, N. (2013). Analysis of electrical properties of Al/p-Si Schottky contacts with and without rubrene layer. *Synthetic Metals, 168*, 16-22.

Karataş, Ş., & Türüt, A. (2004). The determination of interface state energy distribution of the H-terminated Zn/p-type Si Schottky diodes with high series resistance by the admittance spectroscopy. *Vacuum, 74*(1), 45-53.

Karimov, K. S., Fatima, N., Sulaiman, K., Tahir, M. M., Ahmad, Z., & Mateen, A. (2015). Sensitivity enhancement of OD-and OD-CNT-based humidity sensors by high gravity thin film deposition technique. *Journal of Semiconductors, 36*(3), 0340051-0340055.

Karimov, K. S., Saleem, M., Karieva, Z., Mateen, A., Chani, M. T. S., & Zafar, Q. (2012). Humidity sensing properties of Cu2O-PEPC nanocomposite films. *Journal of Semiconductors, 33*(7), 0730011-0730015.

Karimov, K. S., Sulaiman, K., Ahmad, Z., Akhmedov, K. M., & Mateen, A. (2015). Novel pressure and displacement sensors based on carbon nanotubes *Chinese Physics B, 24*(1), 018801-018804.

Kasumov, A. Y., Klinov, D., Roche, P.-E., Gueron, S., & Bouchiat, H. (2004). Thickness and low-temperature conductivity of DNA molecules. *Applied Physics Letters, 84*(6), 1007-1009.

Kasumov, A. Y., Kociak, M., Gueron, S., Reulet, B., Volkov, V., Klinov, D., & Bouchiat, H. (2001). Proximity-induced superconductivity in DNA. *Science, 291*(5502), 280-282.

Katsouras, I., Piliego, C., Blom, P. W., & de Leeuw, D. M. (2013). Transverse charge transport through DNA oligomers in large-area molecular junctions. *Nanoscale, 5*(20), 9882-9887.

Kelley, S. O., Boon, E. M., Barton, J. K., Jackson, N. M., & Hill, M. G. (1999). Single-base mismatch detection based on charge transduction through DNA. *Nucleic Acids Research, 27*(24), 4830-4837.

Khaled, S., & Held, K. D. (2012). Radiation biology: a handbook for teachers and students. *International Journal of Radiation Biology, 88*(11), 858-859.

Khatir, N. M., Abdul-Malek, Z., & Banihashemian, S. M. (2014a). *Investigation of the Electrical Resistivity of 20µm-Gap Gold-DNA-Gold Structure: Exploiting the Current-Voltage Characteristics under a Variable External Magnetic Field.* Paper presented at the Applied Mechanics and Materials.

Khatir, N. M., Abdul-Malek, Z., & Banihashemian, S. M. (2014b). Temperature and Magnetic Field Driven Modifications in the IV Features of Gold-DNA-Gold Structure. *Sensors, 14*(10), 19229-19241.

Khatir, N. M., Abdul-Malek, Z., & Banihashemian, S. M. (2015). Influences of magnetic fields on current–voltage characteristics of gold-DNA-gold structure with variable gaps. *Materials Science in Semiconductor Processing, 36*, 134-139.

Khatir, N. M., Banihashemian, S. M., Periasamy, V., Abd Majid, W. H., Rahman, S. A., & Shahhosseini, F. (2011). DNA strand patterns on Aluminium thin films. *Sensors, 11*(7), 6719-6727.

Khatir, N. M., Banihashemian, S. M., Periasamy, V., Ritikos, R., Majid, W. H. A., & Rahman, S. A. (2012). Electrical characterization of Gold-DNA-Gold structures in presence of an external magnetic field by means of IV curve analysis. *Sensors, 12*(3), 3578-3586.

Kılıçoğlu, T., & Ocak, Y. S. (2011). Electrical and photovoltaic properties of an organic–inorganic heterojunction based on a BODIPY dye. *Microelectronic Engineering, 88*(2), 150-154.

Kim, H. G., CM ;Pique, A ;Horwitz, JS ;Mattoussi, H ;Murata, H ;Kafafi, ZH ;Chrisey, DB. (1999). Electrical, optical, and structural properties of indium–tin–oxide thin films for organic light-emitting devices. *Journal of Applied Physics, 86*(11), 6451-6461.

Kleine, H., Wilke, R., Pelargus, C., Rott, K., Pühler, A., Reiss, G.,.Anselmetti, D. (2004). Absence of intrinsic electric conductivity in single dsDNA molecules. *Journal of Biotechnology, 112*(1), 91-95.

Klug, A. (1968). Rosalind Franklin and the discovery of the structure of DNA. *Nature, 219*, 808-844.

Knapp, F. R., & Dash, A. (2016). *Radiopharmaceuticals for Therapy*. India: Springer New Delhi Heidelberg New York Dordrecht London.

Kodama, T., Jain, A., & Goodson, K. E. (2009). Heat Conduction through a DNA− Gold Composite. *Nano letters, 9*(5), 2005-2009.

Krider, E. S., & Meade, T. J. (1998). Electron transfer in DNA: covalent attachment of spectroscopically unique donor and acceptor complexes. *Journal of Biological Inorganic Chemistry, 3*(2), 222-225.

Kulkarni, A., Kim, B., Dugasani, S. R., Joshirao, P., Kim, J. A., Vyas, C.,.Park, S. H. (2013). A novel nanometric DNA thin film as a sensor for alpha radiation. *Scientific Reports, 3*(2062), 1-5.

Kulwicki, B. M. (1991). Humidity sensors. *Journal of the American Ceramic Society, 74*(4), 697-708.

Kumemura, M., Collard, D., Yamahata, C., Sakaki, N., Hashiguchi, G., & Fujita, H. (2007). Single DNA molecule isolation and trapping in a microfluidic device. *ChemPhysChem, 8*(12), 1875-1880.

Kwon, Y.-W., Choi, D. H., & Jin, J.-I. (2012). Optical, electro-optic and optoelectronic properties of natural and chemically modified DNAs. *Polymer journal, 44*(12), 1191-1208.

Lakhno, V. (2000). Soliton-like solutions and electron transfer in DNA. *Journal of Biological Physics, 26*(2), 133-147.

Lee, C.-Y., & Lee, G.-B. (2005). Humidity sensors: a review. *Sensor Letters, 3*(1-4), 1-15.

Lee, H.-Y., Tanaka, H., Otsuka, Y., Yoo, K.-H., Lee, J.-O., & Kawai, T. (2002). Control of electrical conduction in DNA using oxygen hole doping. *Applied Physics Letters, 80*(9), 1670-1672.

Legrand, O., Côte, D., & Bockelmann, U. (2006). Single molecule study of DNA conductivity in aqueous environment. *Physical Review E, 73*(3), 0319251-0319256.

Leveritt, J. M., Dibaya, C., Tesar, S., Shrestha, R., & Burin, A. L. (2009). One-dimensional confinement of electric field and humidity dependent DNA conductivity. *The Journal of Chemical Physics, 131*(24), 245102-245107.

Lewis, F. D., & Letsinger, R. L. (1998). Distance-dependent photoinduced electron transfer in synthetic single-strand and hairpin DNA. *Journal of Biological Inorganic Chemistry, 3*(2), 215-221.

Li, Y., & Yang, M. (2002). Bilayer thin film humidity sensors based on sodium polystyrenesulfonate and substituted polyacetylenes. *Sensors and Actuators B: Chemical, 87*(1), 184-189.

Li, Y., Yang, M., & She, Y. (2004). Humidity sensors using in situ synthesized sodium polystyrenesulfonate/ZnO nanocomposites. *Talanta, 62*(4), 707-712.

Lin-Vien, D., Colthup, N. B., Fateley, W. G., & Grasselli, J. G. (1991). *The handbook of infrared and Raman characteristic frequencies of organic molecules*. United Kingdom: Acadmic press limited.

Loveland, W., Morrissery, D., & Seaborg, G. (2006). *Modern Nuclear Chemistry*. United States of America: John Wiley & Sons, Inc., Hoboken, New Jersey.

Lu, J., Yang, L., Xie, A., & Shen, Y. (2009). DNA-templated photo-induced silver nanowires: fabrication and use in detection of relative humidity. *Biophysical Chemistry, 145*(2), 91-97.

Lu, S. (2006). *Conductivity measurements of single DNA molecules using conductive-atomic force microscopy.* (Master), Department of Physics-Simon Fraser University.

Lund, J., Dong, J., Mehta, R., Rahimi, M., Ryan, D., & Parviz, B. (2016). *Using Electron Tunneling for Direct Sequencing of DNA.* Paper presented at the proceedings of the NSTI Nanotechnology Conference.

Ma, Y., Zhang, J., Zhang, G., & He, H. (2004). Polyaniline nanowires on Si surfaces fabricated with DNA templates. *Journal of the American Chemical Society, 126*(22), 7097-7101.

Maeda, Y., Tabata, H., & Kawai, T. (2001). Two-dimensional assembly of gold nanoparticles with a DNA network template. *Applied Physics Letters, 79*(8), 1181-1183.

Maiti, A., Rodriguez, J. A., Law, M., Kung, P., McKinney, J. R., & Yang, P. (2003). SnO2 nanoribbons as NO2 sensors: insights from first principles calculations. *Nano Letters, 3*(8), 1025-1028.

Manning, B., Di Salvo, A., Stanca, S., Ongaro, A., & Fitzmaurice, D. (2005). *DNA-templated assembly of nanoscale wires and switches.* Paper presented at the OPTO-Ireland.

Marikkannan, M., Vishnukanthan, V., Vijayshankar, A., Mayandi, J., & Pearce, J. M. (2015). A novel synthesis of tin oxide thin films by the sol-gel process for optoelectronic applications. *American Institute of Physics Advances, 5*(2), 0271221-0271228.

Marples, B., Joiner, M. C., & Skov, K. A. (1994). The effect of oxygen on low-dose hypersensitivity and increased radioresistance in Chinese hamster V79-379A cells. *Radiation Research, 138*(1s), S17-S20.

Martin, B. R., Dermody, D. J., Reiss, B. D., Fang, M., Lyon, L. A., Natan, M. J., & Mallouk, T. E. (1999). Orthogonal self-assembly on colloidal gold-platinum nanorods. *Advanced Materials, 11*(12), 1021-1025.

Martin, L. M., Marples, B., Lynch, T. H., Hollywood, D., & Marignol, L. (2013). Exposure to low dose ionising radiation: molecular and clinical consequences. *Cancer Letters, 338*(2), 209-218.

Massey, T. N. (2005). *A Study Guide For Radiation Biophysics NUC-412-GS.* Distance & Independent Adult Learning at Thomas;Edison State College by Ohio University Independent Study: Thomas Edison State College.

Masuda, H., & Fukuda, K. (1995). Ordered metal nanohole arrays made by a two-step replication of honeycomb structures of anodic alumina. *Science, 268*(5216), 1466-1468.

Matthew, R. P., & Drouin, D. (2010). Cathodoluminescence (CL) using a FESEM, modification to avoid lens aberration, Why use a FESEM? . (pp. 1-17). Australia: University of Technology Sydney.

McCreery, R. L. (2005). *Raman spectroscopy for chemical analysis* (Vol. 157). United State of America: John Wiley & Sons.

Mohanty, S. P., & Kougianos, E. (2006). Biosensors: a tutorial review. *Potentials, IEEE, 25*(2), 35-40.

Montoro, A. S., Natividad;Rodrigo, Regina;Hervas, David;Nacher, Óscar Alonso;Marti, Laura;Jambrina, Esther;Sarrias, Ana ;Perez-Calatayud, Jose ;Garcia, Teresa. (2014). Measuring the radiosensitivity of healthcare personnel in radiation-based medical diagnosis and treatment Industrial Hygiene.

Mott, N. (1938). *Note on the contact between a metal and an insulator or semi-conductor.* Paper presented at the Mathematical Proceedings of the Cambridge Philosophical Society.

Mtangi, W., Auret, F., Nyamhere, C., van Rensburg, P. J., Diale, M., & Chawanda, A. (2009). Analysis of temperature dependent I–V measurements on Pd/ZnO Schottky barrier diodes and the determination of the Richardson constant. *Physica B: Condensed Matter, 404*(8), 1092-1096.

Murakami, M. (1992). *Melt processed high-temperature superconductors* (Vol. 114). Singapor: World Scientific - Singapore

Nickels, P., Dittmer, W. U., Beyer, S., Kotthaus, J. P., & Simmel, F. C. (2004). Polyaniline nanowire synthesis templated by DNA. *Nanotechnology, 15*(11), 1524-1529.

Nikjoo, H. (2003). Radiation track and DNA damage. *Iranian Journal of Radiation Research, 1*(1), 3-16.

Norde, H. (1979). A modified forward I-V plot for Schottky diodes with high series resistance. *Journal of Applied Physics, 50*(7), 5052-5053.

Ohayon, Y. (2011). *Topological bonding of DNA nanostructures.* (PhD), New York University, Ann Arbor -United States.

Okahata, Y., Kobayashi, T., Nakayama, H., & Tanaka, K. (1998). DNA-aligned cast film and its anisotropic electron conductivity. *Supramolecular Science, 5*(3), 317-320.

Okahata, Y., Kobayashi, T., Tanaka, K., & Shimomura, M. (1998). Anisotropic electric conductivity in an aligned DNA cast film. *Journal of the American Chemical Society, 120*(24), 6165-6166.

Okur, S., Yakuphanoglu, F., Ozsoz, M., & Kadayifcilar, P. K. (2009). Electrical and interface properties of Au/DNA/n-Si organic-on-inorganic structures. *Microelectronic Engineering, 86*(11), 2305-2311.

Otsuka, Y., Lee, H.-y., Gu, J.-h., Lee, J.-O., Yoo, K.-H., Tanaka, H.,.Kawai, T. (2002). Influence of humidity on the electrical conductivity of synthesized DNA film on nanogap electrode. *Japanese Journal of Applied Physics, 41*(2A), 891-894.

Paul, A., Bhattacharya, B., & Bhattacharyya, T. K. (2014). Fabrication and performance of solution-based micropatterned DNA functionalized carbon nanotube network as humidity sensors. *Nanotechnology, IEEE Transactions on, 13*(2), 335-342.

Paul, A., Pramanick, B., Bhattacharya, B., & Bhattacharyya, T. K. (2013). Deoxyribonucleic acid functionalized carbon nanotube network as humidity sensors. *Sensors Journal, IEEE, 13*(5), 1806-1816.

Perret, G., Lacornerie, T., Kumemura, M., Lafitte, N., Guillou, H., Jalabert, L.,.Fujita, H. (2013). *Real time bio mechanical characterization of dna damage under therapeutic radiation beams.* Paper presented at the 17th International Conference on Miniaturized Systems for Chemistry and Life Sciences, microTAS 2013.

Porath, D., Bezryadin, A., De Vries, S., & Dekker, C. (2000). Direct measurement of electrical transport through DNA molecules. *Nature, 403*(6770), 635-638.

Požar, T. (2004). Electronic properties of DNA (pp. 1-17). Jadranska cesta 19, 1111 Ljubljana, Slovenia: University of Ljubljana.

Priyadarshy, S., Risser, S. M., & Beratan, D. N. (1998). DNA-mediated electron transfer. *Journal of Biological Inorganic Chemistry, 3*(2), 196-200.

Rakitin, A., Aich, P., Papadopoulos, C., Kobzar, Y., Vedeneev, A., Lee, J., & Xu, J. (2001). Metallic conduction through engineered DNA: DNA nanoelectronic building blocks. *Physical Review Letters, 86*(16), 3670-3673.

Ramaprasad, A., & Rao, V. (2010). Chitin–polyaniline blend as humidity sensor. *Sensors and Actuators B: Chemical, 148*(1), 117-125.

Ratner, M. (1999). Photochemistry: Electronic motion in DNA. *Nature, 397*(6719), 480-481.

Reddy, M. S. P., Kim, B.-J., & Jang, J.-S. (2014). Dual detection of ultraviolet and visible lights using a DNA-CTMA/GaN photodiode with electrically different polarity. *Optics Express, 22*(1), 908-915.

Reddy, V. R., Reddy, M. S. P., Lakshmi, B. P., & Kumar, A. A. (2011). Electrical characterization of Au/n-GaN metal–semiconductor and Au/SiO 2/n-GaN metal–insulator–semiconductor structures. *Journal of Alloys and Compounds, 509*(31), 8001-8007.

Reddy, V. S., Das, K., Dhar, A., & Ray, S. (2006). The effect of substrate temperature on the properties of ITO thin films for OLED applications. *Semiconductor Science and Technology, 21*(12), 1747-1752.

Rhoderick, E. H., & Williams, R. H. (1988). *Metal-semiconductor contacts* (Vol. 129): Clarendon Press Oxford.

Richter, J., Mertig, M., Pompe, W., Mönch, I., & Schackert, H. K. (2001). Construction of highly conductive nanowires on a DNA template. *Applied Physics Letters, 78*(4), 536-538.

Richter, J., Seidel, R., Kirsch, R., Mertig, M., Pompe, W., Plaschke, J., & Schackert, H. K. (2000). Nanoscale Palladium Metallization of DNA. *Nanoscale, 94*, 8720.

Rittersma, Z. (2002). Recent achievements in miniaturised humidity sensors-a review of transduction techniques. *Sensors and Actuators A: Physical, 96*(2), 196-210.

Rothemund, P. W., Papadakis, N., & Winfree, E. (2004). Algorithmic self-assembly of DNA Sierpinski triangles. *PLoS Biology, 2*(12), 2041-2053.

Roy, S., Vedala, H., Roy, A. D., Kim, D.-h., Doud, M., Mathee, K.,.Choi, W. (2008). Direct electrical measurements on single-molecule genomic DNA using single-walled carbon nanotubes. *Nano Letters, 8*(1), 26-30.

Sabet, M., Hassan, A., & Ratnam, C. T. (2012). Mechanical, electrical, and thermal properties of irradiated low-density polyethylene by electron beam. *Polymer Bulletin, 68*(9), 2323-2339.

Saenger, W. (1984). *Principles of Nucleic Acid Structure*. Verlag New York: Springer.

Saghaei, J., Fallahzadeh, A., & Saghaei, T. (2015). ITO-free organic solar cells using highly conductive phenol-treated PEDOT: PSS anodes. *Organic Electronics, 24*, 188-194.

Sakai, Y., Sadaoka, Y., & Matsuguchi, M. (1996). Humidity sensors based on polymer thin films. *Sensors and Actuators B: Chemical, 35*(1), 85-90.

Sartor, V., Boone, E., & Schuster, G. B. (2001). Long-distance radical cation migration through A/T base pairs in DNA: an experimental test of theory. *The Journal of Physical Chemistry B, 105*(45), 11057-11059.

Sawant, S., Zheng, W., Hopkins, K., Randers-Pehrson, G., Lieberman, H., & Hall, E. (2002). The radiation-induced bystander effect for clonogenic survival. *Radiation Research, 157*(4), 361-364.

Saxena, V., & Satheesh, S. K. (2013). Nanobioelectronics-Emerging trends and beyond: A Review. *Indian Journal of Biotechnology and Pharmaceutical Research, 1* (2), 9-16.

Schettino, G., Folkard, M., Prise, K., Vojnovic, B., Bowey, A., & Michael, B. (2001). Low-dose hypersensitivity in Chinese hamster V79 cells targeted with counted protons using a charged-particle microbeam. *Radiation Research, 156*(5), 526-534.

Schmitsdorf, R., Kampen, T., & Monch, W. (1997). Explanation of the linear correlation between barrier heights and ideality factors of real metal-semiconductor contacts by laterally nonuniform Schottky barriers. *Journal of Vacuum Science & Technology B, 15*(4), 1221-1226.

Schottky, W. (1938). Halbleitertheorie der sperrschicht. *Naturwissenschaften, 26*(52), 843-843.

Schuster, G. B. (2000). Long-range charge transfer in DNA: transient structural distortions control the distance dependence. *Accounts of Chemical Research, 33*(4), 253-260.

Schuster, G. B., & Landman, U. (2004). The mechanism of long-distance radical cation transport in duplex DNA: Ion-gated hopping of polaron-like distortions *Long-Range Charge Transfer in DNA I* (Vol. 236, pp. 139-161): Springer Berlin Heidelberg.

Seeman, N. C. (2003). At the crossroads of chemistry, biology, and materials: structural DNA nanotechnology. *Chemistry & Biology, 10*(12), 1151-1159.

Seeman, N. C., & Belcher, A. M. (2002). Emulating biology: building nanostructures from the bottom up. *Proceedings of the National Academy of Sciences, 99*(suppl 2), 6451-6455.

Setter, J., Hesketh, P. J., & Hunter, G. W. (2006). Sensors: engineering structures and materials from micro to nano. *Interface, 15*(1), 66-69.

Shinde, K. N., Dhoble, S., Swart, H., & Park, K. (2012). Basic mechanisms of photoluminescence *Phosphate Phosphors for Solid-State Lighting* (Vol. 174, pp. 41-59): Springer Berlin Heidelberg.

Simmons, J. G. (1971). *DC conduction in thin films* (Vol. 5). London: Mills and Boon Ltd.

Singh, K. V., Alim, K., Wang, X., Balandin, A., Ozkan, C. S., & Ozkan, M. (2005). Bio-assembly of Nanoparticles for Device Applications. *NSTI-Nanotech, 2*, 420-421.

Slinker, J. D., Muren, N. B., Renfrew, S. E., & Barton, J. K. (2011). DNA charge transport over 34 nm. *Nature Chemistry, 3*(3), 228-233.

Sokolov, P., Bazlov, N., Puchkova, A., Vyvenko, O., & Kasyanenko, N. (2011). DNA immobilization on n-type silicon surface and electrophysical properties of Au-DNA-(n-Si) structures. *Protection of metals and physical chemistry of surfaces, 47*(5), 566-571.

Sönmezoğlu, S., Sönmezoğlu, Ö. A., Çankaya, G., Yıldırım, A., & Serin, N. (2010). Electrical characteristics of DNA-based metal-insulator-semiconductor structures. *Journal of Applied Physics, 107*(12), 1245181-1245186.

Štěpán, V., & Davídková, M. (2014). RADAMOL tool: role of radiation quality and charge transfer in damage distribution along DNA oligomer. *The European Physical Journal D, 68*(8), 1-7.

Stetter, J. R., Penrose, W. R., & Yao, S. (2003). Sensors, chemical sensors, electrochemical sensors, and ECS. *Journal of The Electrochemical Society, 150*(2), S11-S16.

Storm, A., Van Noort, J., De Vries, S., & Dekker, C. (2001). Insulating behavior for DNA molecules between nanoelectrodes at the 100 nm length scale. *Applied Physics Letters, 79*(23), 3881-3883.

Stubbe, J., Nocera, D. G., Yee, C. S., & Chang, M. C. (2003). Radical initiation in the class I ribonucleotide reductase: long-range proton-coupled electron transfer? *Chemical Reviews, 103*(6), 2167-2202.

Sun, Y., & Kiang, C.-H. (2005). DNA-based artificial nanostructures: Fabrication, properties, and applications (Vol. 2, pp. 224-246): American Scientific Publishers.

Sze, S. M., & Ng, K. K. (2006). *Physics of semiconductor devices* (3 ed.). Hoboken, New Jersey.: John Wiley & Sons.

Tahir, M., Sayyad, M. H., Shahid, M., Chaudry, J. A., & Munawar, M. (2012). *Fabrication of Al/N-BuHHPDI/ITO Schottky barrier diode and investigation of its electrical properties.* Paper presented at the International Conference on Advances in Electrical and Electronics Engineering (ICAEEE'2012).

Taniguchi, M., Lee, H.-Y., Tanaka, H., & Kawai, T. (2003). Electrical Properties of Poly (dA)-Poly (dT) and Poly (dG)-Poly (dC) DNA Doped with Iodine Molecules. *Japanese Journal of Applied Physics, 42*(3A), L215-L216.

Tans, S. J., Verschueren, A. R., & Dekker, C. (1998). Room-temperature transistor based on a single carbon nanotube. *Nature, 393*(6680), 49-52.

Terawaki, A., Otsuka, Y., Lee, H., Matsumoto, T., Tanaka, H., & Kawai, T. (2005). Conductance measurement of a DNA network in nanoscale by point contact current imaging atomic force microscopy. *Applied Physics Letters, 86*(11), 113901-113903.

Tikhomirov, G., Hoogland, S., Lee, P., Fischer, A., Sargent, E. H., & Kelley, S. O. (2011). DNA-based programming of quantum dot valency, self-assembly and luminescence. *Nature nanotechnology, 6*(8), 485-490.

Torimoto, T., Yamashita, M., Kuwabata, S., Sakata, T., Mori, H., & Yoneyama, H. (1999). Fabrication of CdS nanoparticle chains along DNA double strands. *The Journal of Physical Chemistry B, 103*(42), 8799-8803.

Tran, P., Alavi, B., & Gruner, G. (2000). Charge transport along the λ-DNA double helix. *Physical Review Letters, 85*(7), 1564-1567.

Traversa, E. (1995). Ceramic sensors for humidity detection: the state-of-the-art and future developments. *Sensors and Actuators B: Chemical, 23*(2), 135-156.

Tuğluoğlu, N., & Karadeniz, S. (2012). Analysis of current–voltage and capacitance–voltage characteristics of perylene-monoimide/n-Si Schottky contacts. *Current Applied Physics, 12*(6), 1529-1535.

Tung, R. (1992). Electron transport at metal-semiconductor interfaces: General theory. *Physical Review B, 45*(23), 13509-13523.

Turro, N. J., & Barton, J. K. (1998). Paradigms, supermolecules, electron transfer and chemistry at a distance. What's the problem? The science or the paradigm? *Journal of Biological Inorganic Chemistry, 3*(2), 201-209.

Umana-Membreno, G. A., Dell, J., Parish, G., Nener, B., Faraone, L., & Mishra, U. (2003). 60 Co gamma irradiation effects on n-GaN Schottky diodes. *Electron Devices, IEEE Transactions on, 50*(12), 2326-2334.

Vaishnav, V., Patel, P., & Patel, N. (2005). Indium tin oxide thin film gas sensors for detection of ethanol vapours. *Thin solid films, 490*(1), 94-100.

Varghese, O. K., & Grimes, C. A. (2003). Metal oxide nanoarchitectures for environmental sensing. *Journal of Nanoscience and Nanotechnology, 3*(4), 277-293.

Venkatramani, R., Oh, C., Grote, J., & Beratan, D. (2009). *Photoconductivity and current-voltage characteristics of thin DNA films: experiments and modeling.* Paper presented at the SPIE NanoScience+ Engineering.

Vick, A. J. (2011). *Measuring Low Dimensional Schottky Barriers of Rare Earth Silicide-Silicon Interfaces.* (PhD), University of York.

Voityuk, A. A. (2011). Long-range electron transfer in biomolecules. Tunneling or hopping? *The Journal of Physical Chemistry B, 115*(42), 12202-12207.

Vu, X., GhoshMoulick, R., Eschermann, J., Stockmann, R., Offenhäusser, A., & Ingebrandt, S. (2010). Fabrication and application of silicon nanowire transistor arrays for biomolecular detection. *Sensors and Actuators B: Chemical, 144*(2), 354-360.

Wagenknecht, H. A. (2005). *Charge Transfer in DNA*. VCH Verlag GmbH & Co. KGaA,Weinheim, FRG: Wiley

Wan, C., Fiebig, T., Kelley, S. O., Treadway, C. R., Barton, J. K., & Zewail, A. H. (1999). Femtosecond dynamics of DNA-mediated electron transfer. *Proceedings of the National Academy of Sciences, 96*(11), 6014-6019.

Wang, J., Rivas, G., Ozsoz, M., Grant, D. H., Cai, X., & Parrado, C. (1997). Microfabricated electrochemical sensor for the detection of radiation-induced DNA damage. *Analytical chemistry, 69*(7), 1457-1460.

Wang, S., Kang, Y., Wang, L., Zhang, H., Wang, Y., & Wang, Y. (2013). Organic/inorganic hybrid sensors: A review. *Sensors and Actuators B: Chemical, 182*, 467-481.

Watson, J., & Crick, F. (2003). A structure for deoxyribose nucleic acid *A century of Nature: twenty-one discoveries that changed science and the world* (pp. 82-84). United state of America: University of Chicago Press.

Watson, J. D., & Crick, F. H. (1953). *The structure of DNA.* Paper presented at the Cold Spring Harbor Symposia on Quantitative Biology.

Welch, K., Blom, T., Leifer, K., & Strömme, M. (2011). Enabling measurements of low-conductance single molecules using gold nanoelectrodes. *Nanotechnology, 22*(12), 125707-125713.

Williams, T. T., Odom, D. T., & Barton, J. K. (2000). Variations in DNA charge transport with nucleotide composition and sequence. *Journal of the American Chemical Society, 122*(37), 9048-9049.

Xu, M., Tsukamoto, S., Ishida, S., Kitamura, M., Arakawa, Y., Endres, R., & Shimoda, M. (2005). Conductance of single thiolated poly (GC)-poly (GC) DNA molecules. *Applied Physics Letters, 87*(8), 0839021-0839023.

Yakuphanoglu, F. (2008). Analysis of interface states of metal–insulator–semiconductor photodiode with n-type silicon by conductance technique. *Sensors and Actuators A: Physical, 147*(1), 104-109.

Yamada, M., & Sugiyama, T. (2008). Utilization of DNA-metal Ion Biomatrix as a Relative Humidity Sensor. *Polymer journal, 40*(4), 327-331.

Yamahata, C., Collard, D., Takekawa, T., Kumemura, M., Hashiguchi, G., & Fujita, H. (2008). Humidity dependence of charge transport through DNA revealed by silicon-based nanotweezers manipulation. *Biophysical journal, 94*(1), 63-70.

Yan, H., Park, S. H., Finkelstein, G., Reif, J. H., & LaBean, T. H. (2003). DNA-templated self-assembly of protein arrays and highly conductive nanowires. *Science, 301*(5641), 1882-1884.

Yaworski, B., & Detlaf, A. (1968). *Handbook of physics*. Moscow: Nauka

Yoo, K.-H., Ha, D., Lee, J.-O., Park, J., Kim, J., Kim, J.,.Choi, H. Y. (2001). Electrical conduction through poly (dA)-poly (dT) and poly (dG)-poly (dC) DNA molecules. *Physical Review Letters, 87*(19), 1981021-1981024.

Yudiarsah, E., Suhendro, D. K., & Saleh, R. (2014). *The Effect of Backbone Disorder on Electrical Conductivity of Poly (dG)-Poly (dC) DNA Molecule at Room Temperature.* Paper presented at the Advanced Materials Research.

Zhang, Y., Austin, R., Kraeft, J., Cox, E., & Ong, N. (2002). Insulating behavior of λ-DNA on the micron scale. *Physical Review Letters, 89*(19), 198102.

Zhang, Y., Fu, W., Yang, H., Li, M., Li, Y., Zhao, W.,.Liu, B. (2008). A novel humidity sensor based on Na 2 Ti 3 O 7 nanowires with rapid response-recovery. *Sensors and Actuators B: Chemical, 135*(1), 317-321.

Zhou, Y., Johnson, A. T., Hone, J., & Smith, W. F. (2003). Simple fabrication of molecular circuits by shadow mask evaporation. *Nano Letters, 3*(10), 1371-1374.

Zwolak, M., & Di Ventra, M. (2005). Electronic signature of DNA nucleotides via transverse transport. *Nano Letters, 5*(3), 421-424.

LIST OF PUBLICATIONS

1. **Hassan Maktuff Jaber Al-Ta'ii**, Yusoff Mohd Amin, Vengadesh Periasamy. (2014). Investigations of electrical properties of structures Al-DNA-ITO-Al exposed to alpha particles. *Radiation Measurements*, 72, 85-94. doi.org/10.1016/j.radmeas.2014.11.011

2. **Hassan Maktuff Jaber Al-Ta'ii**, Yusoff Mohd Amin, Vengadesh Periasamy. (2015). Calculation of the electronic parameters of an Al/DNA/p-Si Schottky barrier diode influenced by alpha radiation. *Sensors*, 15, 4810-4822; doi:10.3390 /s15 030 4810.

3. **Hassan Maktuff Jaber Al-Ta'ii**, Vengadesh Periasamy, Yusoff Mohd Amin. (2015). Electronic properties of DNA-based Schottky barrier diodes in response to alpha particles. *Sensors*, 15, 11836-11853; doi : 10.33 90 /s150511836.

4. **Hassan Maktuff Jaber Al-Ta'ii**, Vengadesh Periasamy, Yusoff Mohd Amin. (2015). Detection of alpha particles using DNA/Al Schottky junctions. *Journal of Applied Physics*, 118, 114502; doi.org/10.1063/1.4930888.

5. **Hassan Maktuff Jaber Al-Ta'ii**, Vengadesh Periasamy, Yusoff Mohd Amin. (2015). Electronic characterization of Au/DNA/ITO metal-semiconductor-metal diode and its application as a radiation sensor. *PLOS ONE*, 11, e0145423-e0145440; doi.org:10.1371/journal.pone.0145423.

6. **Hassan Maktuff Jaber Al-Ta'ii**, Vengadesh Periasamy, Yusoff Mohd Amin. (2016). Humidity-dependent characteristics of DNA thin film-based Al/DNA/Al surface-type cell. *Sensors and Actuators B*, 232, 195–202. doi.org/10.1016/j.snb.2016.03.093.

7. **Hassan Maktuff Jaber Al-Ta'ii**, Vengadesh Periasamy, Yusoff Mohd Amin. (2016). Humidity influenced capacitance and resistance of an Al/DNA/Al Schottky diode irradiated by alpha particles. *Scientific Reports*, 6(25519), 1-13. doi.org/10.1038/srep25519.

8. Vengadesh Periasamy, Nastaran Rizan, **Hassan Maktuff Jaber Al-Ta'ii**, Tan Lee Shin, Hairul Annuar Tajuddin and Mitsumasa Iwamoto. (2016). Measuring the Electronic Properties of DNA-Specific Schottky Diodes Towards Detecting and Identifying Basidiomycetes DNA. *Scientific Reports*, 6(29879), 1-9, doi.org/10.1038/srep29879

LIST OF CONFERENCE

1. The 5th International Conference on Functional Materials & Devices 2015 **(ICFMD 2015)**, 3th - 5th August 2015, New York Hotel, Johor Bahru, Malaysia.